UNIVERSIDADE FEDERAL DE PERNAMBUCO
DEPARTAMENTO DE FÍSICA – CCEN
PROGRAMA DE PÓS-GRADUAÇÃO EM FÍSICA

ANDERSON MONTEIRO AMARAL

TRANSVERSE OPTICAL PHENOMENA WITH GAUSSIAN BEAMS AND OPTICAL VORTICES

Recife
2016

ANDERSON MONTEIRO AMARAL

TRANSVERSE OPTICAL PHENOMENA WITH GAUSSIAN BEAMS AND OPTICAL VORTICES

Tese apresentada ao Programa de Pós-Graduação em Física da Universidade Federal de Pernambuco, como requisito parcial para a obtenção do título de Doutor em Física.

Orientador:
Prof. Dr. Cid Bartolomeu de Araújo
Universidade Federal de Pernambuco

Recife
2016

Catalogação na fonte
Bibliotecária Joana D'Arc Leão Salvador CRB 4-572

A485t Amaral, Anderson Monteiro.
Transverse optical phenomena with Gaussian beams and optical vortices / Anderson Monteiro Amaral . – 2016.
171 p.: fig., tab.

Orientador: Cid Bartolomeu de Araújo.
Tese (Doutorado) – Universidade Federal de Pernambuco. CCEN. Física. Recife, 2016.
Inclui referências e apêndices.

1. Óptica física. 2. Óptica não-linear. I. Araújo, Cid Bartolomeu de (Orientador). II. Titulo.

535.2 CDD (22. ed.) UFPE-FQ 2016-27

ANDERSON MONTEIRO AMARAL

TRANSVERSE OPTICAL PHENOMENA WITH GAUSSIAN BEAMS AND OPTICAL VORTICES

Tese apresentada ao Programa de Pós-Graduação em Física da Universidade Federal de Pernambuco, como requisito parcial para a obtenção do título de Doutor em Física.

Aprovada em: 29/02/2016.

BANCA EXAMINADORA

_____
Prof. Dr. Cid Bartolomeu de Araújo
Orientador
Universidade Federal de Pernambuco

_____
Prof. Dr. José Roberto Rios Leite
Examinador Interno
Universidade Federal de Pernambuco

_____
Prof. Dr. José Wellington Rocha Tabosa
Examinador Interno
Universidade Federal de Pernambuco

_____
Prof. Dr. Antonio Zelaquett Khoury
Examinador Externo
Instituto de Física daUniversidade Federal Fluminense

_____
Prof. Dr. Herch Moyses Nussenzveig
Examinador Externo
Universidade Federal do Rio de Janeiro

Acknowledgements

Por mais que a tese seja uma obra identificada por um único autor, este manuscrito não existiria sem o apoio e suporte de tantas pessoas.

Inicialmente, nada disto seria possível sem os meus pais, que sempre me incentivaram e deram um apoio fundamental para que eu avançasse em minha vida acadêmica ao longo de tanto tempo. Devo também agradecer a todos de minha família, pois sempre compreenderam a minha ausência em prol dos estudos e da pesquisa científica. Não posso me esquecer de reafirmar aqui também o suporte de Jessica ao longo do mestrado e doutorado, onde participou dos momentos bons e de outros nem tanto. Foram muitos os momentos de dificuldade pelos quais passei, e teria sido muito mais difícil chegar até este momento sem tanta ajuda e compreensão que recebi.

Devo também agradecer aos professores que tanto me ensinaram até que eu chegasse a este momento. Por mais que eu sempre tenha tido uma inquietude pelo aprendizado, sempre tentei referenciar a minha vida nos valores dos mestres que tive até hoje. Digo mestres num sentido mais amplo, pois também aprendi bastante de pessoas com vasta experiência mas sem títulos acadêmicos. Acredito profundamente na não linearidade do universo, do aprendizado e da vida. Talvez este seja um dos motivos de eu sempre ter me sentido tão bem ao longo destes 6 anos no laboratório de óptica não linear. O Proféssor Cid é uma pessoa altamente não linear (nos melhores sentidos imagináveis), e sempre aparece ideias muito interessantes para diversos projetos. Sinto-me na obrigação de agradecer ao Proféssor não apenas pela instrução e pelas oportunidades que me propiciou, mas também pela liberdade que me deu para seguir minha intuição e pela fonte de inspiração que sempre será. Devo também agradecer à Edilson, que também me acompanhou ao longo destes anos na UFPE desde o mestrado, e me deu bastante apoio nas mais diversas ocasiões. Cid e Edilson me permitiram uma formação científica sólida, tal que hoje em dia eu enxergar o mundo com horizontes mais vastos.

É importante frisar também os amigos me acompanharam ao longo destes anos. Desde o Fábio (“Japonês”) e sua sabedoria nipônica ao grande Murilo (“Marujo”) e suas aventuras pelos sete mares, foram várias as pessoas com que passei momentos importantes. Nos “Matéria Condensada” da vida vários foram os aprendizados com Fábio Ribeiro, sobre grandes problemas de supercondutividade e magnetismo em seu sistema fortemente correlacionado. Também ao Gran Javier del Cristo devo minhas saudações pela sua força e garra, e ao Ceará (também conhecido como Tiago Saraiva) pelas tantas ideias trocadas. No grupo de óptica, onde passei a maior parte destes últimos anos, tive o prazer da companhia de tantas pessoas. Em disparada, meu camarada Albert, com quem compartilho o laboratório a tanto tempo e sempre foi tão acessível, multifuncional e eficiente. Também há Meu Caro Hans e Jamil (“Mr. Jammil”), com quem compartilhei tantas ideias e almoços no IF, e Kelly com sua

impressionante energia para o trabalho experimental. Mas também à todos os membros do laboratório nestes anos, Ronaldo (“Captain”), Gemima, Felipe, Henrique, André, Andreia, Renato, Antônio Marcos (“Nick”), Euclides, Sandra e Whualkuer. Devo também mencionar o pessoal do nosso Student Chapter, como Jaque que me “repassou” a viagem ao Frontiers in Optics, bem como o trio composto ainda por Rafael e Milriam que me deram a oportunidade de ser presidente do grupo em 2014 partindo de um patamar tão elevado. Foram tantas as pessoas que ajudaram nestes momentos que é provável que algum nome deixe de ser escrito abaixo. Mas a realização do simpósio não teria sido possível sem a ajuda de vocês Albert, Jaque, Allan, Milriam, Kelly, Isadora, Marina, Welliton e Péricllles.

Finalmente, é importante agradecer a quem deu o suporte para que eu desenvolvesse minhas atividades. Agradeço ao CNPq, por meio da bolsa de doutorado e por meio do INCT de Fotônica, e à FACEPE pelo suporte ao nosso grupo de pesquisa. Agradeço também aos técnicos do nosso departamento (“São”) Marcos, Daniel, Sergio (“@df”), Virgínia, Severino e João, pois sem eles as atividades seriam exponencialmente mais difíceis, e às nossas secretárias Flávia, Ilaine, Alexsandra e Hilda, pela prestatividade e agilidade.

"... he pursued his way, taking that which his horse chose,

for in this he believed lay the essence of adventures." (Dom Quixote)

"A method is more important than a discovery,

since the right method will lead to new and

even more important discoveries." (Attributed to Lev Landau[1])

"Nunca desista de seu sonho.

Se acabou numa padaria,

procure em outra." (Barão de Itararé)

[1] Attributed by Lance Dixon, on a comment after his APS Sakurai Prize (2013). http://goo.gl/RW5otj (accessed in 15/02/2016)

Abstract

In this thesis are presented various results regarding the transverse structure of light beams in the paraxial propagation regime, with a special concern with singularities in the transverse profile and in nonlinear optics applications. Theoretical and experimental tools were developed for the study of Optical Vortices (OV) and its most important characteristics, as the Orbital Angular Momentum (OAM) and the Topological Charge (TC). In a first step, we theoretically described and experimentally demonstrated that it is possible to shape the intensity profile of a beam containing OV by distributing TC over the plane transverse to the propagation direction [1]. The TC is associated with a phase singularity that implies in points of zero intensity. By distributing the TC on the transverse plane, it is possible to shape the beam dark region and also the OAM profile with the goal of optimizing the light beam for a given application. However, a problem identified in [1] was that most of the current available techniques to characterize OAM light implicitly assume that the beam has cylindrical symmetry, thus being inadequate to characterize fields resulting from more general TC distributions. These problems were approached in a second work [2], where it was shown that by measuring the field transverse amplitude and phase profiles it is possible to measure the OAM and the TC in TC distributions with arbitrary geometries. By combination of the results [1] and [2] it is possible to optimize and characterize the TC distributions for given applications, as for example by designing the transverse forces in an optical tweezer for microparticle manipulation. An important theoretical unfold during these works was the identification of an analogous relation between the field transverse phase in a TC distribution with the Coulomb potential in two-dimensional electrostatics. We then introduced in [3] the Topological Potential (TP) concept which allows the design of structured optical beams with complex spatial profiles inspired by two-dimensional electrostatics analogies. The TP can be used to describe a broad class of TC distributions, as those from [1,2] or the more sophisticate examples in [3]. In another set of results, it is discussed the possibility of using concepts and the formalism of quantum mechanics to solve light propagation problems in the classical approximation. Among the results obtained, it should be remarked that the formalism obtained has a simple and direct relation with ABCD matrices and ray optics [4]. These results were used to understand light propagation in systems containing nonlinear materials, as in SLIM [5] and D4σ [6] techniques. In [5, 6] the theoretical results were compared with experimental data obtained from standard samples, as carbon dissulfide (CS_2), acetone and fused silica. It was obtained a very good agreement between the measured optical nonlinearities and the results established in literature for these materials.

Keywords: Singular optics. Light orbital angular momentum. Optical wavefront. Holography. Nonlinear optics. Physical optics.

Resumo

Nesta tese são apresentados resultados relacionados com a estrutura transversal de feixes de luz no regime paraxial de propagação, com uma atenção especial em singularidades no perfil transversal e em aplicações para óptica não linear. Foram desenvolvidas ferramentas teóricas e experimentais para o estudo de vórtices ópticos (*Optical Vortices* - OVs), e suas características mais importantes, como o momento angular orbital (*Orbital Angular Momentum* - OAM) e a carga topológica (*Topological Charge* - TC). Inicialmente, foi teoricamente descrito e experimentalmente demonstrado como é possível moldar o perfil de intensidade de um feixe contendo OVs usando uma distribuição de TC sobre o plano transversal à direção de propagação [1]. A TC está associada a uma singularidade na fase, o que implica em um zero de intensidade. Ao se distribuir a TC sobre o plano transversal, é possível moldar o formato da região de intensidade nula e também o perfil de OAM no intuito de otimizar o feixe para uma dada aplicação. No entanto, um problema identificado neste trabalho é que a maior parte das técnicas de caracterização disponíveis para luz com OAM implicitamente supunham que o feixe possui simetria cilíndrica, e portanto não eram adequadas para caracterizar campos obtidos a partir de distribuições de TC com geometrias mais gerais. Tais problemas foram abordados em um segundo trabalho [2], onde foi mostrado que por meio de medições dos perfis transversais de amplitude e fase do campo elétrico é possível medir o OAM e a TC em distribuições de TC com formas geométricas arbitrárias. A união dos trabalhos [1] e [2] permite então que as distribuições de TC possam ser adequadamente otimizadas e caracterizadas para aplicações específicas, como por exemplo ao moldar as forças transversais numa pinça óptica para a manipulação de micropartículas. Um desdobramento teórico importante obtido foi identificar uma relação análoga entre o perfil de fase em uma distribuição de TC com o potencial de Coulomb em eletrostática bidimensional. Foi então introduzido em [3] o conceito de potencial topológico (*Topological Potential* - TP) que possibilita a construção de feixes ópticos estruturados com perfis espaciais complexos inspirados em analogias com eletrostática bidimensional. O TP pode ser usado na descrição de uma grande variedade de distribuições de TC, como nos feixes em [1, 2] ou nos exemplos mais sofisticados em [3]. Posteriormente, é discutida a possibilidade de se utilizar conceitos e o formalismo da mecânica quântica na solução de problemas de propagação da luz descrita na aproximação clássica. Dentre os resultados obtidos, destaca-se que o formalismo possui uma relação simples e direta com as matrizes ABCD e a óptica de raios [4]. Estes resultados foram utilizados na compreensão da propagação da luz em sistemas contendo materiais não lineares, como nas técnicas *SLIM* [5] e D4σ [6]. Nos trabalhos [5, 6] os resultados teóricos foram comparados com dados experimentais obtidos em amostras padrão, como dissulfeto de carbono (CS_2), acetona e sílica fundida. Foi obtida uma concordância muito boa entre os

valores medidos para as não linearidades ópticas nestes materiais e os valores estabelecidos na literatura.
Palavras-chave: Óptica singular. Momento angular orbital da luz. Frente de onda da luz. Holografia. Óptica não linear. Óptica física.

List of Figures

List of Tables

Nomenclature

ℓ-OAM	Local orbital angular momentum
HP	Heisenberg Picture
IP	Interaction Picture
NL	Nonlinear
NLC	Nematic liquid crystal
OAM	Orbital Angular Momentum
OV	Optical Vortex
QM	Quantum Mechanics
SDI	Spherical dielectric interface
SLIM	Scattered Light Imaging Method
SLM	Spatial Light Modulator
SP	Schrödinger Picture
SVEA	Slowly Varying Envelope Approximation
TC	Topological Charge
TIM	Transverse Irradiance Moments
TP	Topological Potential

Contents

1 Introduction

This thesis develops a special interest in phenomena related to light's transverse degrees of freedom. While it is a customary simplification to represent an optical beam as a plane wave, or as a bundle of optical rays, these pictures neglect light transverse features. Even though it is possible to adequately explain a wide range of physical processes using these simplifications, both plane waves and optical rays are idealizations. In real world the light beams always have a finite transverse extent, which adds important ingredients to the design of optical systems and to light interactions and manipulation. As examples, we briefly mention how these ideas apply to super-resolution microscopy [7], in the development of the Advanced Laser Interferometer Gravitational-Wave Observatory (Advanced LIGO) [8] and in applications of structured light.

1.1 Light transverse structure as a key element in optics

Super-resolution microscopy

Ernst Abbe found in 1873 that there is a minimum spot diameter d for a beam under focusing, given by

$$d = \frac{\lambda}{2n\sin\theta}, \tag{1.1}$$

where λ is the wavelength of light, n the medium refractive index and θ the half-angle determined by the lens at the focus position. The resolution limit ensures that it is not possible to localize light in a distance smaller than d. Conversely, Abbe's limit also indicates that the images of two objects separated by a distance smaller than d cannot be distinguished in an optical microscope. Since microscopes typically use visible light, it can be estimated that $d \approx 200$ nm. Notice that an increase in the optical resolution by simply reducing λ is often not feasible, since there are various physical difficulties. For instance, ultraviolet light sources are more complex and typically have lower power. Besides that, various optical materials become opaque or highly absorbing in the ultraviolet.

Since there are various structures of physical, chemical and biological interest whose characteristic sizes have tens of nanometers, it was believed for more than a century that optical microscopes could not be used to resolve nanoscale structures. Alternatives to light microscopy were developed to increase the image resolution along the 20th century, as for example electron microscopy, but optical techniques remain as one of the most important approaches in biology and medicine [9]. Only through optical techniques it is feasible to introduce labels that track biological processes and structures in real-time using living samples.

Several ground-breaking experiments were necessary to surpass the diffraction limit, what was ultimately achieved in the 1990's. For instance, E. Schrödinger stated that [10]

> "...we never experiment with just one electron or atom or (small) molecule. In thought-experiments we sometimes assume that we do; this invariably entails ridiculous consequences... In the first place it is fair to state that we are not experimenting with single particles, any more than we can raise Ichthyosauria in the zoo."

and many scientists still believed in 1980's that experimenting a single molecule in a condensed matter sample was an impossible task [11]. However, W. E. Moerner built a spectroscopic setup in which he could find a signature due to isolated single molecules in 1987 [12]. Later on, E. Betzig have developed the idea that by controlling the fluorescence emission, such that closely spaced molecules do not emit light simultaneously, it was possible to localize the molecule position with an accuracy which is not diffraction limited [13]. Therefore, by mapping the fluorescent marker positions it becomes possible to build an image with a resolution greater than that allowed by light diffraction. Following these works, several alternative techniques were adopted to achieve super-resolution through the control of fluorescence emission [11, 14].

While Betzig and Moerner's approach to achieve super-resolution depends on fluorescence emission with some molecular parameter to distinguish the emission from close molecules, S. W. Hell developed an alternative [9]. Suppose that some molecules are excited with a diffraction limited beam. The spot size of the excited molecules fluorescence will also be diffraction limited. However, it is possible to deplete the molecules excitation by using a second beam through stimulated emission, which is the underlying principle behind Stimulated Emission Depletion (STED) microscopy. If the excitation and depletion beams have distinct transverse spatial profiles, it is possible to manipulate the volume of excited molecules through the fine control of molecular excitation and stimulated emission. For example, to obtain a circular spot it is possible to deplete the molecular excitation using a beam containing an optical vortex. The optical vortex ensures that the irradiance is zero at the center of the beam, and grows along the radial direction. Therefore, if only the molecules near the center of the vortex are left in the excited state, it is possible to reduce the effective spot size of excited molecules to

$$d_{\mathrm{STED}} = \frac{\lambda}{2n\sin\theta\sqrt{1+I/I_S}}, \tag{1.2}$$

where I is the depletion beam irradiance and I_S is a saturation intensity [7]. Since the ratio I/I_S can be made arbitrarily large, the minimum spot diameter can be significantly reduced. Therefore, the control of light transverse structure is a key element to surpass the diffraction limit in STED microscopy.

As a final comment, E. Betzig, S. W. Hell and W. E. Moerner have been awarded the Nobel prize in Chemistry in 2014 for the development of super-resolved fluorescence microscopy.

Advanced LIGO

The Advanced LIGO detects gravitational waves by sensing the arm length differences in a Michelson interferometer [8]. Each arm has a length of 4 km, and Fabry-Perot cavities are used to enhance the interaction time between photons and gravitational waves. The apparatus is able to detect arm length variations with exquisite accuracy, detecting strains of 10^{-21}, or much less than the radius of an atomic nucleus. Only with such sensitivity it became possible to perform the first direct gravitational waves observation on September 14 of 2015. In that event it was observed the merging of two black holes at a distance of 1.3 billion light years [15].

Some technical characteristics of Advanced LIGO can be accessed in [8]. The laser passes through various amplification and filtering stages before entering the interferometer, to ensure a high CW input power (125 W) and a single transverse mode operation (TEM_{00}, or a Gaussian beam profile). To reach maximum sensitivity in the detection of gravitational waves, several improvements are necessary to remove various difficulties and noise sources. For example, the residual gas in the vacuum chambers modify the optical path and seismic waves change the arm length. Because of the recycling cavity design, the Fabry-Perot cavities in each Michelson interferometer arm operate with 750 kW of continuous wave optical power. At such power levels, radiation pressure can misalign the interferometer arms and several noise sources due to thermal and quantum effects[1] become relevant. For instance, the thermal noise due to the optical absorption is critical because it generates parametric acousto-optic effects, producing high-order transverse optical modes. At the detection stage there is another mode filter before the homodyne detection to ensure that only the TEM_{00} mode is monitored.

Therefore, it was crucial to consider the transverse structure of light in each design step of Advanced LIGO to obtain the required sensitivity levels.

Applications of structured light and optical vortices

When studying ultrasound scattering, J. Nye and M. Berry have found that the scattered waves contained dislocations, analogously to the defects found in imperfect crystals [16]. At these dislocations, the field amplitude is zero, while the phase changes by a multiple of 2π in a closed contour around it. The presence of dislocations are a general feature observed in waves scattering, and a more complete historical perspective can be appreciated in [17].

In terms of optics, these singularities are evident in speckle due to lasers [18], or may also appear in the polarization degree of freedom [19]. It is remarkable to notice that in the description of light in optical cavities, the mathematical solutions containing phase and polarization singularities were already given in the classical “Laser Beams and Resonators” by

[1] Fluctuations in the photon arrival rate (shot-noise) and in the radiation pressure due to photon number fluctuations inside the Fabry-Perot cavities.

H. Kogelnik and T. Li [20], and were well known at that time. However, the physical importance of these terms was not much appreciated in the optics community until L. Allen and collaborators described that these wavefront singularities were related with the orbital angular momentum of light [21]. Even though the angular momentum of light was measured in 1936 by R. A. Beth [22], by detecting the rotation of a waveplate due to circularly polarized light, it was previously thought that the practical source of angular momentum in light was the polarization only. In the work by Allen and collaborators, it was described that an helical phase profile also provided light with angular momentum. The studies in singularities in light fields have significantly increased since 1992, and also the number of applications envisioned to these light fields increased correspondingly [17, 23]. There are proposals for applications in classical and quantum communications [24–26] and to control the transverse motion of particles in optical tweezers [27, 28].

In the optical spectroscopy community, also there was not much interest in helical wave fronts before 1992. Since atoms and molecules are much smaller than light wavelengths up to the ultraviolet, electric dipole transitions dominate the spectral response of most materials and substances [29]. Electric quadrupole and magnetic dipole transitions are usually called forbidden transitions because their transition probabilities are much smaller than those of nearby electric dipole transitions (allowed transitions). However, since helical wavefronts are easy to produce, it was possible to explore a new phenomenology. In our physics department there are some relevant contributions in this area. For example, the helical wavefront due to an Laguerre-Gauss mode was used to induce rotational motion in an atomic cloud, and later was observed a spectral shift due to rotational Doppler effect [30]. In another study, it was theoretically proposed that helical wavefronts enhance the transition probability of forbidden transitions [31]. This enhancement was recently verified for magnetic dipole transitions [32]. It is also worth mentioning that our physics department optics group already produced experimental thesis in which the light angular momentum was used to manipulate an atomic cloud, or the cloud nonlinear optical properties was used to manipulate the angular momentum of light [33–35].

Besides singularities, the transverse structure of light also gives important corrections to physical phenomena, as in the propagation velocity of light [36] and in the phase-matching condition in nonlinear optics [37].

1.2 This thesis contents

In this thesis, the transverse profile of light beams is studied, with a special emphasis in phase singularities over the wavefront and Gaussian beams in nonlinear optical media for paraxial optical beams. In Chapter 2 we present an advanced introduction to concepts related to light propagation in the linear and nonlinear regime. This chapter is optional for understanding most of the remaining parts of this manuscript, but it is strongly recommended

for readers wanting to follow each detail of the remaining chapters. For instance, the paraxial approximation is rigorously discussed starting from Maxwell equations in sec. 2.2, and as an original result we obtained the expression for the paraxial propagating modes with a finite energy starting from the underlying scaling symmetry. We also discuss in sec. 2.3 how light propagates in nonlinear materials, and a variational approach is introduced to obtain the critical power for self-focusing in third-order media. In sec. 2.4 there are some comments about energy and momentum of a light beam.

To understand various experimental results presented in this thesis it is performed in chapter 3 a discussion of some holography concepts. There is a short introduction to fundamental concepts in sec. 3.2 and a brief introduction to the operation principles of some devices available for amplitude or phase modulation in sec. 3.3. Since the experiments reported in this thesis were performed using a phase-only spatial light modulator, there is a section explaining some details on the phase modulation using a phase modulator in sec. 3.4, and the discussion is later extended in sec. 3.5 to consider simultaneous amplitude and phase modulation. Still in sec. 3.5 there is an original result, in which we perform the analytical inversion of the cardinal sine function using Padé approximants, which is necessary for the simultaneous encoding of amplitude and phase information in a phase hologram.

In chapter 4, some fundamentals of Optical Vortices (OVs) are discussed. The OV has some important characteristics as the Topological Charge (TC) and the Orbital Angular Momentum (OAM). Quite often it is implicitly assumed that the TC is equivalent to the OAM, what is valid only for beams with azimuthal symmetry, as Laguerre-Gauss or Bessel. However, it is necessary to proceed carefully under more general conditions, and the OAM and TC are defined for general beams in sec. 4.2. For instance, it is possible to produce TC distributions with arbitrary geometries over the beam transverse plane, a result that we published in [1] and discussed in sec. 4.3. A subsequent result [3] still in sec. 4.3 is the identification of an analogy between TC distributions and two-dimensional (2D) electrostatics. By performing a mathematical analysis on the possible superpositions of OV through the complex plane, we obtained the Topological Potential (TP) in Eq. (4.23), which has a formal similarity with the complex electrostatic potential in 2D a TC distribution with trivial morphology parameters. There is also a study on properties of the TP, as the equivalents to Gauss' and Ampère's laws in sec. 4.3.1. Since it may be asked when the TP is valid to describe a given TC distribution, we performed in sec. 4.3.2 an analysis of the mathematical principles behind the TP concept. Finally, some nontrivial examples of TC distributions are shown in sec. 4.3.3: a radial TC distribution and TC multipoles.

While in chapter 4 there is a detailed theoretical discussion on TC distributions, in chapter 5 these characteristics are verified experimentally for various examples. Since the goal is to produce and characterize TC distributions over the beam transverse plane, we initially discussed how to characterize the TC and OAM for arbitrary beams. In sec. 5.2 we performed a short review on the triangular slit technique [38], a simple and effective approach to de-

termine the TC in beams with cylindrical symmetry. Then, TC distributions along a line, a corner and a triangle are studied in sec. 5.3, and their TC are determined using the triangular slit, as we published in [1]. When the beam profile deviates too much from a circular profile, the triangular slit becomes inadequate to characterize the beam TC. Then, we discussed in sec. 5.4 a more general approach to characterize the TC and the OAM using a simultaneous retrieval of the field amplitude and phase profile, as we reported in [2]. Later in sec. 5.5 the TC distributions over a line, a corner and a triangle are analyzed again with the simultaneous amplitude and phase characterization. We verified that while the measured TC corresponds to the TC applied to the distribution in the phase mask, the beam OAM is smaller than the TC due to a reduced azimuthal phase variation between separated TC. Later, the radial TC distribution and TC multipoles are characterized in sec. 5.6.

Besides presenting results on optical vortices in linear systems, this thesis also contains in chapter 6 a discussion on how to use techniques of Quantum Mechanics (QM) for the calculation of light propagation in linear and nonlinear optical systems. Due to the wave nature of QM particles and light in a classical approximation, both optics techniques can be applied to QM and vice-versa. In sec. 6.2 we show how to represent the light slowly varying envelope as a Schrödinger-like Eq., and in sec. 6.3 we show how to express the paraxial wave Eq. into an operator Eq. Even though an operator representation for wavefront propagation problems is not a recent idea [39], we only identified previous works using either the Schrödinger Picture (SP) or the Heisenberg Picture (HP). The Interaction Picture (IP, or Dirac Picture) is the representation mostly used to solve or approximate various difficult problems in QM [40, 41], specially nonlinear problems. The IP was introduced for wavefront propagation problems in [4] and the basic ideas are in sec. 6.3. We obtained in sec. 6.3.3 that the IP operators associated with position and angle propagate according to the corresponding ABCD matrices (or ray matrices) for simple paraxial optical systems. This is a remarkable result, since these operators correspond to a full wave solution of the paraxial propagation equation. Simple optical systems are analyzed in sec. 6.4, and the corresponding ABCD matrices and transmittance operators are obtained. A noteworthy result is that through the IP it becomes almost immediate to obtain the propagation of the effective beam width, curvature and divergence angle to characterize beams' propagation as introduced by Siegman [42, 43]. The IP operator formalism is then applied to light propagation in nonlinear media in 6.4.3, where an identification of the obtained results with QM scattering problems is performed. Given the simplicity to express the propagation of the effective beam width using the IP, in sec. 6.5 are described experimental results regarding the beam width evolution inside a nonlinear material using the Scattered Light Imaging Method (SLIM) [5] and also through the D4σ method [6]. While the SLIM technique measures the beam transverse width along the nonlinear material, the D4σ method verifies the beam width of a strong light beam after propagation through the nonlinear sample. For both techniques the IP seems a good theoretical framework for calculations, which is very important for the characterization of nonlinear optical materials.

2 Light properties, propagation and interactions

A deep understanding of some properties of light, such as momentum and its propagation, constitute an important background for the results presented in the later chapters. Thus, in this chapter some already known concepts and results are reviewed. For instance, we discuss some aspects of Maxwell equations that must be considered to describe the light propagation, as the correct expressions for the paraxial approximation. Initially it is considered the light propagation inside linear media, and this assumption will be relaxed later to consider nonlinear optical materials. Finally, it is presented a discussion related to the energy, linear momentum and angular momentum for light.

2.1 Maxwell equations and the wave equation

The description of electromagnetic phenomena is based on the Maxwell equations, and therefore the short review presented in this section is of great utility to introduce the notation used in the remaining of this thesis. After some considerations on the properties of the materials of interest the wave equation which describes light propagation inside material media is obtained.

Given the electric field **E**, displacement field **D**, magnetic induction **B** and magnetic field **H** associated to a distribution of charge density ρ and current density **J**, they must satisfy the following equations

$$\nabla \cdot \mathbf{D} = \rho, \tag{2.1}$$

$$\nabla \cdot \mathbf{B} = 0, \tag{2.2}$$

$$\nabla \times \mathbf{E} = -\frac{\partial \mathbf{B}}{\partial t}, \tag{2.3}$$

$$\nabla \times \mathbf{H} = \mathbf{J} + \frac{\partial \mathbf{D}}{\partial t}. \tag{2.4}$$

The fields **E** and **D**, and **B** and **H** are related respectively by

$$\mathbf{D} = \epsilon_0 \mathbf{E} + \mathbf{P}, \tag{2.5}$$

$$\mathbf{H} = \frac{1}{\mu_0}\mathbf{B} - \mathbf{M}, \tag{2.6}$$

where **P** is the material polarization, **M** its magnetization, ϵ_0 and μ_0 are the vacuum permittivity and permeability, respectively.

The magnetic effects usually affect an atom only at low frequencies (typically smaller than tens of GHz) as in magnetooptical effects [44]. Only in some specific systems the mag-

netic response at visible frequencies might be easily observed as heavy atoms [29], trivalent rare-earth ions [45], or also in adequately designed nanoantennas [46]. In the optical range of frequencies the magnetic response of materials is usually negligible [29, 47], what is strongly related to the large ratio between electric dipole and magnetic dipole transition cross-sections. Therefore, it is assumed that at the frequencies and materials of interest for this work it is possible to consider that $\mathbf{M} = \mathbf{0}$, or

$$\mathbf{B} = \mu_0 \mathbf{H}. \tag{2.7}$$

Contrarily to the magnetization, the polarization $\mathbf{P}$ is very important both in linear and nonlinear optical regimes. If the fields are not sufficiently large to observe nonlinear effects, and the material does not exhibit an intrinsic electric dipole moment, it is possible to obtain in general that $\mathbf{P}$ and $\mathbf{E}$ are related through the linear susceptibility tensor $\chi^{(\mathrm{lin})}$ through

$$(\mathbf{P})_\mu = \epsilon_0 \left(\chi^{(\mathrm{lin})}\right)_{\mu\nu} (\mathbf{E})_\nu, \tag{2.8}$$

where $\left(\chi^{(\mathrm{lin})}\right)_{\mu\nu}$ is the linear susceptibility tensor element μ,ν, and the Einstein summation convention is assumed over the dummy index ν. If the material is isotropic, as a liquid or a glass, one might replace $\left(\chi^{(\mathrm{lin})}\right)_{\mu\nu} = \chi^{(\mathrm{lin})}\delta_{\mu\nu}$, resulting in

$$\mathbf{P} = \epsilon_0 \chi^{(\mathrm{lin})} \mathbf{E}, \tag{2.9}$$

for a linear material. The considerations for a nonlinear material will be given later in this chapter.

We now have sufficient elements for obtaining the wave equation by taking the curl of Faraday's law, Eq. (2.3). Using (2.7) in a space free of charges and currents ($\rho = 0$, $\mathbf{J} = \mathbf{0}$), the wave equation for material media is,

$$\nabla^2 \mathbf{E} - \mu_0 \epsilon_0 \frac{\partial^2 \mathbf{E}}{\partial t^2} = \mu_0 \frac{\partial^2 \mathbf{P}}{\partial t^2} - \nabla\left(\frac{\nabla \cdot \mathbf{P}}{\epsilon_0}\right). \tag{2.10}$$

The last term in (2.10) is usually very small and can be neglected. For instance, for a linear and isotropic material, where (2.9) is valid, one can easily verify from Coulomb's law, Eq. (2.1), that $\nabla \cdot \mathbf{P} = 0$. Consequently, neglecting the last term in (2.10), for a linear isotropic medium we have that

$$\nabla^2 \mathbf{E} - \mu_0 \epsilon \frac{\partial^2 \mathbf{E}}{\partial t^2} = \mathbf{0}, \tag{2.11}$$

where $\epsilon = \epsilon_0 \left(1 + \chi^{(\mathrm{lin})}\right)$ is the material's dielectric constant, and $\left(\mu_0 \epsilon\right)^{-1/2}$ is the light speed in the medium. As a general remark, it should be noticed that a solution to the wave equation (2.11) does not necessarily satisfy Maxwell equations. To obtain a consistent Maxwell wave solution, it is helpful to use other approaches as potentials methods, as will be shown in the next section, or even through the Riemann-Silberstein vector approach [48].

2.2 Propagation of finite beams in free-space

In this section it is described the propagation of finite light beams, as the light emitted by a laser source. In order to achieve such goal, Maxwell equations will be simplified by considering light beams with a large diameter in comparison to the wavelength, and then the general propagator will be given. Green's theorem guarantees that if a given spatially finite field is known in all points along the border of a given volume V free of sources, the field is uniquely determined in all points inside V (see Chapter 10 of [49]). In that way, V can be chosen to be the half-sphere $z > 0$ with radius R whose support is the x, y plane. By taking $R \to \infty$, the field at $z > 0$ can be uniquely determined given its configuration at the plane $z = 0$.

The electromagnetic fields must satisfy all Maxwell equations, and a very convenient way to guarantee this aspect is by describing the fields using the scalar and vector potentials, ϕ and $\mathbf{A}$ respectively. In free-space in a region without charges and currents, the scalar and vector potentials satisfy

$$\mathbf{E} = -\nabla\phi - \frac{\partial \mathbf{A}}{\partial t}, \tag{2.12}$$

and

$$\mathbf{B} = \nabla \times \mathbf{A}. \tag{2.13}$$

Then, the following equations can be obtained from Maxwell equations and (2.12) and (2.13),

$$\nabla^2\phi = -\frac{\partial}{\partial t}\left(\nabla \cdot \mathbf{A}\right), \tag{2.14}$$

$$\left[\nabla^2 - \frac{1}{c^2}\frac{\partial^2}{\partial t^2}\right]\mathbf{A} = \vec{\nabla}\left[\nabla \cdot \mathbf{A} + \frac{1}{c^2}\frac{\partial \phi}{\partial t}\right], \tag{2.15}$$

where it was considered that in free-space the speed of light is $\left(\mu_0\epsilon\right)^{-1/2} = c$.

There are two gauges which are convenient to deal with radiation: Coulomb ($\nabla \cdot \mathbf{A} = 0$) and Lorenz $\left(\nabla \cdot \mathbf{A} + \frac{1}{c^2}\frac{\partial \phi}{\partial t} = 0\right)$ gauges. The first one simplifies the discussion of interaction between plane wave radiation and matter [1], while in the latter both ϕ and $\mathbf{A}$ must satisfy the wave equation.

To obtain diffracting solutions in the paraxial regime the Coulomb gauge is not the most convenient. By requiring that Coulomb's law $\nabla \cdot \mathbf{E} = 0$ must be satisfied, the polarization $\boldsymbol{\epsilon}$ has to be spatially dependent [50]. Therefore, we will adopt the Lorenz gauge, which leads to:

[1] This happens because of two facts: if $\nabla \cdot \mathbf{A} = 0$, one may assume that $\phi = 0$ over all space. Also, the light-matter interaction Hamiltonian has a term proportional to $\nabla \cdot \mathbf{A}$.

$$\left[\nabla^2 - \frac{1}{c^2}\frac{\partial^2}{\partial t^2}\right]\phi = 0, \tag{2.16}$$

$$\left[\nabla^2 - \frac{1}{c^2}\frac{\partial^2}{\partial t^2}\right]\mathbf{A} = 0, \tag{2.17}$$

$$\frac{1}{c^2}\frac{\partial \phi}{\partial t} = -\nabla\cdot\mathbf{A}. \text{ (Lorenz Gauge)} \tag{2.18}$$

Since the derivative operations are linear, it is easy to verify that if $\mathbf{A}$ satisfies the wave equation the gauge condition is sufficient to guarantee that ϕ satisfies (2.16). Therefore, to describe the propagation of electromagnetic fields in a linear isotropic material it is sufficient to solve (2.17) and obtain ϕ through the gauge condition (2.18). This procedure is important to guarantee a physically consistent paraxial approximation, avoiding the apparent paradox noticed by Lax *et Al.* [50], where it is implicitly assumed that $\nabla\cdot\mathbf{E} \neq 0$ [37, 51]. A mathematically precise formulation of the paraxial approximation allows the calculation of higher-order corrections, as discussed in [50], but here only the lowest order correction will be considered.

Therefore, we want to describe beams that have the following characteristics:

1. There is a well defined propagation direction (defined as the $\boldsymbol{z}$ axis).
2. Light polarization does not vary strongly with propagation[2].
3. The beam dimensions in the direction transverse to $\boldsymbol{z}$ vary slowly with z.

Given the above properties, it is possible to visualize as the simplest case the propagation of a monochromatic plane wave, where the conditions 2 and 3 are automatically satisfied. Considering a polarization vector $\boldsymbol{\epsilon}$ constant through all space and a complex amplitude A_0, the wave can be described by

$$\mathbf{A} = \boldsymbol{\epsilon} A_0 e^{i(kz-\omega t)}. \tag{2.19}$$

If A_0 is constant throughout space, it is easy to verify that Maxwell equations require that $\boldsymbol{\epsilon}\cdot\boldsymbol{z} = 0$, or that $\boldsymbol{\epsilon}$ is perpendicular to the propagation direction.

By relaxing the condition of constant A_0, it is possible to describe beams with a transverse structure. The polarization of the electric field of a finite, structured beam will vary during propagation. However, it is not convenient to make this dependence explicitly in $\boldsymbol{\epsilon}$, since (2.17) would become very complicated. Therefore, it is possible to observe an important advantage in using the vector potential in propagation problems: $\mathbf{A}$ is not the physical field and might change its value through gauge transformations, what allows $\boldsymbol{\epsilon}$ to remain fixed while all of Maxwell equations are simultaneously satisfied. $\boldsymbol{\epsilon}$ then becomes the beam polarization

[2] This variation is usually very small and very often neglected in various references about light propagation. However, this effect is essential to understand some effects, as the geometrical Hall effect of light [52, 53].

strictly only in the limit of plane waves. By keeping $\boldsymbol{\epsilon}$ fixed simplifies (2.17), which is now a scalar equation

$$\left[\nabla^2 - \frac{1}{c^2}\frac{\partial^2}{\partial t^2}\right] A_0 e^{i(kz-\omega t)} = 0. \tag{2.20}$$

Supposing now that the amplitude A_0 varies spatially (but is static), and keeping $k = \omega/c$[3], and denoting the transverse Laplacian $\nabla_\perp^2 = \frac{\partial^2}{\partial x^2} + \frac{\partial^2}{\partial y^2}$, it is obtained

$$\nabla_\perp^2 A_0 + \frac{\partial^2 A_0}{\partial z^2} + 2ik\frac{\partial A_0}{\partial z} = 0. \tag{2.21}$$

The calculation carried so far is exact, and at this moment it is convenient to introduce the Slowly Varying Envelope Approximation (SVEA). Without loss of generality, the following dimensionless coordinates (η, ξ, ζ) are introduced, where they are related to the original coordinate system (x, y, z) through $x = w_0\eta$, $y = w_0\xi$, $z = z_0\zeta$. It is possible to rewrite (2.21) as

$$\nabla_{\perp,a}^2 A_0 + \left(\frac{w_0}{z_0}\right)^2 \frac{\partial^2 A_0}{\partial \zeta^2} + 2i\frac{kw_0^2}{z_0}\frac{\partial A_0}{\partial \zeta} = 0,$$

where $\nabla_{\perp,a}^2$ in the transverse Laplacian in the dimensionless coordinates. Notice that, if the scale upon which the beam diffracts is much larger than the region where the beam is concentrated, i.e., $z_0 \gg w_0$, the term involving the second derivative of ζ is much smaller than that involving only the first derivative. As an example, the previous statements can be verified by applying them to the Gaussian beam using the results that will be shown later, where $z_0 = \frac{kw_0^2}{2}$, and $\left(\frac{w_0}{z_0}\right)^2 = \left(\frac{2}{kw_0}\right)^2 \approx \mathcal{O}\left(10^{-8}\right)$ if $\lambda = 500$ nm and $w_0 \approx 1$ mm, while $2i\frac{kw_0^2}{z_0} = 4i$.

Therefore, if the beam intensity profile (envelope) varies slowly with the propagation, it is possible to state that the amplitude A_0 satisfies to a good approximation that

$$\left(\nabla_\perp^2 + 2ik\frac{\partial}{\partial z}\right) A_0 = 0. \tag{2.22}$$

Observe that (2.22) is analogous to the Schrödinger's equation for a free particle in 2 dimensions. This identification is interesting, because it may be used to obtain localized solutions by using the known properties of quantum systems. For example, a quantum particle inside a potential well can exhibith localized solutions. In the context of classical optics this is an interesting kind of solution, because optical waves produced by real-world sources have transverse profiles with a finite width. To obtain localized solutions at a plane borrowing ideas from known properties of Schrödinger's equation, we introduce at the plane $z = 0$ the "potential" $V(x, y)$ and the eigenvalue E, such that

$$2ik\left.\frac{\partial A_0}{\partial z}\right|_{z=0} = -\left[V(x, y) - E\right] A_0. \tag{2.23}$$

This association allows one to obtain a complete set of orthonormal solutions without loss of generality. The "energy" E here is just a constant that must be adjusted in such a way

[3] This is not strictly necessary, since k can be chosen as a propagation constant in a similar fashion to what happens in waveguide theory. See for instance, [54].

that the solution is finite. Notice that the ansatz (2.23) implies that propagation effects are not being considered to calculate the localized solutions, since $z = 0$. Also, since $V(x, y)$ was introduced only to obtain transversely localized field profiles, the field propagates according to (2.22), where $V(x, y) = 0$.

Using the principle of linear superposition, it is possible to obtain other solutions that satisfy the relation (2.23). The simplest case to consider is a quadratic potential, and here it will be considered that the beam has a cylindrical symmetry. Along the radial coordinate ρ, the "potential" V can be written as

$$V(\rho) = V_0 \rho^2. \tag{2.24}$$

The ansatz (2.23) using the potential Eq. (2.24), becomes an eigenvalue problem for E,

$$\left[-\nabla_\perp^2 + V_0 \rho^2 - E\right] A_0 = 0. \tag{2.25}$$

Using separation of variables, the solution can be expressed as $A_0(\rho, \phi) = R(\rho)\Phi(\phi)$. The examination of the asymptotic limits at $R(\rho \to 0)$ and $R(\rho \to \infty)$, and the continuity of $\Phi(\phi)$ under rotation, $\Phi(\phi) = \Phi(\phi + 2\pi k)$ for integer k, indicates that the solution can be written as

$$A_0 = u(\rho)\, \rho^{|m|} e^{-\frac{\sqrt{V_0}}{2}\rho^2} e^{im\phi}, \tag{2.26}$$

where the function which connects the asymptotic behaviors, $u(\rho)$, must satisfy

$$\rho \frac{d^2 u}{d\rho^2} + \left(2|m| + 1 - 2\sqrt{V_0}\rho^2\right) \frac{du}{d\rho} + \left[E - 2(|m| + 1)\sqrt{V_0}\right] \rho u = 0. \tag{2.27}$$

Equation (2.27) assumes a canonical form after a change of coordinates. Using $x = \rho^2$ and $V_0 = 1$, Eq. (2.27) becomes the associated Laguerre equation,

$$x \frac{d^2 u}{dx^2} + (|m| + 1 - x) \frac{du}{dx} + pu = 0, \tag{2.28}$$

where $p = \frac{1}{4}[E - 2(|m| + 1)]$, and whose solutions are the associated Laguerre polynomials, $L_p^{|m|}(\rho^2)$. In order to represent this solution in more usual notation, it is necessary to introduce the characteristic transverse length w_0, which can be achieved through the transformation $\rho^2 \to \frac{2r^2}{w_0^2}$. After normalization, the full solution becomes

$$LG_{p,m}(r, \phi, z = 0) = C \sqrt{\frac{p!}{(p + |m|)!\pi}} \frac{1}{w_0} \left(\frac{2r^2}{w_0^2}\right)^{\frac{|m|}{2}} L_p^{|m|}\left(\frac{2r^2}{w_0^2}\right) e^{-\frac{r^2}{w_0^2}} e^{im\phi}, \tag{2.29}$$

where C is a constant that indicates the field amplitude. This is a general expression for the Laguerre-Gauss modes of the electromagnetic field at $z = 0$, where p and m indicate the radial and azimuthal mode numbers, respectively. p is related to the number of times the field crosses the zero along the radial direction, while m gives the orbital angular momentum

per photon [21]. Various other beam profiles can be described by considering other coordinate systems or by using different profiles for the potential V. For instance, Hermite-Gauss modes can be obtained by using cartesian coordinates, while Bessel beams can be obtained in cylindrical coordinates for $V = 0$. To obtain solutions with a finite energy it is sufficient to have[4]

$$E > min\left(V\right), \text{ and} \tag{2.30}$$

$$E < lim_{r\to\pm\infty} V. \tag{2.31}$$

Since now there is an expression for the initial beam profile, it becomes interesting to calculate its propagation. Remember that the ansatz (2.23) served its purpose, and then we consider $V\left(x,y\right) = 0$ from now on. Observe that both the beam amplitude and derivative with respect to z at $z = 0$ are known. Thus, the requirement that the field configuration at a finite plane must be known, stated at the beginning of this section, is now fulfilled. However, since now the paraxial regime is considered, it is possible to simplify these calculations. According to appendix C.1, the general solution to (2.22) may be written as

$$A_0\left(x,y,z\right) = e^{+\frac{i}{2k}z\nabla_\perp^2} A_0\left(x,y,0\right). \tag{2.32}$$

The solution to (2.32) is very simple for a Gaussian beam ($LG_{0,0}$, according to (2.29)), and this case will be considered initially. In the one dimensional case, if $A_0\left(x\right) = e^{-x^2/w_0^2}$, its Fourier transform is $\tilde{A}_0\left(k_x\right) \propto e^{-k_x^2 w_0^2/4}$. Since $A_0\left(x\right) = \frac{1}{\sqrt{2\pi}} \int dk_x \tilde{A}_0\left(k_x\right) e^{ik_x x}$, it is possible to state that

$$A_0\left(x,z\right) \propto \int dk_x e^{\frac{i}{2k}z(ik_x)^2} e^{-k_x^2 w_0^2/4} e^{ik_x x}. \tag{2.33}$$

Notice that in this case the propagation is equivalent to the transformation $w_0^2 \to w_0^2\left(1 + i\frac{2}{kw_0^2}z\right)$, which naturally introduces the scale in which the beam diffracts, the Rayleigh length $z_0 = \frac{kw_0^2}{2}$. Then, the argument of the field exponent transforms as

$$\frac{x^2}{w_0^2} \to \frac{x^2}{w^2\left(z\right)} - ik\frac{x^2}{2R\left(z\right)}, \tag{2.34}$$

where

$$z_0 = \frac{kw_0^2}{2}, \tag{2.35}$$

$$w\left(z\right) = w_0\sqrt{1 + \left(\frac{z}{z_0}\right)^2}, \tag{2.36}$$

$$R\left(z\right) = z\left[1 + \left(\frac{z_0}{z}\right)^2\right], \tag{2.37}$$

[4] If $E < min\left(V\right)$, $E - V < 0$ and the concavity of A_0 has always the same sign. Therefore, the solution is non normalizable. Simultaneously, if $lim_{x,y\to\pm\infty} V > E$ is verified, then A_0 decays exponentially at large distances and the solution is localized.

where $w(z)$ is the beam waist as a function of z, while $R(z)$ is the beam wavefront curvature radius. Its worth mentioning that for a Gaussian beam in two dimensions the substitution of x by y is immediate.

As a next step, it is possible to verify the behavior of the propagation of the Laguerre-Gauss modes. However, it would seem that the description is somewhat tied to the ansatz (2.23). Instead, a more formal approach based on the ideas of structural stability necessary for discussing spiral light beams [55, 56] is now adopted. The argument below is based on finding a translation symmetry, and to our knowledge, this description is one of the original contributions of this thesis. A self-similar mode of a free propagating wave can be defined as a beam which retain it's shape under propagation, up to a rescaling due to diffraction[5]. In other words, it is assumed that if the mode at $z = 0$ is described by $A_0(\mathbf{r}/w_0)$, where w_0 is a characteristic scale $z = 0$ (minimum beam waist), and the beam translation along z axis can be described by an operator $\hat{G}(z)$. The translation operator, or Green function, $\hat{G}(z)$ will have in general a complex characteristic eigenvalue $W(z)\, e^{i\psi(\mathbf{r}/w(z),z)}$, and its action over A_0 can be summarized as

$$\hat{G}(z)\, A_0\left(\frac{\mathbf{r}}{w_0}\right) = W(z)\, e^{i\psi(\mathbf{r}/w(z),z)}\, A_0\left(\frac{\mathbf{r}}{w(z)}\right). \tag{2.38}$$

$\hat{G}(z)$ must be an unitary operator to conserve the energy. This imposes that

$$\int d^2\mathbf{r}\left|A_0\left(\frac{\mathbf{r}}{w_0}\right)\right|^2 = \int d^2\mathbf{r}\left|W(z)\, e^{i\psi(\mathbf{r}/w(z),z)}\, A_0\left(\frac{\mathbf{r}}{w(z)}\right)\right|^2, \tag{2.39}$$

where $d^2\mathbf{r} = dxdy$.

Upon a rescaling of the integration variables to dimensionless variables $\mathbf{R} = \mathbf{r}/w_0$,$\mathbf{R}' = \mathbf{r}/w(z)$, it is easy to show that the unitary condition is satisfied if and only if

$$W(z) = \frac{w_0}{w(z)}. \tag{2.40}$$

$\hat{G}(z)$ determines the general behavior of the mode propagation, but $w(z)$ and $\psi(\mathbf{r}/w(z), z)$ still have to be determined. To obtain their functional dependency, we observe that they must satisfy the following boundary conditions: $w(0) = w_0$ and $\psi(\mathbf{r}/w_0, 0) = 0$. It can be noticed that $A_0(\mathbf{r}/w(z))$ is the general expression for the mode, and it can be written in terms of the solution at $z = 0$ as

$$A_0\left(\frac{\mathbf{r}}{w(z)}\right) = \frac{w(z)}{w_0} e^{-i\psi(\mathbf{r}/w(z),z)} \hat{G}(z)\, A_0\left(\frac{\mathbf{r}}{w_0}\right). \tag{2.41}$$

The arguments above are general and have not yet referred directly to the equations of light propagation. In order to A_0 represent a light mode in the paraxial approximation, it must satisfy (2.22). Also, since the propagation is given by (2.32), it is useful to first determine the general solution to the SVEA equation, and then apply this solution to the scaling

[5] A mode is an eigenfunction of the system evolution operator. Therefore, the evolution becomes a symmetry of the system. In terms of optics, this concept implies that knowing the mode profile at a given plane, it's profile will be known at different planes.

symmetry that is of interest. Such general solution will be found by using Green's functions, which is reviewed in appendix C.1.

An arbitrary initial configuration of the fields at $z = 0$ can be represented in terms of Dirac delta functions as

$$A(\mathbf{x},0) = \int d^2\mathbf{u}\,\delta(\mathbf{x}-\mathbf{u})\,A(\mathbf{u},0)\,. \tag{2.42}$$

By knowing how the field emitted by a point source in the plane $z = 0$ behaves under propagation, any arbitrary solution can be calculated. This is the fundamental concept that underlies the utility in using the Green's function (or propagator) of a given differential equation. By applying (2.32) to (2.42), and using that $\delta(\mathbf{x}-\mathbf{u}) = (2\pi)^{-2}\int_{-\infty}^{\infty} d^2\mathbf{p}\,e^{i\mathbf{p}\cdot(\mathbf{x}-\mathbf{u})}$, we obtain

$$A(\mathbf{r},z) = \int d^2\mathbf{u}\int \frac{d^2\mathbf{p}}{(2\pi)^2}\exp\left\{-\frac{i}{2k}z\mathbf{p}^2 + i\mathbf{p}\cdot(\mathbf{x}-\mathbf{u})\right\}A(\mathbf{u},0)\,, \tag{2.43}$$

$$= \frac{k}{2\pi i z}\int d^2\mathbf{u}\exp\left\{\frac{ik}{2z}(\mathbf{r}-\mathbf{u})^2\right\}A(\mathbf{u},0)\,. \tag{2.44}$$

The kernel of the integral in (2.44) is also known as Fresnel propagator, and relates arbitrary vector potential profiles between the planes separated by a distance z in the paraxial approximation. Using the general solution (2.44) in (2.41) one can obtain the propagation of modes, since $A_0\left(\frac{\mathbf{r}}{w(z)}\right)$ must satisfy the dynamical equations of the system, and now only $w(z)$ and $\psi(\mathbf{r}/w(z),z)$ must be determined. It is convenient to define the scale-invariant transverse coordinates,

$$\mathbf{R} = \frac{\mathbf{r}}{w(z)}, \tag{2.45}$$

in terms of which (2.41) can be rewritten as as

$$A_0(\mathbf{R}) = \frac{w(z)}{w_0}e^{-i\psi(\mathbf{R},z)}\frac{z_0}{\pi i z}\int d^2\mathbf{U}\exp\left\{\frac{iz_0}{z}\left[\left(\mathbf{R}\frac{w(z)}{w_0}-\mathbf{U}\right)^2\right]\right\}A_0(\mathbf{U},0) \tag{2.46}$$

$$= \int d^2\mathbf{U}\,K(\mathbf{R},z;\mathbf{U},0)\,A_0(\mathbf{U},0) \tag{2.47}$$

where $\mathbf{U} = \mathbf{u}/w_0$, $K(\mathbf{R},z;\mathbf{U},0) = \frac{w(z)}{w_0}e^{-i\psi(\mathbf{R},z)}\frac{z_0}{\pi i z}\exp\left\{\frac{iz_0}{z}\left[\left(\mathbf{R}\frac{w(z)}{w_0}-\mathbf{U}\right)^2\right]\right\}$, and the Rayleigh length $z_0 = kw_0^2/2$ is identified as before. This is a self consistent equation for the scale invariant solutions which must also satisfy (2.22), however with no explicit dependence on z. Thus, by applying (2.22) to (2.46), it is possible to verify after some algebra that

$$\left[4iz_0\partial_z + \left(\frac{w_0}{w}\right)^2\partial^2_{\mathbf{R}}\right]A_0(\mathbf{R}) = \int d^2\mathbf{U}\,(C+iD)\,\frac{w_0}{w(z)}K(\mathbf{R},z;\mathbf{U},0)\,A_0(\mathbf{U},0)\,, \tag{2.48}$$

$$C = \frac{w}{w_0}4z_0\partial_z\psi - 8\frac{z_0^2}{z}\left(\mathbf{R}\frac{w}{w_0}-\mathbf{U}\right)\cdot\mathbf{R}\frac{w}{w_0^2}\partial_z w - \frac{w_0}{w}\left(\partial_{\mathbf{R},i}\psi\right)^2 + \frac{4z_0}{z}\left(\mathbf{R}\frac{w}{w_0}-\mathbf{U}\right)_i\cdot\left(\partial_{\mathbf{R},i}\psi\right), \tag{2.49}$$

$$D = \left(4z_0\frac{\partial_z w}{w_0} - \frac{w_0}{w}\partial^2_{\mathbf{R}}\psi\right), \tag{2.50}$$

where the argument of the functions is implicitly assumed for clarity, and the shorter notation for operators, $\frac{\partial}{\partial z} = \partial_z, \nabla_\perp = \partial_{\boldsymbol{R}}$, is used.

The term D in (2.48) does not depend on $\mathbf{U}$, and can exit the integral. Assuming that at least one of the modes can be described by a purely real function, it is then necessary to assume that[6] $D = 0$, implying that

$$4z_0 \frac{\partial_z w}{w_0} - \frac{w_0}{w} \partial^2_{\mathbf{R}} \psi = 0, \tag{2.51}$$

$$\psi(\mathbf{R}, z) = \frac{z_0}{w_0^2} w(z) \partial_z w(z) \mathbf{R}^2 + f(z). \tag{2.52}$$

It is possible to use (2.52) to simplify C as

$$C = \frac{w_0}{w} \left[\frac{4z_0^2}{w_0^4} w^3 \partial_z^2 w \mathbf{R}^2 + 4z_0 \left(\frac{w}{w_0} \right)^2 \partial_z f \right],$$

leading to the following equation for the field profile

$$\left\{ 4iz_0 \partial_z + \left(\frac{w_0}{w} \right)^2 \left[\partial^2_{\mathbf{R}} - \frac{4z_0^2}{w_0^4} w^3 \partial_z^2 w \mathbf{R}^2 - 4z_0 \left(\frac{w}{w_0} \right)^2 \partial_z f \right] \right\} A_0(\mathbf{R}) = 0. \tag{2.53}$$

It should be now evident that $\partial_z A_0(\mathbf{R}) = 0$ only if

$$\left[\partial^2_{\mathbf{R}} - \frac{4z_0^2}{w_0^4} w^3 \partial_z^2 w \mathbf{R}^2 - 4z_0 \left(\frac{w}{w_0} \right)^2 \partial_z f \right] A_0(\mathbf{R}) = 0, \tag{2.54}$$

and additionally, the Eq. (2.54) should not depend on z by hypothesis, implying the conditions

$$w^3(z) \frac{d^2}{dz^2} w(z) = a = \text{constant}, \tag{2.55}$$

$$w^2(z) \frac{d}{dz} f(z) = b = \text{constant}. \tag{2.56}$$

Using standard integration techniques, it is possible to solve for $w(z)$ and $f(z)$. Since here we want to describe a finite beam, it is required that $a \neq 0$, due to the properties previously discussed of the solutions in a Schrödinger-like equation as (2.54). It can be verified that the solution for $w(z)$ is given by (2.36), while the term $f(z)$ contains the Guoy phase-shift term,

$$f(z) = f_0 + f_1 \arctan\left(\frac{z}{z_0} \right), \tag{2.57}$$

where f_0 and f_1 are constants. These two terms have a distinct meaning. f_0 represents an overall phase offset. Meanwhile, $f_1 \arctan(z/z_0)$ has a deeper meaning. Notice that (2.57) was obtained assuming that $w(z)$ is given by (2.36) in (2.56). If Eq. (2.56) is examined with other dependences in $w(z)$, then it is possible to verify a few aspects of the dynamical term. Since $b = \text{constant}$, $f(z)$ is constant along z in the limit where $w^2(z) \to \infty$, and does not have a dynamical phase term. A typical example are plane waves, which have an infinite transverse width [$w^2(z) \to \infty$].

[6] Notice that $\partial_z A_0(\mathbf{R}) = 0$ implies that the left hand side of (2.48) is real if the profile $A_0(\mathbf{R})$ is real. If the right hand side of (2.48) has a non-zero imaginary part, the equality is inconsistent for this beam profile.

The dynamical term in $f(z)$ is characteristic of finite beams. This can be easily understood by decomposing the transverse field in terms of plane waves. Any physically realizable transverse finite field can be represented in terms of a Fourier expansion. While $w(z)$ is related with the beam width in real space, its inverse, $\frac{1}{w(z)}$, is related to the beam width in the Fourier space. The propagator (2.32) implies that each plane wave component will acquire a different phase upon z propagation. The average phase across the transverse profile due to diffraction is $f(z)$, and is related with the beam width in Fourier space, or the beam momentum uncertainty [57]. An important remark is that Eq. (2.56), as obtained from our scaling argument, agrees with the full expression by Feng and Winfull [57].

Using the solutions for $w(z)$ and $f(z)$, Eq. (2.54) can be simplified again, resulting in

$$\left[\frac{1}{4}\partial_{\mathbf{R}}^2 - \mathbf{R}^2 - f_1\right] A_0(\mathbf{R}) = 0, \tag{2.58}$$

which is an equation analogous to the one described by the ansatz (2.23). Therefore, the Laguerre-Gauss beams satisfy the conditions of self-similarity described in this section, and it is possible to use (2.38) to compute the propagation of these modes, resulting in

$$LG_{p,m}(r,\phi,z) = C\sqrt{\frac{p!}{(p+|m|)!\pi}}\frac{1}{w(z)}\left(\frac{2r^2}{w^2(z)}\right)^{\frac{|m|}{2}} L_p^{|m|}\left(\frac{2r^2}{w^2(z)}\right) e^{-\frac{r^2}{w^2(z)}+\frac{ikr^2}{2R(z)}+im\phi+if(z)}. \tag{2.59}$$

The Laguerre-Gauss beams are modes of light propagation in the paraxial regime, and the previous discussion reveals important concepts about these beam profiles. Notice that the self-similar solutions satisfy (2.58), which is analogous to Schrödinger's Equation for a 2D quantum harmonic oscillator (QHO). Both Hermite-Gauss (HG) and Laguerre-Gauss (LG) solutions satisfy an equation analogous to (2.58) in the QHO. The term $\frac{1}{2}\partial_{\mathbf{R}}^2 - 2\mathbf{R}^2$ is analogous to the QHO Hamiltonian, and it is easy to verify that Laguerre-Gauss and Hermite-Gauss solutions are eigenmodes of this Hamiltonian, whose eigenvalue is $2f_1$.

For the current work, the Laguerre-Gauss solution also has another very special property. As will be later discussed, the Orbital Angular Momentum (OAM) density along z for a paraxial light beam, Eq. (2.115), is proportional to the operator $\frac{\partial}{\partial\phi}$, as seen in Eq. (2.115). Therefore, besides the Hamiltonian operator, $LG_{p,m}$ is an OAM eigenmode whose eigenvalue is m. This is extremely important for applications, because it implies that the initial beam has a well defined OAM value. The Laguerre-Gauss beams are also special in paraxial optics also because they can be easily produced from Gaussian-shaped laser beams.

2.3 Propagation of light in nonlinear media

In this section, some properties of light propagation in nonlinear media will be discussed, with a special focus on nonlinear refraction and absorption of light beams. These are important characteristics, since they are present in all materials. The nonlinear refraction and absorption occurrence in nature can be contrasted, for example, with second-order nonlinearities, which require non centrosymmetric materials or structures. It is remarked here

that, since nonlinear effects are usually very small, the paraxial corrections to the electric and magnetic field considered in sec. 2.2 in terms of the vector potential will be neglected.

The wave equation (2.10) can be rewritten in terms of the field **E** as

$$\left[\nabla^2 - \frac{1}{c^2}\frac{\partial^2}{\partial t^2}\right]\mathbf{E} = \frac{1}{c^2}\frac{\partial^2}{\partial t^2}\left(\frac{\mathbf{P}}{\epsilon_0}\right). \tag{2.60}$$

The distinct components of **E** and **P** at different frequencies can be represented as

$$\mathbf{E} = \frac{1}{2}\sum_{\omega}\mathbf{E}_{\omega}e^{i\omega t} + c.c., \tag{2.61}$$

$$\mathbf{P} = \frac{1}{2}\sum_{\omega}\mathbf{P}_{\omega}e^{i\omega t} + c.c., \tag{2.62}$$

where c.c. denotes the complex conjugate of the preceding expressions.

Separating the terms in Eq. 2.60 by their time dependence, and considering the linear independence between the coefficients of $e^{i\omega t}$ for different ω, Eq. (2.60) implies that $\mathbf{E}_{\omega}$ and $\mathbf{P}_{\omega}$ are related through

$$\left[\nabla^2 + \frac{\omega^2}{c^2}\right]\mathbf{E}_{\omega} = -\frac{\omega^2}{c^2}\frac{\mathbf{P}_{\omega}}{\epsilon_0}. \tag{2.63}$$

If all frequency components of light have the same polarization $\boldsymbol{\epsilon}_{\omega}$, and propagates along the $\boldsymbol{z}$ direction, it is possible to decompose $\mathbf{E}(\mathbf{r}, t)$ as

$$\mathbf{E}_{\omega}(\mathbf{r}) = \boldsymbol{\epsilon}_{\omega}\mathscr{E}_{\omega}(\mathbf{r})\, e^{-ikz}, \tag{2.64}$$

$$\mathbf{E}(\mathbf{r}, t) = \frac{1}{2}\sum_{\omega}\boldsymbol{\epsilon}_{\omega}\mathscr{E}_{\omega}(\mathbf{r})\, e^{i(\omega t - kz)} + c.c., \tag{2.65}$$

where $\mathscr{E}_{\omega}(\mathbf{r})$ represents the slowly varying envelope at frequency ω. Denoting by χ_{ω} the total susceptibility (linear + non linear) associated to the field with frequency ω, one has for the polarization

$$\mathbf{P}_{\omega} = \epsilon_0\chi_{\omega}\mathbf{E}_{\omega}. \tag{2.66}$$

$$\mathbf{P}(\mathbf{r}, t) = \frac{1}{2}\epsilon_0\sum_{\omega}\boldsymbol{\epsilon}_{\omega}\chi_{\omega}\mathscr{E}_{\omega}(\mathbf{r})\, e^{i(\omega t - kz)} + c.c. \tag{2.67}$$

Then, Eq. (2.63) can be rewritten as

$$\left[\nabla^2 + \frac{\omega^2}{c^2}\right]\mathscr{E}_{\omega}e^{-ikz} = -\frac{\omega^2}{c^2}\chi_{\omega}\mathscr{E}_{\omega}e^{-ikz}. \tag{2.68}$$

In SVEA the z derivatives can be simplified as

$$\frac{\partial^2}{\partial z^2}\left[\mathscr{E}_{\omega}e^{-ikz}\right] = e^{-ikz}\left[-k^2\mathscr{E}_{\omega} - i2k\frac{\partial\mathscr{E}_{\omega}}{\partial z} + \frac{\partial^2\mathscr{E}_{\omega}}{\partial z^2}\right] \tag{2.69}$$

$$\approx e^{-ikz}\left[-k^2\mathscr{E}_{\omega} - i2k\frac{\partial\mathscr{E}_{\omega}}{\partial z}\right] \tag{2.70}$$

Using the transverse Laplacian $\nabla_{\perp}^2$, it is possible to find that

$$\left[\nabla_{\perp}^2 - 2ik\frac{\partial}{\partial z} - k^2 + k_{0,\omega}^2\left(1+\chi_\omega\right)\right]\mathscr{E}_\omega = 0, \tag{2.71}$$

where $k_{0,\omega} = \frac{\omega}{c}$ is the wave number of light in free-space.

In the linear case, and when χ_ω is real, it is possible to consider that $-k^2 + \frac{\omega^2}{c^2}\left(1+\chi^{(lin)}\right) = 0$, or

$$k = \frac{\omega}{c}\sqrt{1+\chi_\omega^{(lin)}} = \frac{\omega}{c}\eta_0, \tag{2.72}$$

where η_0 is the real part of the linear refractive index. In the general case there is absorption and $\chi_\omega^{(lin)}$ is complex. Thus, considering that the complex refractive index is given by

$$n = \eta_0 - i\kappa, \tag{2.73}$$

it is true that

$$n^2 = \eta_0^2 - \kappa^2 - 2i\eta_0\kappa = 1 + \chi_\omega^{(lin)}. \tag{2.74}$$

For transparent materials, the intensity loss occurs over distances much longer than a wavelength. This allows a simplification of the expression for n^2. The beam intensity of plane waves propagating inside an absorptive material decays exponentially according to

$$I \propto \left|\exp\left[-ik_0\left(\eta_0 - i\kappa\right)z\right]\right|^2 = \exp\left[-2k_0\kappa z\right]. \tag{2.75}$$

From Beer's law, $I = I_0 e^{-\alpha z}$, and the absorption coefficient is defined as

$$\alpha = 2k_0\kappa. \tag{2.76}$$

Since the absorption in materials with some transparency occurs over distances much longer than a wavelength inside the medium λ, it is possible to state that typically $\alpha\lambda \ll 1$, or $(2k_0\kappa)\left(\frac{2\pi}{k_0\eta_0}\right) \ll 1$, and

$$\kappa \ll \frac{\eta_0}{4\pi}. \tag{2.77}$$

Therefore, it is possible to consider only the first order term in κ. $n^2 = \eta_0^2 - \kappa^2 - 2i\eta_0\kappa \approx \eta_0^2 - \frac{i\eta_0}{k_0}\alpha$. Recovering the nonlinear terms as a nonlinear susceptibility $\chi^{(NL)}$, (2.71) can be written as

$$\left[\nabla_{\perp}^2 - 2ik\frac{\partial}{\partial z} - ik\alpha + k_0^2\chi_\omega^{(NL)}\right]\mathscr{E}_\omega = 0. \tag{2.78}$$

2.3.1 Materials with a nonlinear refractive index

Let us specialize for a moment in describing experimental conditions in which there is no generation of new frequencies. Under such assumption, it is possible to ignore the subscripts ω and consider only

$$\left[\nabla_{\perp}^2 - 2ik\frac{\partial}{\partial z} - ik\alpha + k_0^2\chi^{(NL)}\right]\mathscr{E} = 0. \tag{2.79}$$

In the general case $\chi^{(NL)}$ should be written in terms of a tensorial expansion involving the field components [37]. However, the discussion is simplified for isotropic media, where the nonlinear susceptibility can be described as $\chi^{(NL)} = \chi^{(NL)}\left(|\mathbf{E}|^2\right)$. Also, since the real and imaginary parts of $\chi^{(NL)}$ can be associated with the refractive index and absorption, as in Eq. (2.72), it is also said that such materials display nonlinear refractive index and absorption that vary with the light intensity I,

$$n(I) = \eta_0 + \eta_2 I + \eta_4 I^2 + \ldots, \tag{2.80}$$

$$\alpha(I) = \alpha_0 + \alpha_2 I + \alpha_4 I^2 + \ldots. \tag{2.81}$$

The quantities $n(I), \alpha(I)$ are usually used instead of $\chi^{(NL)}$ because they have physical significance in isotropic materials. As a simple example, lets consider a Gaussian beam impinging a medium of thickness L described by $\eta_0, \eta_2 \neq 0, \alpha_0, \alpha_2 = 0$, and $\eta_j, \alpha_j = 0$ if $j > 2$. Since the optical path is approximately $k_0 L\left(\eta_0 + \eta_2 I\right)$, parallel light rays at different transverse positions propagate distinct effective lengths. This is equivalent to the passage of light through a linear lens, which is an optical medium with a varying thickness. Depending on the sign of η_2, the beam will focus $\left(\eta_2 > 0\right)$ or defocus $\left(\eta_2 < 0\right)$ due to the nonlinearity. The choice of expressing η, α in terms of I instead of $|\mathbf{E}|^2$ becomes reasonable by remembering Eqs. (2.73) and (2.75). Notice that the intensity decay is directly related to α and I, and a relation as $\alpha(I)$ is natural. On the other hand, n and α are the real and imaginary parts of the same complex refractive index, and in principle could be expressed in terms of the same quantities.

The distinction between I and $|\mathbf{E}|^2$ requires that the proper conversions are performed. Defining the intensity as the Poynting vector along the z axis, it is possible to use Eq. (2.114), which by neglecting the small paraxial terms can be written as

$$I(\boldsymbol{r}) = \frac{1}{2} c\epsilon_0 \eta_0 |\mathscr{E}(\boldsymbol{r})|^2. \tag{2.82}$$

Another very important quantity is the power P, which is simply related to I,

$$P = \int d^2\boldsymbol{r}\, I(\boldsymbol{r}) = \frac{1}{2} c\epsilon_0 \eta_0 \int d^2\boldsymbol{r}\, |\mathscr{E}(\boldsymbol{r})|^2. \tag{2.83}$$

Relation between the nonlinear susceptibility and the complex refractive index

Since (2.79) describes the propagation of $\mathscr{E}$, all nonlinear terms must be expressed in terms of $\mathscr{E}$. Also, it is very important to be able to convert between $\chi^{(NL)}$ and $n(I), \alpha(I)$.

A typical nonlinear susceptibility term of odd order, $\chi^{(NL)} = \cdots + \chi^{(2j+1)} |\mathbf{E}|^{2j} + \ldots$, can be rewritten in terms of $\mathscr{E}$ with the help of the binomial expansion theorem. Selecting only the terms oscillating with frequency ω, it can be seen that the following substitution must be performed [58]

$$\chi^{(2j+1)} |\mathbf{E}|^{2j+1} \rightarrow \frac{1}{2^{2j+1}} \frac{(2j+1)!}{j!(j+1)!} \chi^{(2j+1)} \mathscr{E}^{*j} \mathscr{E}^{(j+1)}, \tag{2.84}$$

since terms proportional to $\mathscr{E}$ have a time dependence as $\frac{1}{2}e^{i\omega t}$ while $\mathscr{E}^*$ varies with $\frac{1}{2}e^{-i\omega t}$. Eq. (2.84) indicates the only term in the binomial expansion with the overall $e^{i\omega t}$ dependence. Therefore in the propagation equation,

$$\chi^{(NL)} = \cdots + \frac{1}{2^{2j}} \frac{(2j+1)!}{j!(j+1)!} \chi^{(2j+1)} |\mathscr{E}|^{2j} + \ldots. \tag{2.85}$$

To relate $\chi^{(NL)}$ and $n(I), \alpha(I)$, we notice that, from the definition of the complex refractive index

$$n^2 = 1 + \chi, \tag{2.86}$$

the following decomposition is possible

$$n^2(I) = \left[\eta_0 + \eta(I) - i \frac{\alpha(I)}{2k_0} \right]^2, \tag{2.87}$$

$$= 1 + \chi^{(lin)} + \chi^{(NL)}(I). \tag{2.88}$$

The previous definition in Eq. (2.72) stated that $\eta_0^2 = 1 + \mathfrak{Re}\{\chi^{(lin)}\}$. So, expanding the nonlinear terms squared in Eq. (2.87) in terms of $|\mathscr{E}|^2$, and considering only the first order terms due to the smallness of the nonlinearities, it is obtained that

$$\eta_0^2 = 1 + \mathfrak{Re}\left\{\chi^{(lin)}\right\}, \tag{2.89}$$

$$\alpha_0 = -\frac{k_0}{\eta_0} \mathfrak{Im}\left\{\chi^{(lin)}\right\}, \tag{2.90}$$

$$\eta_{2j} = \frac{1}{2\eta_0 (2c\epsilon_0\eta_0)^j} \frac{(2j+1)!}{j!(j+1)!} \mathfrak{Re}\left\{\chi^{(2j+1)}\right\}, \tag{2.91}$$

$$\alpha_{2j} = -\frac{k_0}{\eta_0 (2c\epsilon_0\eta_0)^j} \frac{(2j+1)!}{j!(j+1)!} \mathfrak{Im}\left\{\chi^{(2j+1)}\right\}. \tag{2.92}$$

By having the explicit relations between η_{2j}, α_{2j} and $\chi^{(2j+1)}$, it becomes possible to convert between them when necessary.

As a final remark, we notice that there is another representation for the complex nonlinear refractive index, using $|\mathscr{E}|^2$ instead of I,

$$n\left(|\mathscr{E}|^2\right) = \eta_0 + \overline{\eta}_2 \frac{|\mathscr{E}|^2}{2} + \overline{\eta}_4 \left(\frac{|\mathscr{E}|^2}{2}\right)^2 + \ldots, \tag{2.93}$$

$$\alpha\left(|\mathscr{E}|^2\right) = \alpha_0 + \overline{\alpha}_2 \frac{|\mathscr{E}|^2}{2} + \overline{\alpha}_4 \left(\frac{|\mathscr{E}|^2}{2}\right)^2 + \ldots, \tag{2.94}$$

and as can be easily verified, this representation is related to the previous through

$$\eta_{2j} = \frac{\overline{\eta}_{2j}}{(c\epsilon_0\eta_0)^j}, \tag{2.95}$$

$$\alpha_{2j} = \frac{\overline{\alpha}_{2j}}{(c\epsilon_0\eta_0)^j}. \tag{2.96}$$

An example: critical self-focusing in a cubic medium

Suppose that a Gaussian beam impinges a medium which contains as the only relevant nonlinear term $\overline{\eta}_2 > 0$. Since the nonlinearity $\overline{\eta}_2 > 0$ tends to focalize the light beam, while $\overline{\eta}_2 < 0$ enhances light diffraction, there is a characteristic regime of $\overline{\eta}_2 > 0$ in which the diffraction can be compensated by the nonlinear term, here denominated by critical self-focusing regime. The contents of this subsection are strongly related to the initial part of the Chapter 17 of [44].

For simplicity, the absorption is neglected in this discussion. Then, $\chi^{(NL)}\left(|\mathbf{E}|^2\right) = \mathfrak{Re}\left\{\chi^{(3)}\right\}|\mathbf{E}|^2$, or in terms of the SVEA field,

$$\chi^{(NL)}\left(|\mathscr{E}|^2\right) = \frac{3}{4}\mathfrak{Re}\left\{\chi^{(3)}\right\}|\mathscr{E}|^2, \tag{2.97a}$$

$$= 2\eta_0\overline{\eta}_2\frac{|\mathscr{E}|^2}{2}, \tag{2.97b}$$

which by substitution in Eq. (2.79), becomes

$$\left[\nabla_\perp^2 - 2ik\frac{\partial}{\partial z} + k^2\frac{\overline{\eta}_2}{\eta_0}|\mathscr{E}|^2\right]\mathscr{E} = 0. \tag{2.98}$$

The Gaussian envelope at the minimum beam waist can be described as

$$\mathscr{E} = U\exp\left(-\frac{r^2}{w_0^2}\right), \tag{2.99}$$

where w_0 is the minimum beam waist, r is the radial coordinate and U the field amplitude. A way to understand the self-focusing or defocusing starts by a parabolic approximation of the nonlinear field term near the maximum field amplitude,

$$|\mathscr{E}|^2 \approx \left(1 - \frac{2r^2}{w_0^2}\right)U^2. \tag{2.100}$$

The parabolic approximation, Eq. (2.100), applied to the SVEA for a cubic medium, Eq. (2.98), indicates that the beam propagation inside the NL material can be approximated by the behavior of a graded-index medium [51, 59, 60]. To understand the self-focusing or self-defocusing in a cubic medium, we consider for simplicity the light propagation in the geometrical optics regime. Considering $\overline{\eta}_2 > 0$, then the beam tends to self-focus upon propagation, because the beam ray matrix elements are given in terms of $\sin(gz)$ and $\cos(gz)$, where $g = 2k_0\overline{\eta}_2U^2/\eta_0 w_0^2$. See for example Refs. [51, 59, 60] or Eq. (6.107). By the other hand, if $\overline{\eta}_2 < 0$ and the previously oscillatory terms become $\sinh(gz)$ and $\cosh(gz)$, and the beam defocus.

To obtain a more quantitative description, we consider (2.98) and that the beam impinges the nonlinear material at $z = 0$. The diffraction compensation by the nonlinearity can be expressed as the condition $\frac{\partial\mathscr{E}}{\partial z} \approx 0$, or the field does not vary much upon propagation,

$$\left[\nabla_\perp^2 + k^2\frac{\overline{\eta}_2}{\eta_0}|\mathscr{E}|^2\right]\mathscr{E} \approx 0. \tag{2.101}$$

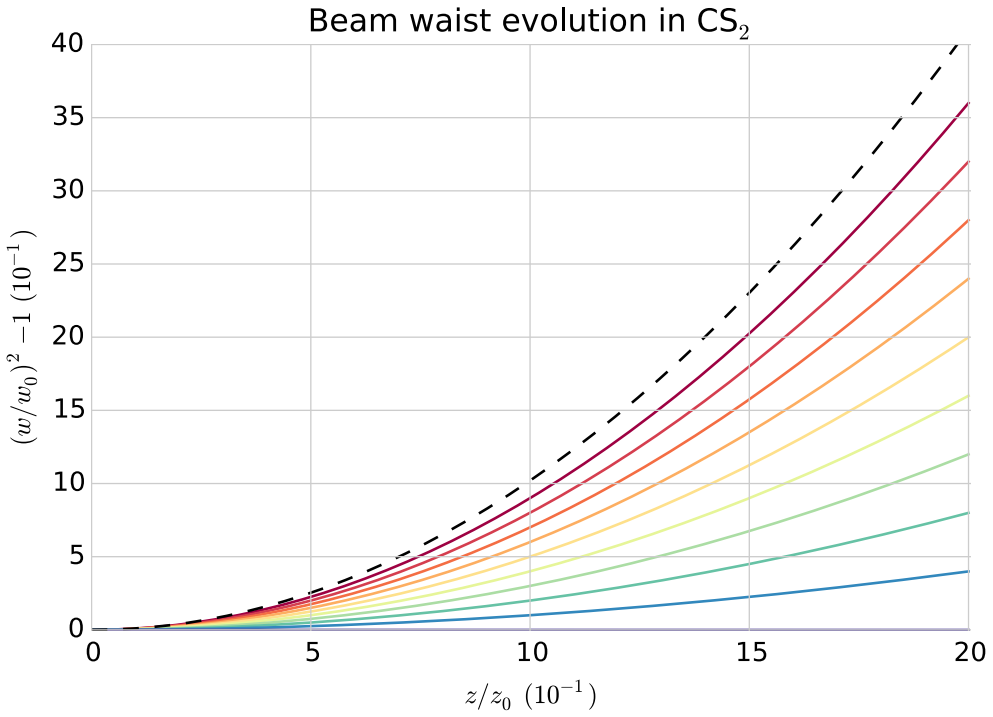

(a)

Figure 1 – (a) An example of the evolution of the beam waist w for a Gaussian beam propagating inside a material with a positive cubic nonlinearity. Carbon Dissulfide (CS_2), whose material parameters are $\eta_0 = 1.63$, $\eta_2 = 3.2 \cdot 10^{-14}$ cm^2·GW^{-1} was considered in this example, and the beam has $\lambda = 500$ nm and $w_0 = 50$ μm. As can be easily verified, $P_C = 7.6$ KW for this set of parameters. The beam power P was varied from $0.1P_C$ (red) until P_C (purple), and the dashed line represents the behavior associated when the nonlinear effects are negligible.

Since the field is a function of r, it is possible express Eq. (2.101) as a series of r powers. Performing the r series expansion to zero order, it is obtained the condition

$$\left(1 - \frac{P}{\mathscr{P}_{\text{Char}}}\right) = 0, \tag{2.102}$$

$$\mathscr{P}_{\text{Char}} = \frac{c\epsilon_0\lambda^2}{4\pi\overline{\eta}_2} = \frac{\lambda^2}{4\pi\eta_0\eta_2}, \tag{2.103}$$

where $\mathscr{P}_{\text{Char}}$ is a characteristic power of the self-focusing and $P = \frac{1}{4}c\epsilon_0\eta_0 U^2\pi w_0^2$ is the beam power. If $P \ll \mathscr{P}_{\text{Char}}$, diffraction dominates, and the beam will increase its size upon propagation. However, if $P \gg \mathscr{P}_{\text{Char}}$, it can be verified that the beam will be focused without limits (in this approximation). Thus, the beam will reduce its size until another physical mechanisms not considered in this analysis becomes important. For example, the increase in the light intensity can be such that the material becomes ionized.

Notice that in the previous paragraph, it was not claimed that $\mathscr{P}_{\text{Char}}$ is *the* critical power for self-focusing. Since it is related to the minimization of only one coefficient series expansion in r of Eq. (2.101), it is an approximate solution to the true critical power. A better

estimate can be made using a variational argument over (2.101). For instance, it is possible to use a least-squares argument to verify which optical power better satisfies the condition expressed by Eq. (2.101) across the entire transverse profile. At the critical condition for self-focusing, (2.101) is approximately zero, or $\left|\nabla_\perp^2 \mathscr{E} + k^2 \frac{\overline{\eta}_2}{\eta_0} |\mathscr{E}|^2 \mathscr{E}\right|^2$ is a minimum. Thus, if we define

$$S = \int_0^\infty \left|\nabla_\perp^2 \mathscr{E} + k^2 \frac{\overline{\eta}_2}{\eta_0} |\mathscr{E}|^2 \mathscr{E}\right|^2 2\pi r dr, \tag{2.104}$$

the critical power for self-focusing is precisely P_C such that

$$\left.\frac{dS}{dP}\right|_{P=P_C} = 0. \tag{2.105}$$

Using that for this Gaussian beam $\nabla_\perp^2 \mathscr{E} = \frac{4}{w_0^2}\left[\frac{r^2}{w_0^2} - 1\right]\mathscr{E}$, and $k^2 \frac{\overline{\eta}_2}{\eta_0} |\mathscr{E}|^2 = \frac{4}{w_0^2} \frac{P}{\mathscr{P}_{\text{Char}}} e^{-2r^2/w_0^2}$, and also performing the substitution $a = r^2/w_0^2$, the condition (2.105) can be restated as

$$P_C = \mathscr{P}_{\text{Char}} \frac{\int_0^\infty da\,(1-a)\,e^{-4a}}{\int_0^\infty da e^{-6a}}. \tag{2.106}$$

The remaining integrals are elementary and the critical power for self-focusing is $P_C = \frac{15}{8}\mathscr{P}_{\text{Char}} \approx 2\mathscr{P}_{\text{Char}}$, or

$$P_C \approx \frac{c\epsilon_0 \lambda^2}{2\pi \overline{\eta}_2} = \frac{\lambda^2}{2\pi \eta_0 \eta_2}, \tag{2.107}$$

which agrees with the critical power for self-focusing calculated in [61] in an aberrationless approximation of the Gaussian beam propagation.

As an illustration, it is shown in Fig. 1 the behavior of the beam width of a light beam for powers P such that $0 < P \lesssim P_C$, where it is considered that the nonlinear material starts at the beam waist. The beam width at each z plane is calculated through the transverse irradiance moment[7],

$$w = 2\sqrt{\frac{\int 2\pi r dr\, r^2 |\mathscr{E}|^2}{\int 2\pi r dr\, |\mathscr{E}|^2}}. \tag{2.108}$$

Since for a Gaussian beam in free-space, $w^2 = w_0^2 + \theta_0^2 z^2$, where θ_0 is the beam divergence angle, the data in Fig. 1 is more conveniently expressed in terms of the normalized and shifted term $w^2/w_0^2 - 1$. For a Gaussian beam propagating in a linear medium, the expressed quantity has a parabolic dependence on z. Notice that at the critical power, for $P \approx P_C$, the beam width remains relatively constant in the calculated z range.

2.4 Energy, linear momentum and angular momentum in paraxial beams

In this session we consider, as before, an uniformly polarized optical beam propagating nearly parallel to the $\boldsymbol{z}$ direction on paraxial regime, described by the following (complex)

[7] The transverse irradiance moments will be discussed in more details later in Secs. 6.4.1 and 6.4.3

vector potential

$$\mathbf{A} = \boldsymbol{\epsilon} A_0 e^{i(kz-\omega t)}. \tag{2.109}$$

Using the Lorenz gauge condition, Eq. (2.18), to obtain an electric field consistent in paraxial approximation[8] with the Coulomb law in free-space, $\nabla \cdot \mathbf{E} = 0$, the following expressions for **E** and **B** are obtained

$$\mathbf{E} = i\omega \left[\boldsymbol{\epsilon} A_0 + \frac{i}{k} (\boldsymbol{\epsilon} \cdot \nabla A_0) \boldsymbol{z} \right] e^{i(kz-\omega t)}, \tag{2.110}$$

$$\mathbf{B} = ik \left[\left(\boldsymbol{z} A_0 - \frac{i}{k} \nabla A_0 \right) \times \boldsymbol{\epsilon} \right] e^{i(kz-\omega t)}. \tag{2.111}$$

The above corrections to the usual paraxial equations are important in describing optical vortices. The derivatives over the envelope are necessary to obtain solutions consistent with all Maxwell equations, and must be used to correctly describe the angular momentum of a light beam. Also, notice that as would be expected from the transversality of electromagnetic fields, the fields of a wave must have a non-zero component on $\boldsymbol{z}$ direction under focusing and also under defocusing.

Two fundamental properties of any physical system are its energy and linear momentum. For a monochromatic field in free space, the time averaged Poynting vector gives the momentum density and is defined by

$$\overline{\mathbf{S}} = \frac{1}{2\mu_0} \mathfrak{Re} \left\{ \mathbf{E} \times \mathbf{B}^* \right\}, \tag{2.112}$$

where the overline indicates a time average.

If we define the energy current density as

$$\mathbf{j} = i \left[A_0 \nabla A_0^* - A_0^* \nabla A_0 \right], \tag{2.113}$$

it may be shown that

$$\overline{\mathbf{S}} = \frac{\omega k}{2\mu_0} \left[|A_0|^2 \mathbf{z} + \frac{1}{2k} \mathbf{j} + \frac{\sigma}{2k} \nabla \times \left(|A_0|^2 \mathbf{z} \right) \right], \tag{2.114}$$

where $\sigma = i \left(\epsilon_x \epsilon_y^* - \epsilon_x^* \epsilon_y \right) = \pm 1, 0$ for, respectively, circularly and linearly polarized beams.

The first term in (2.114) asserts that in this regime, the photon momentum $\mathbf{k} \approx k\mathbf{z}$ is almost aligned with the **z** axis, as would be expected, since this was one of the initial assumptions for the paraxial approximation. The energy current density, which arises on the second term, can be interpreted as another connection with the probability current density in Schrödinger's wave equation. A slight difference that must be noticed is that here the gradients involve the z axis as well, and not only the transverse coordinates. However, working only on the transverse plane, it is possible to visualize that A_0 carries linear momentum. Also, since an electron in a plane can have a non-zero orbital angular momentum perpendicular to the plane, the same is possible for light. Finally, it may be seen that the light polarization σ also contributes to the momentum flow.

[8] In other words, we retain only the first corrections in $1/k$, where the wavenumber k is a large number.

In this work, there is a special concern with the Orbital Angular Momentum (OAM) of light. One must always remember that in classical mechanics, the angular momentum is a quantity defined with respect to a reference point [62]. If this reference is given by $\mathbf{r} = \mathbf{0}$, we may say that the average OAM density along $\mathbf{z}$ is given by

$$L_z = \frac{1}{c^2}\mathbf{z}\cdot\left(\mathbf{r}\times\overline{\mathbf{S}}\right). \tag{2.115}$$

Although there may be OAM perpendicular to the propagation direction (see for example [63, 64]), its description is outside the scope of this work.

As expected, the first term in (2.114) automatically disappears from L_z. By expressing the gradients in cylindrical coordinates, it may be seen that

$$\mathbf{z}\cdot\left(\mathbf{r}\times\vec{\nabla}\right) = \frac{\partial}{\partial\phi}, \tag{2.116}$$

and the description of beams with azimuthal phase dependence $A_0 \propto e^{im\phi}$ become simple,

$$\mathbf{z}\cdot\left(\mathbf{r}\times\mathbf{j}\right) = 2m\left|A_0\right|^2. \tag{2.117}$$

Lastly, it may be shown that neglecting a 2D surface term[9],

$$\mathbf{z}\cdot\left\{\mathbf{r}\times\left[\sigma\nabla\times\left(\left|A_0\right|^2\mathbf{z}\right)\right]\right\} = 2\sigma\left|A_0\right|^2. \tag{2.118}$$

Summing all contributions, the angular momentum along the z axis is

$$L_z = \frac{\epsilon_0\omega}{2}\left|A_0\right|^2(m+\sigma). \tag{2.119}$$

It therefore becomes evident the separation between orbital and polarization angular momenta for paraxial beams. The OAM is m, due to its association with the spatial field dependence, and σ is the polarization contribution to angular momentum. Similarly to what happens in quantum mechanics, the orbital contribution comes from the wave function (here the envelope A_0) while the spin angular momentum comes from a spinor (here the polarization). Under strong focusing, the separation between orbital and polarization angular momenta it is not meaningful, since only the total angular momentum is conserved during propagation [65]. For example, in optical tweezers it is necessary to have a strong field confinement to manipulate dielectric particles with the gradient forces. Therefore, in an optical tweezer it is important to consider all contributions to the light angular momentum.

As will be later shown in Eq. (2.124), $\frac{\epsilon_0\omega^2}{2}\left|A_0\right|^2$ gives the energy density in a zero order approximation. So if a photon has energy $\hbar\omega$, Eq. (2.119) says that on a LG beam with $N \gg 1$ photons each carries the following angular momentum on average

$$\frac{L_z}{U} = \frac{N\hbar(m+\sigma)}{N\hbar\omega}. \tag{2.120}$$

[9] This surface term arises from a 2D integral over beam boundaries. Assuming a finitely extended beam, this may be safely considered as zero. However, if there is interest in local effects, it is necessary to be more careful in performing this transformation.

The energy density at a point may be expressed as

$$U = U_E + U_B = \frac{\epsilon_0}{4}|\mathbf{E}|^2 + \frac{1}{4\mu_0}|\mathbf{B}|^2. \tag{2.121}$$

So, using the expressions (2.110) and (2.111) for the fields, we have

$$U_E = \frac{\epsilon_0}{4}|\mathbf{E}|^2 = \frac{\epsilon_0\omega^2}{4}\left[|A_0|^2 + \frac{1}{k^2}|\boldsymbol{\epsilon}\cdot\nabla A_0|^2\right], \tag{2.122}$$

$$U_B = \frac{1}{4\mu_0}|\mathbf{B}|^2 = \frac{k^2}{4\mu_0}\left[|A_0|^2 + \frac{1}{k^2}\left(|\nabla A_0|^2 - \left|\boldsymbol{\epsilon}^*\cdot\nabla A_0\right|^2\right)\right], \tag{2.123}$$

$$U = \frac{\epsilon_0\omega^2}{2}|A_0|^2 + \frac{\epsilon_0\omega^2}{4k^2}\left[|\nabla A_0|^2 + \left(\boldsymbol{\epsilon}^*\times\boldsymbol{\epsilon}\right)\cdot\left(\nabla A_0^*\times\nabla A_0\right)\right]. \tag{2.124}$$

As pointed out in the recent literature, although there may be regions where the field amplitude is zero, the electric or magnetic energy density may be non null due to the field gradients [31]. The non-zero energy density means that there are photons available to interact with matter. This is interesting specially for optical vortices, which have zero electric field at the vortex core. As an example, it has been suggested that LG photons may favor electric dipole forbidden transitions in atomic/molecular systems [31], what was recently verified for magnetic dipole transitions [32].

3 Basic concepts in digital holography with phase modulators

3.1 Introduction

In the real world the physical phenomena involving light always have some dependence on the beam wavefront. Therefore, it is convenient to have good flexibility and control of the beam wavefront, that can be achieved by using digital holography techniques. In this approach, it is possible to use a computer to adjust the beam local amplitude, phase and polarization using spatial light modulators (SLMs)[60, 66]. Wavefront modulation is at the core of several important applications, as in security labels, adaptative optics systems for advanced telescopes [67] and microscopes [68], and also for measuring the position and orientation of single molecules [69]. Another important application of spatial light modulators is in display technology, as for example in the projection displays in movie theaters or in LCD displays.

Since wavefront modulation techniques are of fundamental importance for this thesis, this chapter begins with the introduction of some concepts behind holography, then some techniques for spatial light modulation are mentioned. Since in our laboratory we have access to liquid crystal phase-only SLMs, it is later described how does one may modulate a transverse phase profile, and also how to simultaneously modulate an amplitude and phase profile.

3.2 Brief introduction to holography

The fundamental concept behind holography arises from the initial argument contained in sec. 2.2: if a field configuration is given at an infinite plane ($z = 0$), the field is also automatically determined at $z > 0$. Therefore, if one manages to build a system which can precisely shape the amplitude and phase of the field at a plane, it should be possible to reproduce any field configuration throughout the space. Interestingly enough, such amplitude and phase profile can be obtained from a simple interference pattern between a plane wave and the beam of interest. These concepts were introduced by Dennis Gabor [70, 71], by which he was awarded the 1971 Nobel prize in Physics. Here only a short discussion on the topic will be performed, mainly focusing on the aspects relevant for the remaining of this manuscript. As references for the reader, an introduction to holography can be seen in [60], while a deeper discussion can be found in [66].

Mathematically the concept can be described as follows. Initially it is necessary to record the field profile over some plane, and later the fields must be reconstructed. Suppose that there is a complex field A_s to be reproduced. Since it is necessary to obtain both the ampli-

tude and the phase profiles, A_s must interfere with some reference field A_r, coherent with A_s. For simplicity we assume perfect coherence between fields A_r and A_s, and that A_s propagates along the $\hat{z}$ direction ($A_s \approx A_{s,0}e^{ik_0 z}$). Then at some plane $z = 0$ the interference between A_r and A_s gives the intensity profile

$$I = |A_s|^2 + |A_r|^2 + A_s e^{i\theta} A_r^* + A_s^* e^{-i\theta} A_r, \tag{3.1}$$

where θ represents the relative phase between A_r and A_s.

Suppose that it is possible to produce a grating whose transmission T is spatially modulated according to the profile determined by I. It is evident that the mask transmission is limited to the range $0 \leq T \leq 1$, what can be accomplished for example by

$$T = \gamma \left(|A_s|^2 + |A_r|^2 + A_s A_r^* e^{i\theta} + A_s^* A_r e^{-i\theta} \right), \tag{3.2}$$

where $\gamma \leq 1/\max\left(\left|A_r + A_s e^{i\theta}\right|^2\right)$. For off-axis holography, these masks can be recorded as described in Fig. 2(a). If a reconstruction beam characterized by a complex amplitude profile A_p illuminates the mask whose transmission is T, the beam amplitude after the mask is exactly given by

$$A'_p = \gamma \left(|A_s|^2 + |A_r|^2 + A_s A_r^* e^{i\theta} + A_s^* A_r e^{-i\theta} \right) A_p. \tag{3.3}$$

Observe that if the reference wave, $A_r = A_0 e^{i\boldsymbol{k}\cdot\boldsymbol{r}}$, and the impinging illumination beam, $A_p = d A_0 e^{i\boldsymbol{k}\cdot\boldsymbol{r}}$, are collinear plane waves, then A_0 and d are real quantities. It is easy to verify that

$$A'_p = \gamma d A_0 \left[\left(|A_s|^2 + |A_0|^2 \right) e^{i\boldsymbol{k}\cdot\boldsymbol{r}} + A_s^* A_0 e^{i2\boldsymbol{k}\cdot\boldsymbol{r}} e^{-i\theta} + A_s A_0 e^{i\theta} \right]. \tag{3.4}$$

Several important features can be seen in Eq. (3.4). There are various terms modulating the beam profile after the transmission mask. However, since A_0, γ, d are constants, the last term is directly proportional to the original complex field A_s. It should be remarked that, as was done at the beginning of this section, the correct amplitude and phase profile determined at a plane also uniquely determines the beam evolution. Thus, as long as one develops a method to correctly isolate the last term from Eq. (3.4), it is possible to reconstruct the field complex amplitude A_s. The beam conjugate to A_s is also produced, and there is a simple amplitude modulation given by $\left(|A_s|^2 + |A_0|^2\right)$ in the direction of the reference beam.

To perform a good modulation of the beam complex amplitude profile, it is of fundamental importance to separate the terms in Eq. (3.4), and some approaches are discussed below. Even though our discussion will be limited to transmission gratings, the ideas are also applicable to phase masks.

3.2.1 In-line holography

Before the invention of the laser, it was relatively difficult to obtain light sources with long coherence times. The coherence of light sources was a major limitation for holography, and as such the initial research was mainly limited to proofs-of-concept like experiments [72].

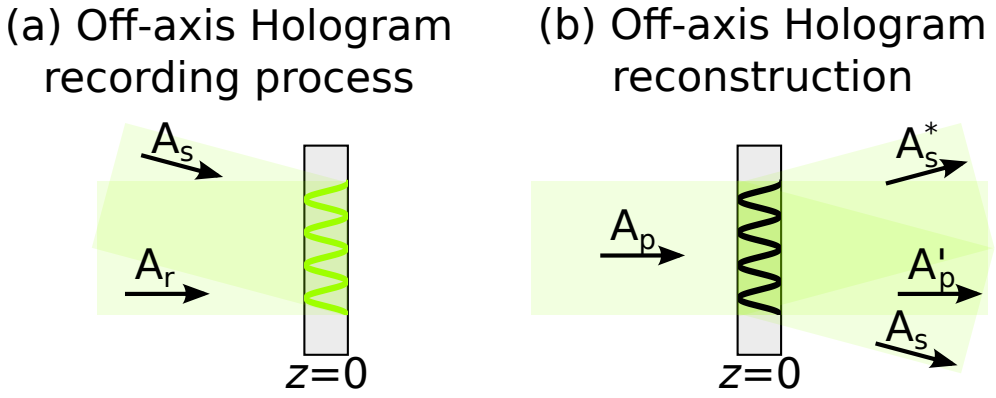

Figure 2 – Off-axis hologram optical recording (a) and reconstruction (b). (a) For the hologram recording, a photosensitive material is placed at the plane $z = 0$, where two fields A_r and A_s interfere. The continuous exposition to radiation imprints the interference profile (green line) in the film, which is later developed. (b) When A_p illuminates the developed hologram (black line), the fields A_s and A_s^* are simultaneously produced.

One important limitation due to the short coherence time is that it is difficult to produce interference patterns between light beams forming large relative angles, and thus the initial experiments were limited to holograms produced by a nearly collinear A_r and A_s ($\boldsymbol{k}\cdot\boldsymbol{r} \approx k_0 z$).

In the case of in-line holography, it is very difficult to separate the individual terms contained in Eq. (3.4), and thus this approach usually is not very good in providing accurate phase and amplitude modulation.

3.2.2 Off-axis holography

Contrarily to the case of in-line holography, in off-axis holography the wavevector $\boldsymbol{k}$ forms an angle with the direction $\boldsymbol{z}$, such that each term in Eq. (3.4) propagates along a distinct direction. It is thus possible to separate each term through a spatial filter. Only with the advent of lasers in 1960 that light sources with long coherence times became widely available. Lasers allowed off-axis hologram recording and retrieval, and gave a substantial momentum to holographic techniques.

For simplicity, suppose that $\boldsymbol{k} = \hat{x}k_0 \sin\phi + \hat{z}k_0 \cos\phi \approx \hat{x}k_0\phi + \hat{z}k_0$, where ϕ is the small angle between the reference beam propagation axis and $\hat{z}$. The field after the transmission mask becomes

$$A'_p = \gamma s A_0 e^{ik_0 z}\left[\left(|A_s|^2 + |A_0|^2\right)e^{ik_0\phi x} + A_s^* A_0 e^{i2k_0\phi x}e^{-i\theta} + A_s A_0 e^{i\theta}\right]. \tag{3.5}$$

It is possible to use a lens to spatially separate the above terms using the Fourier trans-

form property of the lens of focal distance f. In the Fourier plane, the field becomes

$$\tilde{A}'_p \propto \left[\left(|A_s|^2 + |A_0|^2 \right) \delta \left(f\phi - x \right) + A_s^* A_0 e^{-i\theta} \delta \left(2f\phi - x \right) + A_s A_0 e^{i\theta} \delta \left(x \right) \right], \tag{3.6}$$

where it is approximated that the spatial structure of $|A_s|^2$ varies very slowly in the transverse plane. Thus, each term will appear at a distinct transverse position along the $\hat{x}$ axis (at $x = f\phi$, $x = 2f\phi$ and $x = 0$). If an aperture is placed at the Fourier plane, it becomes possible to select and isolate each term in (3.5) separately. A more detailed description of this spatial filtering process will be given later in sec. 6.4.2.

3.3 Spatial light modulators

A fundamental step in performing holography consists in obtaining the optical elements which have the adequate transmission properties. Some possibilities includes an optical record of the electric field transverse amplitude or amplitude and phase profiles in photographic film, or using a device that can store information about the optical field [66]. While optically addressed holography is fundamental for many important applications, as in security labels, for research purposes it is often more convenient to produce holographic masks by digital methods and then apply the modulation pattern at a SLM. Below there is a small discussion relative to some of the currently available digital SLM technology. In practical terms the digital SLM's can modulate the field amplitude or its phase. It should be stated that although a given SLM physically modulate only one quantity (amplitude or phase), it is possible to encode both amplitude and phase information using the same device with the appropriate procedures.

Amplitude masks are the most simple method for beam modulation. This procedure is precisely the example considered in Sec. 3.2, where the transmission mask has the intensity profile associated with the interference between the reference field and the modulated field. Such a mask can be produced, for example, by printing the adequate profile on a transparent film. While the transmittance may vary smoothly in such masks, it is also possible to obtain designed field profiles given a binary amplitude grating, where the transmittance at each pixel is either 0 or 1.

The phase modulators usually vary the optical path in a controllable manner. The transmittance of a phase mask is complex, $T = e^{i\chi}$, indicating that the energy is conserved in the ideal case. In practice however there might be several loss mechanisms, but phase modulators usually do have a higher efficiency than amplitude modulators. This is very important in some applications, as in super-resolution microscopy [69], or in correcting the wavefront aberrations introduced by the atmosphere in images formed by telescopes [67].

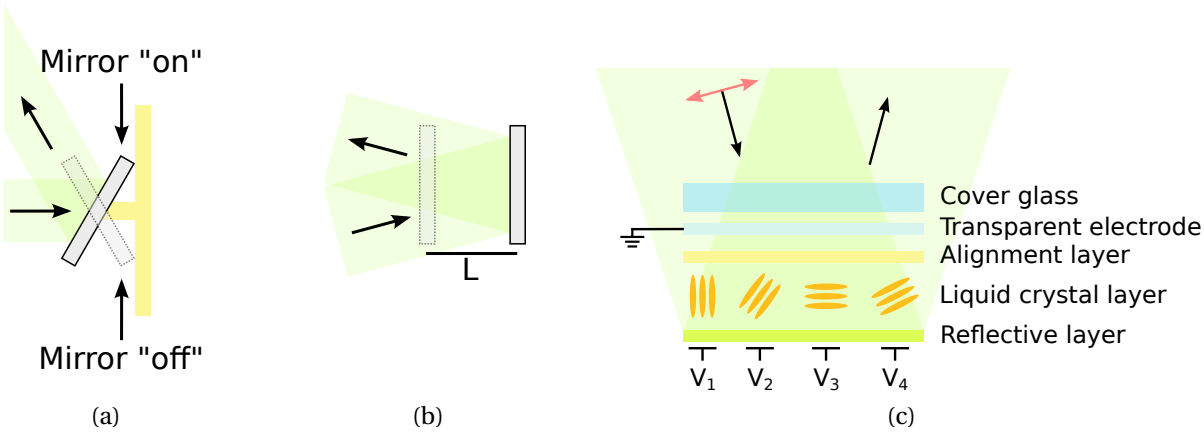

Figure 3 – Schematics of some spatial light modulators. (a) Mirror-based amplitude modulation. When the mirror is in the “on” state, the light is reflected along a direction of interest, while if it is in “off state”, the light is rejected. (b) By displacing the mirror by a distance L along the propagation direction, a monochromatic beam acquires a phase e^{i2kL}, where k is the wavenumber. (c) Representation of a reflective nematic liquid crystal (NLC) SLM. The NLCs can change the optical path of light parallel to its longer axis. Thus, the incident light polarized according to the red double arrow will gain a phase depending on the orientation of the NLC.

3.3.1 Mirrors arrays

Maybe the most intuitive system which is able to modulate the wavefront are mirror arrays. They can be used to modulate the beam amplitude or its phase. One important feature of using mirrors is that the modulation can be very efficient and also operates over a broadband of wavelengths.

A simple method to modify the field amplitude using a mirror consists in tilting the mirror to a specific angle. According to the schematic in Fig. 3 (a), if the mirror is in the “on” state, there will be light reflected along a given direction. For the “off” state, the light is deflected along a non-detectable direction. By having an array of sufficiently small mirrors it is possible to locally modulate the beam amplitude with high spatial resolution. An important characteristic of micro-mirror arrays is that the information can be encoded very quickly, much faster than in liquid crystal devices [73]. Therefore, while the previous description of the modulation process is binary, no light or full light, it is possible to control the average amplitude by controlling the time spent on “on” and “off” states using a pulse-width modulated control signal. Since this is a dynamic modulation, some precautions must be taken when using this kind of modulation directly for scientific applications [73]. For simultaneous amplitude and phase encoding it is preferable to use the binary grating. However, the modulation switching can be averaged in applications involving slow detectors such as the human eye. For that reason digital micro-mirror devices are applied in projection screens for consumer products and also in movie theaters.

In another configuration a mirror can modify the beam phase by being displaced along

the light propagation direction. Thus, if a mirror contains sections that can increase or decrease the optical path in fine steps it is possible to apply a transverse phase to the optical field, as represented in Fig. 3 (b). Therefore, by sectioning a telescope mirror and controlling each element independently, it becomes possible to compensate for atmospheric induced aberrations [67]. A disadvantage of this approach is that with current technology the minimum size of the mirror is various hundreds of microns. Practical laboratory-scale devices have a small transverse resolution, with less than 100x100 mirror elements. Therefore, while these devices are ideal for compensating aberrations due to large scale features, they are not the very adequate for high-resolution wavefront transverse modulation.

3.3.2 Liquid crystal display

Liquid crystal displays are widely used in consumer products and also for scientific applications. Physically, the crystals are aligned in a way to modify the optical polarization in proportion to an applied voltage. Even though there is an important class of modulators based on ferroelectric liquid crystals, the modulation by uniaxial nematic liquid crystals (NLC) is found in a larger set of devices and will be the only case discussed in this work. NLC's can be used either to rotate the polarization, that becomes an amplitude modulator if polarizers are used, or the optical path by adjusting the refractive index for a given polarization component.

The schematic in Fig. 3 (c) correspond to the structure of the SLM used in the experiments for this thesis. The NLC are rod-like crystals that have the tendency to be parallel to each other. By performing an adequate polishing process in the alignment layer, it is possible to guarantee the NLC orientation across the device when the voltage applied between electrodes is zero. When the maximum voltage $V_{\max}$ is applied, the NLC are designed to be oriented along the electric field lines. According to Fig. 3 (c), the transparent electrode is held at a voltage of 0 V, while $0 \leq V_i \leq V_{\max}$ is used to change the local NLC orientation. In Fig. 3 (c), $V_3 = 0$ V, $V_1 = V_{\max}$ and V_2, V_4 represent intermediate applied voltages. In general the NLC are birefringent, such that the refractive index of light propagating parallel to the NLC axis will be different from that of light whose polarization is along the NLC axis. Therefore, by orienting the NLC axis relative to the light incident polarization it is possible to change the optical phase. The maximum phase shift at the design wavelength is typically larger than 2π, such that it is possible to imprint an arbitrary phase profile over the transverse plane. While in principle it is possible to use transparent electrodes to control V_i in a transmissive SLM, for higher spatial resolution the electrodes are usually made on a silicon substrate. This forces the SLM to have a reflective layer above the electrodes, as is represented in the schematic.

NLC devices that behave as explained above behave as phase modulators with a strong polarization dependence. Thus, if the incident light is polarized at 45^o to the modulation axis

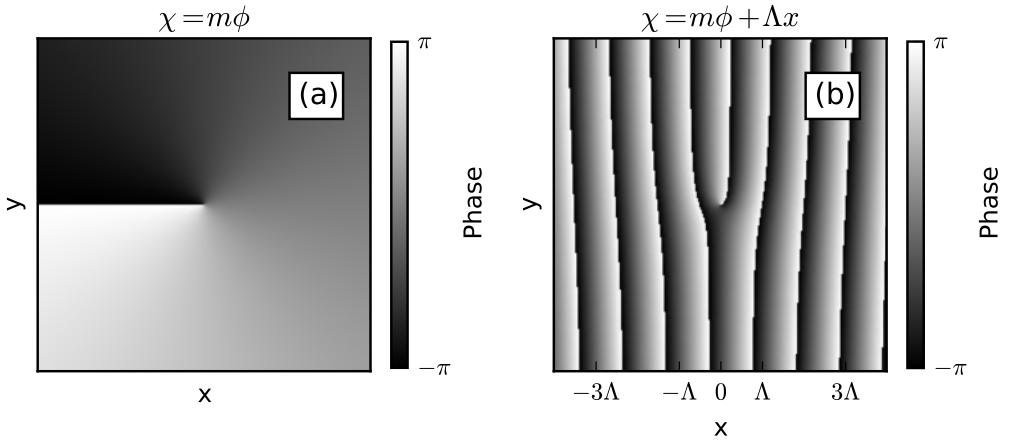

Figure 4 – (a) In line hologram for the production of an OV characterized by $m = 1$. (b) Off-axis hologram for an OV with $m = 1$. Notice the characteristic forked pattern.

the SLM behaves as a position dependent waveplate. By adding a polarizer after the SLM it is possible to use it as an amplitude modulator.

In terms of applications, NLC are broadly used for transmission amplitude modulation in LCD screens. Appropriate alignment layers can twist the NLC axis by 90^o or 270^o between incidence and output planes. If the NLC are placed between crossed polarizers, it is possible to modulate the beam transmitted amplitude with a high efficiency at each pixel. There is also a growing number of scientific applications for NLC SLM, ranging from super-resolution microscopy [69], classical and quantum optical communications [24, 26], fundamental studies of the orbital angular momentum of light [23], and also in a recent demonstration that finite light beams propagate with a speed smaller than the speed of light [36].

3.4 Phase modulation in phase-only SLMs

Even though it seems simple to modulate the beam phase using a phase-only SLM, there are some nontrivial aspects worth remarking. As an example case, it will be mentioned the modulation of an optical vortex (OV) whose phase is $\chi = m\phi$, where ϕ is the azimuthal angle.

In a first approach, one would like to directly reproduce the target transverse phase in the SLM display. A simple way to obtain numerically the phase profile of the OV is by using complex numbers. Technically this is very simple to implement and very efficient, because there are many tools for handling complex numbers in numeric calculation softwares.

Considering x and y are the coordinates along the SLM display, it is known that $\left(x + iy\right)^m =$

$|\boldsymbol{r}|^m e^{im\phi}$. By retrieving the argument of the associated complex profile,

$$\chi_i(\boldsymbol{r}) = \arg\left[\left(x+iy\right)^m\right] = m\phi, \tag{3.7}$$

which is represented in Fig. 4 (a).

If in-line holography is used, there must be some care, because in the real world the modulation is not perfect. Representing the field before and after modulation as $\mathscr{E}^{(\mathrm{inc})}$ and $\mathscr{E}^{(\mathrm{mod})}$, respectively, a possible representation to the non-ideal modulation is given by

$$\mathscr{E}^{(\mathrm{mod})}(\boldsymbol{r}) = \frac{1}{N}\left(ae^{i\xi} + e^{i\chi_i(\boldsymbol{r})}\right)\mathscr{E}^{(\mathrm{inc})}(\boldsymbol{r}), \tag{3.8}$$

where the parameter a indicates the fraction of non modulated light, assumed to be small ($a \sim 0$), and ξ indicates a possible relative phase. To ensure the conservation of energy, the normalization factor $N = \sqrt{1+a^2+2a\cos\left[\xi-\chi_i(\boldsymbol{r})\right]}$ was introduced. To first order in a, it is found that

$$\mathscr{E}^{(\mathrm{mod})}(\boldsymbol{r}) \approx \left(e^{i\chi_i(\boldsymbol{r})} - \frac{a}{2}e^{i[2\chi_i(\boldsymbol{r})-\xi]} + \frac{a}{2}e^{i\xi}\right)\mathscr{E}^{(\mathrm{inc})}(\boldsymbol{r}), \tag{3.9}$$

which indicates that the beam contains a phase term with the correct modulation, and extra terms which contains a wrong phase profile whose amplitude is determined by the parameter a. Although the toy-model from (3.8) is very simple, it indicates that an in-line approach is very susceptible to deviations from the desired behavior. This should pose no problems for phase profiles determined from automated procedures, as those obtained using the Gerchberg-Saxton algorithms [74] or those used to explore coherent atomic/molecular processes [75]. However, since we are interested in correctly modulating the beam transverse profile according to a desired prescription, it is easier to use an off-axis approach.

To go from in-line to off-axis, we just add a linear phase term, also known as carrier, to the desired phase pattern,

$$\chi_o(\boldsymbol{r}) = m\phi + \Lambda x, \tag{3.10}$$

where for simplicity it is assumed that the carrier is along the x axis. The transverse phase associated with $\chi_o(\boldsymbol{r})$ is represented in Fig. 4 (b). Assuming the same perturbation as before, in the off-axis case the modulated field becomes

$$\mathscr{E}^{(\mathrm{mod})}(\boldsymbol{r}) \approx \left(e^{im\phi+i\Lambda x} - ae^{2im\phi+2i\Lambda x-i\xi} + \frac{a}{2}e^{i\xi}\right)\mathscr{E}^{(\mathrm{inc})}(\boldsymbol{r}), \tag{3.11}$$

and now it is possible to select only the modulated field using a spatial filter, according to the same argument as in sec. 3.2.2.

3.5 Simultaneous amplitude and phase modulation in phase-only SLMs

Since usual SLM's modulate either amplitude or phase, an approach that allows the simultaneous modulation of both quantities would be very useful, because it enables a full struc-

turing of the transverse optical field. Then, it will be discussed below an approach to modulate the transverse amplitude and phase of an optical beam by properly adjusting the transverse phase of the mask. The ideas explained below were introduced by [76], and more recently were nicely implemented with current technologies by [77,78]. While the mathematical problem is well understood from these previous works, there still remains a practical difficulty to evaluate some inverse functions, as the inverse of the cardinal sine [77,78] or Bessel functions [77]. The numerical evaluation of these inverse functions can be very demanding, and an original contribution of this thesis is performing an analytical approximation to the inverse of the cardinal sine using Padé approximants, accurate to almost 12 bits of amplitude encoding.

Suppose a phase mask characterized by the transmittance

$$T(\boldsymbol{r}) = e^{iM(\boldsymbol{r})\Phi(\boldsymbol{r})}, \tag{3.12}$$

where $\Phi(\boldsymbol{r})$ is a transverse phase, such that $0 \leq \Phi(\boldsymbol{r}) \leq 2\pi$, and $M(\boldsymbol{r})$ is a factor related to the phase modulation amplitude defined in the interval $0 \leq M(\boldsymbol{r}) \leq 1$. Under off-axis holography it should be expected that $M(\boldsymbol{r})$ can be related to the beam amplitude and $\Phi(\boldsymbol{r})$ to its phase. For simplicity, suppose that the phase profile is that of a blazed diffraction grating, $\Phi(\boldsymbol{r}) = \mathrm{Mod}(kx, 2\pi)$, where $\mathrm{Mod}(x,d)$ represents the remainder of x when divided by d (modulo operation). If the amplitude is $M(\boldsymbol{r}) = 1$, it should be expected that a beam parallel to the optical axis to be fully deflected to the first diffracted order. On the other hand, no energy is expected in the first diffracted order of the grating if $M(\boldsymbol{r}) = 0$. Therefore, intuitively it is expected that by correctly modulating the depth of the grating, $M(\boldsymbol{r})$, it becomes possible to modulate the amplitude of the electric field [76]. However, this amplitude modulation factor also modifies the transverse phase nonlinearly, and it is extremely relevant to describe the diffracted orders correctly. As a final remark, the prescription in (3.12) for amplitude modulation is not unique [77], but shows good modulation properties [78].

Since the phase term in the transmission mask is defined within $[0, 2\pi)$, then it is possible to perform a Fourier expansion of $T(\boldsymbol{r})$ in terms of $\Phi(\boldsymbol{r})$,

$$T(\boldsymbol{r}) = \sum_{n=-\infty}^{\infty} T_n(\boldsymbol{r})\, e^{in\Phi(\boldsymbol{r})}, \tag{3.13}$$

$$T_n(\boldsymbol{r}) = \frac{1}{2\pi} \int_0^{2\pi} e^{iM(\boldsymbol{r})\Phi(\boldsymbol{r})} e^{-in\Phi(\boldsymbol{r})}\, d\Phi(\boldsymbol{r}), \tag{3.14}$$

where the expansion is valid for all values of the transverse coordinates. As a curiosity, this mathematical procedure is equivalent to that used for the decomposition of fractional optical vortices in terms of a basis of well defined angular momentum states [79,80]. The integral in (3.14) is elementary, and can be written as

$$T_n(\boldsymbol{r}) = e^{i\pi[M(\boldsymbol{r})-n]} \frac{\sin \pi\,[M(\boldsymbol{r}) - n]}{\pi\,[M(\boldsymbol{r}) - n]}. \tag{3.15}$$

If the phase profile contains the blazed grating pattern, most of the beam energy will be diffracted to the first diffraction order, where the beam complex transverse profile is $B_1(\boldsymbol{r}) =$

$T_1(\boldsymbol{r})\, e^{i\Phi(\boldsymbol{r})}$, or

$$B_1(\boldsymbol{r}) = \operatorname{sinc}\{\pi[M(\boldsymbol{r})-1]\}\, e^{i\{\Phi(\boldsymbol{r})+\pi[M(\boldsymbol{r})-1]\}}, \tag{3.16}$$

where it is identified the cardinal sine, $\operatorname{sinc}(x) = \sin x/x$. Suppose that there is interest in modulating an impinging plane wave such that the output field is

$$A(\boldsymbol{r}) = \mathscr{A}(\boldsymbol{r})\, e^{i\chi(\boldsymbol{r})}, \tag{3.17}$$

for some amplitude and phase profiles $\mathscr{A}(\boldsymbol{r})$ and $\chi(\boldsymbol{r})$, respectively. By equating $A(\boldsymbol{r}) = B_1(\boldsymbol{r})$, it is possible to obtain the transmission grating parameters, $M(\boldsymbol{r})$ and $\Phi(\boldsymbol{r})$, with the target modulated field. Thus, to produce the field (3.17), one promptly identifies that

$$\begin{cases} \mathscr{A}(\boldsymbol{r}) &= \operatorname{sinc}\{\pi[M(\boldsymbol{r})-1]\}, \\ \chi(\boldsymbol{r}) &= \Phi(\boldsymbol{r}) + \pi[M(\boldsymbol{r})-1], \end{cases} \tag{3.18}$$

and, since the mask is designed using $M(\boldsymbol{r})$ and $\Phi(\boldsymbol{r})$, the above relations must be inverted, resulting in

$$\begin{cases} M(\boldsymbol{r}) &= 1 + \frac{1}{\pi}\operatorname{sinc}^{-1}\mathscr{A}(\boldsymbol{r}), \\ \Phi(\boldsymbol{r}) &= \chi(\boldsymbol{r}) - \operatorname{sinc}^{-1}\mathscr{A}(\boldsymbol{r}). \end{cases} \tag{3.19}$$

The result presented in Eq. (3.19) is very important because it describes the relation between the phase-mask transmission parameters with the amplitude and phase of the field of interest. Therefore, it significantly simplifies the experimental setup and optimizes the usage of the SLM. However, there is an implementation problem with this technique, which is related to the difficulty in numerically calculating the $\operatorname{sinc}^{-1}\mathscr{A}(\boldsymbol{r})$ term. If a direct approach is considered, or even a lookup table is used, the procedure can be very time-consuming for a 2D phase mask containing millions of pixels. In what follows, we suggest here a more efficient approach to calculate the inverse based on standard functions. A good accuracy is obtained and the expressions can be quickly evaluated in current computers.

Analytical approximation to the $\operatorname{sinc}^{-1}\mathscr{A}$ problem

Given the function $\operatorname{sinc}(x) = \sin x/x$ and its inverse, $\operatorname{sinc}^{-1}\mathscr{A}$, for the current purposes it is necessary to restrict the domain of x to the range $-\pi \le x \le \pi$, since $0 < \mathscr{A} < 1$. x is further restricted to the interval $-\pi \le x \le 0$ if we require that $0 \le M \le 1$ in (3.19). In Fig. 5 (a) the $\operatorname{sinc}^{-1}\mathscr{A}$ is represented, as given by numerical inversion.

There are various routes to approximate $\operatorname{sinc}^{-1}\mathscr{A}$. A major requirement in such approximations is that they must correctly describe the field amplitude near $\mathscr{A} \sim 0$, what is very relevant for example in fields containing optical vortices, and also near $\mathscr{A} \sim 1$, where most of the beam energy is contained. Distortions of the modulation near $\mathscr{A} \sim 1$ must be very important in applications involving the encoding of information in the transverse modes, since the experimentally obtained modes will contain contributions not associated with the

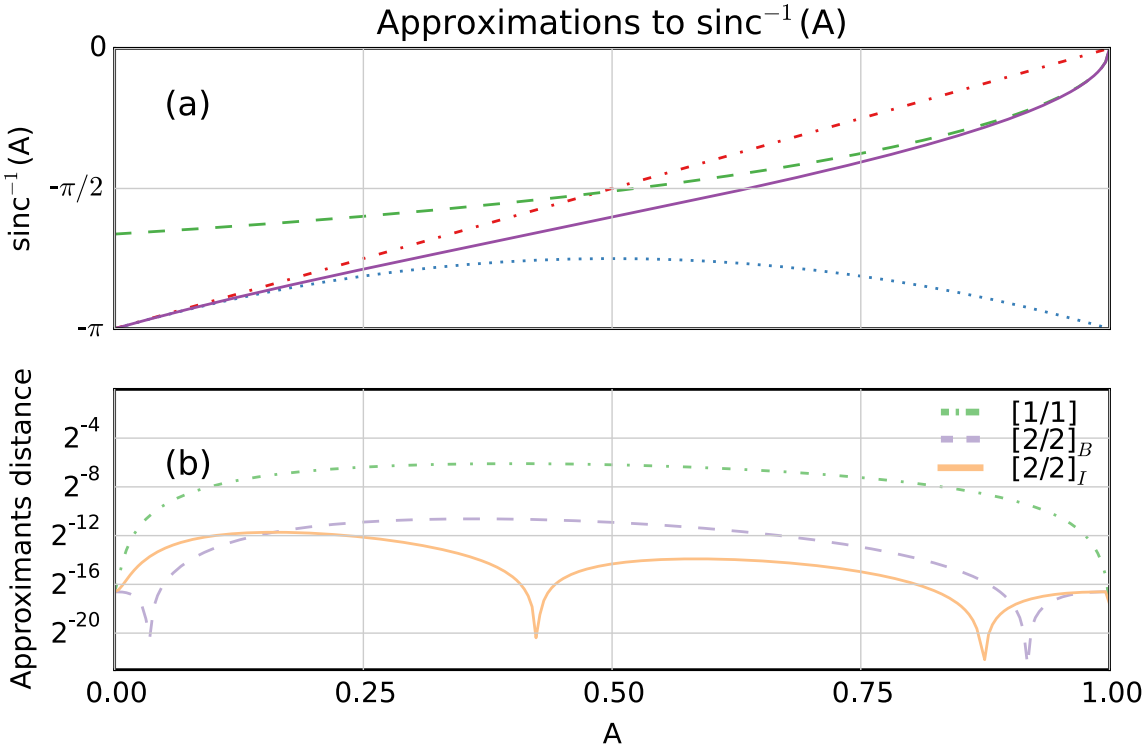

Figure 5 – (a) The inverse of the cardinal sine (continuous) and several approximating functions near the edges of the interval of interest. The dashed line represents an expansion of the solution near $\mathscr{A} = 1$, while the dash-dotted line and dotted line represents the first and second order Taylor expansions of the solution near $\mathscr{A} = 0$, respectively. (b) The proposed approximations are accurate for all values of $\mathscr{A}$, and the distance between the approximation and the exact values, $\left|\text{sinc}^{-1}(\mathscr{A}) - \text{sinc}^{-1}_{[n/n]}(\mathscr{A})\right|$, is very small. The maximum distance is smaller than $2^{-6.1}$, $2^{-10.6}$ and $2^{-11.7}$ for the $[1/1]$, $[2/2]_B$ and $[2/2]_I$ Padé approximants, respectively plotted with dash-dot, dashed and solid lines. The B and I subscripts indicate different approaches to obtain the Padé coefficients, according to the paragraph after Eq. (3.28).

desired mode structure. Another constraint is that the approximation must be easily calculable, since a difficult approach does not bring any advantage.

The simplest approximation consists in perform a Taylor expansion of the sinc(x) around $x = -\pi$, where $\text{sinc}^{-1}\mathscr{A} = 0$, and inverting the associated series. To second order in $\mathscr{A}$, it is obtained

$$\text{sinc}^{-1}\mathscr{A} \approx \pi\left(-1 + \mathscr{A} - \mathscr{A}^2\right). \tag{3.20}$$

In Fig. 5 (a) it can be seen that over the full range of interest, retaining the expansion only over the first order series expansion has a smaller distance to $\text{sinc}^{-1}\mathscr{A}$ than the second order approximation. It is noted that by using more terms in the series expansion it should be possible to improve the accuracy of the approximation, but this increases significantly the computational time.

Another possible approximation consists in inverting $\mathrm{sinc}(x)$ near $x = 0$. Notice that $\mathrm{sinc}(x) \approx 1 - \frac{x^2}{3!} + \frac{x^4}{5!}$, and by inverting the series with the previous assumptions, it is obtained

$$\mathrm{sinc}^{-1}\mathscr{A} \approx -\sqrt{6}\sqrt{1-\mathscr{A}}\left[1 + \frac{3}{20}(1-\mathscr{A})\right]. \tag{3.21}$$

The approximation in (3.21) is also represented in Fig. 5 (a). As can be observed, there is a good agreement between the approximation and the true function for $\mathscr{A} \approx 1$, while for smaller values of $\mathscr{A}$ the disagreement becomes considerable. An important aspect of the expansion in (3.21) is that the $\mathrm{sinc}^{-1}\mathscr{A}$ function does not have an exact Taylor series expansion around $\mathscr{A} \approx 1$, because all the derivatives of $\mathrm{sinc}^{-1}\mathscr{A}$ are singular at $\mathscr{A} = 1$. However, by factoring $\sqrt{1-\mathscr{A}}$ of the expansion, it is possible to have a well defined series expansion in terms of powers of $(1-\mathscr{A})$.

After gaining some knowledge on the asymptotic behavior of $\mathrm{sinc}^{-1}\mathscr{A}$ near the extrema at $\mathscr{A} = 0$ and 1, it is possible to smoothly match these approximations across the range of interest by using Padé approximants, which are shortly reviewed for convenience in appendix **??**. The $[n/m]$ approximation to the $\mathrm{sinc}^{-1}\mathscr{A}$ is defined as

$$\mathrm{sinc}^{-1}_{[n/m]}(\mathscr{A}) = \sqrt{1-\mathscr{A}}\,\frac{\sum_{i=0}^{n} a_i \mathscr{A}^i}{1 + \sum_{j=1}^{m} b_j \mathscr{A}^j}, \tag{3.22}$$

where the singular behavior near $\mathscr{A} = 1$ shall be correctly described by the multiplicative factor of $\sqrt{1-\mathscr{A}}$. It is advantageous to use Padé approximants in this problem because it naturally extrapolates the results of a simple series expansion, by adding extra terms for larger values of the argument $\mathscr{A}$. In order to have a solution that matches the exact function, the coefficients a_i and b_j are chosen such that the series expansion of $\mathrm{sinc}^{-1}_{[n/m]}(\mathscr{A})$ is equivalent to that of $\mathrm{sinc}^{-1}(\mathscr{A})$ at one or more values of $\mathscr{A}$. Although various sets of n, m can be used, it is often true that the Padé approximants become more accurate when $n = m$, and thus only this case will be considered here. For $\mathrm{sinc}^{-1}_{[1/1]}(\mathscr{A})$ and based in the expansions (3.20) and (3.21), the following conditions were used

$$\mathrm{sinc}^{-1}_{[1/1]}(\mathscr{A})\big|_{\mathscr{A}=0} = -\pi, \tag{3.23}$$

$$\frac{d}{d\mathscr{A}}\mathrm{sinc}^{-1}_{[1/1]}(\mathscr{A})\bigg|_{\mathscr{A}=0} = \pi, \tag{3.24}$$

$$\mathrm{sinc}^{-1}_{[1/1]}(\mathscr{A})\big|_{\mathscr{A}=1} = -\sqrt{6}. \tag{3.25}$$

The condition (3.23) implies that $a_0 = -\pi$. The conditions (3.24) and (3.25) can be used to solve for a_1 and b_1, and the values described in Table 1 are obtained. The distance between the approximant $\mathrm{sinc}^{-1}_{[1/1]}(\mathscr{A})$ and $\mathrm{sinc}^{-1}(\mathscr{A})$ very small, as can be seen in Fig. 5 (b). The maximum distance is 1.5%, indicating a resolution of 6.1 bits in amplitude modulation, which is much closer to the exact function than in the implementation applied in [78], where the maximum deviation can reach 16%. The above resolution in amplitude modulation is not completely satisfactory, since various of the current SLM's have a phase resolution of 8 bits. Thus, the previous analysis was extended to [2/2] approximants.

Approximant	a_1	a_2	b_1	b_2
$\text{sinc}^{-1}_{[1/1]}$	$\pi\frac{3/2-\pi/\sqrt{6}}{1-\pi/\sqrt{6}}$	0	$\frac{-1+\pi/2\sqrt{6}}{1-\pi/\sqrt{6}}$	0
$\text{sinc}^{-1}_{[2/2]_B}$	-8.15161	-1.74204	3.09474	1.22688
$\text{sinc}^{-1}_{[2/2]_I}$	-7.20646	-1.29906	2.79389	0.961026

Table 1 – Coefficients of the Padé approximants used in approximating $\text{sinc}^{-1}(\mathscr{A})$.

Two sets of coefficients were obtained for the $[2/2]$ approximant, $[2/2]_B$ and $[2/2]_I$. The conditions expressed in Eqs. (3.23)-(3.25) were used for both sets, in addition to

$$\frac{d}{d\mathscr{A}}\text{sinc}^{-1}_{[2/2]}(\mathscr{A})\bigg|_{\mathscr{A}=1} = \frac{3\sqrt{6}}{20}. \tag{3.26}$$

The distinction between $[2/2]_B$ and $[2/2]_I$ approximants consists in the last constraint,

$$\frac{d^2}{d\mathscr{A}^2}\text{sinc}^{-1}_{[2/2]_B}(\mathscr{A})\bigg|_{\mathscr{A}=0} = -2\pi, \tag{3.27}$$

$$\text{sinc}^{-1}_{[2/2]_I}(\mathscr{A})\bigg|_{\mathscr{A}=\frac{3\sqrt{3}}{4\pi}} = -\frac{2\pi}{3}. \tag{3.28}$$

For $[2/2]_B$ the final constraint is related to the curvature of the function near the boundary, in a similar fashion to what was performed for the $[1/1]$ case. The constraint in $[2/2]_I$ is based on the observation from Fig. 5 (b) that the maximum distance between the $[1/1]$ approximant and $\text{sinc}(\mathscr{A})$ occurs near $\mathscr{A} \approx 0.41$, where $\text{sinc}\left(-\frac{2\pi}{3}\right) = \frac{3\sqrt{3}}{4\pi}$ is exactly known. From Fig. 5 (b) it is clear that while both approaches significantly improve the modulation relative to the $[1/1]$ approximant, it can be seen that $[2/2]_I$ gives results better than $[2/2]_B$ by a factor of 2 over the range of physical values for $\mathscr{A}$. Notice that the maximum distance for $[2/2]_I$ implies in a resolution of nearly 12 bits in the modulation of amplitude.

For usage in 8 bits SLM's, the accuracy of the approximation proposed here should be sufficient to ensure a nearly ideal phase encoding. The modulation problems then should be related to issues not related to numerical innacuracy. Performing the calculations using python's numpy package [81], and evaluating the calculation time within the IPython framework [82], it was verified that the time for calculating the approximants here described can be smaller than 10 ms for an image with 1024x1024 pixels in an ordinary laptop. The 10 ms timescale directly indicates the possibility to update the hologram near or above to the maximum refresh rate of typical liquid crystal SLM's (60 - 120 Hz). As a final comment, an equivalent analysis of approximants can also be performed for other transfer functions relevant for amplitude modulation, as Bessel functions [77].

A numerical experiment

As an example of the previous discussion, it will be discussed below an analysis for the simultaneous amplitude and phase encoding of a Laguerre-Gauss mode at its minimum beam waist.

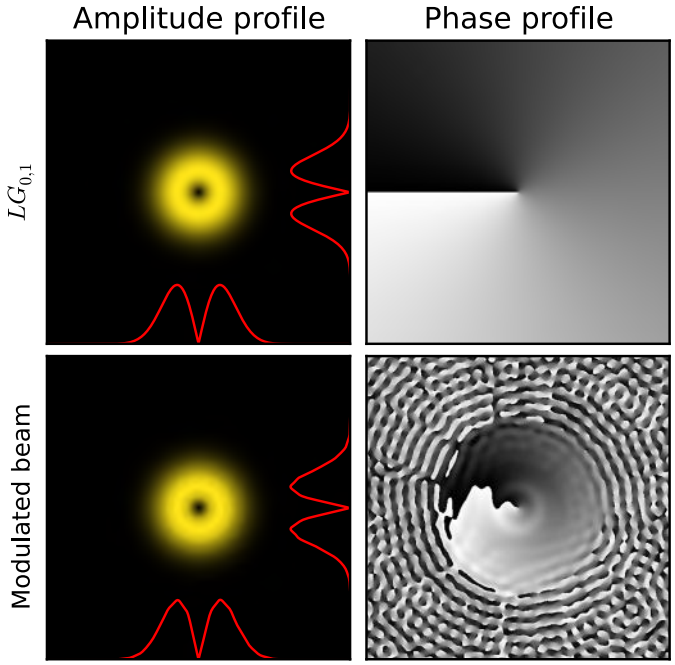

Figure 6 – Comparison between the ideal amplitude and phase profiles of the $LG_{0,1}$ mode at the minimum beam waist (upper row) with the spatial filtered beam plane wave modulated by a simultaneous amplitude and phase modulation phase mask (lower row). The insets in the amplitude profiles represent the cross-sections along the beam center. The carrier was removed for a better comparison. The modulated beam intensity profile follows closely that expected for the $LG_{0,1}$ mode. Meanwhile, the modulated phase profile has some small distortions near the central region with respect to the target phase profile, and it is not well defined at low intensities.

The transverse profile of the $LG_{0,1}$ mode is mathematically described by Eq. (2.59), and the associated amplitude and phase profiles can be seen in Fig. 6. It is assumed here that a plane wave is normally incident to mask whose phase profile may be modulated. If the $LG_{0,1}$ amplitude and phase profiles (with a carrier) are substituted in (3.19), it is obtained a mask phase profile, $M(\boldsymbol{r})\Phi(\boldsymbol{r})$, as represented in Fig. 7. Due to the carrier, it is necessary to perform a filtering in the Fourier plane of the optical system. The intensity profile in the Fourier plane can also be seen in Fig. 7. Notice that the grating profile produces several diffraction orders which spatially redistribute the energy of the incident plane wave. By filtering only the first diffracted order (surrounded by the white circle), the modulated beam profiles shown in Fig. 6 is obtained. Even though this discussion is merely based on numerical manipulations, a conceptually similar procedure is performed in the experiment.

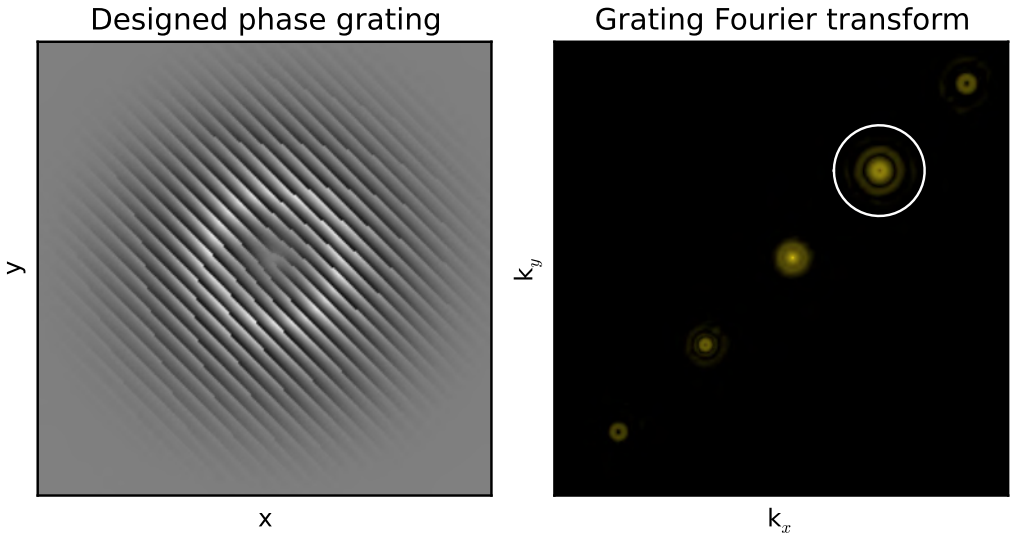

Figure 7 – Phase profile which simultaneously encodes amplitude and phase information of a $LG_{0,1}$ mode and the associated 2D power spectrum of the Fourier transform (log scale). The white circle represents the aperture used for spatial filtering.

4 Optical vortices and their properties

4.1 Introduction

In the recent literature there is a growing number of studies involving the fundamentals and applications of Optical Vortices (OVs) and light beams carrying Orbital Angular Momentum (OAM) [23]. These studies gained momentum after the seminal work by Allen and collaborators [21], which explains that several important light fields have OAM. An OV is a topological feature of the beam, characterized by a region in which the phase profile has an integer number of jumps, q, between $-\pi$ and π along a closed contour encircling a phase singularity. The number q is also known as the topological charge (TC). Although in the optics literature it seems sometimes that OV are unique features that appear only in some specific contexts, as for example in Laguerre-Gauss modes or Bessel Beams, they are ubiquitous. For example, if one superimposes three non-colinear plane waves, several pairs of OV can appear [17], as represented in Fig. 8. Therefore, since it is possible to produce OV under such simplistic circumstances, it should be expected that they arise in various contexts. Indeed, OV appear naturally for example in speckle patterns [83–86].

In several applications there are some characteristics of OV that become more important than others. For example, in optical communications both in classical [24] and quantum regimes [26], the orthogonality among modes enables the multiplexing and demultiplexing of information, enhancing the data transmission rate of these systems. In applications as

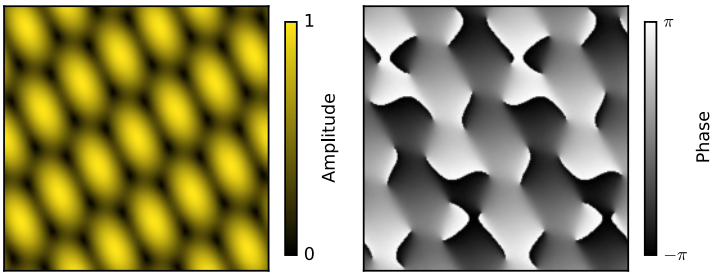

Figure 8 – Interference between three non-collinear plane waves. Notice that there are several points where the amplitude is 0. In a sufficiently small closed contour around such points the phase profile jumps between $-\pi$ and π. The phase singularity at these points requires a vanishing amplitude. To conserve the total angular momentum, the OV are produced in pairs with opposed charges.

optical tweezers, the OAM profile enables the control of the particle motion along the plane transverse to the beam propagation [23, 87]. The stability of the singular region and the amplitude growth ratio are very important in optical trapping applications [88]. In plasmonics it is possible to have a selective excitation of surface plasmon modes[89, 90]. Therefore, it is extremely important to understand how the OV properties can be optimized for a given application, and also the mechanisms which destabilize the light characteristics from its optimum values.

Most of the works in current literature in OV uses cylindrically shaped beams, and there are many degrees of freedom almost unexplored until recently. A result developed in this thesis is that beams with non-zero OAM can have any shape, and at the same time be constructed in a single spatial light modulator (SLM) [1]. Previous works which generated shaped OAM beams resorted on two SLM's [91] or Lissajous patterns [92]. The development of theoretical and technical tools described below enables simpler experimental setups and higher conversion efficiencies from input light to OAM beam. Also, the concepts developed can enable novel applications in diverse areas as optical traps and tweezers, pre-compensation of geometric aberrations, topological quantum computing and plasmonics.

In this chapter there is an initial discussion on the TC and OAM in a paraxial light beam. Then, the next sections contains the following original contributions of this thesis: (1) it will be shown that the association of q with a charge can be made clearer and more intuitive by developing an analogy between the topological charge and two-dimensional (2D) electrostatics; (2) since the TC distributions have important distinctions relatively to electrostatics, some formal mathematical results are briefly commented on the validity of the results presented; (3) Then, some TC distributions are considered, as the TC distributions along lines and the 2D radial TC distribution; (4) Finally, the concept of optical vortex multipoles is introduced and a relation between beam's phase pitch and shape is obtained.

4.2 TC and OAM in a light beam

In cylindrical coordinates $\mathbf{r} = \mathbf{r}(\rho, \phi, z)$ a paraxial monochromatic field may be represented at a plane z through

$$\mathbf{A}(\mathbf{r}, t) = \hat{\epsilon}\left(\frac{2\mu_0}{\omega k}P_0\right)^{\frac{1}{2}} \mathscr{A}(\mathbf{r}) \exp i\left[\chi(\mathbf{r}) + kz - \omega t\right], \tag{4.1}$$

where P_0 is the optical power, μ_0 is the vacuum permeability, ω and k are the light angular frequency and wave number, respectively. The remaining terms are the beam transverse phase profile $\chi(\mathbf{r})$ and $\mathscr{A}(\mathbf{r})$ is the vector potential amplitude envelope, normalized such that $\int \rho d\rho d\phi |\mathscr{A}(\mathbf{r})|^2 = 1$. It is considered a linearly polarized field, such that the Poynting vector, Eq. (2.114), does not have the spin contribution.

The total TC, Q_T, contained inside a contour C of radius c, at the plane $z = z_0$, i.e. on the plane ρ, ϕ perpendicular to the propagation direction, may be written as [79, 93]

$$Q_T = \frac{1}{2\pi} \oint_C d\mathbf{x} \cdot \vec{\nabla}_\perp \chi(\mathbf{r}), \tag{4.2}$$

where $d\mathbf{x}$ is the infinitesimal displacement along C. The TC informs how many times the beam phase pass through the interval $[0, 2\pi]$ following the curve C. If the contour C does cross a singularity, Q_T is an integer even when $\chi(\mathbf{r})$ has discontinuities [79]. A single TC is positioned at any point $\mathbf{r}$ in the plane z_0 such that $\Re\mathfrak{e}\{\mathbf{A}(\mathbf{r}, t)\} = \Im\mathfrak{m}\{\mathbf{A}(\mathbf{r}, t)\} = 0$ and the integral in Eq. (4.2) is nonzero when C is a circle of infinitesimal radius encircling $\mathbf{r}$. For example, supposing that the field of interest has a finite region containing singularities, C may be chosen as a circle of radius $\rho = c$ enclosing such region.

From the definition in Eq. (4.2), Q_T is independent of the shape of C. It is possible to consider, for example, that C is a circle of radius c, what simplifies Eq. (4.2) to

$$Q_T = \frac{1}{2\pi} \int_0^{2\pi} w\left(\rho = c, \phi, z_0\right) d\phi, \tag{4.3}$$

where $w(\mathbf{r})$ is the local OAM (ℓ-OAM) [94],

$$w(\mathbf{r}) = \frac{\partial \chi}{\partial \phi}(\mathbf{r}). \tag{4.4}$$

The chosen contour has some advantages, as the ability to observe a spatial profile relative to the TC distribution through $w(\mathbf{r})$, and it is directly related to the beam ℓ-OAM. The evaluation of $w(\mathbf{r})$ is important because it associates a designed OV phase structure to the experimentally obtained profile, both qualitatively (spatial profile) and quantitatively (through Eq. 4.3). $w(\mathbf{r})$ characterizes the OV morphology[95, 96], and will be used here to associate a spatial profile to the beam topological properties. It should be remarked that the ℓ-OAM can assume any value in principle. In the general case, the connection between the ℓ-OAM and the TC is through Eq. (4.3). *The TC is the average value of the ℓ-OAM through the contour C. Therefore if $w(\mathbf{r}) > Q_T$ at some portion of the curve C, there must be another portion in which $w(\mathbf{r}) < Q_T$.*

Another quantity of general interest in OV is the classical OAM density of light, L_z, along the propagation direction $\hat{z}$. Using (2.115), it can be shown that $L_z = \frac{\epsilon_0 \omega}{2} \Re\left\{\mathbf{A}(\mathbf{r}, t)\left(-i\frac{\partial}{\partial \phi}\right)\mathbf{A}^*(\mathbf{r}, t)\right\}$, and by direct substitution of Eq. (4.1), we obtain

$$L_z = \frac{P_0}{\omega c}\left[\mathscr{A}^*(\mathbf{r})\frac{\partial \chi}{\partial \phi}\mathscr{A}(\mathbf{r})\right]. \tag{4.5}$$

Since $P_0 = N\hbar\omega$, where N is the number of photons carrying energy $\hbar\omega$ impinging on the plane $\rho\phi$ per second, the ℓ-OAM value per photon at a given position is $\hbar w = \hbar\partial\chi/\partial\phi$ [94]. Considering that the product $\mathscr{A}^*(\mathbf{r})\mathscr{A}(\mathbf{r})$ is related to the electromagnetic energy density at

a given point[1], the semi-classical average OAM per photon may be determined from Eq. (4.5) as

$$\hbar \langle l \rangle = \hbar \int \rho d\rho d\phi \mathscr{A}^* (\mathbf{r}) \frac{\partial \chi}{\partial \phi} \mathscr{A} (\mathbf{r}) . \tag{4.6}$$

A comparison between Eqs. (4.3) and (4.6) shows $Q_T \neq \langle l \rangle$ in general. We therefore remark that usually there is no direct relation between OAM and total TC [98]. Even for beams with azimuthal symmetry, it is possible to obtain exotic configurations in which these quantities are distinct. For example, by embedding a Laguerre-Gauss beam characterized by a TC $m_{\text{inner}} > 0$ inside the core of another Laguerre-Gauss beam characterized by a TC $m_{\text{outer}} > m_{\text{inner}} > 0$, it can be observed that the superposition of these beams leads to $Q_T = m_{\text{outer}}$, while $\langle l \rangle < m_{\text{outer}}$. Also, although the intensity profile of a beam is related to its TC distribution [1, 79, 92], it does not carry information about the topological or OAM properties of a beam [99]. *Therefore in a general OV, by measuring Q_T one does not necessarily have information about $\langle l \rangle$ and vice-versa. However, both quantities are related to the ℓ-OAM which can be obtained from $\chi (\mathbf{r})$.*

4.3 Optical vortices at $z = 0$

Remembering that an optical beam is defined everywhere in space if the complex electric field is completely known in a infinite plane on paraxial regime, the current analysis starts by considering an homogeneously polarized electric field containing a vortex at the plane $z = 0$. Given the vector potential $\mathbf{A} (\mathbf{r}, z) = \hat{\epsilon} \mathscr{A} (\mathbf{r}, z) e^{i(kz - \omega t)}$, representing a light field propagating along $\hat{z}$ direction, it must satisfy Eq. (2.22),

$$\left(\nabla_\perp^2 + 2ik \frac{\partial}{\partial z} \right) \mathscr{A} (\mathbf{r}, z) = 0, \tag{4.7}$$

where $\mathbf{r}$ represents a vector along the plane transverse to z and $\nabla_\perp$ indicates the gradient operator over the transverse plane.

The goal in this section is to study generic OV configurations in a plane, defined at a plane $z = 0$. We begin the analysis by considering the asymptotic behavior of $\mathscr{A} (\mathbf{r}, z)$ near the region $\mathbf{r} = 0$. The vector potential envelope, $\mathscr{A} (\mathbf{r}, 0)$, can be factored in two terms. $f (\mathbf{r})$ has a fast variation near $\mathbf{r} = 0$, while $A_0 (\mathbf{r})$ changes slowly, such that

$$\mathscr{A} (\mathbf{r}, 0) = f (\mathbf{r}) A_0 (\mathbf{r}) , \tag{4.8}$$

and only the transverse derivatives over $f (\mathbf{r})$ are significant near $\mathbf{r} = 0$. Then, we obtain that $f (\mathbf{r})$ is an harmonic function over the transverse coordinates,

$$\nabla_\perp^2 f (\mathbf{r}) = 0. \tag{4.9}$$

[1] Notice that in quantum mechanics the spatial localization of the photon is a problematic concept [48, 97], and therefore the relation of this product with the probability to find the photon at a given transverse position should be avoided.

Solving for $f(\mathbf{r})$ near $\mathbf{r}=0$ in cylindrical coordinates, there are two orthogonal solutions well behaved at the origin: $r^q e^{iq\phi}$ and $r^q e^{-iq\phi}$, where $\pm q$ is the TC of the associated OV, r is the radial coordinate and ϕ is the azimuthal angle. An important point to notice is that q must be integer valued to guarantee the single-valuedness of $f(\mathbf{r})$. In order to represent arbitrary OV configurations, it is necessary to combine both contributions from the OV with positive and negative TC. This is a problem similar to representing a generic state of a spin 1/2 system, or the Jones representation of light polarization [95, 100]. Given the two morphological parameters α and β, such that $0 \leq \alpha \leq \pi$ and $0 \leq \beta \leq 2\pi$, the most general representation of an OV in the vicinity of $\mathbf{r}=0$ is

$$f_0(r,\phi) = \cos\frac{\alpha}{2} e^{i\frac{\beta}{2}} \left(r^q e^{iq\phi}\right) + \sin\frac{\alpha}{2} e^{-i\frac{\beta}{2}} \left(r^q e^{-iq\phi}\right), \tag{4.10}$$

where it can be observed that α indicates the relative amplitude of the positive and negative OV, and β is an OV orientation angle.

While Eq. (4.10) represents an OV at $\mathbf{r}=0$, it cannot express a distribution of TC over the transverse plane. In order to describe generic OV configurations, Eq. (4.10) must be generalized for TC distributions. While in this paragraph we perform an intuitive picture based in physical ideas, these concepts will be mathematically stated rigorously in terms of entire functions later in Sec. 4.3.2. Notice that the solution with positive TC can be represented as the complex variable $u^q = (x+iy)^q = r^q e^{iq\phi}$, which allows the generalization of the initial solutions by performing translations along the xy plane. Since u^q represents an OV whose TC is q at the position $\mathbf{r}=0$, $(u-\delta)^q$ represents the same OV but at a distinct location. For example, if $\delta = a+ib$ the OV is centered at $x=a$ and $y=b$. Another possible extension consists in distributing the TC over the transverse plane. Notice that $\lim_{\delta_1,\delta_2\to 0}(u-\delta_1)^{q_1}(u-\delta_2)^{q_2} = u^q$ if $q_1+q_2=q$. In this case, δ_i represents the displacement of a TC fraction q_i relative to $\mathbf{r}=0$. A similar generalization can be carried for the solution $r^q e^{-iq\phi}$ if it is identified that $(u^*)^q = r^q e^{-iq\phi}$, where $*$ represents the complex conjugation.

Thus, considering various operations in which the TC is divided and displaced results in a generalization of Eq. (4.10),

$$f(u) = \prod_{i=1}^{N} \left[\cos\frac{\alpha_i}{2} e^{i\frac{\beta_i}{2}} (u-\delta_i)^{q_i} + \sin\frac{\alpha_i}{2} e^{-i\frac{\beta_i}{2}} \left(u^* - \delta_i^*\right)^{q_i}\right], \tag{4.11}$$

where it is assumed that $\sum_{i=1}^{N} q_i = Q_N$, where Q_N and q_i must be integers to ensure the single-valuedness of $f(u)$. It is also important to remark that the current discussion assumes that $q_i > 0$. When $u = \delta_j + \epsilon$ for a very small ϵ,

$$f(\delta_j+\epsilon) \approx \left(\cos\frac{\alpha_j}{2} e^{i\frac{\beta_j}{2}} \epsilon^{q_j} + \sin\frac{\alpha_j}{2} e^{-i\frac{\beta_j}{2}} \epsilon^{*q_j}\right) \prod_{i=1, i\neq j}^{N} \left[\cos\frac{\alpha_i}{2} e^{i\frac{\beta_i}{2}} (\delta_j-\delta_i)^{q_i} + \sin\frac{\alpha_i}{2} e^{-i\frac{\beta_i}{2}} \left(\delta_j^* - \delta_i^*\right)^{q_i}\right]. \tag{4.12}$$

such that $f(\delta_j+\epsilon)$ has an OV at δ_j whose TC modulus is q_j, and the associated morphological parameters are α_j and β_j.

In what follows a full consideration of Eq. (4.11) is very difficult, thus it is assumed for simplicity that $\alpha_i = 0$ for all i. After a coordinate rescaling, $v = w_0 u$ and some algebraic manipulations,

$$f_+(v) = (w_0)^{-\sum_{i=1}^{N} q_i} \exp\left\{ \sum_{i=1}^{N} \left[q_i \log(v - v_i) + i\frac{\beta_i}{2} \right] \right\}, \tag{4.13}$$

where $f_+(v)$ indicates that this is a distribution of positive TC, $v_i = \delta_i / w_0$ and log is the natural logarithm. For negative TC, $f_-(v) = f_+^*(v)$ can be taken. Since the term $\sum_{i=1}^{N} i\frac{\beta_i}{2}$ here represents only an overall transverse phase, it is ignored below. It is possible to perform a continuum generalization by rewriting $q_i \to \rho_+(v_i)\, da'$, where $\rho_+(v_i)$ represents a positive density of TC at the position v_i, and da' is the normalized area element at v_i, such that

$$\sum_{i=1}^{N} q_i \to \int_D da' \rho_+(v') = Q_+, \tag{4.14}$$

$$\sum_{i=1}^{N} q_i \log(v - v_i) \to \int_D da' \rho_+(v') \log(v - v') = V_+(v), \tag{4.15}$$

where D is the integration domain. Notice that the real part of $V_+(v)$ is formally identical to the complex electric potential in 2D electrostatics [101, 102], and the expression for only negative TC can be obtained through the complex conjugate of (4.15). This analogy seems interesting for designing OV for specific applications, because it is possible to use concepts and results from a well established field. It is worth noticing that the factorization of solutions that leads to Eq. (4.15) can be stated more precisely in terms of the Weierstrass product, as will be done later. An arbitrary OV can be represented by the product between an envelope with a Gaussian decay and an entire analytical function of a single complex variable $f(u)$ [55, 56, 103]. In terms of the Weierstrass product, it is possible to represent $f(u)$ as a product of its zeros, $f(u) = \prod_{i=1}^{N} (u - u_i)^{q_i}$, where u_i and q_i are, respectively the position of the zero and its associated TC.

To have a more general representation for OV it is necessary to describe fields containing positive and negative TC. A direct exponentiation of (4.11), as was used to obtain (4.15) is very difficult. Another aspect worth noticing is that the continuum generalization only makes sense for an expression linear in q_i. However, it is possible to use the identity

$$a^{\epsilon} = e^{\epsilon \log a} = \sum_{k=0}^{\infty} \frac{(\epsilon \log a)^k}{k!}, \tag{4.16}$$

for small values of the exponent ϵ to cast the multiplicative factors in (4.11) for a simpler handling. Assuming $q_i \left|\log(v - v_i)\right| \ll 1$, it is possible to approximate to first order in q_i that

$$\begin{aligned} &\cos\frac{\alpha_i}{2} e^{i\frac{\beta_i}{2}} (v - v_i)^{q_i} + \sin\frac{\alpha_i}{2} e^{-i\frac{\beta_i}{2}} \left(v^* - v_i^*\right)^{q_i} \\ &\qquad \approx \cos\frac{\alpha_i}{2} e^{i\frac{\beta_i}{2}} \left[1 + q_i \log(v - v_i)\right] + \sin\frac{\alpha_i}{2} e^{-i\frac{\beta_i}{2}} \left[1 + q_i \log\left(v^* - v_i^*\right)\right] \qquad (4.17) \\ &= \left(\cos\frac{\alpha_i}{2} e^{i\frac{\beta_i}{2}} + \sin\frac{\alpha_i}{2} e^{-i\frac{\beta_i}{2}}\right) \left[1 + q_i \frac{\cos\frac{\alpha_i}{2} e^{i\frac{\beta_i}{2}} \log(v - v_i) + \sin\frac{\alpha_i}{2} e^{-i\frac{\beta_i}{2}} \log\left(v^* - v_i^*\right)}{\cos\frac{\alpha_i}{2} e^{i\frac{\beta_i}{2}} + \sin\frac{\alpha_i}{2} e^{-i\frac{\beta_i}{2}}}\right]. \end{aligned} \tag{4.18}$$

The overall multiplicative factor in (4.18) can usually be included in the field normalization constant when $\beta \neq \pi$, since then $\left(\cos\frac{\alpha_i}{2}e^{i\frac{\beta_i}{2}} + \sin\frac{\alpha_i}{2}e^{-i\frac{\beta_i}{2}}\right) \neq 0$. The logarithms can be simplified. For instance, using that $\log z = \log|z| + i\arg z$, and $\log z^* = \log|z| - i\arg z$,

$$\frac{\cos\frac{\alpha_i}{2}e^{i\frac{\beta_i}{2}}\log(v-v_i) + \sin\frac{\alpha_i}{2}e^{-i\frac{\beta_i}{2}}\log\left(v^*-v_i^*\right)}{\cos\frac{\alpha_i}{2}e^{i\frac{\beta_i}{2}} + \sin\frac{\alpha_i}{2}e^{-i\frac{\beta_i}{2}}} = \log|v-v_i| + iD_i\arg(v-v_i), \tag{4.19}$$

$$D_i = \frac{\cos\frac{\alpha_i}{2}e^{i\frac{\beta_i}{2}} - \sin\frac{\alpha_i}{2}e^{-i\frac{\beta_i}{2}}}{\cos\frac{\alpha_i}{2}e^{i\frac{\beta_i}{2}} + \sin\frac{\alpha_i}{2}e^{-i\frac{\beta_i}{2}}} = \frac{\cos\alpha + i\sin\alpha\sin\beta}{1+\sin\alpha\cos\beta}, \tag{4.20}$$

The simplified expression in (4.19) already embodies a very important information. The morphological parameters are strongly coupled with the phase structure of the beam through the parameter D_i, while the amplitude profile dependence on α_i and β_i is less pronounced. D_i contains the morphology information, and is such that for $\beta_i = 0$, $-1 \leq D_i \leq 1$ and it varies almost linearly with α_i, indicating that it contains the information about the contribution due to the positive and the negative TC at a point. According to the parametrization in (4.20), it can be noticed that the real and imaginary parts of D_i are defined in the intervals $-\infty < \Re\{D_i\} < \infty$ and $-\infty < \Im\{D_i\} < \infty$, respectively, indicating that D_i can assume values over a large portion of the complex plane.

If the result (4.19) is substituted in (4.18), and the approximation $1 + x \approx \exp(x)$ is performed, it is obtained that

$$\cos\frac{\alpha_i}{2}e^{i\frac{\beta_i}{2}}(v-v_i)^{q_i} + \sin\frac{\alpha_i}{2}e^{-i\frac{\beta_i}{2}}\left(v^*-v_i^*\right)^{q_i} \approx \left(\cos\frac{\alpha_i}{2}e^{i\frac{\beta_i}{2}} + \sin\frac{\alpha_i}{2}e^{-i\frac{\beta_i}{2}}\right)\exp\left[q_i\log|v-v_i| + iq_iD_i\arg(v-v_i)\right], \tag{4.21}$$

where it can be observed that (4.21) is exact for $\alpha_i = 0, \pi$. When $\alpha_i \to \pi/2$ and $\beta_i \to \pi$, Eq. (4.21) correctly approximates the superposition of oppositely charged OV with small values of q_i. The divergence of D_i is compensated by the factor multiplying the exponential. Another interesting aspect of (4.19) is that its continuum generalization can be visualized intuitively by a direct comparison with (4.13). Starting from (4.11), including the overall multiplication factor in the field normalization constant and using (4.21), one arrives at $f(v) \approx (w_0)^{-\sum_{i=1}^N q_i}\exp\left\{\sum_{i=1}^N q_i\left[\log|v-v_i| + iD_i\arg(v-v_i)\right]\right\}$, whose continuum limit is

$$f(v) = w_0^{-Q}e^{V(v)}, \tag{4.22}$$

$$V(v) = \int_D da'\rho\left(v'\right)\left[\log\left|v-v'\right| + iD\left(v'\right)\arg\left(v-v'\right)\right], \tag{4.23}$$

$$D\left(v'\right) = \frac{\cos\frac{\alpha(v')}{2}e^{i\frac{\beta(v')}{2}} - \sin\frac{\alpha(v')}{2}e^{-i\frac{\beta(v')}{2}}}{\cos\frac{\alpha(v')}{2}e^{i\frac{\beta(v')}{2}} + \sin\frac{\alpha(v')}{2}e^{-i\frac{\beta(v')}{2}}}, \tag{4.24}$$

$$Q = \int_D da'\rho\left(v'\right). \tag{4.25}$$

Notice that if $D\left(v'\right)$ is real, the real part of $V\left(v\right)$ still is equivalent to the expression for a 2D distribution of positive electric charges in electrostatics [101, 102]. Therefore, $V\left(v\right)$ is called here the Topological Potential (TP) due to a distribution of TC over the transverse plane, and is the major original contribution within this chapter. A distinctive characteristic is that while in electrostatics the most relevant part of the expression is the real part, in the context of OV the imaginary part of the potential contains the most relevant information. Another aspect is that $\rho\left(v'\right) > 0$, since according to the previous definitions $q_i > 0$. This is important to ensure that the amplitude profile is not singular near the charge distribution. A crucial characteristic of the TP is the morphology modulation parameter, $D\left(v'\right)$, which encodes the local morphology structure. Relative to the case where there is only a distribution of positively charged TC, Eq. (4.15), the general case described by (4.23) can be obtained by multiplying the imaginary part of the integrand in (4.15) by $D\left(v'\right)$. As a remark to our interpretation of Eq. (4.23), the reader should notice that in a very brief comment, M. V. Berry stated in [16] that the vortex phase could be understood as a potential, and the TP introduced in this work extends this concept by adding the spatial structure.

In the next subsection there is a discussion on the formal mathematical grounds that should give some insights on the meaning of the discussed TC distributions and the scope of the proposed approach. Although not strictly necessary for operating over the following results, the next section is useful to understand some of the constraints for using the TP formalism.

4.3.1 Some electrostatics concepts applied to the topological potential

Since it was shown an equivalence between the TP and 2D electrostatics, it is useful to remember some of the established tools for 2D electrostatics that might be useful for problems involving the design of OV.

Circular harmonics and Dirac delta distribution in 2D

An harmonic function f is a solution to the Laplace equation $\nabla^2 f = 0$, a condition also satisfied by an OV, as explained before in Eq. (4.10). Since circular harmonics form a complete set of orthogonal functions in 2D, they can be used to represent square integrable functions as

$$f\left(r,\phi\right) = \left(A_0\phi + B_0\right)\left(C_0 \log r + D_0\right) + \int_{\epsilon}^{\infty} dm \left[A\left(m\right)\cos\left(m\phi\right) + B\left(m\right)\sin\left(m\phi\right)\right]\left[C\left(m\right)r^m + D\left(m\right)r^{-m}\right]. \quad (4.26)$$

Free-space solutions are well defined at every azimuthal angle and must satisfy $f\left(r,\phi\right) =$

$f(r,\phi+2\pi)$. This selects $A_0=0$ and only integer values of m,

$$f'(r,\phi)=(C_0\log r+D_0)+\sum_{m=1}^{\infty}\left[A_m\cos(m\phi)+B_m\sin(m\phi)\right]\left[C_m r^m+D_m r^{-m}\right], \text{ or} \tag{4.27}$$

$$=(C_0\log r+D_0)+\sum_{m\neq 0}\left[C_m r^m+D_m r^{-m}\right]e^{im\phi}. \tag{4.28}$$

With the above expressions it is possible to represent generic solutions to the Laplace equation in free-space and also square integrable functions. It is also of great interest is the Dirac delta distribution which, via the identity $\delta(\phi-\phi')=\frac{1}{2\pi}\sum_m \exp(im\phi)$, can be expressed as

$$\delta(\mathbf{r}-\mathbf{r}')=\frac{1}{r'}\delta(r-r')\,\delta(\phi-\phi')=\frac{1}{2\pi}\sum_{m=-\infty}^{\infty}\left[\frac{\delta(r-r')}{r'}\right]\exp(im\phi). \tag{4.29}$$

Green's functions

The formalism of Green's functions is a mathematical tool used to express the solution in terms of a sum (or integral) of the contributions due to individual sources. The interest here is to describe the Green function $G(\mathbf{r},\mathbf{r}')$ over 2D in circular coordinates that describes the potential amplitude and phase profiles due to an arbitrary distribution of TC. $\mathbf{r}$ represents the coordinate where the potential is being evaluated, while $\mathbf{r}'$ represents the source position. Also, since the physical effects must depend only on the distance, $G(\mathbf{r},\mathbf{r}')$ must be symmetric under the interchange of $\mathbf{r}\leftrightarrow\mathbf{r}'$. For a point source,

$$\nabla'^2 G(\mathbf{r},\mathbf{r}')=2\pi\delta(\mathbf{r}-\mathbf{r}'), \tag{4.30}$$

where the prime denotes that the Laplacian acts only over the primed coordinates. The 2π factor is a normalization constant. Assuming the following expansion for $G(\mathbf{r},\mathbf{r}')$,

$$G(\mathbf{r},\mathbf{r}')=g_0(\mathbf{r},\mathbf{r}')+\frac{1}{2\pi}\sum_{m\neq 0}g_m(\mathbf{r},\mathbf{r}')\,e^{im(\phi-\phi')}, \tag{4.31}$$

it is obtained for $m\neq 0$ that

$$\frac{1}{r'}\frac{\partial}{\partial r'}\left(r'\frac{\partial g_m}{\partial r'}\right)-\frac{m^2}{r'^2}g_m=2\pi\delta(r-r'). \tag{4.32}$$

The Dirac delta gives just a derivative discontinuity at $r=r'$, while anywhere else $g_m=A_m r'^m+B_m r'^{-m}$. The coefficients A_m and B_m are different for $r>r'$ and $r<r'$. But considering that g_m is well behaved at $r'=0$ and $r'=\infty$, and the interchange symmetry of $\mathbf{r}\leftrightarrow\mathbf{r}'$,

$$g_m=-\frac{\pi}{2m}\left(\frac{r_<}{r_>}\right)^m, \tag{4.33}$$

where $r_>$ ($r_<$) refers to the larger (smaller) between r and r'.

To determine $g_0(\mathbf{r},\mathbf{r}')$ it is possible to calculate the derivative discontinuity of the logarithmic term at $\mathbf{r}=\mathbf{r}'$, and with the interchange symmetry,

$$g_0(\mathbf{r},\mathbf{r}')=\log(r_>). \tag{4.34}$$

Collecting the above results,

$$G\left(\mathbf{r},\mathbf{r}'\right) = \log\left(r_>\right) - \sum_{m\neq 0} \frac{1}{2m}\left(\frac{r_<}{r_>}\right)^m e^{im(\phi-\phi')}. \tag{4.35}$$

$$= \log\left(r_>\right) - \sum_{m=1}^{\infty} \frac{1}{m}\left(\frac{r_<}{r_>}\right)^m \cos\left[m\left(\phi-\phi'\right)\right]. \tag{4.36}$$

The Green function presented here is purely real, and adequate for calculations in electrostatics. It can be shown that $G\left(\mathbf{r},\mathbf{r}'\right) = \log\left|\mathbf{r}-\mathbf{r}'\right|$. However, for the purposes of this work, there is interest in a similar expansion of the complex logarithm. Considering $u = re^{i\phi}$ and $u' = r'e^{i\phi'}$, while representing by $r_>, \phi_>$ $\left(r_<, \phi_<\right)$ the quantities associated with the respective coordinates of u, u' with larger (smaller) radial coordinate, it can be shown that

$$\log\left(u-u'\right) = \log r_> + i\phi_> - \sum_{m=1}^{\infty} \frac{1}{m}\left(\frac{r_<}{r_>}\right)^m e^{im(\phi_<-\phi_>)}. \tag{4.37}$$

An identification of the real and imaginary parts on both sides of $\log\left(u-u'\right) = \log\left|u-u'\right| + i\theta\left(u-u'\right)$ provides

$$\log\left|u-u'\right| = \log\left(r_>\right) - \sum_{m=1}^{\infty} \frac{1}{m}\left(\frac{r_<}{r_>}\right)^m \cos\left[m\left(\phi_<-\phi_>\right)\right], \tag{4.38}$$

$$\theta\left(u-u'\right) = \phi_> - \sum_{m=1}^{\infty} \frac{1}{m}\left(\frac{r_<}{r_>}\right)^m \sin\left[m\left(\phi_<-\phi_>\right)\right]. \tag{4.39}$$

The expression of the Green function in terms of circular harmonics facilitates the later discussion of TC multipoles. It is interesting to note the following general relations

$$r_> \frac{\partial \log\left|u-u'\right|}{\partial r_>} = \frac{\partial \theta\left(u-u'\right)}{\partial \phi_>}, \tag{4.40}$$

$$\frac{\partial \log\left|u-u'\right|}{\partial \phi_>} = -r_> \frac{\partial \theta\left(u-u'\right)}{\partial r_>}. \tag{4.41}$$

These derivatives are the Cauchy-Riemann conditions in polar coordinates and can be removed from the integral in specific cases. Within the context of OV they mean that phase and amplitude profiles are intimately coupled near the OV core.

For completeness, the discussion on Green's functions finishes here with the calculation of the imaginary part of $\nabla^2 \log\left(u-u'\right)$. Remembering the Cauchy-Riemann conditions in Cartesian coordinates, given an analytic function $g(u) = w(u) + i\,t(u)$, where w and t are real functions of the complex variable $u = x + i\,y$,

$$\frac{\partial w}{\partial x} = \frac{\partial t}{\partial y}, \tag{4.42}$$

$$\frac{\partial t}{\partial x} = -\frac{\partial w}{\partial y}. \tag{4.43}$$

With Cauchy-Riemann conditions, it can be verified that $\nabla^2\theta\left(u-u'\right) = \frac{\partial}{\partial x}\left(-\frac{\partial \log|u-u'|}{\partial y}\right) + \frac{\partial}{\partial y}\left(\frac{\partial \log|u-u'|}{\partial x}\right) = \left(\frac{\partial}{\partial y}\frac{\partial}{\partial x} - \frac{\partial}{\partial x}\frac{\partial}{\partial y}\right)\log\left|u-u'\right| = 0$, for $u \neq u'$. At the point $u = u'$ there may be a

Dirac delta singularity, which can be verified after the integration the Laplacian over a transverse area A whose boundary curve is ∂A. Using Green's theorem,

$$\int_A dxdy\nabla^2 \log\left(u-u'\right) = \int_{\partial A} dl\,\hat{n}\cdot\vec{\nabla}\log\left(u-u'\right), \tag{4.44}$$

where dl is the line element along ∂A, and $\hat{n}$ is the exterior normal. Since $\vec{\nabla}\log\left(u-u'\right) = \frac{d}{du}\log\left(u-u'\right)\vec{\nabla}u = \vec{\nabla}u/\left(u-u'\right)$, and considering that A is a small circle of radius b around u', it is useful to perform the transformation $u = u'+re^{i\phi}$. Then, $\hat{n} = \hat{r}$, $dl = bd\phi$, $\vec{\nabla}\log\left(u-u'\right) = \left(\hat{r}+i\hat{\phi}\right)/r$, and the integration limits are $\phi = 0$ and $\phi = 2\pi$,

$$\int_{\partial A} dl\,\hat{n}\cdot\vec{\nabla}\log\left(u-u'\right) = \int_0^{2\pi} bd\phi\,\hat{r}\cdot\left(\frac{\hat{r}}{b}+i\frac{\hat{\phi}}{b}\right). \tag{4.45}$$

$$= 2\pi, \tag{4.46}$$

indicating that only the real part has a Dirac delta singularity. Since the imaginary part of $\nabla^2\log\left(u-u'\right)$ is zero when $u \neq u'$ and does not have a Dirac-delta like contribution at $u = u'$,

$$\nabla^2\log\left(u-u'\right) = 2\pi\delta\left(u-u'\right). \tag{4.47}$$

Gauss' and Ampère's laws

One of the most useful results within 2D electrostatics is Gauss' law, which relates the electric field at a closed contour to the enclosed charge. If the symmetry of the problem is appropriate, Gauss' law simplifies the calculation of the electric potential and electric field over the whole space. Within the context of the TP, it is also possible to obtain a relation similar to the one found in electrostatics.

Applying the identity (4.47) to the TP, Eq. (4.23), a relation analogous to the differential Gauss' law can be obtained

$$\nabla_v^2 V(v) = \int_D da'\,\rho\left(v'\right)2\pi\delta\left(v-v'\right),$$

$$= 2\pi\rho(v), \tag{4.48}$$

where the Laplacian ∇_v^2 is considered in terms of the normalized coordinates v. Since $\rho(v) > 0$ is the local density of the TC distribution, the Laplacian of the TP can be used to have a local information of the existence of OV at a given position. Notice that since (4.48) is real, the morphological parameters vanished and thus there is no information about parameters as the TC. Eq. (4.48) may also be expressed in integral form as

$$\int_D da\,\rho(v) = \frac{1}{2\pi}\int_D da\nabla_v^2 V(v), \text{ or} \tag{4.49}$$

$$= \frac{1}{2\pi}\int_{\partial D} ds\,\hat{n}\cdot\vec{\nabla}_v V(v). \tag{4.50}$$

While Gauss' law is related to the outward flux crossing a given boundary ∂D, there is also the complimentary relation due to Ampère's law, which is associated with the flux along the boundary. For the radially symmetric flux $\vec{\nabla}\log\left(re^{i\phi}\right) = \left(\hat{r} + i\hat{\phi}\right)/r$, Gauss' law selects the radial term while Ampère's law selects the azimuthal term. More generally, the flux of $V(v)$ along the boundary is given by

$$\int_{\partial D} ds\, \hat{t} \cdot \vec{\nabla}_v V(v), \tag{4.51}$$

where $\hat{t}$ is the unit vector tangent to the boundary curve ∂D. Near the core of an OV, Eq. (4.51) can be easily calculated along a circular contour of radius b. Given $\hat{t} = \hat{\phi}$, $ds = bd\phi$, and assuming that $\vec{\nabla}_v V(v)$ is continuous along the integration interval,

$$\begin{aligned}\int_{\partial D} ds\, \hat{t} \cdot \vec{\nabla}_v V(v) &= \int_0^{2\pi} bd\phi\hat{\phi} \cdot \int_D da'\rho\left(v'\right)\left[\hat{r} + iD\left(v'\right)\hat{\phi}\right]/b, \\ &= 2\pi i \int_D da'\rho\left(v'\right)D\left(v'\right).\end{aligned} \tag{4.52}$$

The reader should notice that, while (4.52) is adequate for regions containing trivial morphological parameters, $D\left(v'\right) = \pm 1, 0$ within D, and discrete distributions of TC, where $\rho(v) = \sum_{j=1}^{N} q_j \delta\left(v - v_j\right)$, Eq. (4.52) is not general because it does not accounts for singularities and discontinuities in $\vec{\nabla}_v V(v)$. From Eq. (4.2), it can be seen that the left hand side of Eq. (4.51) determines the total TC enclosed by ∂D, and must be an integer valued quantity. Meanwhile $\int_D da'\rho\left(v'\right)D\left(v'\right)$ may assume any complex value, according to the previous definitions of $\rho(v)$ and $D(v)$. The beam phase profile is given by $\Im[V(v)]$, and it is considered a point p over a closed curve C. It is assumed that C does not pass through any singularity. Since the phase is defined up to multiples of 2π, the phase at p after following the closed curve C, $\Phi\left(p, C\right)$, can be characterized as $\Phi\left(p, C\right) = \Phi_0 + 2\pi m$, where $m = 0, \pm 1, \pm 2, \ldots$ and $0 \leq \Phi_0 < 2\pi$ [93, 104]. Eq. (4.51) results in $2\pi m$ along C, and m is the total TC enclosed by C. Therefore, if $D(v)$ assumes only trivial values within D, and $\rho(v)$ is a discrete distribution, the discrete spacing of (4.51) can be ensured, while that is not true for arbitrary $\rho(v)$ and $D(v)$ profiles.

Assuming the validity of (4.52), it can be reorganized in a relation similar to Ampère's law in integral form,

$$\int_D da'\rho\left(v'\right)D\left(v'\right) = \frac{1}{2\pi i}\int_{\partial D} ds\, \hat{t} \cdot \vec{\nabla}_v V(v), \tag{4.53}$$

where $\int_D da'\rho\left(v'\right)D\left(v'\right)$ can be understood as the total TC enclosed within D. Eq. (4.53) is analogous to (4.2).

4.3.2 Vortex profile factorization and the topological potential

In this section there is a short discussion on some of the fundamentals behind the mathematical operations necessary to obtain the TP. It is worth to mention that representing a function in terms of a product, which is the underlying mechanism behind the TP, is of extreme importance for mathematics both in complex analysis [105] and for multiplicative cal-

culus [106]. While the factorization in complex analysis is crucial for several important theorems, as the fundamental theorem of algebra and the Weierstrass factorization theorem, the multiplicative calculus can be applied in obtaining properties of Schrödinger's equation solutions [107] or in imaging problems [108, 109].

Consider in general the phase due to a single OV with arbitrary morphological parameters and position,

$$\cos\frac{\alpha_i}{2}e^{i\frac{\beta_i}{2}}\left(v-v_i\right)^{q_i}+\sin\frac{\alpha_i}{2}e^{-i\frac{\beta_i}{2}}\left(v^*-v_i^*\right)^{q_i}. \tag{4.54}$$

Since v and v^* are linearly independent, (4.54) is a problem involving two degrees of freedom in the general case. The case $\alpha_i = 0$ will be considered first for simplicity. Then, some examples on the applicability of the TP to represent entire functions will be performed. Even though only a few examples are performed here, its worth to mention that there are specialized mathematical works devoted to the discussion of entire functions and the distributions of their zeros [110]. Later there is a small comment on the possibility of representing generic configurations as (4.54).

Factorization of functions involving a single complex variable v

For a single complex variable v the fundamental theorem of algebra guarantees that it is always possible to factor an arbitrary polynomial $p_{1\mathrm{D}}(v)$ in terms of its zeros as

$$p_{1\mathrm{D}}(v)=\sum_{r=0}^{M}c_r v^r, \tag{4.55}$$

$$=C\prod_{i=1}^{M}\left(v-p_i\right), \tag{4.56}$$

where $p_{1\mathrm{D}}\left(p_i\right)=0$ and C is an overall multiplicative constant. The theorem can be intuitively understood if it is considered that the set $\left\{C,\, p_i\right\}$ contains $M+1$ terms, while (4.55) has $M+1$ coefficients. It is then plausible that p_i can be expressed uniquely in terms of c_r. The fundamental theorem of algebra is important for the current discussion because it guarantees the existence of an exact factorization as (4.13) for arbitrary TC distributions containing only OV characterized by $\alpha_i = 0$ or $\alpha_i = \pi$. Therefore, it should be expected that (4.23) adequately represent the arbitrary distributions under the constraint that there are no superpositions of oppositely charged OV at any position across the transverse plane.

Notice that the TP as given in (4.15) is based in a continuum generalization of a product of zeros. If it is considered that both $\prod_{i=1}^{M} p_i$ and $\prod_{i=1}^{M} v$ will usually diverge when $M\to\infty$, Eq. (4.56) should be expected to diverge as it stands. However, the Weierstrass factorization theorem [105] ensures that by using adequate convergence factors it is possible to represent an entire function as a product of its zeros. Since entire functions are those that can be represented by power series over the whole complex plane, they form a very important class of functions, including polynomials, exponentials, and trigonometric functions. Below there

are some examples of entire functions that can be expressed through the TP. It should be reminded that since the TP did not consider an infinite number of zeros, some divergences may appear. Another aspect is that to represent OV it was requested that $\rho(v) \geq 0$, what indicates that the associated field profile $f(v)$ does not have singularities in the amplitude profile. In terms of representing generic functions, notice that it is useful to include $\rho(v) < 0$, which allows the description of meromorphic and rational functions on the complex plane.

Exponential function

Since $f(v) = C \exp V(v)$, an exponential function is one of the simplest nontrivial examples of the TP ability to represent entire functions. A typical exponential solution is $V(v) = \alpha v + \beta$, where α and β are constants. Within electrostatics, it is known that the electric potential due to an infinite plane of charges varies linearly with the distance to the plane, and due to the symmetry this result can be easily obtained from Gauss' law. A similar route can be performed in the present case, where the infinite plane is replaced by an infinite line.

Suppose that the TC is distributed along a straight line parametrized by $b(v)$, with a density $\rho(v) = \sigma\delta[v - b(v)]$ and the morphological parameter $D(v) = 1$ over the whole complex plane. The Gauss' law integration region D is rectangular and centered on $b(v)$, with sides whose lengths are c and d along the axes parallel and perpendicular to the TC line, respectively. Then, Eq. (4.50) becomes

$$\sigma c = \frac{1}{2\pi} \int_{\partial D} ds\, \hat{n} \cdot \vec{\nabla}_v V(v). \tag{4.57}$$

The integral along ∂D can be split among the line segments. Due to the source symmetry, $\vec{\nabla}_v V(v)$ must be constant over the sides of length c. Moreover, the integration along the sides of length d have the same $\vec{\nabla}_v V(v)$ and opposite signs, due to the direction of $\hat{n}$. It is then possible to state that

$$\sigma c = \frac{1}{2\pi} c \left(\hat{n} \cdot \vec{\nabla}_v V_1 - \hat{n} \cdot \vec{\nabla}_v V_2 \right), \tag{4.58}$$

where $\vec{\nabla}_v V_i$ represent the constant vectors associated with $\vec{\nabla}_v V(v)$ at each side of the TC line, and $\hat{n}$ is a vector normal to the TC line. Again, due to symmetry, $\vec{\nabla}_v V_2 = -\vec{\nabla}_v V_1$, indicating that

$$\hat{n} \cdot \vec{\nabla}_v V_1 = \pi\sigma. \tag{4.59}$$

Following the argument, since the operator $\hat{n} \cdot \vec{\nabla}_v$ is equivalent to a derivative along the direction of the unit length vector $\hat{n} = e^{-i\xi}\left(\cos\gamma\,\hat{x} - i\sin\gamma\,\hat{y}\right)$, it is possible to integrate V to

$$V\left(v_x, v_y\right) = \pi\sigma e^{i\xi}\left(v_x \cos\gamma + i\, v_y \sin\gamma\right), \tag{4.60}$$

where $v_x = x/w_0$ and $v_y = y/w_0$, and it is assumed that the potential is zero at $v = 0$. An interesting specific case occurs for $\gamma = \pi/4$, where the potential is proportional to v,

$$V(v) = \frac{\pi\sigma e^{i\xi}}{\sqrt{2}} v. \tag{4.61}$$

Cosine function

Another remarkable example is using the TP to represent a function which has an infinite number of zeros in terms of the position of the zeros. For simplicity the cosine function will be chosen, since the zeros are equally spaced throughout the complex plane.

To obtain simpler expressions the TP will be used to describe $f(v) = \cos \pi x$, which is zero whenever $x = m + 1/2$ for integer m. Since the cosine zeros are all of multiplicity one, the density becomes

$$\rho\left(v'\right) = \sum_{m=-M}^{M-1} \delta\left(v' - m - 1/2\right), \tag{4.62}$$

if only the $2M$ zeros closest to $x = 0$ are included. All the zeros of $\cos \pi x$ will be included at the end. Using Eq. (4.22),

$$f_{NN}(v) = C \prod_{m=-M}^{M-1} (v - m - 1/2), \tag{4.63}$$

where C is an overall multiplicative constant, and $w_0 = 1$ for a simpler expression. The subscript NN indicates that (4.63) is not adequately normalized in the limit $M \to \infty$.

Due to the infinite TC distribution, it becomes necessary to introduce the convergence factors to the TP. The procedure described below is a TP-based argument to the Weierstrass factorization applied to the cosine function. Remember that it was previously stated that Eq. (4.56) diverges in general due to the product of the positions of the zeros, $\prod_{m=1}^{M} p_m \to \infty$ when $M \to \infty$. One way to remove this divergence is by rescaling $C \to C \prod_{m=-M}^{M-1} \left(-p_m\right)^{-1}$, where the minus sign is inserted for convenience. The next problem is that even after the normalization rescaling, the product $g(v) = C \prod_{m=1}^{M} \left(1 - \frac{v}{p_m}\right)$ does not necessarily converge over the whole complex plane for all values of v. Weierstrass proved that it is possible to ensure the convergence by multiplying $\left(1 - \frac{v}{p_m}\right)$ by adequate exponentials as $\exp\left(\sum_{k=1}^{M_m} \frac{\left(v/p_k\right)^k}{k}\right)$, where M_m is an integer related to the function to be represented. Specifically for the cosine function, $M_m = 1$, what simplifies significantly the final expression.

After the introduction of the convergence factors,

$$f(v) = C \prod_{m=-M}^{M-1} \left(1 - \frac{2v}{2m+1}\right) e^{\frac{2v}{2m+1}}, \tag{4.64}$$

$$= C \prod_{m=1}^{M} \left(1 - \frac{2v}{2m-1}\right) e^{\frac{2v}{2m-1}} \prod_{m=1}^{M} \left(1 + \frac{2v}{2m-1}\right) e^{-\frac{2v}{2m-1}}, \tag{4.65}$$

$$= C \prod_{m=1}^{\infty} \left[1 - \left(\frac{2v}{2m-1}\right)^2\right] = C \cos \pi v, \tag{4.66}$$

where some algebraic manipulations were performed from (4.64) to (4.66), and the limit $M \to \infty$ was taken in the final expression. The infinite product representation for the cosine function can be seen for example at the expression 1.431.3 in [111].

The tools presented above give an intuition on the possibilities of the functions that may be represented through (4.23). This is important verification, since it indicates that (4.23) can describe a broad class of OV profiles.

Factorization of functions involving v and v^*

In 2D there is no equivalent to the fundamental theorem of algebra. Thus, it is not possible in general to factorize an arbitrary 2D polynomial $p_{2\mathrm{D}}(v, v^*)$ as

$$p_{2\mathrm{D}}\left(v, v^*\right) = \sum_{r=0}^{M_1}\sum_{s=0}^{M_2} c_{r,s}\, v^r\, v^{*s}, \tag{4.67}$$

$$\neq C\prod_{i=1}^{M_1}\left(v - p_i\right)\prod_{j=1}^{M_2}\left(v^* - q_j^*\right), \tag{4.68}$$

which can also be easily understood. While the set of coefficients $c_{r,s}$ has $(M_1+1)\times(M_2+1)$ distinct terms, the set $\left\{C, p_i, q_j^*\right\}$ in (4.68) has only M_1+M_2+1 terms. Hence it is very reasonable to assume that $\left\{C, p_i, q_j^*\right\}$ does not have enough degrees of freedom to represent the arbitrary 2D complex polynomial in (4.67). This discussion is extremely important for the applicability of the TP in general cases, because the procedure leading to (4.23) is based on a factorization of (4.11). The study of the factorization of functions of several complex variables is an advanced topic well beyond the scope of this manuscript, but can be found in the mathematical literature as the second (or multiplicative) Cousin problem [112].

Since in this work we are interested in OV, there is an important simplification that can be performed. It is assumed that the OV singularities are isolated in the transverse plane, such that Eq. (4.11) correctly expresses the OV transverse profile at $z = 0$. It is possible to write $(v-\delta_i)^{q_i} = |v-\delta_i|^{q_i}\exp\left[i q_i \arg(v-\delta_i)\right]$, and $\left(v^*-\delta_i^*\right)^{q_i} = |v-\delta_i|^{q_i}\exp\left[-i q_i \arg(v-\delta_i)\right]$, implying that each product term in (4.11) can be separated as

$$\cos\frac{\alpha_i}{2}e^{i\frac{\beta_i}{2}}\left(v-\delta_i\right)^{q_i} + \sin\frac{\alpha_i}{2}e^{-i\frac{\beta_i}{2}}\left(v^*-\delta_i^*\right)^{q_i} = |v-\delta_i|^{q_i}\, g\left[\arg(v-\delta_i)\right], \tag{4.69}$$

$$g(x) = \cos\frac{\alpha_i}{2}e^{i\frac{\beta_i}{2}+iq_i x} + \sin\frac{\alpha_i}{2}e^{-i\frac{\beta_i}{2}-iq_i x}, \tag{4.70}$$

where $g(x)$ is an entire function of x. Since the TP can be used to represent entire functions, and each product term in (4.11) can be separated as a product of entire functions, the TP can represent a broad class of field profiles, even though it might be difficult to represent a given specific function in terms of a TC distribution. Since both terms can be represented in terms of the TP, it is also possible to rewrite (4.69) as

$$\cos\frac{\alpha_i}{2}e^{i\frac{\beta_i}{2}}\left(v-\delta_i\right)^{q_i} + \sin\frac{\alpha_i}{2}e^{-i\frac{\beta_i}{2}}\left(v^*-\delta_i^*\right)^{q_i} = \exp\left\{q_i\log|v-\delta_i| + V\left[e^{i\arg(v-\delta_i)}\right]\right\}, \tag{4.71}$$

where $V\left[e^{i\arg(v-\delta_i)}\right]$ is the TP associated with an arbitrary TC distribution evaluated over the unit circle, $|v|=1$, and $q_i\log|v-\delta_i|$ can be understood as a TP characterized by $\rho(v) = q_i\delta(v-\delta_i)$ and $D(v)=0$. As will be shown later, the TP represented as $V\left[e^{i\arg(v-\delta_i)}\right]$ is very important to characterize nontrivial OV morphologies.

4.3.3 Topological charge distributions

I present in this subsection the results for the amplitude and phase profiles associated with TC distributions. At each result it is necessary to remember that in the general case $\rho(v)$

do not necessarily represent the TC density and $D(v)$ morphology parameters according to (4.24).

To define $\rho(v)$ and $D(v)$ it is assumed a continuous distribution of TC containing a large number of OV. Since the TC distributions discussed below have a small number of OV, the meaning of $\rho(v)$ and $D(v)$ has to be reinterpreted. For example in the radial distribution of TC, where $\rho(v) = \rho_0 |v|^n$ and $D(v) = 1$, it will be shown below that even though it is assumed a smooth density, the TC are localized at well defined positions. This characteristic is not exclusive to the TP formalism only, but it does also occur within electrostatics under equivalent conditions. Fixing a radially smooth charge density profile is an inaccurate assumption if the total electric charge is a few multiples of e, where e is the elementary charge allowed at a point, precisely because the electric charge quantization becomes relevant in determining the potential profile.

In the general case, the distribution $\rho(v)$ represents a local amplitude modulation, while $D(v)$ represents a phase modulation with non-zero vorticity due to the modulation $\rho(v)$.

Radial distribution of TC

Perhaps the simplest case involving a 2D distribution of TC is a radial distribution of TC along a circle of radius $|v| \leq b$. Considering $\rho\left(v'\right) = \rho_0 |v|^n$, where ρ_0 is constant, over the circle of radius b and the total TC distributed is Q_T. It is assumed that $D(v) = 1$ is constant over the transverse plane. The case $D = -1$ is obtained by complex conjugation of the TP obtained.

The initial step is to fix the value of ρ_0 to ensure that the total TC is Q_T. Using (4.24) and that $Q = |Q_T|$,

$$|Q_T| = \int_{|v|\leq b} da' \rho_0 \left|v'\right|^n, \tag{4.72}$$

$$= 2\pi\rho_0 \int_0^b \left|v'\right|^{1+n} d\left|v'\right|, \tag{4.73}$$

$$= 2\pi\rho_0 \frac{b^{n+2}}{n+2}, \tag{4.74}$$

$$\rho_0 = (n+2)\frac{|Q_T|}{2\pi b^{n+2}}, \tag{4.75}$$

where it is assumed that $n > -2$.

The next step is the calculation of the TP over the transverse plane. Considering first the case where $|v| \leq b$, Eq. (4.23) can be separated as

$$V(v) = \int_{|v'|<|v|} da' \rho_0 \left|v'\right|^n \log\left(v - v'\right) + \int_{|v|<|v'|<b} da' \rho_0 \left|v'\right|^n \log\left(v - v'\right). \tag{4.76}$$

Using (4.37), it can be verified that

$$\int_{|v'|<|v|} da' \rho_0 |v'|^n \log(v - v') = |Q_T| \left(\frac{|v|}{b}\right)^{n+2} \left(\log|v| + i\phi\right), \tag{4.77}$$

$$\int_{|v|<|v'|<b} da' \rho_0 |v'|^n \log(v - v') = |Q_T| \left\{\log b - \left(\frac{|v|}{b}\right)^{n+2} \log|v| + \left[1 - \left(\frac{|v|}{b}\right)^{n+2}\right] \left(-\frac{1}{n+2} + i\pi\right)\right\}. \tag{4.78}$$

Therefore, the total TP for $|v| < b$ becomes

$$V(v) = |Q_T| \left\{\log b - \frac{1}{n+2} \left[1 - \left(\frac{|v|}{b}\right)^{n+2}\right]\right\} + iQ_T \left[(\phi - \pi) \left(\frac{|v|}{b}\right)^{n+2} + \pi\right], \tag{4.79}$$

if the solution is extended to include the case $D(v) = -1$. The TP for $|v| > b$ can be obtained from (4.77),

$$V(v) = |Q_T| \log|v| + iQ_T\phi. \tag{4.80}$$

Now, some characteristics of the radial distribution can be remarked. Notice that $V(v)$ is smooth over the whole complex plane, even at $|v| = b$. For large values of n, the amplitude profile only varies significantly near $|v| = b$. Assuming that $-\pi \leq \phi < \pi$, it can be seen that at $\phi = 0$ the field phase varies smoothly between πQ_T and 0, while there are discontinuities at the opposite side. Identifying the phase discontinuity as an odd multiple of π, such that $(2k+1)\pi$ for integer k,

$$V\left(|v|_k, \phi = \pi\right) - V\left(|v|_k, \phi = -\pi\right) = (2k+1)\pi, \tag{4.81}$$

$$2\pi Q_T \left(\frac{|v|_k}{b}\right)^{n+2} = (2k+1)\pi, \tag{4.82}$$

$$\frac{|v|_k}{b} = \left(\frac{k + 1/2}{Q_T}\right)^{1/(n+2)}. \tag{4.83}$$

Since $\lim_{n\to\infty} x^{1/n} = 1$, the TC are displaced to the borders of the TC distribution. Also notice that for an integer Q_T, $0 \leq k \leq Q_T - 1$ to ensure that $0 \leq \frac{|v|_k}{b} \leq 1$, what indicates that there are Q_T singularities within the circle of radius b. These results were experimentally verified, as shown in Sec. 5.6.

Multipoles

A natural question arises from the established knowledge on electrostatics. The distribution of TC, as described before, consists of a spatial distribution of monopoles. However, it is also possible to argue about the existence of TC multipoles and how to describe these wavefront features. While within electrostatics there exists only localized multipoles, where the potential decays with distance, the TP can also describe an spatially extended multipole moment. Both possibilities are described below.

The simpler case is the localized multipole. Considering a finite distribution of TC over the plane, and an observation point v always outside the distribution, one may assume $r' < r$

within the integration domain D and substitute $r_< = \left|v'\right|$ and $r_> = |v|$ in Eq. (4.37). In this case, one can write Eq. (4.23) as

$$\Re\left[V(v)\right] = A_0(1)\log r - \sum_{m=1}^{\infty} \frac{1}{m|v|^m}\left[A_m(1)\cos\left(m\phi\right) + B_m(1)\sin\left(m\phi\right)\right], \tag{4.84}$$

$$\Im\left[V(v)\right] = A_0\left[D\left(v'\right)\right]\phi - \sum_{m=1}^{\infty} \frac{1}{m|v|^m}\left[-A_m\left[D\left(v'\right)\right]\sin\left(m\phi\right) + B_m\left[D\left(v'\right)\right]\cos\left(m\phi\right)\right], \tag{4.85}$$

$$A_m\left[f\left(v'\right)\right] = \int_D da'\rho\left(v'\right) f\left(v'\right)\left|v'\right|^m \cos\left(m\phi'\right), \tag{4.86}$$

$$B_m\left[f\left(v'\right)\right] = \int_D da'\rho\left(v'\right) f\left(v'\right)\left|v'\right|^m \sin\left(m\phi'\right), \tag{4.87}$$

where $A_m\left[f\left(v'\right)\right]$ and $B_m\left[f\left(v'\right)\right]$ are functionals determined by $\rho\left(v'\right)$ and $D\left(v'\right)$ and $\phi = \arg v$, $\phi' = \arg v'$. Then, up to a possible sign, the coefficients $A_m[\pm 1]$ and $B_m[\pm 1]$ can be related to localized multipole moments in electrostatics, and are here called localized multipole moments. Thus, the localized multipoles determine the TP asymptotic behavior at large $|v|$ for a given TC distribution. Except for the monopole terms, $A_0(1)$ and $A_0\left[D\left(v'\right)\right]$, all coefficients vanish when $|v| \to \infty$.

While the localized multipoles do describe a broad class of OV, they do not cover a very important case. For example, the dipole term in (4.84) and (4.85) can be interpreted as the limit of two charges with opposite sign at an infinitesimal distance. However, it is also possible to place two TC at the same point while obtaining a nontrivial field transverse profile. For simplicity, consider $\alpha = \pi/2$ and $\beta = 0$ in (4.10), which results after some rearrangements in

$$\log f_0\left(|v|,\phi\right) = \log\sqrt{2} + q\log|v| + \log\left|\cos q\phi\right| + i\pi\Theta\left(\cos q\phi\right), \tag{4.88}$$

where $\Theta(x)$ is the Heaviside step function, such that $\Theta(x>0) = 1$ and $\Theta(x<0) = 0$. The superposition in (4.88) has a nontrivial phase structure when $|v| \to \infty$ given by the term $\Theta\left(\cos q\phi\right)$, and that cannot be described from the localized multipole moments, as was explained in the OV factorization which leaded to Eq. (4.69).

From Eq. (4.69), the nontrivial phase structure should be obtained in general from an infinitely extended TC distribution characterized by given $\rho(v)$ and $D(v)$ profiles, and evaluated at $|v| = 1$. In such case, the TP can be written as

$$V(|v|=1) = \int_{|v'|<1} da'\rho\left(v'\right)\left[\log\left|v-v'\right| + iD\left(v'\right)\arg\left(v-v'\right)\right] + \int_{|v'|>1} da'\rho\left(v'\right)\left[\log\left|v-v'\right| + iD\left(v'\right)\arg\left(v-v'\right)\right]. \tag{4.89}$$

A procedure similar to the one carried for the localized multipole moments can be performed for each integral in (4.89). Using (4.38) and (4.39), it can be obtained after an exercise

of algebra that

$$V(|v|=1) = i\phi A_0^{<}\left[D\left(v'\right)\right] - \sum_{m=1}^{\infty}\frac{1}{m}\left(C_m\cos m\phi - iS_m\sin m\phi\right) + \int_{|v'|>1} da'\rho\left(v'\right)\log\left|v'\right| + i\int_{|v'|>1} da'\rho\left(v'\right)D\left(v'\right)\phi', \tag{4.90}$$

$$C_m = A_m^{>}(1) + iB_m^{>}\left[D\left(v'\right)\right] + A_m^{<}(1) - iB_m^{<}\left[D\left(v'\right)\right], \tag{4.91}$$

$$S_m = A_m^{>}\left[D\left(v'\right)\right] + iB_m^{>}(1) - \left\{A_m^{<}\left[D\left(v'\right)\right] - iB_m^{<}(1)\right\}, \tag{4.92}$$

$$A_m^{<}\left[f\left(v'\right)\right] = \int_{|v'|<1} da'\rho\left(v'\right)f\left(v'\right)\left|v'\right|^m\cos\left(m\phi'\right), \tag{4.93}$$

$$B_m^{<}\left[f\left(v'\right)\right] = \int_{|v'|<1} da'\rho\left(v'\right)f\left(v'\right)\left|v'\right|^m\sin\left(m\phi'\right), \tag{4.94}$$

$$A_m^{>}\left[f\left(v'\right)\right] = \int_{|v'|>1} da'\frac{\rho\left(v'\right)f\left(v'\right)}{\left|v'\right|^m}\cos\left(m\phi'\right), \tag{4.95}$$

$$B_m^{>}\left[f\left(v'\right)\right] = \int_{|v'|>1} da'\frac{\rho\left(v'\right)f\left(v'\right)}{\left|v'\right|^m}\sin\left(m\phi'\right). \tag{4.96}$$

Notice that the several terms in (4.90) can be easily understood. The term $i\phi A_0^{<}\left[D\left(v'\right)\right]$ considers the possible existence of a TC within $\left|v'\right|<1$. The terms $\int_{|v'|>1} da'\rho\left(v'\right)\log\left|v'\right|$ and $i\int_{|v'|>1} da'\rho\left(v'\right)D\left(v'\right)\phi'$ represent constant amplitude and phase modulations, respectively, and can be incorporated at the overall field normalization constant. The nontrivial terms left are associated with the specific $\rho(v)$ and $D(v)$ profiles through the complex constants C_m and S_m. Assuming that $A_m^{\lessgtr}$ and $B_m^{\lessgtr}$ are finite, C_m and S_m are also finite. This has an important implication for a generic and localized TC distribution. Since the extended multipole is also due to point sources, they can be part of a localized TC distribution, and must be included in the general expansion. The contributions due to localized and extended multipoles is additive, implying that a generic localized TC distribution can be represented through

$$\Re\left[V(v)\right] = A_0(1)\log|v| - \sum_{m=1}^{\infty}\frac{1}{m}\left\{\left[\frac{A_m(1)}{|v|^m} + \Re\left(C_m\right)\right]\cos\left(m\phi\right) + \left[\frac{B_m(1)}{|v|^m} + \Im\left(S_m\right)\right]\sin\left(m\phi\right)\right\}, \tag{4.97}$$

$$\Im\left[V(v)\right] = A_0\left[D\left(v'\right)\right]\phi - \sum_{m=1}^{\infty}\frac{1}{m}\left\{\left[-\frac{A_m\left[D\left(v'\right)\right]}{|v|^m} - \Re\left(S_m\right)\right]\sin\left(m\phi\right) + \left[\frac{B_m\left[D\left(v'\right)\right]}{|v|^m} + \Im\left(C_m\right)\right]\cos\left(m\phi\right)\right\}. \tag{4.98}$$

Thus, the coefficients of $\cos\left(m\phi\right)$ and $\sin\left(m\phi\right)$ decay with distance from the TC distribution, but tends to a value determined by C_m and S_m as $|v|\to\infty$.

As a final step, it is considered the modulation of the OV dark core profile due to a TC distribution localized near $|v|=0$. If the intensity profile is given by the TP within a Gaussian envelope, $I(v)\propto\exp\left\{-|v|^2/b^2 + 2\Re\left[V(v)\right]\right\}$, it is possible to verify that the maximum along the radial direction is given by

$$\frac{d}{d|v|}I(v)\propto e^{-|v|^2/b^2+2\Re[V(v)]}\left\{-\frac{2|v|}{b^2} + 2\frac{d\Re\left[V(v)\right]}{d|v|}\right\} = 0. \tag{4.99}$$

Remember that if $D(v) = 1$ across the whole space, $V(v)$ satisfies the Cauchy-Riemann conditions, implying that the maximum intensity condition becomes

$$-\frac{|v|}{b^2} + \frac{1}{|v|}\frac{d\Im[V(v)]}{d\phi} = 0, \text{ or} \tag{4.100}$$

$$|v|^2 = b^2\frac{d}{d\phi}\Im[V(v)]. \tag{4.101}$$

Since the case $D(v) = -1$ can be accounted for through a proper change of sign in the Cauchy-Riemann conditions, (4.101) is slightly generalized by

$$|v|^2 = b^2\left|\frac{d}{d\phi}\Im[V(v)]\right|. \tag{4.102}$$

Thus, if $\Im[V(v)]$ does not depend on $|v|$ it becomes very simple to obtain the OV core profile as

$$|v|_{\text{core}} = b\sqrt{\left|\frac{d}{d\phi}\Im[V(v)]\right|}. \tag{4.103}$$

5 Production of topological charge distributions and their characterization

5.1 Introduction

In chapters 2 and 3 some fundamentals of light propagation and modulation were introduced, respectively. Then, some characteristics of optical vortices (OV) were introduced and generalized in chapter 4. There are now enough elements to perform and analyze experiments. Within this chapter, the theoretical results obtained in chapter 4 are experimentally verified through various Topological Charge (TC) distributions. The results herein presented demonstrate how the Topological Potential (TP) can be used to shape the profile of beams containing OV, what is important in several applications. For example, it becomes possible to adjust the transverse forces in optical tweezers or in an optical trap.

Since the discussion in chapter 4 is of a more mathematical nature, experimental tools must be introduced to verify the properties of TC distributions. For instance, it is necessary to introduce methods to verify the beam TC and also the Orbital Angular Momentum (OAM). Also, it is highly desirable to have both the field transverse amplitude and phase profiles for a more complete wavefront characterization, even though the retrieval of the phase transverse profile is not a trivial problem [113–116]. The most simple techniques to characterize the TC in an OV beam consists in analyzing the diffraction pattern due to a designed screen [38,117]. For example, the triangular slit technique [38] is very easy to implement and effective, being used to characterize the TC configurations in our work [1] and is briefly discussed below. However, since designed screen techniques require the matching between the slit profile with the incident light, by changing the OV profile these techniques tend to measure only part of the total TC. For example, in [1] it is verified that the triangular slit technique is usually inadequate for non-cylindrical beams. Another usual procedure to measure the TC consists of counting the number of spirals when interfering an OV with a reference wave [118]. This allows in principle an analysis of the total TC of an OV beam, but without any information about its spatial distribution. A more complete method to characterize TC requires the simultaneous measurement of the beam amplitude and phase, as in [115, 119]. Even though phase retrieval increase the complexity of the experimental system, this approach allows a deeper analysis of the beam properties. To measure the classical OAM of a beam, one may perform a modal decomposition [120] or a simultaneous retrieval of the beam phase and amplitude. In our work [2] it was used a Michelson interferometer to characterize the field amplitude and phase profiles, and the beam OAM and TC could be determined using the formulas in chapter 4.

In this chapter, the production and characterization of TC distributions is discussed. The

characterization through the triangular slit is presented, then there is an initial analysis of TC distributions over simple geometries (a line, a corner and a triangle). These initial results were reported in [1]. Since a more complete characterization of the TC distributions requires the knowledge of the field amplitude and phase transverse profiles, we introduced an approach to obtain the TC and OAM to characterize the previous TC distributions. This second part is based on the results in Ref. [2]. Finally, the distributions discussed in sec. 4.3.3, the 2d radial distribution and the TC multipoles are presented. This part of the chapter is not published yet.

5.2 Triangular slit technique

The diffraction of light through the triangular slit [38] is one of the simplest approaches to characterize the TC of a light beam. When an OV is diffracted by a single slit, the diffracted pattern has a spatial shift proportional to the impinging beam TC [121], and the Fraunhofer diffraction profile of light impinging over a polygon shaped slit produces a pattern that encodes information about the TC [122]. While it is possible in principle to determine the TC using regular polygons with an arbitrary number of sides n, the TC evaluation becomes more difficult if n is too large. If an OV beam with azimuthal symmetry, as a Laguerre-Gauss beam, impinges over a nearly circular slit (large n), the diffracted field pattern has a similar intensity structure for a non-null TC [123]. Thus, the pattern due to a slit with $n = 3$ both the simplest geometry and is able to retrieve the TC information more easily [124]. Another nontrivial and important characteristic of the triangular slit is that it is able to retrieve the sign of the TC, or if the wavefront helix turns clockwise or counter-clockwise. The orientation of the pattern diffracted by the slit indicates the charge sign [38]. In Fig. 9 (a) it can be seen a schematic of the experimental setup for TC measurement through the triangular slit technique, while in (b) there is an example of the expected triangular lattice profile. Fig. 9 (c) contains an experimental result for a beam whose TC is 1. Our triangular slit was built according to the proposal in [125].

5.3 TC distributions with simple geometries

As a first experimental test of the ideas discussed in chapter 4, some tests were performed for TC distributions over simple geometries in an attempt to shape the spatial profile of the dark region. Since the modulation of both field amplitude and phase profile is extremely important in various applications of OAM light, a controllable modulation is highly desired for optimizing a given application. The phase singularities due to the TC require that the field amplitude vanish where the TC is distributed. Therefore, it seems possible to design the field amplitude and phase profiles using TC distributions. The results within this subsection were published in [1]. It was considered TC distributions over a finite line, a corner (L-shape), and

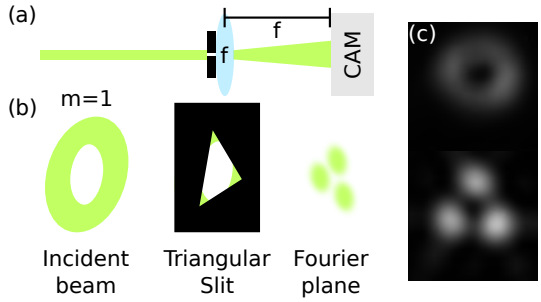

Figure 9 – (a) Typical experimental setup for TC characterization using the triangular slit technique. A collimated incident beam whose TC is m diffracts due to a triangle-shaped slit. The slit Fourier plane is accessible by placing a camera (CAM) at a distance f from a lens whose focal distance is f. It can be seen that if the incident beam has a TC m, at the Fourier plane there will appear a triangular lattice whose number of bright-spots correspond to $m+1$. In the example shown in (b), the diffraction of an OV with $m = 1$ gives a triangular lattice containing 2 bright spots at the side. (c) Experimental example of the light intensity profiles at Fourier plane without and with the triangular slit for a beam where $m = 1$.

a triangle. The phase profiles associated with these TC distributions were obtained by using Eq. 4.11 with $\alpha_i = \beta_i = 0$ and are shown in Fig. 10. For the discrete TC distributions, $q_i = 1$ was chosen, while in the continuous case $q_i \to 0$ at each point of the designed geometry. Notice that discrete or continuous TCs distributions present only a subtle difference in the central region of the phase masks shown in Fig. 10(a) and Fig. 10(b).

In order to produce the TC distributions in Fig. 10, it was used the experimental setup described in Fig. 14 with arm 2 mirror at the off position. Only the TC distribution phase profile was modulated in this experiment. Figure 11 shows the spatial light intensity profile obtained using either discrete or continuous distributions of TCs on a line of length L parallel to the horizontal axis. Fig. 11(a) and 11(b) shows numerical results for discrete and continuous TCs distributions, respectively, while Figs. 11(c) and 11(d) exhibit the corresponding experimental results. The region of maximum intensity is distorted when L is increased up to a length such that ring-like structures start to appear ($L = 4$ mm, see video 1). For the discrete TCs distribution, this is a result of the spatial separation of 5 $q_i = 1$ vortices, as can be seen for larger values of L. Figs. 11(e) and 11(f) show the diffraction profile using the triangular slit to determine the total TC. The six brilliant spots in each side of the triangle at Fig. 11(Media 1) when $L = 0$ mm and its orientation indicates that $Q = +5$ (the triangular slit was aligned such that one of the sides is perpendicular to the line of charges). This side corresponds to the bottom edge of the triangle on Figs. 11(e), 11(f) and 11(Media 1). As would be expected from the patterns in Fig. 10 (a)-10(b), the respective beam profiles in Figs. 11(a,c) and 11(b,d) are essentially equal. One remarkable aspect of the obtained profiles is that the dark region which contains the TCs distribution is rotated in respect to the horizontal axis. This rotation is due to the Guoy phase shift, as discussed in refs. [126–128]. By increasing

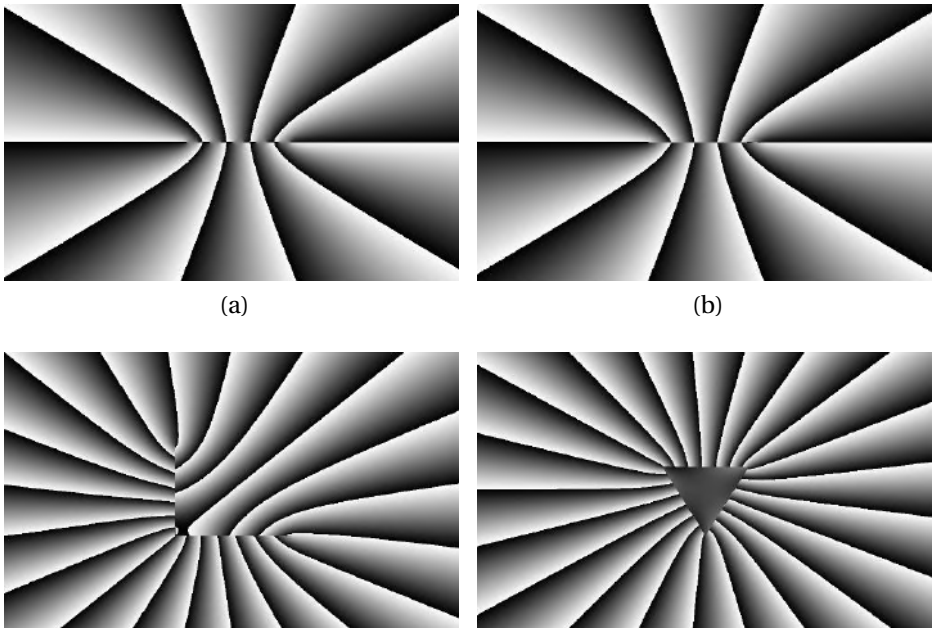

Figure 10 – Examples of obtained phase patterns (without the blazed grating pattern). Arrangement of TCs on a line: (a) discrete ($q_i = 1$) and (b) continuous ($q_i \to 0$) distributions for $Q = 10$. There is only a subtle difference between the phase masks at the central region. (c) Corner shaped ($Q = 20$) and (d) triangular shaped ($Q = 21$) TCs arrangements.

L we observed that the diffraction pattern deforms and most of triangle peaks are blurred. However, the number of peaks on the triangle's edge remains equal to 6, with some peaks fading away on for $L = 7$ mm. This can be understood as a limitation of the measurement technique to highly deformed beams. Since the measurement is carried only at a finite region, for sufficiently large values of L the slit cannot diffract the whole beam. Therefore, it will measure only part of the beam's TC.

The experimental results are in good agreement with the reasoning that leads to Eq. 4.15. Using Ampère's law, Eq. 4.53, it can also be shown that the total TC for the above distributions is [1]

$$Q = \frac{1}{2\pi} \int_{\partial D} ds\, \hat{t} \cdot \vec{\nabla}_v \Im [V(v)] \approx \sum_{i=1}^{N} q_i. \tag{5.1}$$

Thus, the current set of experiments support the assumption that one can deform the beam intensity profile by distributing the TCs over sufficiently small distances while having a designed total TC, as given by the sum of the distributed q_i.

In order to demonstrate the validity of TC distributions to produce more complex geometrical structures, we constructed L-shaped (corner) and triangular OAM beams. Fig. 12 shows the profile obtained considering (a) discrete and (b) continuous distribution of TCs. The value of $Q = 10$ was chosen to minimize the amount of light at the TCs distribution, and at the same time preserving the L-shape. When a smaller value of Q is selected, the vortices

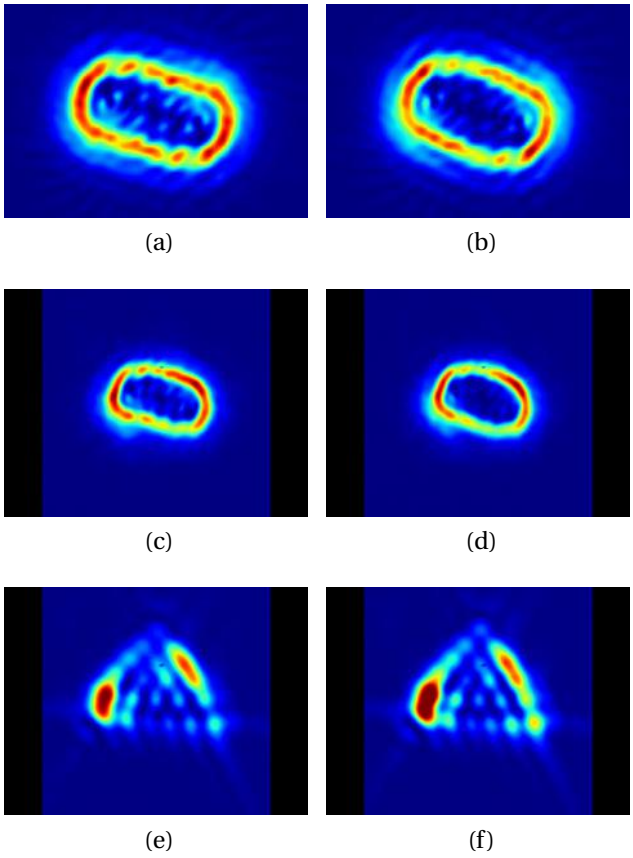

Figure 11 – Beam's profiles for a linear distribution of TCs with $L = 3$ mm. The total topological charge is $Q = 5$. Numerical results: (a) discrete and (b) continuous charge distribution. Experimental results: (c) and (d) correspond to discrete and continuous TCs distributions, respectively. (e) and (f) show the measurements of the total TC using a triangular slit. For experimental results at various L values, see (Media 1).

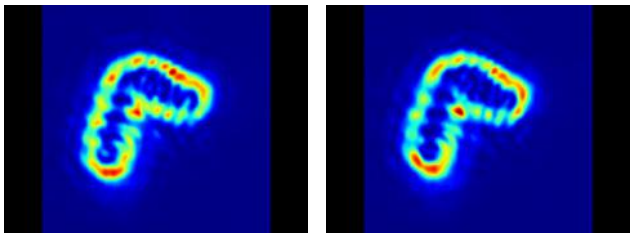

Figure 12 – Experimental beam profile for L-shaped (corner) TCs distributions with $Q = 10$. Discrete (a) and continuous (b) TCs distributions.

of a discrete TCs distribution are well separated, and the destructive interference between them is less effective. On the other hand, if a very large value of Q is used, according to the argument leading to Eq. (4.11), the intense region radius can become so large that the profile tends to a deformed circle.

To analyze the case of TCs distributed along the sides of a triangle we must consider the

existence of two regions: i - inside the triangle there are no charges and thus the winding number of any curve is zero; ii - for curves encircling the triangle, the winding number is Q. We show in Fig. 13 the experimental results where we apodized the central region without charge. Fig. 13(a) shows the beam triangular profile and Fig. 13(b) confirms the charge $Q = 3$. Fig. 13(Media 2) shows that the pattern expands for increasing Q and becomes more rounded for larger TC values.

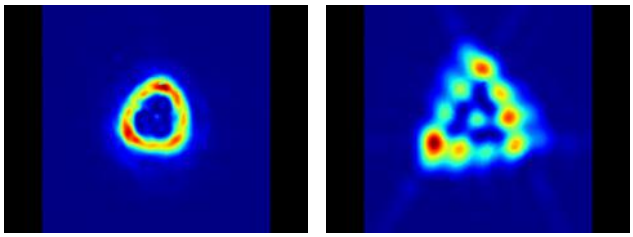

(a) (b)

Figure 13 – Intensity profile (a) and charge measurement (b) of a triangular charges arrangement with $Q = 3$. For more Q values, see (Media 2).

The examples discussed illustrate that TC distributions can be used to shape OAM beams with a large variety of geometries. The simple geometries presented are building blocks for more complex arrangements. An immediate application of the concepts developed above is to pre-compensate on the SLM aberrations affecting vortex beams during propagation, as in [129]. Ref. [88] shows that laser traps formed by LG beams have higher Bose-Einstein condensation temperatures due to modification of trapping potential by changing Q values. With the method proposed here, novel trapping potentials can be designed such as to increase transition temperatures and/or shaping the condensate. In optical tweezers, this method is a simpler alternative to shape non-circular routes for suspended particles [130]. In plasmonics this shaping may allow selective excitation of plasmonic modes, such as [89].

While the above results seem promising, the characterization of the TC distributions using only the triangular slit does not answer various important questions for the applications. For example, in an optical tweezer it is important to know the OAM profile, since it is related to the force that light can produce upon a particle. Thus, in the next section it is shown how to characterize the amplitude and phase profiles of these TC distributions, and later this approach is applied to the TC distributions discussed within this section.

5.4 Measurements of the beam amplitude and phase using a Michelson interferometer

The simultaneous characterization of the beam amplitude and phase transverse profiles is very important for a detailed characterization of generic wavefronts, as is of interest for this work. The approach below was introduced by us in Ref. [2]. Using the experimental setup

shown in Fig. 14(a) it is possible to produce various OV configurations and characterize their amplitude and phase profiles using a single spatial light phase modulator (SLM). The OV are generated in the SLM by applying a hologram χ_{SLM} which contains the OV phase profile χ_{OV} superimposed with a blazed grating χ_{OV}. The blazed grating directs the OV of interest to the SLM first diffracted order, as explained in sec. 3.4. The spatial filter selects only the field with the correct phase modulation, and blocks unwanted light from the SLM. If the Arm-2 mirror is off the beam line, only the intensity profile $I_{\mathrm{OV}}(\mathbf{r})$ of the produced OV will reach the CCD camera. In this case, the amplitude profile is given by $\mathscr{A}(\mathbf{r}) = \sqrt{I_{\mathrm{OV}}(\mathbf{r})}$. The CCD was positioned at the SLM image plane, which we defined as $z = 0$ cm.

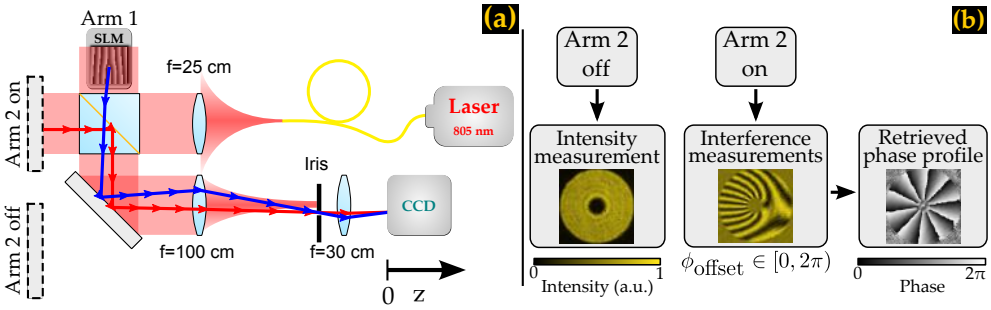

Figure 14 – (a) Experimental setup schematic. The output of a fiber coupled laser diode emitting at 805 nm is collimated with a lens with long focal distance ($f = 25$ cm), producing a nearly plane wave. The collimated light goes to a Michelson interferometer (MI) in which the arm 1 contains a SLM (Hamamatsu - LCOS X10468-02). The MI arm 2 provides the plane wave reference when the mirror is on the beam line, or allows intensity measurements when the mirror is off the beam line. The reference (red line) and modulated (blue line) beams have a small relative angle and are spatially filtered and then imaged on a CCD camera (Thorlabs - DCC1240M) positioned at the SLM image plane ($z = 0$ cm). (b) Fluxogram of the experimental procedure to determine the beam amplitude and phase profiles, as described in the text.

To measure the phase profile, $\chi(\mathbf{r})$, we followed an approach similar to that described in [115, 119]. We add to χ_{SLM} a spatial DC phase offset $\phi_{\mathrm{Offset}} \in [0, 2\pi]$ and place the MI Arm-2 mirror on the beam line. The intensity pattern at the CCD plane for a perfectly coherent light consists of

$$I_{\mathrm{CCD}}(\phi_{\mathrm{Offset}}) = I_{\mathrm{OV}} + I_{\mathrm{Ref}} - 2\sqrt{I_{\mathrm{OV}} I_{\mathrm{Ref}}}\cos(\chi_{\mathrm{Rel}} + \phi_{\mathrm{Offset}}), \tag{5.2}$$

where I_{Ref} is the intensity profile of the reference beam, and χ_{Rel} is the relative phase between the reference beam and the OV. The position $\mathbf{r}$ is implicitly considered in each term for improved clarity.

Since ϕ_{Offset} can be adjusted *a priori* on the phase mask, one may retrieve the spatial phase profile by virtue of Fourier orthogonality. Multiplying the measured intensity profile $I_{\mathrm{CCD}}(\phi_{\mathrm{Offset}})$ by $\exp(-i\phi_{\mathrm{Offset}})$, and numerically integrating over ϕ_{Offset} one has

$$\frac{1}{2\pi}\int_0^{2\pi} d\phi_{\mathrm{Offset}} I_{\mathrm{CCD}}(\phi_{\mathrm{Offset}})\, e^{-i\phi_{\mathrm{Offset}}} = -\sqrt{I_{\mathrm{OV}} I_{\mathrm{Ref}}} e^{i\chi_{\mathrm{Rel}}}, \tag{5.3}$$

and the argument of the resulting complex number is $\chi_{\mathrm{Rel}}(\mathbf{r})+\pi$. The above approach allows the retrieval of χ_{Rel} at each CCD pixel, and it is a simple and effective way to retrieve spatial phase profiles. To obtain a better signal/noise ratio, we used 10 values of ϕ_{Offset} [119]. Two relevant characteristics of this method are worth noticing. When the reference wave is an ideal plane wave propagating parallel to the modulated beam, $\chi_{\mathrm{Rel}}(\mathbf{r}) = \chi_{\mathrm{OV}}(\mathbf{r}) + \text{constant}$, and since $I_{\mathrm{OV}} \to 0$ near a TC, $\sqrt{I_{\mathrm{OV}}}$ is amplified by a factor of $\sqrt{I_{\mathrm{Ref}}}$. Therefore, although this experimental phase-retrieval method requires more data and acquisition time than those based on the Fourier transform method [113, 115], it shows an improved sensitivity, the output is automatically determined in complex notation and it does not require filtering in the momentum space.

Usually the reference beam is not an ideal plane wave propagating parallel to the modulated beam. However, this poses no problem to the approach described above. Since any optical phase retrieval method will always measure a relative phase, it is possible to design a reference wave at the SLM. For an OV labeled by the superscript n, one has in general that $\chi^{n}_{\mathrm{Rel}}(\mathbf{r}) = \chi^{n}_{\mathrm{OV}}(\mathbf{r}) + \chi^{0}_{\mathrm{Rel}}(\mathbf{r})$. If a flat phase profile is applied to the SLM (no OV), this returns the overall phase $\chi^{0}_{\mathrm{Rel}}(\mathbf{r})$. By subtracting $\chi^{0}_{\mathrm{Rel}}(\mathbf{r})$ from $\chi^{n}_{\mathrm{Rel}}(\mathbf{r})$ it is possible to obtain only the OV phase profile.

After measuring the spatial profiles of amplitude and phase, the ℓ-OAM, Eq. (4.4), OAM, Eq. 4.6, and TC, Eq. 4.3, may be calculated. To compute the azimuthal derivative in the ℓ-OAM, and to avoid the unphysical discontinuities when the phase χ goes from 0 to 2π, it is here introduced the identity

$$w(\mathbf{r}) = \frac{\partial \chi}{\partial \phi} = \mathfrak{Re}\left\{ e^{-i\chi}\left[-i\left(x\frac{\partial}{\partial y} - y\frac{\partial}{\partial x}\right)\right] e^{i\chi}\right\}, \tag{5.4}$$

where the derivatives were calculated via a Fourier spectral method with a smoothing Gaussian filter [131]. Notice that the derivatives in Eq. (5.4) act over the well behaved function $\exp(i\chi)$, which is insensitive to the modulus 2π phase jumps that may be present in the originally retrieved phase profile χ. This fact must be remarked because the unphysical discontinuities are significant when $\partial\chi/\partial\phi$ is calculated directly.

To ensure the numerical stability when evaluating Q_T from the phase profile via Eq. (4.3), it is necessary to weaken the condition $\rho = c$. This can be achieved by generalizing $w(\rho = c, \phi, z_0) = \int_0^\infty \rho d\rho\, p(\rho)\, w(\rho, \phi, z_0)$, where $p(\rho)$ is a radial probability distribution strongly concentrated near $\rho = c$. For simplicity we assume that for a sufficiently small thickness ϵ, $p(\rho) = 0$, if $|\rho - c| > \epsilon$, and $p(\rho) = (2\epsilon\rho)^{-1}$, if $|\rho - c| \le \epsilon$. This approach allows the line integral in Eq. (4.3) to be approximated by a surface integral over the plane $z = z_0$

$$Q_T = \frac{1}{2\pi}\int \rho d\rho d\phi\, p(\rho)\, w(\rho, \phi, z_0). \tag{5.5}$$

To gain insight on the meaning of the quantities discussed above, it is shown in Fig. 15 how the quantities discussed above behave in an experimental measurement of a beam obtained containing a point TC whose charge is 5 in the SLM. Notice that the amplitude profile

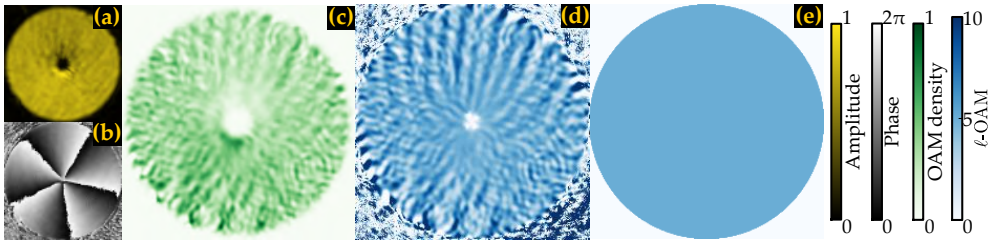

Figure 15 – Application of the concepts developed in sec. 3 to a beam where $\chi_{OV} = 5\phi$. Experimentally measured amplitude (a) and phase (b) beam profiles. OAM density profile (c), from which it was determined that $\langle l \rangle = 4.9$. Experimental (d) and theoretically expected (e) ℓ-OAM profiles for this beam. For this beam it was measured $Q_T = 5.0$.

is very uniform in Fig. 15 (a) and the measured phase profile in Fig. 15 (b) is consistent to what is expected for a point TC. The semi-classical OAM density is given by the integrand of Eq. (4.6) and can be obtained by multiplying the result of Eq. (5.4) with the measured intensity profile. The normalized experimental OAM density, L_z, is flat in Fig. 15 (c), up to experimental error. Another quantity of interest is the average semi-classical OAM per photon $\langle l \rangle$, which is obtained by performing the integral in Eq. (4.6). For the beam in Fig. 15, it was measured that $\langle l \rangle = 4.9$. Figs. 15 (d)-(e) show the experimental and theoretically expected ℓ-OAM profiles, respectively, for this beam. It can be noticed that there is a good agreement between both in the color scale. The experimental determination of the TC, Q_T, was performed using Eq. (5.5) with $c = 0.85 r_{\max}$, $\epsilon = 0.1 r_{\max}$, where $r_{\max}$is the external radius of the amplitude profile. As a result, it was measured that the produced beam has $Q_T = 5.0$.

5.5 OAM and TC characterization of TC distributions

In this section we experimentally characterized the ℓ-OAM and the OAM density in the TC distributions described in sec. 5.3 and in Ref. [1]. Some typical amplitude and phase profiles of these TC distributions at $z = 0$ cm are shown in Fig. 16. The results for each TC distribution are discussed in the subsections below. From the experimental amplitude and phase profiles, $\langle l \rangle$ was calculated by applying Eq. (4.6), while for Q_T it was used Eq. (5.5) with $c = 0.85 r_{\max}$, $\epsilon = 0.1 r_{\max}$, where $r_{\max}$is the external radius of the amplitude profile.

5.5.1 Linear distributions of TC

Since the linear distribution of TC forms is the prototype for more complex geometries, it is discussed first. Although the linear distribution of TC discussed here is designed on the SLM, its worth noticing that they can appear naturally from point TC perturbed by the optical system [132]. The OV core of a TC line of infinitesimal length has a circular shape. By increasing the TC line length and keeping the total TC fixed, the core becomes elongated until a point in which the multiple OV cores of unit charge become discernible. For a fixed TC of 10 these

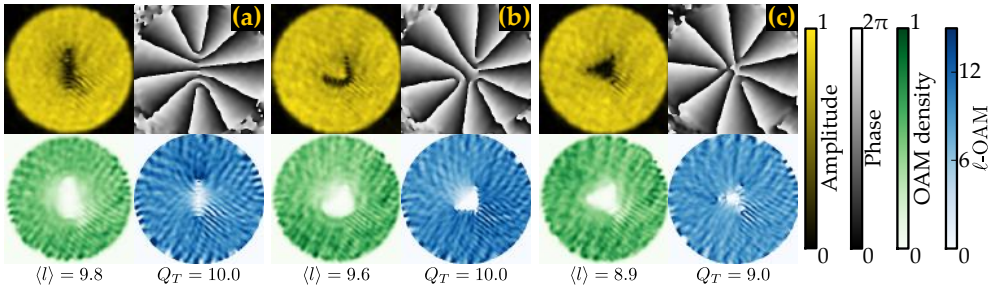

Figure 16 – Typical experimental profiles of amplitude and phase, and the corresponding ℓ-OAM and OAM density for the TC distributions. The data represent TC distributed over a line (a), a corner (b) and a triangle (c). The values of $\langle l \rangle$ and Q_T were calculated, respectively, by applying Eqs. (4.6) and (5.5) to the experimental data.

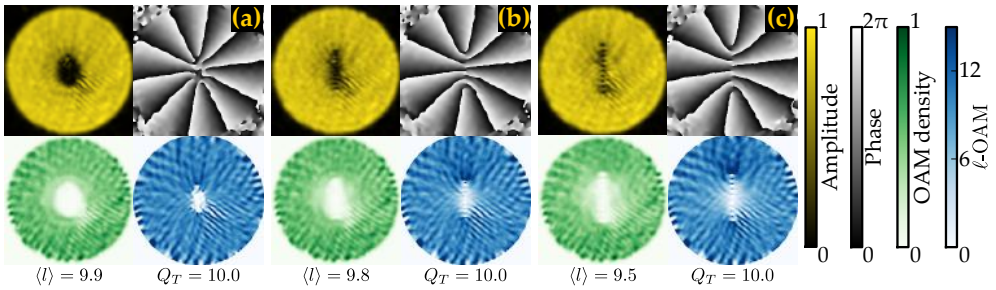

Figure 17 – Experimental data for TC lines with different line lengths and a fixed total applied TC= 10 at $z = 0$ cm. The line length increases from (a) to (c), and the respective OV are in the regimes of high TC density, elongated OV core and small TC density.

three regimes can be visualized in Figs. 17(a)-(c) as, high TC density, elongated OV core and small TC density, respectively. An important remark is that the measured value of Q_T obtained from Eq. (5.5) agrees with the applied value for all the geometries shown in Fig. 17 and also in all the other cases discussed below. Another observation is that the ℓ-OAM magnitude, $|w(\mathbf{r})|$, is reduced near the center of the TC line. This can be understood by noticing that between adjacent equally-charged OV the azimuthal phase variation is smaller than if both OV were at the same point. Far from the TC distribution the phase profile must depend only on the value of Q_T and therefore the ℓ-OAM, $w(\mathbf{r})$, should have similar magnitudes in all regimes [1]. This can be observed in Figs. 17(a)-(c). The OAM densities follows the beam intensity profile but are reduced near the OV core. The reduced OAM density, L_z, follows the ℓ-OAM, $w(\mathbf{r})$, reduction, and as a result we observed that $\langle l \rangle \leq Q_T$.

Also, it was investigated how the linear distributions of TC propagate, and a typical example is shown in Fig. 18. Notice that the OV core rotates and expands under propagation, but remains line-shaped. The rotation is due to the Guoy phase shift [56, 126], and can be seen as a signature of the structural stability of the OV profiles under propagation [56]. Another important point is that both Q_T and $\langle l \rangle$ are conserved under propagation. This is important because establishes that the characterization approach discussed in this work does not

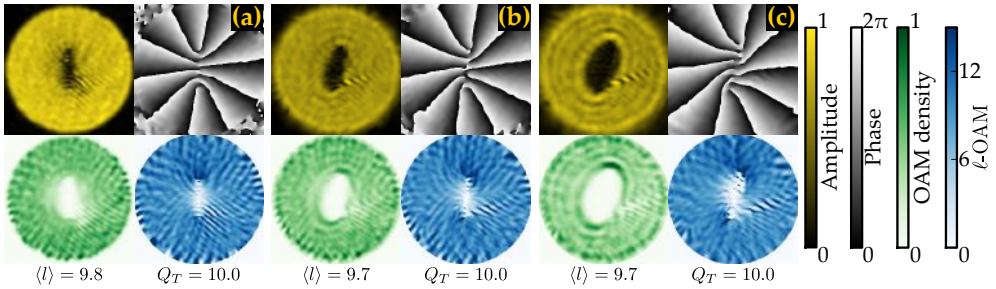

Figure 18 – Measurements corresponding to a TC line at distinct z planes. z = 0 cm, 5 cm, 10 cm respectively in (a-c). Notice that both Q_T and $\langle l \rangle$ are conserved under propagation.

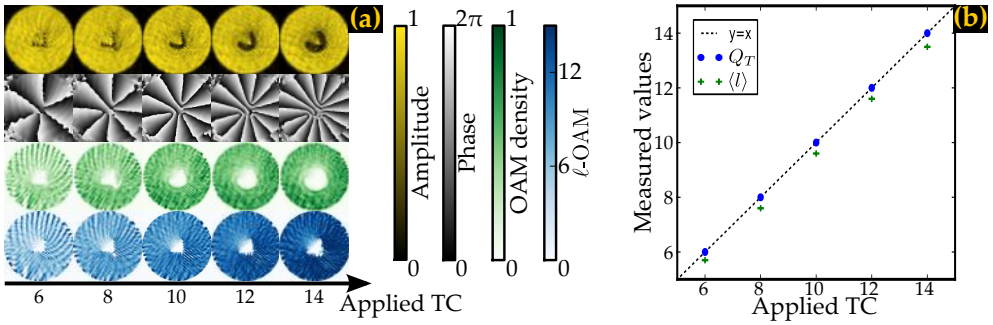

Figure 19 – (a) Profiles of amplitude, phase, OAM density and ℓ-OAM for a corner-shaped TC distribution with a fixed geometry and varying total applied TC. (b) Relation between the measured Q_T and $\langle l \rangle$ in terms of the applied TC at the SLM. All measurements were taken at $z = 0$ cm.

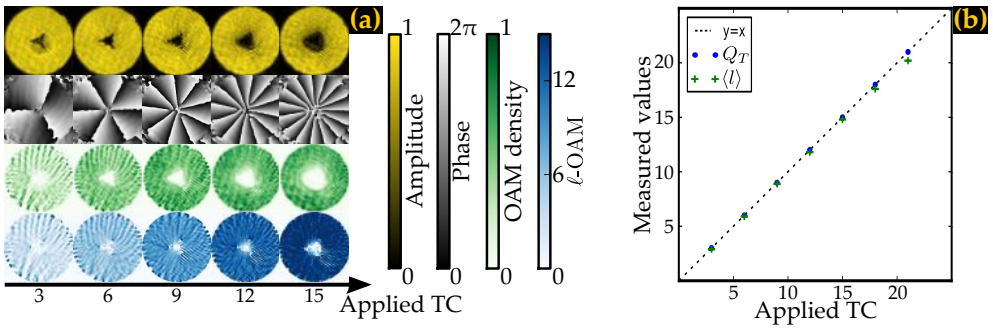

Figure 20 – (a) Profiles of amplitude, phase, OAM density and ℓ-OAM for a triangle-shaped TC distribution with a fixed geometry and varying total applied TC. (b) Relation between the measured Q_T and $\langle l \rangle$ in terms of the applied TC at the SLM. All measurements were taken at $z = 0$ cm.

depend on the CCD position.

5.5.2 Corner- and triangle-shaped distributions of TC

After discussing the behavior of a TC line, the next step in complexity are two TC lines. The data for a corner-shaped distribution of TC is shown in Fig. 19. By fixing the geometry of the TC distribution, the OV core also can be characterized by the three regimes discussed for TC lines as illustrated in Fig. 19(a). A high TC density was observed when $Q_T \geq 12$, since the OV

core profile becomes more rounded and tends to a circular shape. At smaller TC densities, $Q_T \leq 8$, it can be observed that multiple OV cores are distinguishable. When $Q_T = 10$, the OV core is corner-shaped. From the ℓ-OAM profiles, it can be seen that the ℓ-OAM is very small inside the triangle determined by the corner extremities. This fact can also be inferred from the relative uniformity of the phase profiles, and implies that the OAM density core profile is more rounded than the OV core at the amplitude profile. This conclusion is important for optical tweezers applications, in which someone wants to transport a dielectric particle along a specified route. On the other hand, it can be seen in Fig. 19(b) that the measured values of Q_T corresponds to the applied TC values and for these beams the reduction in $\langle l \rangle$ with respect to a point TC is small.

The experimental results for a triangle-shaped TC distribution are shown in Fig. 20. In Fig. 20(a) it can be seen that the OV core profiles are triangle-shaped and the intensity profile regimes are high TC density at $Q_T \geq 12$, elongated OV core at $Q_T = 9$ and small TC density at $Q_T \leq 6$. The ℓ-OAM and the OAM density profiles follows the TC distribution geometry, and therefore are suitable for applications in optical tweezers. Also it can be seen that, similarly to the corner-shaped TC distribution, Q_T corresponds to the applied value of TC and for these beams the reduction in $\langle l \rangle$ with respect to a point TC is smaller than in the Corner-shaped distribution.

5.6 TC Multipoles and 2D radial distribution

As a prototype for more complex TC distributions, TC multipoles and the 2D radial distribution were produced and characterized using the setup presented in sec. 5.4. Unless otherwise stated, the data was collected at the SLM image plane ($z = 0$). To our knowledge, the following interpretation of the phase profiles below was never reported in the literature.

5.6.1 TC Multipoles

As was discussed in subsec. 4.3.3, the TP associated with a finite TC distribution can be separated in contributions that vanish at very large distances and asymptotically nontrivial terms. For simplicity only the asymptotic behavior is studied here, and it is assumed a distribution such that

$$\chi_{\mathrm{OV}} = \Im\left[V\left(v\right)\right] = \alpha \sin\left[j\left(\phi+\beta\right)\right]/j, \tag{5.6}$$

where α is constant and $j \neq 0$. To avoid an azimuthal discontinuity in the phase profile j must be an integer. A fractional j leads to a line of phase discontinuity similar to those of [79, 119]. β is an orientation offset while α determines beam core local radius via Eq. (4.103), such that

$$|v|_{\mathrm{core}}\left(\phi\right) = b\sqrt{\left|\alpha\cos\left[j\left(\phi+\beta\right)\right]\right|}. \tag{5.7}$$

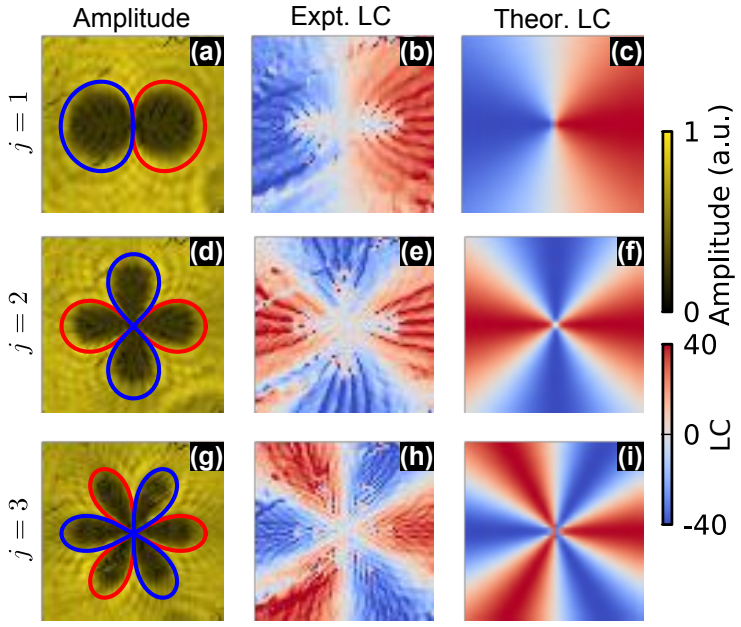

Figure 21 – Multipoles of TC at $z = 0$. The rows correspond to the data for a dipole (a, b, c), quadrupole (d, e, f) and an hexapole (g, h, i). In columns we display the beam amplitude profiles (a,d,g), the experimental ℓ-OAM (b, e, h) and theoretical ℓ-OAM obtained from Eq. (5.6) (c, f, i). The solid lines in (a, d, g) corresponds to the expected OV core profile from Eq. (5.7), and their colors (red, blue) represent the enclosed TC sign (+, -).

We show in Figs. 21 (a, d, g) the experimental intensity profiles for TC multipoles of order j =1, 2 and 3 by applying the phase profile of Eq. (5.6) to the SLM. The solid lines represent the expected core profile as given by Eq. (5.7). Blue and red lines surround, respectively, regions of negative and positive ℓ-OAM. The solid lines have only the radius scale as an adjustable parameter, and since $\alpha = 40$ for all j, the same scale was used for all curves. Figs. 21 (b, e, h) show the ℓ-OAM profiles, and Figs. 21 (c, f, i) exhibits the expected ℓ-OAM according to Eq. (5.6). A good agreement is found between the theoretically expected results and the experimental findings. A disagreement exists only at the darkest regions near the profile center, where we were not able to properly measure the phase. A technical aspect which is worth noticing is that the intensity profile of multipoles is very sensitive to the spatial filter iris transverse position, and misalignments makes the lobes profile nonsymmetrical.

An important property of TC multipoles is that their ℓ-OAM is stable under propagation, as can be seen by varying the position of the CCD along the z axis. Experimental amplitude and ℓ-OAM at different values of z are shown in Fig. 22 for $j = 4$. It may be observed in the amplitude profiles, Figs. 22 (a-d), that pairs of amplitude lobes with opposed ℓ-OAM signs annihilate under propagation. The resulting bright spots are located at zero ℓ-OAM regions. Creation and annihilation of oppositely charged OV pairs under propagation are well established in literature [16, 126, 133, 134], but to our knowledge the previous descriptions were always associated with, respectively, creation and destruction of TC. In the case described

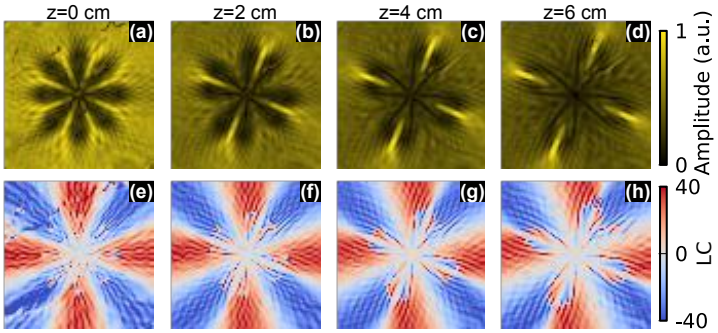

Figure 22 – Propagation of a vortex octupole $(j = 4)$ in free-space. In the top row (a-d) it is displayed the amplitude profile at increasing propagation distance from the SLM image plane ($z = 0$ cm), while in the bottom row (e-h) is shown the experimental ℓ-OAM. Notice that the ℓ-OAM remains stable under propagation.

here, the beam's phase topological structure is preserved under propagation, as can be seen from the ℓ-OAM in Fig. 22 (e-h). For negative z, the amplitude lobes rotate in the opposite direction to that shown in Figs. 22 (a-d).

5.6.2 2D radial TC distribution

Since only the phase is being modulated in the experiments presented, only the imaginary part of the TP (4.79) is considered here,

$$\chi_{\mathrm{OV}} = \begin{cases} Q_T \left[\left(\frac{r}{a}\right)^{n+2} (\phi - \pi) + \pi \right] & , r < a, \\ Q_T \phi & , r \geq a, \end{cases} \tag{5.8}$$

It should be remarked that Eq. (5.8) is a generalization which smoothly connects the phase profiles of a usual OV ($n = -2$) to helico-conical beams, or optical twisters [135, 136] in which $n = -1$. Optical twisters are interesting because they carry angular momentum and also have a higher photon density than the usual Laguerre-Gauss or Bessel beams [136]. Therefore they are of interest for manipulating particles [136] and may also be of interest for nonlinear optics with OAM carrying beams [137]. To our knowledge, other values of n were never previously reported in the literature.

We experimentally produced beams with the phase profile given by Eq. (5.8), with $Q_T = 5$, fixed a and varying n, and the results are shown in Fig. 23. In the phase profiles, Fig. 23(a-d), it can be seen that larger n increase the phase twisting at $r < a$ and reallocates the TC towards the border along $\phi = \pi$, as predicted in Eq. 4.83. Notice that even though the TC density has azimuthal symmetry, the positions of the singularities over the phase profile, Eq. (5.8), break this symmetry due to the phase jump at the branch line at $\phi = \pm\pi$, similar to the case of fractional OV [79, 119]. The TC displacement can be seen also in the zeros of the amplitude profiles, as shown in Fig. 23(e-h). The ℓ-OAM profiles, Fig. 23(i-l), shows that larger n values decrease the LC near the center of the circle. In Fig. 23(m-p) we show the mean ℓ-OAM as

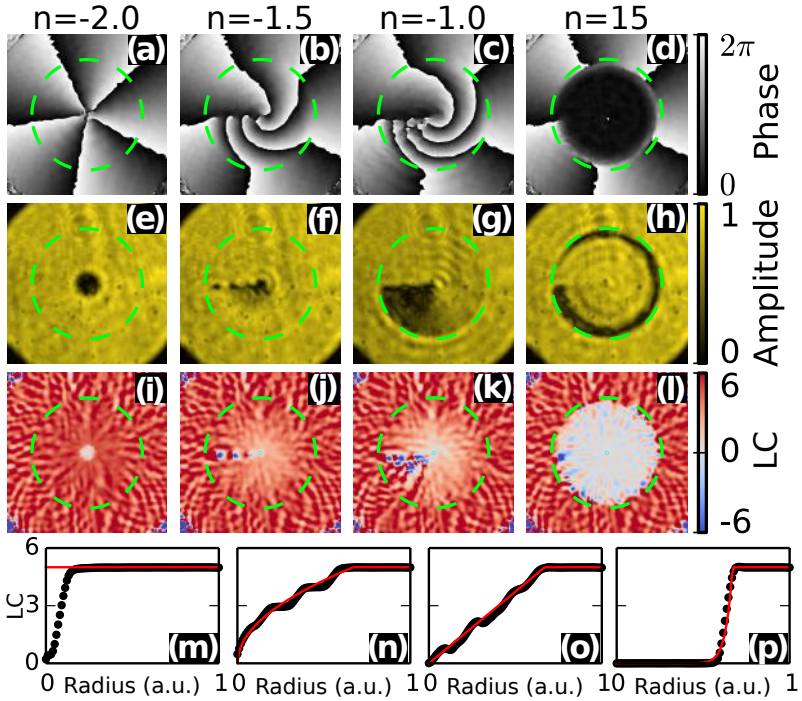

Figure 23 – Data for 2D radial distribution, Eq. (5.8), with $Q_T = 5$, fixed a and varying n (columns) at $z = 0$ cm. a is graphically represented by green dashed lines. The determined ℓ-OAM (black dots) at (m-p) corresponds to the azimuthally averaged LC at a given radial distance from the center of the circle as a function of the radial distance. The red solid lines in (m-p) correspond to the values expected from the applied phase mask, neglecting the discreteness of the TC.

a function of the radial distance to the center of the circle. The values obtained (black dots) agree with the theoretically expected from the phase profile (solid red) via Eq. (5.8). The ℓ-OAM reduction in the center can be understood by considering that larger n push ρ to the boundaries of the circle a.

5.7 Summary

In this chapter some consequences of the Topological Potential (TP) concept were investigated experimentally. In one of our results it was shown that by using TC distributions it is possible to have light beams with designed dark regions, and the total Topological Charge (TC) can be controlled through the distribution. Another important aspect discussed in this work is that the Orbital Angular Momentum (OAM) and TC are distinct physical quantities. While a clear distinction between OAM and TC can be seen in TC distributions, such distinction is not very clear in the more commonly used OAM light beams, as Bessel or Laguerre-Gauss beams. This distinction is not very clear within the literature, which is mainly concerned with beams with point TC, and there is much confusion between topological and physical arguments when explaining the observed phenomena.

Several TC distributions were considered in this chapter. First it was introduced the TC

distribution along a line, a corner and a triangle, as we reported in [1]. It was verified that the TC distributions can be used to shape the dark region of an OAM beam, since the TC phase singularity ensures that the field amplitude is zero. This is specially important because the intensity modulation was achieved by using only the phase profile of the TC distribution. This is very important because it allows to design the intensity profile of OAM beams using only phase masks. Since the intensity profile is extremely important in various applications, as in optical tweezers and traps, these TC distributions may be useful in optical manipulation systems [138].

The fields produced were initially characterized using the triangular slit technique [121], and later it was used a more complete characterization of the wavefront proposed by us in [2]. The simultaneous retrieval of phase and amplitude information was very important for determining the beam OAM profile, and also in observing the singularities' positions. The proposed characterization approach is very general, and can be applied to various beams. An important advantage is that it does not require a matching between the field and a specific geometrical feature, as in [38,117,118], thus being more adapted for generic TC distributions. For the line- and triangle-shaped TC distributions it was observed that both amplitude and OAM density profiles followed the designed geometry. Meanwhile, it was found that the ℓ-OAM and OAM profiles for the corner-shaped distribution is a rounded version of the associated TC distribution profile. As an application, it is remarked that the matching of an OV to a surface plasmon may require a non-cylindrical OAM beam [139]. Therefore, our approach can be applied to characterize the OAM beams produced by plasmonic structures. Finally, since the procedure in sec. 5.4 is general, it can be applied also to beams as Bessel or Laguerre-Gauss.

Other consequences of the TP were also explored. The TC multipole is related to the asymptotic phase profile due to nontrivial superpositions of OV, while the 2D radial TC distribution is a simple prototype. We believe that the bridge between 2D electrostatics and OV provided by the TP is important for optical tweezers [27], laser traps [88] or atom guides [140]. However, while the present work can be directly used to describe the field at the focus, further development is necessary to understand the effects of propagation and address issues as the field profile stability [56].

Another important point is that both the TC multipole and the 2D radial distribution might be useful in some applications. For instance, the intensity profile instability of TC multipoles may be used to determine the position of an extended object image plane, and in aligning spatial filters. Another possibility is that, since multipoles form a complete (Fourier) basis of orthogonal modes on the azimuthal phase, it is possible that they describe the morphology in noncanonical OV [133,141] and they may also be suited for applications in quantum communications [26]. In telecommunications, they are an alternative to Laguerre-Gauss beams for data multiplexing [142] that can be more stable to turbulence [142,143], since the topological properties of the phase profile are distributed over the beam profile.

6 Transverse effects in linear and non-linear light propagation

6.1 Introduction

In I. Newton's times there was a debate related to the fundamental structure of light. C. Huygens defended that light was a wave, but Newton believed that since light travels along straight lines, then it should be composed of small particles [144]. Newton's scientific prestige ultimately persuaded the mainstream understanding for a reasonable time. Later, the work of A. Fresnel and T. Young among others, have refuted the theory of corpuscular light through experiments involving light diffraction and interference phenomena[1]. However, since light indeed travels nearly along straight lines, it was important to understand how the *corpuscular-like* straight trajectories arise in Fresnel's theory. One approach is to use Fermat's principle, to verify that wavefronts propagate along minimum-length paths.

The knowledge acquired in the centuries old debate in the optics community later had a great importance in the development of Quantum Mechanics (QM). The dual behavior of quantum particles challenged the QM pioneers, which understood mechanical waves and mechanical point particles as distinct physical entities [145]. The connection between Fermat's principle and optical waves was essential to find the wavelength associated to a physical particle by L. de Broglie. As stated in his Ph.D. thesis [146],

> *Fermat's Principle applied to a phase wave is equivalent to Maupertuis' Principle applied to a particle in motion; the possible trajectories of the particle are identical to the rays of the phase wave.* We believe that the idea of an equivalence between the two great principles of Geometric Optics and Dynamics might be a precise guide for effecting the synthesis of waves and quanta.

Therefore, various of the principles behind QM were developed based on the previous optics knowledge.

In the last century there was a fast advancement in the theoretical tools to describe quantum phenomena, as wave and matrix mechanics and Dirac notation [40]. Meanwhile, even though classical optics and QM share various important common properties, the mathematical language currently used to describe optical systems often uses theoretical tools and concepts which are not amenable to a direct application of the most recent problem-solving

[1] More specifically, Fresnel's work predicted that light diffraction around a circular obstacle would produce a bright spot at the center of the dark region. Young's slit experiment showed interference profiles at a distant target. Both phenomena can be explained in the wave interpretation of light, but are not natural in the particle description of light.

developments from QM. Thus, the application of modern QM analytical tools to optics problems may improve the current understanding of some optical systems and can also provide solutions to currently open problems. The effort in applying tools commonly used in QM to classical wavefront propagation in optics already gave several results [147–155], but its use is reasonably limited within the optics community. There are several reasons why operator techniques are applied only within a niche. One that can be easily quoted is that they are often applied only to simple optical systems, as free-space propagation, parabolic lenses and GRIN media. Thus, the appeal for introducing a whole new formalism is severely reduced if it cannot expand the class of solvable problems or those with accurate approximations.

In this context, we remind here that the representation of QM problems in terms of operators is not unique. For instance, two common approaches are the Heisenberg Picture (HP) and the Interaction Picture (IP) [40]. To our knowledge, the previous works on optical wavefront propagation through operators are based on the HP only. Since the IP is widely used in QM and quantum field theory [40,41] for interacting and complex systems, its application in wavefront propagation can be relevant for example in describing light beams through complex optical systems, nonlinear optical materials, and in scattering media. Optical resonators and light propagation through free-form optical elements can also benefit if represented in the IP, since as will be later shown, the operators obtained are a natural extension of the ABCD matrices. The IP is currently used in optics in the temporal domain to express light-matter interactions [37, 51], or to describe the temporal evolution of light pulses [156, 157]. The major contribution of this chapter is introducing the IP in the spatial domain for wavefront propagation of paraxial light in the classical approximation. An important point at the core of the results is that by using the IP it is possible to obtain the transmittance function of arbitrary linear and nonlinear optical elements fully within the operator formalism. Thus, we believe that the IP provides an interesting framework for an analytical description of wavefront propagation in optical systems, complimentary to the existing techniques.

In the IP, the system's evolution can be split in linear (solvable) and nonlinear (NL, non-solvable) terms. The IP becomes very powerful for perturbative solutions, because the NL terms can be expressed in terms of the known linear terms, improving the approximation accuracy. This approach allows to describe how realistic, finite-sized beams behave under propagation through general optical systems. It is herein described how the IP can be applied to calculate the propagation of paraxial light beams under the action of a spatially varying refractive index for some simple transverse refractive index profiles and also for NL optical samples. In sec. 6.2 the paraxial wave equation is obtained in Dirac notation, and the most important hypothesis are introduced. In sec. 6.3 it is described how to represent and formally solve the paraxial equation, Eq. (6.6), for the three pictures previously described (SP, HP and IP). The IP is introduced in subsec. 6.3.3, and several important properties are introduced. In sec. 6.4 there are some simple applications of the IP to light propagation in simple linear paraxial optical systems as lenses, wedges and diffraction gratings. An important subsec.

is 6.4.3, where it is described how NL optical effects modify the beam effective width, curvature radius and divergence angle. Still in subsec. 6.4.3, it is showed how to calculate the curves from Z-scan technique [158] using the IP. Later in sec. 6.5 the IP calculations are experimentally verified for some NL optical problems. We used the IP to obtain the beam width propagation inside a thick NL sample through the Scattered Light Imaging Method (SLIM) [5], and to analytically describe the experimental curves with the D4σ technique [6].

6.2 Paraxial wave optics

In this section, the general notation and some definitions will be introduced. For simplicity, it is considered an homogeneously polarized, monochromatic electric field propagating along the $\boldsymbol{\epsilon}_3$ direction, that can be written as $\mathbf{E} = \boldsymbol{s}\psi(\mathbf{r},z)\,e^{i(kz-\omega t)}$, where $k = \omega/c$ is the wavenumber, z is the coordinate along the propagation direction, t is the time, $\mathbf{r} = x_1\boldsymbol{\epsilon}_1 + x_2\boldsymbol{\epsilon}_2$ represents the transverse coordinates, $\boldsymbol{s}$ is the polarization , and it is assumed that the extra polarization terms discussed in sec. 2.2 have a negligible effect. From Maxwell equations, the wave equation for this field is given by $\left[\nabla^2 - \frac{n^2(\mathbf{r},z)}{c^2}\frac{\partial^2}{\partial t^2}\right]\mathbf{E} = \mathbf{0}$, where $n(\mathbf{r},z) = \eta(\mathbf{r},z) + i\kappa(\mathbf{r},z)$ is the complex refractive index of the medium. For a description in terms of permittivity and permeability, one should use $n^2/c^2 \equiv \mu\epsilon$. To avoid the creation of counter-propagating waves [159], it is assumed a slow variation of $n(\mathbf{r},z)$ along z. Besides that, if the variation of $\psi(\mathbf{r},z)$ is also slow along the propagation direction, it can be approximated that $\frac{d^2}{dz^2}\psi \sim 0$ [51]. The field envelope then satisfies

$$\left\{\nabla_\perp^2 + 2ik\frac{\partial}{\partial z} + \left[n^2(\mathbf{r},z)\,k_0^2 - k^2\right]\right\}\psi(\mathbf{r},z) = 0, \tag{6.1}$$

where $\nabla_\perp^2$ means a Laplacian that acts only over the transverse coordinates, and $k_0 = \omega/c$ is the wavenumber in free space.

Equation (6.1) has the same mathematical structure as a 2D Schrödinger equation in Schrödinger Picture (SP) [40], where time is replaced by z. In Eq. 6.1 a quantity analogous to the potential is within square brackets and is not necessarily Hermitean, because the material can exhibit losses or gain depending on the imaginary part of $n^2(\mathbf{r},z)$. It should also be noticed that the value of k^2 can be chosen in a convenient way, depending on the specific spatial profile of $n(\mathbf{r},z)$. For example, if the material is uniform such that $n(\mathbf{r},z) = n_0$, the natural choice becomes $k = n_0 k_0$, which is the usual expression for the wavenumber inside an homogeneous material.

To simplify the term inside square brackets in Eq. (6.1), it is considered a simplifying assumption that the material is sufficiently transparent such that the absorption becomes significant only after the light propagates over many wavelenghts [51]. Then, in terms of the absorption coefficient α, $n^2 \approx \eta^2 - i\eta\alpha/k_0$, where the spatial dependencies were omitted for simplicity. Also, it is considered that both $\eta(\mathbf{r},z)$ and $\alpha(\mathbf{r},z)$ can be represented by an average (or effective) value and their spatial dependence are given by $\eta = n_0(z) + n'(\mathbf{r},z)$,

where $n'(\mathbf{r},z) \ll n_0$, and $\alpha(\mathbf{r},z) = \alpha_0 + \alpha'(\mathbf{r},z)$, where $\alpha'(\mathbf{r}) \ll \alpha_0$. Under this representation, the natural choice for k is

$$k = n_0(z)\, k_0, \tag{6.2}$$

and this will be assumed through the following discussion. Also, since both $n'(\mathbf{r},z)$ and α_0 are assumed to be small, the term $n'(\mathbf{r},z)\,\alpha_0/n_0$ was neglected. Then, $\left[n^2(\mathbf{r},z)\,k_0^2 - k^2\right] = ik\alpha_0 - 2kV(\mathbf{r},z)$, where it is defined the potential $V(\mathbf{r},z)$ that contains the spatial dependence of $\eta(\mathbf{r},z)$ and $\alpha(\mathbf{r},z)$ due to the optical elements traversed by the light beam,

$$V(\mathbf{r},z) = -k_0 n'(\mathbf{r},z) - i\frac{\alpha'(\mathbf{r},z)}{2}. \tag{6.3}$$

The reason for calling $V(\mathbf{r},z)$ a potential comes from the analogy of the paraxial equations with Schrödinger's wave equation, and will be more explicitly stated in subsec. (6.3.1).

The field $\psi(\mathbf{r},z)$ can also be represented in Dirac notation as

$$\psi(\mathbf{r},z) \equiv \langle \mathbf{r}|\psi,z\rangle, \tag{6.4}$$

$$\psi^*(\mathbf{r},z) \equiv \langle \psi,z|\mathbf{r}\rangle. \tag{6.5}$$

$\langle \mathbf{r}|\psi,z\rangle$ can be understood as the projection over the transverse coordinates $\mathbf{r}$ of the field ψ when the position along the propagation direction is z [149, 153]. Dirac notation is both powerful and flexible, and well suited to the operator language used throughout this work. In terms of $V(\mathbf{r},z)$ and in Dirac notation, Eq. (6.1) can be rewritten as

$$i\frac{\partial}{\partial z}\langle \mathbf{r}|\psi,z\rangle = \left[-\frac{1}{2k}\nabla_\perp^2 - i\frac{\alpha_0}{2} + V(\mathbf{r},z)\right]\langle \mathbf{r}|\psi,z\rangle. \tag{6.6}$$

Spatial dispersion was not introduced in the previous considerations for simplicity, but it can be added by generalizing $V(\mathbf{r},z) \to V\left(\mathbf{r},\nabla_\perp,z,\frac{\partial}{\partial z}\right)$. Also, in this work it will be considered only the transmission properties of the media.

6.3 Three pictures for paraxial optics

To obtain the solutions of Eq. (6.6), it is possible to use at least the three different pictures discussed below. In order to not confuse the different representations, a subscript S, H, I is placed to identify quantities in SP, HP and IP, respectively. What follows in this section can be considered as a translation of the well-known QM results [40] to the optics language. A very important remark is that all calculations below are purely classical, and only the language of QM is used. For example, our implementation of dissipation involves a non-Hermitian Hamiltonian and certainly does not apply to most quantum systems. The validity of description performed below should be strictly considered only in the classical optics regime.

Since SP, HP and IP are different representations for the same physical problem, the physical answer shall not depend on the representation. However, each picture has its own advantages and disadvantages. For example, the SP becomes very simple only when there is

a known set of eigenmodes of Eq. (6.6), which is usually a mathematically complex problem. However, the SP has simple solutions when there is no optical element, $V(\mathbf{r},z)=0$, or when diffraction effects are not relevant, $\frac{1}{2k}\nabla_\perp^2 \approx 0$. In HP it is simple to describe how beam quantities evolve under propagation, as the centroid or the beam width, and there is a direct connection with geometrical optics. On the other hand, it is difficult in HP to describe systems including generic profiles of $V(\mathbf{r},z)$, specially when the system has absorption. In that context, the IP is a very interesting representation for optical problems, because it is a mixed representation between SP and HP. Thus, the IP can be used to obtain the best characteristics of SP and HP to analytically solve complex propagation problems.

6.3.1 Schrödinger picture (SP)

The most usual approach to solve Eq. (6.6) consists in assuming that field $\langle \mathbf{r}|\psi,z;a\rangle_S$ is defined at a plane $z=a$ and changes with z, while the operators (terms within brackets) are fixed. It is then necessary to solve the associated differential equation for the given initial condition, which is difficult for arbitrary $V(\mathbf{r},z)$. This is a very complex mathematical problem in the general case but that has been discussed thoroughly in optics literature, since it is a traditional approach to solve Gaussian beam propagation [51, 59, 60].

Before explicitly stating the problem in HP or IP, the first step necessary is to describe Eq. (6.6) in terms of operators (here identified by carets). Given $\hat{\mathbf{x}}_S$ an operator representing the transverse coordinates, while $\hat{\mathbf{p}}_S$ represents the spatial frequencies in the transverse plane,

$$\hat{\mathbf{x}}_S = \hat{x}_{1,S}\boldsymbol{\epsilon}_1 + \hat{x}_{2,S}\boldsymbol{\epsilon}_2, \tag{6.7}$$

$$\hat{\mathbf{p}}_S = \hat{p}_{1,S}\boldsymbol{\epsilon}_1 + \hat{p}_{2,S}\boldsymbol{\epsilon}_2, \tag{6.8}$$

where $\boldsymbol{\epsilon}_1$ and $\boldsymbol{\epsilon}_2$ represent the unit vectors along the directions transverse to z.

$\hat{\mathbf{x}}_S$ and $\hat{\mathbf{p}}_S$ are such that the commutator (see Eq. (C.38)) between their components satisfy

$$\left[\hat{x}_{j,S},\hat{p}_{k,S}\right] = i\delta_{j,k}, \tag{6.9}$$

$$\left[\hat{x}_{j,S},\hat{x}_{k,S}\right] = 0 = \left[\hat{p}_{j,S},\hat{p}_{k,S}\right], \tag{6.10}$$

where $\delta_{j,k}$ is the Kronecker delta.

The position eigenkets $|\mathbf{r}\rangle_S$ return its eigenvalue under the action of $\hat{\mathbf{x}}_S$ and form a complete orthonormal basis,

$$\hat{\mathbf{x}}_S|\mathbf{r}\rangle_S = \mathbf{r}|\mathbf{r}\rangle_S, \tag{6.11}$$

$$\langle \mathbf{r}|\mathbf{r}'\rangle_S = \delta^{(2)}\left(\mathbf{r}-\mathbf{r}'\right), \tag{6.12}$$

$$\int d^2\mathbf{r}\,[|\mathbf{r}\rangle\langle\mathbf{r}|]_S = \hat{1} \tag{6.13}$$

where $\delta^{(2)}\left(\mathbf{r}-\mathbf{r}'\right)$ is a Dirac delta for the two transverse coordinates and $d^2\mathbf{r}$ is the area element over the transverse plane.

The commutation relations can be applied to evaluate the representation of $\hat{\mathbf{p}}_S$ in terms of coordinates, such that (see, for example, Appendix C.3)

$$\langle \mathbf{r}|_S \, \hat{\mathbf{p}}_S \equiv -i\nabla_\perp \langle \mathbf{r}|_S \,. \tag{6.14}$$

Thus, from Eqs. (6.11) and (6.14), Eq. (6.6) can be rewritten in terms of operators by substituting $\mathbf{r} \to \hat{\mathbf{x}}_S$ and $\nabla_\perp \to i\hat{\mathbf{p}}_S$,

$$i\frac{\partial}{\partial z}\left|\psi, z; a\right\rangle_S = \hat{H}_S \left|\psi, z; a\right\rangle_S, \tag{6.15}$$

$$\hat{H}_S = \hat{L}_S + \hat{V}_S\left(\hat{\mathbf{x}}_S, z\right). \tag{6.16}$$

$$\hat{L}_S = \frac{1}{2k}\hat{\mathbf{p}}_S^2 - i\frac{\alpha_0}{2}. \tag{6.17}$$

The quantity $\hat{H}_S$ can be understood as the optical system evolution operator, if we recognize the mathematical equivalence between Eq. (6.15) and Schrödinger's equation. Notice that $\hat{H}_S \neq \hat{H}_S^\dagger$ and the current description consider only forward propagation of light waves. Since z always increases, the inclusion of absorptive terms do not lead to divergences upon propagation. Thus, some care must be exerted to consider reflected waves. When the absorptive terms are absent, $\hat{H}_S$ becomes a Hamiltonian. The evolution operator in Eq. (6.16) includes absorption terms, and is a generalization of the case described in [39]. A short discussion of the results in [39] is performed in subsec. 6.3.2.

Equation (6.15) can be formally integrated as

$$\left|\psi, z; a\right\rangle_S = \left|\psi, a; a\right\rangle_S + \int_a^z \frac{dz'}{i}\hat{H}_S\left|\psi, z'; a\right\rangle_S, \tag{6.18}$$

The solution in SP is not easy to calculate for arbitrary $\hat{V}_S$, since $\hat{H}_S = \hat{H}_S\left(\hat{\mathbf{x}}_S, \hat{\mathbf{p}}_S, z\right)$, and $\left[\hat{H}_S\left(\hat{\mathbf{x}}_S, \hat{\mathbf{p}}_S, z\right), \hat{H}_S\left(\hat{\mathbf{x}}_S, \hat{\mathbf{p}}_S, z'\right)\right] \neq 0$ in general. The detailed mathematical procedure to arrive at the solution to Eq. (6.18) are detailed in Appendix C.4, resulting in

$$\left|\psi, z; a\right\rangle_S = \hat{G}_S(z, a)\left|\psi, a; a\right\rangle_S, \tag{6.19}$$

$$\hat{G}_S(z, a) = \hat{Z}\left\{\exp\left[-i\int_a^z dz'\hat{H}_S\left(\hat{\mathbf{x}}_S, \hat{\mathbf{p}}_S, z'\right)\right]\right\}. \tag{6.20}$$

Equations (6.19)-(6.20) exhibit several important quantities. First there is the propagator $\hat{G}_S(z, a)$, which indicates how does the initial state $\left|\psi, a; a\right\rangle_S$ is modified after propagation through an optical system described by $\hat{H}_S$. Due to optical absorption, $\hat{H}_S \neq \hat{H}_S^\dagger$, implying that $\hat{G}_S(z, a)\,\hat{G}_S^\dagger(z, a) \neq \hat{1}$. Therefore, the transverse profile does not remain normalized upon propagation, and ${}_S\left\langle\psi, z; a|\psi, z; a\right\rangle_S \neq$constant. Unfortunately, to exhibit Eq. (6.20) in such short notation, it becomes necessary to introduce the concept of the z-ordering operator $\hat{Z}$, which is necessary because $\hat{H}_S$ does not commute at different z planes. There are, however, three limits in which Eq. (6.20) can be stated in simple terms. The first occurs when it is possible to obtain the set of eigenmodes of $\hat{H}_S$. For a general $\hat{V}_S$ the eigenmodes are very difficult to obtain, and this approach is not considered in this work.

If light does propagate inside an homogeneous material, where $\hat{V}\left(\hat{\mathbf{r}}_S, z'\right) = 0$, $\hat{H}_S = \hat{L}_S$, the integrand in Eq. (6.20) commutes with itself, and becomes

$$\hat{G}_S^{(0)}(z,a) = \exp\left[-i\,(z-a)\,\hat{L}_S\right]. \tag{6.21}$$

Equation (6.21) is very important in evaluating the beam propagation, since it is an operator representation of the Fresnel diffraction integral, as previously stated in Eq. (2.32).

Another limit which simplifies Eq. (6.20) is when there is a very thin sample, such that the diffraction effects on the beam are negligible. The diffraction is mathematically represented by the term $\hat{\mathbf{p}}_S^2/2k$ in $\hat{L}_S$, and it is approximated that $\hat{\mathbf{p}}_S^2/2k \approx 0$. Neglecting dispersion, $\hat{H}_S$ does not depend on $\hat{\mathbf{p}}_S$ anymore, and the effect of the optical element can be represented by a transfer matrix operator $\hat{T}_{z,a}$ defined by $\hat{G}_S^{(\text{no diff.})}(z,a) = \hat{T}_{z,a}^{(0)}$,

$$\hat{T}_{z,a}^{(0)} = \exp\left\{-i\int_a^z dz'\left[-i\frac{\alpha_0}{2} + \hat{V}_S\left(\hat{\mathbf{x}}_S, z'\right)\right]\right\}. \tag{6.22}$$

Both Eqs. (6.21) and (6.22) are simple to evaluate because they do not display $\hat{Z}$ and also because they are well defined in the ket basis $\left|\mathbf{p}\right\rangle$ and $|\mathbf{r}\rangle$, respectively. As a remark, it should be noticed that the validity limits of Eq. (6.22) is not exactly clear in the SP formulation of the problem. This is to be contrasted with the solution in IP, in which the evaluation of the no diffraction approximation is easily formulated. The application of an Eq. very similar to (6.22) to important optical elements will be done below in the context of IP.

As a concluding remark for this subsection, it is worth mentioning that the mean value of a generic operator $\hat{O}_S\left(\hat{\mathbf{x}}_S, \hat{\mathbf{p}}_S, z\right)$ with respect to the field is defined as

$$\left\langle \hat{O}_S \right\rangle = \frac{{}_S\left\langle \psi, z; a \left| \hat{O}_S\left(\hat{\mathbf{x}}_S, \hat{\mathbf{p}}_S, z\right) \right| \psi, z; a \right\rangle_S}{{}_S\left\langle \psi, z; a | \psi, z; a \right\rangle_S}. \tag{6.23}$$

6.3.2 Heisenberg picture (HP)

Another approach to solve the operator Eq. (6.15) consists in representing the operators as changing with z while the field $\left|\psi, z; a\right\rangle_H$ is fixed, $\left|\psi, z; a\right\rangle_H = \left|\psi, a; a\right\rangle_H = \left|\psi, a; a\right\rangle_S$. In this way, one can obtain the general properties of a given optical system, while the field initial conditions can be applied at a final stage. This is also a very common approach to describe light propagation, usually by means of the Fresnel diffraction integral [51, 59, 60, 144]. The choice made in this work consists in representing the problem in terms of operators, as in [147–155].

Since in HP the state is assumed to be static, while the operators are dynamic, the bras and kets in SP and HP are related through

$$\left|\psi, z; a\right\rangle_S = \hat{G}_H(z,a)\left|\psi, z; a\right\rangle_H, \tag{6.24}$$

$$\left\langle \psi, z; a\right|_S = \left\langle \psi, z; a\right|_H \hat{G}_H^{\dagger}(z,a), \tag{6.25}$$

where the propagation operator $\hat{G}_H(z,a)$ contains all of the propagation dynamics due to the optical system. The consistency between Eqs. (6.19) and (6.24) requires that $\hat{G}_H(z,a) = \hat{G}_S(z,a)$. However, since Eq. (6.19) has no simple solution, the assignment of an explicit formula for $\hat{G}_H(z,a)$ will be performed only in connection with the IP.

Using Eqs. (6.24) and (6.25) in (6.23), it is possible to obtain the representation of a generic operator in HP,

$$\hat{O}_H = \hat{G}_H^{\dagger}(z,a)\,\hat{O}_S\hat{G}_H(z,a)\,. \tag{6.26}$$

Notice that the representation of $\hat{O}_H$ as in Eq. (6.26) implicitly assumes that the normalization factor in Eq. (6.23) remains constant, $\left({}_S\langle\psi,z;a|\psi,z;a\rangle_S\right)^{-1} = \left({}_S\langle\psi,a;a|\psi,a;a\rangle_S\right)^{-1}$, indicating that $\hat{G}_H^{\dagger}(z,a)\,\hat{G}_H(z,a) = \hat{1}$. However, as was previously stated, the normalization ${}_S\langle\psi,z;a|\psi,z;a\rangle_S$ is a function of z due to absorption or the presence of apertures. Substitution of Eq. (6.24) in (6.15) indicates that

$$i\frac{\partial\hat{G}_H(z,a)}{\partial z} = \hat{H}_S\hat{G}_H(z,a)\,, \tag{6.27}$$

Since in HP the operators evolve, while the state is fixed with z, it is important to know how does $\hat{O}_H$ depends on z. Using Eqs. (6.26) and (6.27), it can be obtained that (see details in Appendix C.5)

$$i\frac{d\hat{O}_H}{dz} = \hat{O}_H\hat{H}_{H'} - \hat{H}_{H'}^{\dagger}\hat{O}_H + i\left[\frac{\partial\hat{O}_S}{\partial z}\right]_H, \tag{6.28}$$

$$\hat{H}_{H'} = \hat{G}_H^{-1}(z,a)\,\hat{H}_S\hat{G}_H(z,a)\,. \tag{6.29}$$

As mentioned before for the SP, it is very difficult to compute Eqs. (6.28) and (6.29) in the general case. However, there is a very important class of solutions that can be evaluated exactly, and also connect wave optics and geometrical optics through the Ehrenfest's theorem, as described below.

Ehrenfest's Theorem

The concepts discussed in this subsection are deeply related to the discussion in Ref. [39]. Although it is possible to obtain a rigorous proof of the operator representation for systems in HP with loss or gain in systems containing up to quadratic terms in $\hat{\mathbf{x}}_H$ [151], in this work such task will be performed in IP. Thus, assuming an absorption-less optical system, $\hat{G}_H^{-1}(z,a) = \hat{G}_H^{\dagger}(z,a)$, and in this limit

$$\hat{H}_{H'} = \hat{H}_H = \hat{H}_H^{\dagger}. \tag{6.30}$$

Also, given the identity (C.40), $\hat{H}_H$ can be obtained from $\hat{H}_S$ by substituting $\hat{\mathbf{x}}_S \to \hat{\mathbf{x}}_H$ and $\hat{\mathbf{p}}_S \to \hat{\mathbf{p}}_H$. Then, it can be observed that the transverse position and momentum operators, $\hat{\mathbf{x}}_H$ and $\hat{\mathbf{p}}_H$, must evolve as described by Eq. (6.28). Using Eqs. (C.42) and (C.43),

$$\frac{d\hat{\mathbf{x}}_H}{dz} = \frac{\hat{\mathbf{p}}_H}{k}, \tag{6.31}$$

$$\frac{d\hat{\mathbf{p}}_H}{dz} = -\nabla_{\hat{\mathbf{x}}_H}\hat{V}_H\left(\hat{\mathbf{x}}_H, z\right), \tag{6.32}$$

where $\nabla_{\hat{\mathbf{x}}_H}\hat{V}_H$ represents the gradient of $\hat{V}_H$ is taken with respect to $\hat{\mathbf{x}}_H$. This set of equations can be understood in the simple case of free-space propagation, where $\hat{V}_H = \hat{0}$. Eq. (6.32) has as solution $\hat{\mathbf{p}}_H(z) = \hat{\mathbf{p}}_H(0)$, while Eq. (6.31) implies that $\hat{\mathbf{x}}_H(z) = \hat{\mathbf{x}}_H(0) + z\hat{\mathbf{p}}_H(0)/k$. The operator $\hat{\mathbf{p}}_H(0)/k$ is associated to the beam lateral spreading, and behaves like the beam angle to the propagation axis z in paraxial regime. Care must be taken to not take such analogy too far, because $\hat{\mathbf{p}}_H(0)/k$ represents the beam angle only in some limiting cases, as when the beam is a tilted plane wave.

Equations (6.31) and (6.32) resemble the canonical equations of Hamilton for a conservative mechanical system [39, 62]. However, while Eqs. (6.31) and (6.32) are a relation between functions of operators, the canonical equations of Hamilton involves functions of coordinates and momenta. To transform the operators in Eqs. (6.31) and (6.32) into functions it is necessary to consider the mean values over some ket $|\psi\rangle$, resulting in

$$\frac{d\langle\hat{\mathbf{x}}_H\rangle}{dz} = \frac{\langle\hat{\mathbf{p}}_H\rangle}{k}, \tag{6.33}$$

$$\frac{d}{dz}\frac{\langle\hat{\mathbf{p}}_H\rangle}{k} = -\left\langle\frac{1}{k}\nabla_{\hat{\mathbf{x}}_H}\hat{V}_H\left(\hat{\mathbf{x}}_H, z\right)\right\rangle. \tag{6.34}$$

This is an optical version of the famous Ehrenfest's theorem [40], as previously discussed in [39]. However, Eqs. (6.33) and (6.34) will satisfy paraxial geometrical optics exactly only if [39]

$$\left\langle\nabla_{\hat{\mathbf{x}}_H}\hat{V}_H\left(\hat{\mathbf{x}}_H, z\right)\right\rangle = \nabla_{\langle\hat{\mathbf{x}}_H\rangle}\hat{V}_H\left(\langle\hat{\mathbf{x}}_H\rangle, z\right), \tag{6.35}$$

or, in other words, if $\hat{V}_H$ is fully described in terms of coordinates instead of operators, Eq. (6.35) can be satisfied. It can be showed that, irrespective to the initial ket $|\psi\rangle$, the center of gravity of a light beam, $\langle\hat{\mathbf{x}}_H\rangle$, will move as an optical ray in any square law medium [39], where

$$\hat{V}_H\left(\hat{\mathbf{x}}_H, z\right) = \frac{k_0}{2}n_x\hat{x}_H^2 + \frac{k_0}{2}n_y\hat{y}_H^2. \tag{6.36}$$

Although the square law medium is very important, since it can be used as the first approximation to spherical lenses and mirrors, there is a need for describing more general optical systems. For example, optical systems containing free-form optical surfaces. Also, since the ray optics approach is usually more intuitive for designing optical systems, an approach that allows a direct connection between wave and ray optics should be very fruitful in the development of general optical systems.

6.3.3 Interaction (or Dirac) picture (IP)

From the previous subsecs. 6.3.1 and 6.3.2, it should be now clear that it is difficult to obtain solutions of Eq. (6.6) for a generic $V(\mathbf{r}, z)$ in SP, while in HP it is not very easy to introduce absorption effects. Just for remembering the basics of SP and HP, in SP the field evolves with z while the operators are held fixed, and in HP the operators evolve while the field is kept fixed. More specifically to SP, it was described that there are two important limiting cases in which the solution can be more easily obtained: when $V(\mathbf{r}, z) = 0$, in Eq. (6.21), and when diffraction is not relevant, Eq. (6.22). The idea behind IP is to evolve both states and operators, in such a way that each part solves a simpler problem. Such decomposition is not unique, and for specific problems the approach below is not the optimal. To our knowledge, the IP is being introduced for wavefront propagation by our group.

Since it is of interest to include the effects of diffraction, it is assumed that the operators evolve according to $\hat{L}_S$, while if $\hat{V}_S$ is present, it will only affect the IP field. Mathematically, it is considered that the free-propagator is factored of the IP field, as

$$\left|\psi, z; a\right\rangle_S = \hat{G}^{(0)}_{z,a} \left|\psi, z; a\right\rangle_I, \tag{6.37}$$

$$\left\langle\psi, z; a\right|_S = \left\langle\psi, z; a\right|_I \hat{G}^{(0)\dagger}_{z,a}, \tag{6.38}$$

$$\hat{G}^{(0)}_{z-a} = \exp\left[-i\,(z-a)\,\hat{L}_S\right], \tag{6.39}$$

where the notation $\hat{G}^{(0)}_{z-a}$ for the free-propagator was made more compact due to its ubiquitous appearance in the remaining of this chapter. Given $\hat{L}_S$ as in Eq. (6.17), some important properties can be readily verified,

$$\hat{G}^{(0)\dagger}_{z-a}\hat{G}^{(0)}_{z-a} = \exp\left[-(z-a)\,\alpha_0\right], \tag{6.40}$$

$$\hat{G}^{(0)-1}_{z-a}\hat{G}^{(0)}_{z-a} = \hat{1}, \tag{6.41}$$

$$\hat{G}^{(0)-1}_{z-a} = \exp\left[(z-a)\,\alpha_0\right]\hat{G}^{(0)\dagger}_{z-a}, \tag{6.42}$$

$$\hat{G}^{(0)}_{a-a} = \hat{1}. \tag{6.43}$$

Equations (6.40) to (6.42) can be summarized as that for a system including linear absorption, the Hermitian conjugate of the propagator, $\hat{G}^{(0)\dagger}_{z-a}$, is not the inverse operator $\hat{G}^{(0)-1}_{z-a}$. Also, if there is no propagation, Eq. (6.43) states that $\hat{G}^{(0)}_{a-a}$ does nothing to the initial state. This is very important because it relates the initial IP and SP fields.

If the definition (6.37) is substituted into (6.15), we obtain

$$i\frac{\partial}{\partial z}\left|\psi, z; a\right\rangle_I = \hat{V}_I(\hat{\mathbf{x}}_I, z)\left|\psi, z; a\right\rangle_I, \tag{6.44}$$

$$\hat{V}_I(\hat{\mathbf{x}}_I, z) = \hat{G}^{(0)-1}_{z,a}\,\hat{V}_S(\hat{\mathbf{x}}_S, z)\,\hat{G}^{(0)}_{z,a}. \tag{6.45}$$

So, as first remarks regarding IP, it can be noticed that the field $\left|\psi, z; a\right\rangle_I$ propagates due to $\hat{V}_I(\hat{\mathbf{x}}_I, z)$ only. Also, the IP representation of generic operators can be explicitly made in terms of $\hat{G}^{(0)-1}_{z-a}$ instead of $\hat{G}^{(0)\dagger}_{z-a}$, and thus the formalism is more appropriate for absorptive

systems in comparison to HP. Since Eq. 6.45 is a similarity transformation, it can be seen from Appendix C.2 that $\hat{V}_I(\hat{\mathbf{x}}_I, z)$ can be obtained from $\hat{V}_S(\hat{\mathbf{x}}_S, z)$ by replacing $\hat{\mathbf{x}}_S \rightarrow \hat{\mathbf{x}}_I$. Thus, the IP operators have a simple representation.

Notice that using Eqs. (6.37) and (6.38) in Eq. (6.17), and the identity (6.42), it is true that $\langle \hat{O}_I \rangle = \langle \hat{O}_S \rangle$ such that

$$\langle \hat{O}_I \rangle = \frac{{}_I\langle \psi, z; a | \hat{O}_I(\hat{\mathbf{x}}_I, \hat{\mathbf{p}}_I, z) | \psi, z; a \rangle_I}{{}_I\langle \psi, z; a | \psi, z; a \rangle_I}, \tag{6.46}$$

$$\hat{O}_I(\hat{\mathbf{x}}_I, \hat{\mathbf{p}}_I, z) = \hat{G}_{z,a}^{(0)-1} \hat{O}_S(\hat{\mathbf{x}}_S, \hat{\mathbf{p}}_S, z) \hat{G}_{z,a}^{(0)}. \tag{6.47}$$

To obtain the general solution of the IP field, it is formally equivalent to the procedure adopted for going from Eq. (6.15) to Eq. (6.19), and the result is

$$|\psi, z; a\rangle_I = \hat{T}_{z,a} |\psi, a; a\rangle_I, \tag{6.48}$$

$$\hat{T}_{z,a} = \hat{Z}\left\{ \exp\left[-i \int_a^z dz' \hat{V}_I(\hat{\mathbf{x}}_I, z') \right] \right\}. \tag{6.49}$$

Thus, given the unitarity at zero propagation, Eq. (6.43), the initial condition is $|\psi, a; a\rangle_I = |\psi, a; a\rangle_S$. It is remarked that the transmission operator in Eq. (6.49), $\hat{T}_{z,a}$, still requires the use of the z ordering operator, $\hat{Z}$. Although the z dependence is omitted, $\hat{\mathbf{x}}_I = \hat{\mathbf{x}}_I(z)$ depends on both $\hat{\mathbf{x}}_I(a)$ and $\hat{\mathbf{p}}_I(a)$, such that $[\hat{\mathbf{x}}_I(z), \hat{\mathbf{x}}_I(z')] \neq 0$ if $z \neq z'$. $\hat{\mathbf{x}}_I$ plays a very important role in IP and its propagation will be discussed more carefully below. For now, it is only stated without proof that in the limit of very thin samples, $\hat{T}_{z,a}$ reduces to $\hat{T}_{z,a}^{(0)}$, Eq. (6.22).

By having an explicit representation of $|\psi, z; a\rangle_I$, Eq. (6.48), it becomes possible to evaluate the evolution of a generic operator $\hat{O}_I$ with z in a similar way to the HP discussion. Since there is interest in including absorption effects, the normalization contribution will not be neglected, as occurred for HP. The detailed calculation is similar to that for HP and is performed in Appendix C.6, resulting in

$$i\frac{d}{dz}\hat{O}_I = [\hat{O}_I, \hat{H}_I] - i(\hat{\alpha}_I - \langle \hat{\alpha}_I \rangle)\hat{O}_I + i\left[\frac{\partial}{\partial z}(\hat{O}_S) \right]_I. \tag{6.50}$$

Equation (6.47) is a very important result obtained in this work, since it involves only terms represented in IP. This must be contrasted with Eq. (6.28), which depends on $\hat{H}_{H'}$, an operator in HP only in the limit of a system without absorption. Thus, the IP is specially interesting for describing optics in non-conservative systems, and can be used to extend the operator formalism to this regime. An interesting point regarding Eq. (6.47) is the explicit appearance of the absorption $\hat{\alpha}_I$ in the evolution equation for the operator $\hat{O}_I$, and the dependence on the current field through $\langle \hat{\alpha}_I \rangle$. In the limit of $\hat{\alpha}_I$ =constant, it can be seen that $\hat{\alpha}_I - \langle \hat{\alpha}_I \rangle = 0$ and Eq. (6.47) is equivalent to the evolution of HP operators in a conservative system. Under more general absorption profiles, the term $\hat{\alpha}_I - \langle \hat{\alpha}_I \rangle$ will significantly modify the evolution of $\hat{O}_I$.

Since $\hat{H}_I$ is the operator that determines the propagation of all operators, it is important to verify its behavior. Any operator $\hat{A}$ satisfies $\left[\hat{A}, \hat{A}\right] = \hat{A}\hat{A} - \hat{A}\hat{A} = 0$, and (6.50) becomes

$$\frac{d}{dz}\hat{H}_I = -\left(\hat{\alpha}_I - \langle\hat{\alpha}_I\rangle\right)\hat{H}_I, \text{ or} \tag{6.51}$$

$$\hat{H}_I(z) = \hat{Z}\left\{\exp\left[-\int_a^z dz'\left(\hat{\alpha}_I - \langle\hat{\alpha}_I\rangle\right)\right]\right\}\hat{H}_I(a). \tag{6.52}$$

If $\hat{\alpha}_I$ does not vary along the transverse direction, then $\hat{H}_I$ is a constant throughout propagation. By the other hand, in the limit where $\hat{\alpha}_I - \langle\hat{\alpha}_I\rangle$ does have a spatial structure homogeneous along the propagation direction, $\hat{H}_I(a)$ is magnified where $\hat{\alpha}_I < \langle\hat{\alpha}_I\rangle$ and reduced where $\hat{\alpha}_I > \langle\hat{\alpha}_I\rangle$. This can be intuitively understood as the field profile being described by the regions which suffered less absorption during propagation.

Operators $\hat{\mathbf{x}}_I$ and $\hat{\mathbf{p}}_I$

The operator evolution equation, (6.47), is applicable to any operator, and ultimately these can be decomposed in terms of $\hat{\mathbf{x}}_I$ and $\hat{\mathbf{p}}_I/k$. Therefore, the position and momentum operators are very important, and some of their properties are discussed in this subsection. By direct substitution, and using Eqs. (C.42) and (C.43),

$$\frac{d}{dz}\hat{\mathbf{x}}_I = \nabla_{\hat{\mathbf{p}}_I}\hat{H}_I - \left(\hat{\alpha}_I - \langle\hat{\alpha}_I\rangle\right)\hat{\mathbf{x}}_I, \tag{6.53}$$

$$\frac{d}{dz}\frac{\hat{\mathbf{p}}_I}{k} = -\frac{1}{k}\nabla_{\hat{\mathbf{x}}_I}\hat{H}_I - \left(\hat{\alpha}_I - \langle\hat{\alpha}_I\rangle\right)\frac{\hat{\mathbf{p}}_I}{k}, \tag{6.54}$$

Equations (6.53) and (6.54) resemble Hamilton's canonical equations of motion for a point particle, but in terms of operators. Inside absorptive media, the propagation of $\hat{\mathbf{x}}_I$ and $\hat{\mathbf{p}}_I/k$ has the same interpretation as in Eq. 6.52, where the propagation reduces the influence of operators from regions with a strong absorption. Notice also that the reasoning that led to HP Ehrenfest's theorem in sec. 6.3.2 can also be applied for $\hat{\mathbf{x}}_I$ and $\hat{\mathbf{p}}_I/k$, and it should be possible in some cases to observe a ray-like behavior of these operators. This is very important from a practical viewpoint, since there are many tools to describe and design the geometrical propagation of light rays. An important example are the ABCD matrices, which allow the description of various optical systems. Thus, developing a generalization of the concepts behind the ABCD matrix in terms of the IP description is important, and is performed in what follows.

The operator $\hat{\mathbf{x}}_I$ behaves as the ray position along the transverse axis, while $\hat{\mathbf{p}}_I/k$ is associated to the beam angle with respect to the propagation axis z. Therefore, both from the classical reasoning associated with these operators and from the mathematical structure of Eqs. (6.53) and (6.54), it is natural to reorganize the evolution of $\hat{\mathbf{x}}_I$ and $\hat{\mathbf{p}}_I/k$ as

$$\hat{\boldsymbol{\eta}}_I = \begin{pmatrix} \hat{\mathbf{x}}_I \\ \hat{\mathbf{p}}_I/k \end{pmatrix}, \tag{6.55}$$

$$\frac{d}{dz}\hat{\boldsymbol{\eta}}_I = -i\left[\hat{\boldsymbol{\eta}}_I, \hat{H}_I\right] - \left(\hat{\alpha}_I - \langle\hat{\alpha}_I\rangle\right)\hat{\boldsymbol{\eta}}_I. \tag{6.56}$$

In the general case, the commutator $\left[\hat{\boldsymbol{\eta}}_I, \hat{H}_I\right]$ cannot be simply decomposed in terms of $\hat{\boldsymbol{\eta}}_I$. However, there are many important cases in which $\left[\hat{\boldsymbol{\eta}}_I, \hat{H}_I\right] = \mathsf{M}\hat{\boldsymbol{\eta}}_I$, where M is a matrix with constant coefficients. For example, if the largest power of both $\hat{\mathbf{x}}_I$ and $\hat{\mathbf{p}}_I/k$ in $\hat{H}_I$ is not superior to two, it is easy to verify that the gradient terms in Eqs. (6.53) and (6.54) will result in terms at most linear in the components of $\hat{\boldsymbol{\eta}}_I$. Under such kind of systems, the calculation of $\hat{\boldsymbol{\eta}}_I(z)$ involves a linear first order differential equation, that can be simplified in terms of the ABCD matrices as will be exemplified below in sec. 6.4. For general $\hat{H}_I$, however, it is necessary to solve Eq. (6.56) directly.

A full paraxial optical system is usually composed of elements with a finite thickness, traversed sequentially by light along the z direction. Therefore, if the solution to Eq. (6.56) is splitted to describe each optical element separately, it becomes simpler to describe complex optical systems. Assuming that the i-th optical element along the optical path is between $z = a_i$ and $z = a_{i+1}$, the solution to Eq. (6.56) for $a_i < z < a_{i+1}$ can be stated as $\hat{\boldsymbol{\eta}}_{I,i}(z) = \hat{\mathsf{T}}_i(z)\,\hat{\boldsymbol{\eta}}_I(a_i)$, where $\hat{\mathsf{T}}_i(z)$ represents the solution to the initial condition $\hat{\boldsymbol{\eta}}_I(a_i)$. If the initial condition for the beam is given at a_0, the full solution can be stated as

$$\hat{\boldsymbol{\eta}}_{I,i}(z) = \hat{\mathsf{T}}_i(z)\,\hat{\mathsf{T}}_{i-1}(a_i)\ldots\hat{\mathsf{T}}_1(a_1)\,\hat{\boldsymbol{\eta}}_I(a_0)\,. \tag{6.57}$$

Since usual free-space optical systems contains many elements that are adequately described by ABCD matrices, as lenses and propagation in an homogeneous material, Eq. (6.57) can be used to simplify at least some products of $\hat{\mathsf{T}}_i$. The exception occurs when $\hat{H}_I$ contains $\hat{\mathbf{x}}_I$ and $\hat{\mathbf{p}}_I/k$ with exponents higher than 2 for a given optical element[2], because the operators propagate nonlinearly at that region. However, the expansion in (6.57) can be valid before and after such optical element, what simplifies most of the light propagation problem.

6.4 Applications for the IP formalism

In this section, it will be shown how to apply the concepts developed above in various applications. There is an initial consideration of free-propagation and simple optical elements, as wedges and lenses. For simplicity only stigmatic optical elements are considered in this work, and they are described by $2x2$ matrices. In order to describe astigmatic elements, it is simple to extend the following results by considering separately each transverse spatial direction in $\hat{\mathbf{x}}_I$ and $\hat{\mathbf{p}}_I/k$. $\hat{\boldsymbol{\eta}}_I$ can be extended to a 4-vector and the matrices to dimension $4x4$. As a composite system, it is developed the analysis of spatial filter, which is useful for holographic techniques. Later, there are some applications to nonlinear optics.

[2] As an example, these effects can arise due to spherical aberration and spatial dispersion for $\hat{\mathbf{x}}_I$ and $\hat{\mathbf{p}}_I/k$, respectively.

6.4.1 Light propagation in homogeneous materials, Siegman's formulas and Fresnel propagator

The simpler and most basic application to be considered is the light propagation inside an homogeneous material, where $\hat{H}_I = \hat{L}_I$. In this case it is noticed that $-i\left[\hat{\boldsymbol{\eta}}_I, \hat{H}_I\right] = \mathsf{M}_{\text{free}}\hat{\boldsymbol{\eta}}_I$, where

$$\mathsf{M}_{\text{free}} = \begin{pmatrix} 0 & 1 \\ 0 & 0 \end{pmatrix}. \tag{6.58}$$

Equation (6.56) in terms of M_{free} becomes

$$\frac{d}{dz}\hat{\boldsymbol{\eta}}_I = \mathsf{M}_{\text{free}}\hat{\boldsymbol{\eta}}_I. \tag{6.59}$$

The solution to (6.59) can be obtained by solving explicitly the set of differential equations, but here it is chosen a full matrix method. Given Eq. (6.59) and considering that the initial conditions are given at $z = a$, it is reasonable to guess the ansatz

$$\hat{\boldsymbol{\eta}}_I(z) = \exp\left(\int_a^z dz' \mathsf{M}_{\text{free}}\right)\hat{\boldsymbol{\eta}}_I(a). \tag{6.60}$$

Since $\int_a^z dz' \mathsf{M}_{\text{free}} = (z-a)\,\mathsf{M}_{\text{free}}$ and $(\mathsf{M}_{\text{free}})^2 = 0$, the series expansion of the exponential in (6.60) becomes $\mathsf{I} + (z-a)\,\mathsf{M}_{\text{free}}$, where I is the identity matrix. Then, it is easy to verify that both the initial condition is satisfied, $\hat{\boldsymbol{\eta}}_I(z=a) = \hat{\boldsymbol{\eta}}_I(a)$, and also that Eq. (6.59) is satisfied by expanding the exponential in powers of $\int_a^z dz' \mathsf{M}_{\text{free}}$. Thus, (6.60) is the solution to (6.59), which can be re-expressed as

$$\hat{\boldsymbol{\eta}}_I(z) = \mathsf{T}_{\text{free}}\hat{\boldsymbol{\eta}}_I(a), \tag{6.61}$$

$$\mathsf{T}_{\text{free}} = \begin{pmatrix} 1 & z-a \\ 0 & 1 \end{pmatrix}. \tag{6.62}$$

T_{free} is precisely the ABCD matrix associated with the propagation of a light ray from a to z inside an homogeneous material. However, it should be remarked that the current description is fully within the paraxial wave optics domain. As an interesting implication, it is noticed that the important formulas obtained by Siegman to characterize beam propagation [42, 43] arise naturally in IP. In these works, Siegman showed an approach for the definition of effective beam width, curvature radius and divergence angle for arbitrary wavefronts, besides of the introduction of the beam propagation factor M^2 (or "beam quality" factor[3]). From (6.61), it might be verified that

$$\hat{\mathbf{x}}_I(z) = \hat{\mathbf{x}}_I(a) + (z-a)\,\hat{\mathbf{p}}_I(a)/k. \tag{6.63}$$

$$\hat{\mathbf{p}}_I(z)/k = \hat{\mathbf{p}}_I(a)/k. \tag{6.64}$$

[3] The M^2 factor is obtained from beam propagation considerations, but its usage as an indicator of beam quality is controversial for various profiles, as a top-hat beams [160]. Following the discussion in [160], M^2 is herein referred as a propagation factor.

If the beam is centered on the z axis, $\langle \hat{\mathbf{x}}_I(a) \rangle = 0$. Also, for simplicity, it is assumed that $\langle \hat{\mathbf{p}}_I(a) \rangle = 0$, or the beam centroid $\langle \hat{\mathbf{x}}_I(z) \rangle = 0$ propagates parallel to the z axis. Since the beam width squared can be defined in terms of the irradiance transverse variance in position space [42], one can also express in our operator language as $\hat{W}^2(z) = 2\hat{\mathbf{x}}_I^2(z)$, where

$$\hat{\mathbf{x}}_I^2(z) = \hat{\mathbf{x}}_I^2(a) - (z-a)\,\hat{A}(a) + (z-a)^2\,\hat{\mathbf{p}}_I^2(a)/k^2, \tag{6.65}$$

$$\hat{A}(a) = -\frac{1}{k}\left[\hat{\mathbf{x}}_I(a)\cdot\hat{\mathbf{p}}_I(a) + \hat{\mathbf{p}}_I(a)\cdot\hat{\mathbf{x}}_I(a)\right]. \tag{6.66}$$

Averaged over an arbitrary initial field,

$$\left\langle \hat{W}^2(z) \right\rangle = \left\langle 2\hat{\mathbf{x}}_I^2(a) \right\rangle - 2(z-a)\left\langle \hat{A}(a) \right\rangle + (z-a)^2 \left\langle 2\hat{\mathbf{p}}_I^2(a) \right\rangle / k^2, \tag{6.67}$$

and some interesting remarks can be already performed. The average $\left\langle 2\hat{\mathbf{p}}_I^2(a) \right\rangle$ is the beam width in the spacial frequency domain, and as such is a positive quantity, implying that (6.67) grows approximately as z^2 for $|z| \gg a$. This implies that, as previously shown by Siegman [42, 43], for any arbitrary beam it is possible to define a plane $z = z_{\min}$ such that the beam waist is a minimum. Also, it is possible to show that $\left\langle \hat{A}(z_{\min}) \right\rangle = 0$, what indicates that $\hat{A}(z)$ is related to an effective radius of curvature [43].

The averages in (6.67) are very simple to evaluate explicitly for a Gaussian beam. This case is also interesting because there are well known analytic solutions. At $z = a$, the operators are equivalent in the three pictures discussed in sec. 6.3. Thus, it can be stated that

$$\left\langle \boldsymbol{r} | \psi, a; a \right\rangle = N \exp\left[ik\boldsymbol{r}^2/2q(a)\right], \tag{6.68}$$

where $q(z) = z - iz_0$ is the complex curvature of the beam, $z_0 = kw_0^2/2$ is the Rayleigh length, w_0 is the beam waist, and N is a normalization factor. After some manipulations of the Gaussian integrals, its possible to obtain that $\left\langle 2\hat{\mathbf{x}}_I^2(a) \right\rangle = w^2(a)$, $\left\langle \hat{A}(a) \right\rangle = -w^2(a)/R(a)$ and $\left\langle 2\hat{\mathbf{p}}_I^2(a)/k^2 \right\rangle = 4/k^2w_0^2 = \theta_0^2$, where $w(z) = w_0\sqrt{1 + z^2/z_0^2}$ is the beam width, $R(z) = z\left(1 + z_0^2/z^2\right)$ is the curvature radius and $\theta_0 = 2/kw_0$ is the Gaussian beam divergence angle. The substitution of these averages in (6.67) shows that the IP description indeed returns correctly the known result for a Gaussian beam, $\left\langle \hat{W}^2(z) \right\rangle = w^2(z)$.

While the solution (6.61) is very useful to evaluate mean values over a given initial beam profile, as shown by Siegman's formulas, in many times it is important to evaluate the electric field profile at a plane $z \neq a$. Thus, considering (6.37) and (6.39),

$${}_S\left\langle \boldsymbol{r} | \psi, z; a \right\rangle_S = \int d^2\boldsymbol{r}' \; {}_S\langle \boldsymbol{r} | G_{z-a}^{(0)} \left| \boldsymbol{r}' \right\rangle_S \; {}_S\left\langle \boldsymbol{r}' | \psi, z; a \right\rangle_I. \tag{6.69}$$

Since $\hat{V}_I = 0$ for a beam propagating in an homogeneous medium, (6.48) implies that $\left|\psi, z; a\right\rangle_I = \left|\psi, a; a\right\rangle_I = \left|\psi, a; a\right\rangle_S$. Therefore, the only part that needs to be calculated is the matrix element ${}_S\langle \boldsymbol{r} | G_{z-a}^{(0)} \left| \boldsymbol{r}' \right\rangle_S$. Using that $\int d\boldsymbol{p} \left|\boldsymbol{p}\right\rangle\langle\boldsymbol{p}| = \hat{1}$ and (C.48),

$${}_S\langle \boldsymbol{r} | G_{z-a}^{(0)} \left| \boldsymbol{r}' \right\rangle_S = \frac{n_0}{i\lambda(z-a)} e^{\frac{ik\left(\boldsymbol{r}-\boldsymbol{r}'\right)^2}{2(z-a)} - \frac{\alpha_0}{2}(z-a)}. \tag{6.70}$$

It can be seen that (6.70) is, apart from the absorptive term, the well known Fresnel propagator. This implies that beam field at a plane $z > a$ is given by the well known Fresnel diffraction integral,

$$ {}_S\langle \boldsymbol{r}|\psi,z;a\rangle_S = \frac{n_0 e^{-\frac{\alpha_0}{2}(z-a)}}{i\lambda(z-a)} \int d^2\boldsymbol{r}' e^{\frac{ik(\boldsymbol{r}-\boldsymbol{r}')^2}{2(z-a)}} {}_S\langle \boldsymbol{r}'|\psi,a;a\rangle_S. \tag{6.71} $$

The Fresnel propagator can also be obtained directly from (6.63). Notice that the eigenfields of the operator $\hat{\mathbf{p}}_I(z)/k$, Eq. (6.64), are simply tilted plane waves. It should be then interesting to investigate the eigenfields of $\hat{\mathbf{x}}_I(z)$. Defining ψ such that

$$ \hat{\mathbf{x}}_I(z)\left|\psi,z;a\right\rangle = \boldsymbol{u}\left|\psi,z;a\right\rangle. \tag{6.72} $$

For simplicity, the calculations will initially be performed in one transverse dimension. Representing the operators in the plane $z = a$.

$$ \int dx\,|x\rangle\langle x|\,\hat{x}_I(z)\left|\psi,z\right\rangle = u\int dx\,|x\rangle\langle x|\left|\psi,z\right\rangle, \tag{6.73} $$

$$ \left[x + i\frac{(z-a)}{k}\frac{d}{dx}\right]\psi(x) = u\psi(x), \tag{6.74} $$

$$ \psi(x) = \frac{1}{N}e^{\frac{ik(x-u)^2}{2(z-a)}}, \tag{6.75} $$

where $\psi(x) = \langle x|\psi,z\rangle$ and N is a normalization constant.

The generalization to two transverse dimensions is simply

$$ \psi_{\mathbf{u}}(\boldsymbol{r}) = \frac{1}{N}e^{\frac{ik(\boldsymbol{r}-\mathbf{u})^2}{2(z-a)}}. \tag{6.76} $$

It remains necessary to find the normalization constant, which can be found through the orthonormality condition

$$ \int d^2\mathbf{r}\psi^*_{\mathbf{u}'}(\mathbf{r})\,\psi_{\mathbf{u}}(\mathbf{r}) = \delta\left(\mathbf{u}-\mathbf{u}'\right), \tag{6.77} $$

from where it is obtained

$$ |N| = \left|\frac{\lambda(z-a)}{in_0}\right|. \tag{6.78} $$

Thus, the solution

$$ \psi_{\mathbf{u}}(\boldsymbol{r}) = \frac{in_0}{\lambda(z-a)}e^{\frac{ik(\boldsymbol{r}-\mathbf{u})^2}{2(z-a)}} \tag{6.79} $$

is a normalized eigenfield of the position operator in IP. The eigenfield analysis as sketched above is also useful to obtain properties of propagating modes, as Laguerre- and Hermite-Gauss modes [152] and modes of a cavity with parabolic mirrors [161], because they are eigenfields of operators similar to $\hat{\mathbf{x}}_I(z)$.

Dielectric slab

A slab is the simplest possible optical element. In a notation consistent with that of sec. 6.4.2, the slab can be described by $\mathbf{s}_1(\mathbf{r},z) = a\boldsymbol{\epsilon}_3$ and $\mathbf{s}_2(\mathbf{r},z) = b\boldsymbol{\epsilon}_3$, such that the refractive index profile along the propagation direction can be written as

$$n_{\text{slab}}(z) = n_0 + (n_1 - n_0)\,\Theta(z-a)\,\Theta(b-z), \tag{6.80}$$

for a system composed of slab whose thickness is $b-a$ and has a refractive index n_1, embedded in a medium whose refractive index is n_0.

As can be seen by applying (6.80) to (6.56), it is easy to verify that $-i\left[\hat{\boldsymbol{\eta}}_I, \hat{H}_I\right] = \mathsf{M}_{\text{free}}\hat{\boldsymbol{\eta}}_I$. Therefore, the light propagation inside the slab is equivalent to that in free-space. By the other hand, recalling the definition of k, Eq. (6.2), it can be seen that $k(z) = k_0 n'_{\text{slab}}(z)$ has discontinuities at $z=a$ and $z=b$ that modify $\hat{\mathbf{p}}_I$. For example, at $z=a$ one has that $\frac{d}{dz}\left(\hat{\mathbf{p}}_I/k\right) = 0$ implies in Snell's law, $\hat{\mathbf{p}}_I\left(a^+\right)/k\left(a^+\right) = \hat{\mathbf{p}}_I(a^-)/k(a^-)$. Since $\hat{\mathbf{p}}_I(a^-)/k(a^-)$ must be multiplied by n_0/n_1 to obtain $\hat{\mathbf{p}}_I\left(a^+\right)/k\left(a^+\right)$, this dielectric interface is summarized by

$$\mathsf{T}_{\text{interface},z=a} = \begin{pmatrix} 1 & 0 \\ 0 & n_0/n_1 \end{pmatrix}. \tag{6.81}$$

The propagation inside the slab is described by (6.62), while the interface at $z=b$ can be represented as (6.81) with n_0 and n_1 interchanged. Multiplying the associated matrices, it is obtained that the input-output T matrix for a dielectric slab is

$$\mathsf{T}_{\text{slab}} = \begin{pmatrix} 1 & (b-a)\,n_0/n_1 \\ 0 & 1 \end{pmatrix}. \tag{6.82}$$

Thus, light propagates in the slab as in free-space, Eq. (6.62), but travels a different optical path, $(b-a)\,n_0/n_1$.

6.4.2 Thin optical elements

In subsec. 6.4.1 some important results of light propagation in homogeneous materials were obtained. In terms of increasing the system complexity, the next step consists in obtaining the effect of optical elements with a transverse profile modulation over the beam propagation. When possible, both the associated ABCD matrix and the associated transmittance operator will be obtained.

It is assumed that the element is contained between $a \le z \le b$ and reflection effects are neglected for simplicity. Another important point is that it is approximated for thin elements that they do not change the transverse position operator, $\frac{d}{dz}(\hat{\mathbf{x}}_I) = 0$. For simplicity, it is considered that a volume V has two arbitrarily shaped surfaces, described by the vectors $\mathbf{s}_1(\mathbf{r},z)$ and $\mathbf{s}_2(\mathbf{r},z)$. It is defined that $\mathbf{s}_1$ represents the first surface and $\mathbf{s}_2$ the last surface at every x, y, or $\boldsymbol{\epsilon}_3 \cdot \mathbf{s}_1(\mathbf{r},z) < \boldsymbol{\epsilon}_3 \cdot \mathbf{s}_2(\mathbf{r},z)$. Therefore, in terms of the unit step function Θ, given a fixed

transverse position x, y, a point $\mathbf{r}$ is inside V if $\Theta(z-\boldsymbol{\epsilon}_3\cdot[\mathbf{s}_1(\mathbf{r},z)])\,\Theta(\boldsymbol{\epsilon}_3\cdot[\mathbf{s}_2(\mathbf{r},z)]-z)=1$. If the refractive index at V is n_1, while outside it is n_0, it becomes easy to verify that over the whole region $a\leq z\leq b$,

$$n(\mathbf{r},z)=n_0+(n_1-n_0)\,\Theta(z-\boldsymbol{\epsilon}_3\cdot[\mathbf{s}_1(\mathbf{r},z)])\,\Theta(\boldsymbol{\epsilon}_3\cdot[\mathbf{s}_2(\mathbf{r},z)]-z)\,. \tag{6.83}$$

For this refractive index, $k=k_0 n_0$, while $n'(\mathbf{r},z)=(n_1-n_0)\,\Theta(z-\boldsymbol{\epsilon}_3\cdot[\mathbf{s}_1(\mathbf{r},z)])\,\Theta(\boldsymbol{\epsilon}_3\cdot[\mathbf{s}_2(\mathbf{r},z)]-z)\,.$ The above ideas can be extended to geometries containing holes, or even multiple materials, by taking into account the extra surfaces, while the relation for the absorption is analogous.

Given the profiles for n' and α', the total effect of the optical element over the beam can be considered from the evolution equation for $\hat{\mathbf{p}}_I/k$. Since $\frac{d}{dz}(\hat{\mathbf{x}}_I)=0$, the integral in z and $\nabla_{\hat{\mathbf{x}}_I}$ can be interchanged, what allows us to write $\hat{\mathbf{p}}_I(b)/k=\hat{\mathbf{p}}_I(a)/k-k^{-1}\nabla_{\hat{\mathbf{x}}_I(a)}\int_a^b dz'\hat{V}_I\left[\hat{\mathbf{x}}_I(a),z'\right]$. In many cases, another expression can give more insight in the behavior of an element. Considering that according to (C.43), $-\nabla_{\hat{\mathbf{x}}_I}f(\hat{\mathbf{x}}_I)=\left[\hat{\mathbf{p}}_I,-if(\hat{\mathbf{x}}_I)\right]$, and using the Baker-Hausdorff lemma, Eq. (C.39), it is possible to state that for thin elements,

$$\frac{\hat{\mathbf{p}}_I(b)}{k}=\hat{T}_{b,a}^{-1}\frac{\hat{\mathbf{p}}_I(a)}{k}\hat{T}_{b,a}, \tag{6.84}$$

$$\hat{\mathbf{x}}_I(b)=\hat{\mathbf{x}}_I(a)\,, \tag{6.85}$$

$$\hat{T}_{b,a}=\exp\left(-i\int_a^b dz'\hat{V}_I\left[\hat{\mathbf{x}}_I(a),z'\right]\right), \tag{6.86}$$

since $\left[\hat{G},\left[\hat{G},\hat{\mathbf{p}}_I(a)\right]\right]=0$ for $\hat{G}=\int_a^b dz'\hat{V}_I\left[\hat{\mathbf{x}}_I(a),z'\right]$.

According to (6.84), the optical element modifies $\hat{\mathbf{p}}_I(a)/k$ according to a similarity transformation defined by its transmittance $\hat{T}_{b,a}$ [Eqs. (6.84) and (6.86)]. This is the operator version of the widely used expression where the effects of thin optical refractive elements are considered through the associated phase transformations only [60, 66].

Dielectric wedge

We consider that the wedge starts at $z=a$ and has a refractive index n_1, and that its surfaces are described by the vectors $\mathbf{s}_1(\mathbf{r},z)=a\boldsymbol{\epsilon}_3$ and $\mathbf{s}_2(\mathbf{r},z)=a\boldsymbol{\epsilon}_3+x(\sin\alpha\boldsymbol{\epsilon}_3+\cos\alpha\boldsymbol{\epsilon}_1)\approx a\boldsymbol{\epsilon}_3+x(\alpha\boldsymbol{\epsilon}_3+\boldsymbol{\epsilon}_1)$. The angle α has to be small to maintain the paraxial approximation [60]. Immediately after the wedge, it is assumed that the refractive index is n_0. Using Eq. (6.83) for $z>a$, the refractive index at the vicinity of the wedge is described by

$$n_{\text{wedge}}(\mathbf{r},z)=n_0+(n_1-n_0)\,\Theta[\alpha x-(z-a)]\,. \tag{6.87}$$

In this case it can be seen that

$$\hat{T}_{\text{wedge}}=e^{ik_0(n_1-n_0)\alpha\hat{x}_{1,I}}, \tag{6.88}$$

implying that

$$\frac{\hat{\mathbf{p}}_I(b)}{k}=\frac{\hat{\mathbf{p}}_I(a)}{k}+\frac{n_1-n_0}{n_0}\alpha\boldsymbol{\epsilon}_1, \tag{6.89}$$

or the beam propagation angle with respect to the z axis changes by a factor of $\frac{n_1-n_0}{n_0}\alpha$ along the direction $\boldsymbol{\epsilon}_1$. A more explicit way to verify this is by calculating the evolution of the position operator after the wedge. It is easy to verify that if before the wedge the beam is centered on the axis, such that $\langle \boldsymbol{\epsilon}_1 \cdot \hat{\mathbf{x}}_I (z < a) \rangle = 0$, after the wedge the centroid position increases linearly as $\langle \boldsymbol{\epsilon}_1 \cdot \hat{\mathbf{x}}_I (z > b) \rangle = (z-b)\,\frac{n_1-n_0}{n_0}\alpha$.

Diffraction grating

Another important thin element is the diffraction grating, which consists essentially of a periodic modulation of optical path along a specified direction. Consider that $\hat{s}_1(\mathbf{r},z) = a\boldsymbol{\epsilon}_3$, while $\hat{s}_2(\mathbf{r},z) = \{d + A[1+\cos(\Lambda x)]\}\boldsymbol{\epsilon}_3$. d is the mean position of the refractive index modulation, while A is the modulation amplitude and Λ is the period along the $\boldsymbol{\epsilon}_1$ direction. From the condition that $\boldsymbol{\epsilon}_3 \cdot \hat{s}_1(\mathbf{r},z) < \boldsymbol{\epsilon}_3 \cdot \hat{s}_2(\mathbf{r},z)$, it is required that $a < d - A$. Thus, the refractive index profile becomes

$$n_{\text{grating}}(\mathbf{r},z) = n_0 + (n_1 - n_0)\,\Theta\{d + A[1+\cos(\Lambda x)] - z\}, \tag{6.90}$$

and thus, $\hat{T}_{\text{grating}} = \exp\left[ik_0(n_1-n_0)A\cos\left(\Lambda\hat{x}_{1,I}\right)\right]$. Using the identity [111] $\exp\left(iz\cos\phi\right) = \sum_{j=-\infty}^{\infty} i^j J_j(z)\,e^{ij\phi}$, where $J_j(z)$ is the Bessel function, it is possible to express

$$\hat{T}_{\text{grating}} = \sum_{j=-\infty}^{\infty} i^j J_j\left[k_0(n_1-n_0)A\right] e^{ij\Lambda\hat{x}_{1,I}}. \tag{6.91}$$

A comparison between (6.91) and (6.88) indicates that each term j in the sum will produce a new beam propagating at an angle $j\Lambda/k$ relative to the original beam axis. The isolation of the diffraction order $j = j'$ gives

$$\frac{\hat{\mathbf{p}}_I(b)}{k} = \frac{\hat{\mathbf{p}}_I(a)}{k} + \frac{j'\Lambda}{k}\boldsymbol{\epsilon}_1, \tag{6.92}$$

if the field overall amplitude modulation factor, $J_{j'}\left[k_0(n_1-n_0)A\right]$, and phase modulation factor, $i^{j'}$, are factored.

Spherical dielectric interface and thin lens

Both usual lenses and spherical mirrors have spherical surfaces. Therefore, since the shape of the surface will be the most important factor in determining the complex transmittance, the general concepts of both cases can be considered together using spherical dielectric interfaces (SDI). Without loss of generality, it is considered that the SDI is represented by a sphere of radius R and refractive index n_1 placed at the origin of the coordinate system, which is cut at the plane $z = a$. The resulting spherical cap has surfaces described by the vectors $\hat{s}_1(\mathbf{r},z) = a\boldsymbol{\epsilon}_3$ and $\hat{s}_2(\mathbf{r},z) = R\left(x\boldsymbol{\epsilon}_1 + y\boldsymbol{\epsilon}_2 + z\boldsymbol{\epsilon}_3\right)/\sqrt{x^2+y^2+z^2}$. Outside the sphere, there is a material whose refractive index is n_0. For simplicity it is assumed that $a < R < b$. The refractive index encompassing the region $0 < a \le z \le b$ can then be described by

$$n_{\text{SDI}}(\mathbf{r},z) = n_0 + (n_1 - n_0)\,\Theta\left[\sqrt{R^2 - \mathbf{r}^2} - z\right], \tag{6.93}$$

and

$$\hat{T}_{\mathrm{SDI}} = \exp\left[i k_0 (n_1 - n_0) \sqrt{R^2 - \hat{\mathbf{x}}_I^2(a)} \right]. \tag{6.94}$$

For simplicity, it can be considered that the beam pass through the SDI only near the axis. This allows the use of the parabolic approximation, $\sqrt{R^2 - \hat{\mathbf{x}}_I^2(a)} \approx R - \hat{\mathbf{x}}_I^2(a)/2R$. Neglecting the transversely constant term, we obtain

$$\hat{T}_{\mathrm{SDI}} \approx \exp\left[-i \frac{k_0 (n_1 - n_0)}{2R} \hat{\mathbf{x}}_I^2(a) \right]. \tag{6.95}$$

Given (6.95), it can be obtained

$$\frac{\hat{\mathbf{p}}_I(b)}{k} = \frac{\hat{\mathbf{p}}_I(a)}{k} - \frac{n_1 - n_0}{R n_0} \hat{\mathbf{x}}_I(a). \tag{6.96}$$

Since $\hat{\mathbf{p}}_I(b)$ is linear in both $\hat{\mathbf{p}}_I(a)$ and $\hat{\mathbf{x}}_I(a)$, the SDI can be represented through the ABCD matrix

$$\mathsf{T}_{\mathrm{SDI}} = \begin{pmatrix} 1 & 0 \\ -\frac{n_1 - n_0}{R n_0} & 1 \end{pmatrix}. \tag{6.97}$$

Remind that $\mathsf{T}_{\mathrm{SDI}}$ can also be written in terms of the focal distance $f = R n_0/(n_1 - n_0)$. Also, if the medium at $z \geq b$ has a refractive index n_1, the matrix $\mathsf{T}_{\mathrm{interface}} \mathsf{T}_{\mathrm{SDI}}$ must be used.

As an application of $\mathsf{T}_{\mathrm{SDI}}$, it will be considered the focusing of a collimated, generic, light beam by a lens at $z = 0$. Before the lens, the collimation implies that the beam effective curvature is infinite, or $\langle \hat{A}(0) \rangle = 0$ [43]. If the initial beam waist and divergence are denoted by $w_0^2 = \langle 2\hat{\mathbf{x}}_I^2(0) \rangle$ and $\theta_0^2 = \langle 2\hat{\mathbf{p}}_I^2(0)/k^2 \rangle$, respectively, then

$$\langle \hat{W}^2(z<0) \rangle = w_0^2 + \theta_0^2 z^2. \tag{6.98}$$

The position operator at a distance z after the lens is given by $\begin{pmatrix} \mathbf{1} & \mathbf{0} \end{pmatrix} \cdot \mathsf{T}_{\mathrm{free}} \mathsf{T}_{\mathrm{SDI}} \hat{\boldsymbol{\eta}}_I(0)$, or $\hat{\mathbf{x}}_I(z) = \left(1 - \frac{z}{f}\right) \hat{\mathbf{x}}_I(0) + z \hat{\mathbf{p}}_I(0)/k$. Thus, if the beam waist is calculated as previously performed for the Siegman formulas, the result is

$$\langle \hat{W}^2(z>0) \rangle = \left(1 - \frac{z}{f}\right)^2 w_0^2 + \theta_0^2 z^2. \tag{6.99}$$

Now, the beam waist has a minimum at

$$z_{\min} = \frac{f}{1 + \left(\frac{\theta_0 f}{w_0}\right)^2}, \tag{6.100}$$

where the beam waist is

$$\sqrt{\langle \hat{W}^2(z_{\min}) \rangle} = \frac{\theta_0 f}{\sqrt{1 + \left(\frac{\theta_0 f}{w_0}\right)^2}}. \tag{6.101}$$

Notice that the formalism here developed allowed us to obtain the wave optics focusing properties of a generic light beam passing through a parabolic lens. Eq. (6.100) has the wave optics correction to the minimum beam waist position predicted by geometrical optics. Also, according to (6.101), the transverse extent of the light beam never becomes zero for a real beam, since $\theta_0 > 0$ for a finite-sized beam. The geometrical optics results can be retrieved in the limit $\theta_0 \to 0$, when the light beam is an infinitely extended plane wave.

Quadratic index media

If the refractive index has a quadratic transverse profile, it is known that there is an exact ABCD matrix solution [51, 60]. It is thus assumed that

$$n_{\mathrm{QIM}}(\mathbf{r}, z) = n_0\left(1 - \frac{g^2}{2}\mathbf{r}^2\right). \tag{6.102}$$

Considering that $n' = -n_0 g^2 \mathbf{r}^2$, it is possible to follow the same argument used to solve the free-space propagation problem in subsec. 6.4.1. Notice that $\frac{d}{dz}\hat{\boldsymbol{\eta}}_I = \mathsf{M}_{\mathrm{QIM}}\hat{\boldsymbol{\eta}}_I$, where

$$\mathsf{M}_{\mathrm{QIM}} = \begin{pmatrix} 0 & 1 \\ -g^2 & 0 \end{pmatrix}, \tag{6.103}$$

and then the formal solution becomes

$$\hat{\boldsymbol{\eta}}_I(z) = \exp\left(\int_a^z dz' \mathsf{M}_{\mathrm{QIM}}\right)\hat{\boldsymbol{\eta}}_I(a). \tag{6.104}$$

Then, $\hat{\boldsymbol{\eta}}_I(z)$ can be obtained by exponentiation of the matrix $\int_a^z dz' \mathsf{M}_{\mathrm{QIM}} = (z-a)\,\mathsf{M}_{\mathrm{QIM}}$. How to calculate the exponential of a matrix can be found in various references, as for example in [40]. Here just a short comment is performed below.

Consider a diagonalizable 2x2 matrix A, whose eigenvalues are λ_1, λ_2, and the matrix P that diagonalizes A such that

$$\mathsf{P}^{-1}\mathsf{A}\mathsf{P} = \begin{pmatrix} \lambda_1 & 0 \\ 0 & \lambda_2 \end{pmatrix}, \tag{6.105}$$

and $\mathsf{P}^{-1}\mathsf{P} = \mathsf{I}$. Since $\exp\mathsf{A} = \sum_{n=0}^{\infty}(n!)^{-1}\mathsf{A}^n$, by performing a procedure similar that which led to Eq. (C.40) it can be obtained that

$$\exp\mathsf{A} = \mathsf{P}\begin{pmatrix} e^{\lambda_1} & 0 \\ 0 & e^{\lambda_2} \end{pmatrix}\mathsf{P}^{-1}, \tag{6.106}$$

which is simply a product of three 2x2 matrices for systems with azimuthal symmetry. The difficulty lies in finding the eigenvalues and P.

Then, $(z-a)\,\mathsf{M}_{\mathrm{QIM}}$ can be obtained after several mathematical steps, resulting in $\hat{\boldsymbol{\eta}}_I(z) = \mathsf{T}_{\mathrm{QIM}}\hat{\boldsymbol{\eta}}_I(a)$, where the associated ray matrix is

$$\mathsf{T}_{\mathrm{QIM}} = \begin{pmatrix} \cos g(z-a) & \frac{1}{g}\sin g(z-a) \\ -g\sin g(z-a) & \cos g(z-a) \end{pmatrix}. \tag{6.107}$$

An interesting aspect of quadratic index media is that the profile of Gaussian beams remain stable under propagation [51, 60]. Also, they can be used as a first approximation to the nonlinear response of optical media, as performed in Eq. (2.100). While our discussion contains only refractive effects, it is also possible to include loss or gain both in SP [162] and in an operator formalism [151, 163].

6.4.3 Light propagation inside an isotropic nonlinear medium

As a final example of the application of IP in calculation of wave optics problems, it will be considered in this subsection the propagation of light inside an isotropic nonlinear (NL) optical medium. This problem contains two important ingredients that are present in many optical systems, which are the NL response and geometrical aberrations. For example, the third-order Kerr nonlinearity is a very important process because, due to its symmetry, it is present is all ordinary materials [37]. From a technological point of view such NL processes are also interesting, because they are used in saturable absorbers for achieving passive mode-locking in ultrafast lasers [51, 60].

It is considered that the nonlinear terms can be described as

$$\hat{V}_I = -k_0 n' \left[I\left(\hat{\mathbf{x}}_I, z\right) \right] - i \frac{\alpha' \left[I\left(\hat{\mathbf{x}}_I, z\right) \right]}{2}, \tag{6.108}$$

where $I\left(\hat{\mathbf{x}}_I, z\right)$ is the field irradiance profile at the plane z, and n' and α' are the NL refractive index and absorption, respectively.

A very important quantity in these experiments is the beam power, that might change due to α'. Since the power $P(z)$ is proportional to ${}_S\langle \psi, z; a | \psi, z; a \rangle_S$, it is possible to use the bra and ket definitions in the IP, Eqs. (6.37) and (6.38), and the general solution to the field in IP, Eq. (6.48), to represent

$$P(z) = c e^{-\alpha_0 (z-a)} \, {}_I\left\langle \psi, a | \hat{T}^{\dagger}_{z,a} \hat{T}_{z,a} | \psi, a \right\rangle_I, \tag{6.109}$$

where c is an overall constant. Denoting $P_0 = c \, {}_S\langle \psi, a | \psi, a \rangle_S$ as the initial beam power, $c = P_0 / \, {}_S\langle \psi, a | \psi, a \rangle_S$, and

$$\frac{P(z)}{P_{\text{lin}}(z)} = \frac{\langle \psi, a | \hat{B}_{z,a} | \psi, a \rangle}{\langle \psi, a | \psi, a \rangle}, \tag{6.110}$$

$$\hat{B}_{z,a} = \hat{T}^{\dagger}_{z,a} \hat{T}_{z,a}, \tag{6.111}$$

where $P_{\text{lin}}(z) = P_0 e^{-\alpha_0 (z-a)}$, and for simplicity the initial state is represented as $\left|\psi, a; a\right\rangle_S = \left|\psi, a; a\right\rangle_I = \left|\psi, a\right\rangle$. In the thin sample limit, $\hat{T}_{z,a}$ can be represented by (6.86) and the power can be expressed more intuitively in terms of the NL absorption as

$$\frac{P(z)}{P_{\text{lin}}(z)} = \frac{\left\langle \psi, a | e^{-\int_a^z dz' \alpha' \left[I\left(\hat{\mathbf{x}}_I, z'\right) \right]} | \psi, a \right\rangle}{\langle \psi, a | \psi, a \rangle}. \tag{6.112}$$

It is thus very intuitive to understand that the optical power varies only due to the absorption terms. There is an effective absorbance profile defined by $\int_a^z dz' \alpha' \left[I\left(\hat{\mathbf{x}}_I, z'\right) \right]$ that removes energy from the beam. The average of this NL absorbance over the initial beam profile indicates the total power loss. It should be stressed that Eq. (6.110) is an exact result, while (6.112) is valid in the thin sample limit.

While NL absorption effects can be easily detected by measurements of the beam power transmitted by a NL sample, accounting for NL refraction in general is slightly more difficult. A prototypical quantity that depends on the refractive terms is the divergence angle, $\theta_{NL}^2(z) = \left\langle \frac{2\hat{\mathbf{p}}_I^2(z)}{k^2} \right\rangle$. For example, a NL sample changes the beam divergence in the Z-scan technique [158], which modulates the light transmitted by a small aperture in the far field. Obtaining an evaluable expression for the operator $\hat{\mathbf{p}}_I^2(z)$ is difficult in general. However, for thin samples it is possible to use both (6.84) and (6.112) to simplify calculations.

Notice that until now the beam was considered to have azimuthal symmetry, such that each direction of $\hat{\mathbf{x}}_I$ propagated similarly. Inside NL refractive media this is usually not true for astigmatic beams, because along each direction the beam will focus at a distinct z plane, and NL refraction is very sensitive to the irradiance profile. Therefore, squared operators as the beam width will be evaluated through tensorial products over the transverse components. Instead of computing $\langle \hat{\mathbf{x}}_I^2(z) \rangle$, it is preferred to use terms as $\langle \hat{x}_{m,I}(z)\, \hat{x}_{n,I}(z) \rangle$. Besides the tensorial generalization, another aspect becomes relevant for the following discussion. Since the operator $\hat{H}_I$ is complex, an arbitrary real-valued operator $\hat{O}_I$ will usually become complex after propagation. For example, the imaginary part of the beam width $\langle \hat{x}_{m,I}(z)\, \hat{x}_{n,I}(z) \rangle$ does not have any specific meaning. Therefore, it is enforced that only the real part of such averages is considered.

Consider the beam Transverse Irradiance Moments (TIM), defined as [164]

$$\mu_{\nu,\sigma}(z) = \left\langle \left[\hat{x}_{1,I}(z) - \langle \hat{x}_{1,I}(z) \rangle \right]^{\nu} \left[\hat{x}_{2,I}(z) - \langle \hat{x}_{2,I}(z) \rangle \right]^{\sigma} \right\rangle, \tag{6.113}$$

such that ν and σ are integers. The experimental determination of TIM requires that the field transverse profile is imaged on a camera, for example, which is a relatively straightforward procedure. Knowing the physical dimensions of the camera sensor, $\mu_{\nu,\sigma}(z)$ can be obtained. The TIM propagation is simple in linear optics, and several properties have already been established [42, 43, 160, 165]. Thus, we are interested in understanding how a thin NL sample modifies the TIM propagation.

For simplicity we assume that the beam centroid satisfies $\langle \hat{x}_{m,I}(z) \rangle = 0$ for $m = 1, 2$ at all z, and only the second order TIM will be considered

$$m_{m,n}(z) = \langle \hat{x}_{m,I}(z)\, \hat{x}_{n,I}(z) \rangle, \tag{6.114}$$

where $\nu + \sigma = 2$ in Eq. (6.113). If a thin NL optical sample is introduced at the beam line at the plane $z = a$ it is possible to use the IP results to evaluate the change in TIM due to the NL response at a detector positioned at $z = d$.

Even though Eqs. (6.113) and (6.114) are being discussed in a classical context, they have similarities with the problem of entangled continuous variables in quantum information and we now open a small parenthesis on this subject. Since $\hat{x}_{m,I}(z)$ contains both canonical conjugate operators $\hat{x}_{m,I}(a)$ and $\hat{p}_{m,I}(a)/k$, the averages in (6.113) and (6.114) contain terms as $\langle \hat{x}_{m,I}(a)\, \hat{x}_{n,I}(a) \rangle$, $\langle \hat{x}_{m,I}(a)\, \hat{p}_{n,I}(a) \rangle$, $\langle \hat{p}_{n,I}(a)\, \hat{x}_{m,I}(a) \rangle$ and $\langle \hat{p}_{m,I}(a)\, \hat{p}_{n,I}(a) \rangle$.

Each of the previous averages can be measured to determine $\langle \Delta \hat{u}^2 \rangle$ and $\langle \Delta \hat{p}^2 \rangle$, where $\hat{u} = \hat{x}_{1,I}(a) + \hat{x}_{2,I}(a)$ and $\hat{v} = \hat{p}_{1,I}(a) - \hat{p}_{2,I}(a)$. $\hat{u}$ and $\hat{v}$ are a pair of Einstein-Podolsky-Rosen type operators [166], and can be used to quantify the inseparability of bipartite continuous variable states through the Duan-Simon criteria [166, 167]. This is an important remark because inseparable (entangled) states can be used to increase the sensitivity of experimental measurements [168–170]. Therefore, even though we are not taking advantage of this relation, it may be possible to increase the sensitivity of the classical measurements specified below by developing analogies with quantum metrology.

Using (6.63) we obtain that after a thin NL sample whose thickness is $b-a$,

$$\hat{x}_{m,I}(z) = \hat{x}_{m,I}(a) + (z-b)\frac{\hat{p}_{m,I}(a)}{k}. \tag{6.115}$$

Then, the second order TIM becomes

$$m_{m,n}^{(NL)}(z) = \langle \hat{x}_{m,I}(a)\,\hat{x}_{n,I}(a) \rangle - (z-b)\langle \hat{A}_{m,n}^{+}(a) \rangle + (z-b)^2 \left\langle \frac{\hat{p}_{m,I}(a)}{k}\frac{\hat{p}_{n,I}(a)}{k} \right\rangle, \tag{6.116}$$

$$\hat{A}_{m,n}^{\pm}(a) = -\frac{\hat{x}_{m,I}(a)\,\hat{p}_{n,I}(a) \pm \hat{p}_{m,I}(a)\,\hat{x}_{n,I}(a)}{k}, \tag{6.117}$$

where the superscript NL indicates that the TIM has NL contributions in general. Notice that the NL contributions to Eq. (6.116) are implicit, because in IP the field evolves with $\hat{V}_I$, Eq. (6.108), through Eq. (6.48). To make the implicit dependence more clear, it is useful to express the averages in terms of the field before the sample, $|\psi_a\rangle$, as

$$\begin{aligned} m_{m,n}^{(NL)}(d) = &\frac{\left\langle \psi_a \left| \hat{x}_m \hat{x}_n e^{-\hat{A}^{(NL)}} \right| \psi_a \right\rangle}{\left\langle \psi_a \left| e^{-\hat{A}^{(NL)}} \right| \psi_a \right\rangle} - (d-b)\frac{\left\langle \psi_a \left| e^{-\frac{\hat{A}^{(NL)}}{2} - i\hat{\Phi}^{(NL)}} \hat{A}_{m,n}^{+} e^{-\frac{\hat{A}^{(NL)}}{2} + i\hat{\Phi}^{(NL)}} \right| \psi_a \right\rangle}{\left\langle \psi_a \left| e^{-\hat{A}^{(NL)}} \right| \psi_a \right\rangle} + \\ &(d-b)^2 \frac{\left\langle \psi_a \left| e^{-\frac{\hat{A}^{(NL)}}{2} - i\hat{\Phi}^{(NL)}} \frac{\hat{p}_m}{k}\frac{\hat{p}_n}{k} e^{-\frac{\hat{A}^{(NL)}}{2} + i\hat{\Phi}^{(NL)}} \right| \psi_a \right\rangle}{\left\langle \psi_a \left| e^{-\hat{A}^{(NL)}} \right| \psi_a \right\rangle}, \end{aligned} \tag{6.118}$$

$$\hat{A}^{(NL)} = \int_a^b dz' \alpha' \left[I\left(\hat{\mathbf{x}}, z'\right) \right], \tag{6.119}$$

$$\hat{\Phi}^{(NL)} = k_0 \int_a^b dz' n' \left[I\left(\hat{\mathbf{x}}, z'\right) \right], \tag{6.120}$$

and all transverse operators are evaluated at $z = a$ and the TIM are considered at the detector plane, $z = d$. The nonlinearly modified second order TIM, Eq. (6.118), can be expressed as a ratio to the corresponding linear values, $m_{m,n}^{(lin)}(d)$, where $\hat{A}^{(NL)} = \hat{\Phi}^{(NL)} = \hat{0}$, and also Eq. (6.112). After an exercise of operator algebra,

$$\frac{m_{m,n}^{(NL)}(d)}{m_{m,n}^{(lin)}(d)} = \frac{P_{\text{lin}}(b)}{P(b)}\left[1 + \frac{\langle\psi_a|\hat{\mathscr{P}}\hat{x}_m\hat{x}_n|\psi_a\rangle}{m_{m,n}^{(lin)}(d)\langle\psi_a|\psi_a\rangle} - \frac{(d-b)}{m_{m,n}^{(lin)}(d)}\frac{\left\langle\psi_a\left|\hat{\Delta A}_{m,n}^{+}\right|\psi_a\right\rangle}{\langle\psi_a|\psi_a\rangle} + \frac{(d-b)^2}{m_{m,n}^{(lin)}(d)}\frac{\left\langle\psi_a\left|\frac{\hat{\Delta p^2}_{m,n}}{k^2}\right|\psi_a\right\rangle}{\langle\psi_a|\psi_a\rangle}\right], \tag{6.121}$$

$$\hat{\Delta A}_{m,n}^{+} = \frac{i}{k}\left[\hat{x}_m\frac{\partial}{\partial\hat{x}_n}\left(-\frac{\hat{A}^{(NL)}}{2} + i\hat{\Phi}^{(NL)}\right) + \hat{x}_n\frac{\partial}{\partial\hat{x}_m}\left(\frac{\hat{A}^{(NL)}}{2} + i\hat{\Phi}^{(NL)}\right)\right]e^{-\hat{A}^{(NL)}} - \frac{\hat{\mathscr{P}}\hat{x}_m\hat{p}_m + \hat{p}_m\hat{x}_m\hat{\mathscr{P}}}{k}, \tag{6.122}$$

$$\frac{\hat{\Delta p^2}_{m,n}}{k^2} = \frac{\hat{p}_m}{k}\hat{\mathscr{P}}\frac{\hat{p}_n}{k} + \left(-\frac{i}{k}\right)^2\left(-\frac{1}{4}\frac{\partial\hat{A}^{(NL)}}{\partial\hat{x}_m}\frac{\partial\hat{A}^{(NL)}}{\partial\hat{x}_n} + \frac{i}{2}\frac{\partial\hat{A}^{(NL)}}{\partial\hat{x}_m}\frac{\partial\hat{\Phi}^{(NL)}}{\partial\hat{x}_n} - \frac{i}{2}\frac{\partial\hat{A}^{(NL)}}{\partial\hat{x}_n}\frac{\partial\hat{\Phi}^{(NL)}}{\partial\hat{x}_m} - \frac{\partial\hat{\Phi}^{(NL)}}{\partial\hat{x}_m}\frac{\partial\hat{\Phi}^{(NL)}}{\partial\hat{x}_n}\right)e^{-\hat{A}^{(NL)}} + e^{-\hat{A}^{(NL)}}\left(\frac{-i}{2k\hat{x}_m}\frac{\partial\hat{A}^{(NL)}}{\partial\hat{x}_m} + \frac{1}{k\hat{x}_m}\frac{\partial\hat{\Phi}^{(NL)}}{\partial\hat{x}_m}\right)\frac{\hat{x}_m\hat{p}_n}{k} + \frac{\hat{p}_m\hat{x}_n}{k}\left(\frac{i}{2k\hat{x}_n}\frac{\partial\hat{A}^{(NL)}}{\partial\hat{x}_n} + \frac{1}{k\hat{x}_n}\frac{\partial\hat{\Phi}^{(NL)}}{\partial\hat{x}_n}\right)e^{-\hat{A}^{(NL)}} \tag{6.123}$$

$$\hat{\mathscr{P}} = e^{-\hat{A}^{(NL)}} - 1, \tag{6.124}$$

where the operators $\hat{\Delta A}_{m,n}^{+}$ and $\hat{\Delta p^2}_{m,n}$ represent the NL-induced variation of the beam's effective curvature and divergence angle. The operator $\hat{\mathscr{P}}$ is an absorptive correction to the linear field averages, and is such that $\hat{\mathscr{P}} = \hat{0}$ if $\hat{A}^{(NL)} = \hat{0}$.

Equation (6.121) was obtained by considering the full tensorial response of the second order TIM, and assuming that $m_{m,n}^{(lin)}(d) \neq 0$. However, experiments often use beams whose profiles do not rotate around the propagation axis, where without loss of generality $m_{m,n}^{(lin)}(d) = 0$ if $m \neq n$ [164] if $\boldsymbol{\epsilon}_1$ and $\boldsymbol{\epsilon}_2$ are the beam principal axes, and only the diagonal terms are relevant in the problem. This simplifies considerably the previous expressions,

$$\hat{\Delta A}_{m,m}^{+} = -\frac{2\hat{x}_m}{k}\frac{\partial\hat{\Phi}^{(NL)}}{\partial\hat{x}_m}e^{-\hat{A}^{(NL)}} - \frac{\hat{\mathscr{P}}\hat{x}_m\hat{p}_m + \hat{p}_m\hat{x}_m\hat{\mathscr{P}}}{k}, \tag{6.125}$$

$$\frac{\hat{\Delta p^2}_{m,m}}{k^2} = \frac{\hat{p}_m}{k}\hat{\mathscr{P}}\frac{\hat{p}_m}{k} - \left(-\frac{i}{k}\right)^2\left[\left(\frac{1}{2}\frac{\partial\hat{A}^{(NL)}}{\partial\hat{x}_m}\right)^2 + \left(\frac{\partial\hat{\Phi}^{(NL)}}{\partial\hat{x}_m}\right)^2\right]e^{-\hat{A}^{(NL)}} + e^{-\hat{A}^{(NL)}}\left(\frac{-i}{2k\hat{x}_m}\frac{\partial\hat{A}^{(NL)}}{\partial\hat{x}_m} + \frac{1}{k\hat{x}_m}\frac{\partial\hat{\Phi}^{(NL)}}{\partial\hat{x}_m}\right)\frac{\hat{x}_m\hat{p}_m}{k} + \frac{\hat{p}_m\hat{x}_m}{k}\left(\frac{i}{2k\hat{x}_m}\frac{\partial\hat{A}^{(NL)}}{\partial\hat{x}_m} + \frac{1}{k\hat{x}_m}\frac{\partial\hat{\Phi}^{(NL)}}{\partial\hat{x}_m}\right)e^{-\hat{A}^{(NL)}} \tag{6.126}$$

In experimental terms, NL effects often occur near the focus, while the TIM are more easily evaluated for the expanded beam. For sufficiently large d,

$$m_{m,m}^{(lin)}(d) \approx (d-b)^2\frac{\left\langle\psi_a\left|\left(\hat{p}_m/k\right)^2\right|\psi_a\right\rangle}{\langle\psi_a|\psi_a\rangle}, \tag{6.127}$$

and Eq. (6.121) can be approximated as

$$\frac{m_{m,m}^{(NL)}(FF)}{m_{m,m}^{(lin)}(FF)} = \frac{P_{\text{lin}}(b)}{P(b)}\left[1+\frac{\left\langle\psi_a\left|\Delta\hat{p}^2{}_{m,m}\right|\psi_a\right\rangle}{\left\langle\psi_a\left|\left(\hat{p}_m\right)^2\right|\psi_a\right\rangle}\right], \tag{6.128}$$

where FF indicates that the detector is in the far field. The result expressed in (6.128) is remarkable, specially because it does not depend on the detector position. There is a simple general relation between linear and NL TIM along the beam principal directions in the far-field of the thin NL sample, for a material that exhibits an arbitrary absorptive and refractive response. Thus, the far-field beam width encode lots of information about the processes occurring at nonlinear materials, and $m_{m,m}^{(NL)}(FF)$ should be an interesting quantity to encode information about NL properties for spectroscopic applications. This is the fundamental principle behind the D4σ technique [171], and was also verified through experiments in sec. 6.5. An important comment regarding (6.128) is that the IP formalism as described in this chapter does not account for the temporal dependence of light, what is very important in ultrafast phenomena. The modification to be introduced for a slow-detector in the far-field consists simply in performing the temporal average of the transverse averages, or

$$\frac{\widetilde{m_{m,m}^{(NL)}(FF)}}{\widetilde{m_{m,m}^{(lin)}(FF)}} = \frac{\widetilde{P_{\text{lin}}(d)}}{\widetilde{P(d)}}\left[1+\frac{\int dt\left\langle\psi_a(t)\left|\Delta\hat{p}^2{}_{m,m}(t)\right|\psi_a(t)\right\rangle}{\int dt\left\langle\psi_a(t)\left|\left(\hat{p}_m\right)^2\right|\psi_a(t)\right\rangle}\right], \tag{6.129}$$

where the tilde represents the time averaging. Eq. (6.129) is an original result that will be applied while discussing our measurements using the D4σ method in section 6.5.

Z-scan with a Gaussian beam in third-order Kerr media

The beam profile of most lasers can be well approximated by a Gaussian profile, such that the irradiance inside the sample follows

$$I(\mathbf{r},z) = I_0\left(\frac{w_0}{w(z)}\right)^2 e^{-\frac{2\mathbf{r}^2}{w^2(z)}}, \tag{6.130}$$

where $w(z) = w_0\sqrt{1+z^2/z_R^2}$ is the beam waist at a position z when the Rayleigh length is z_R. The field at a longitudinal position z can be represented by

$$\left\langle \boldsymbol{r}|\psi,z\right\rangle = N\exp\left[ik\boldsymbol{r}^2/2q(z)\right], \tag{6.131}$$

and it is assumed that for the sample nonlinearity is $n'[I(\hat{\mathbf{x}}_I,z)] = n_2 I(\hat{\mathbf{x}}_I,z)$ for a third-order Kerr nonlinearity.

One of the most used procedures to characterize NL optical materials is applying the Z-scan technique [158], in which a thin sample of length l varies its position along the light beam propagation axis. To retrieve information about the NL refraction modulation, a thin aperture is positioned at the optical axis at a large distance d from the sample. The refractive NL modifies the beam divergence, and thus the light transmitted through the aperture.

However, the on-axis field cannot be obtained directly through the TIM, and it is necessary to calculate the field propagation from the sample to the aperture. After the thin sample, the on-axis field amplitude might be represented by $\langle \mathbf{0}|\psi,d\rangle = \int d^2\boldsymbol{r}' \langle \mathbf{0}|\hat{G}^{(0)}_{d-a}|\boldsymbol{r}'\rangle\langle \boldsymbol{r}'|\hat{T}_{b,a}|\psi,a\rangle$. For a distant aperture, it is possible to verify from (6.70) that $\langle \mathbf{0}|G^{(0)}_{d-a}|\boldsymbol{r}'\rangle \approx (i\lambda d)^{-1}$, or

$$\langle \mathbf{0}|\psi,d\rangle_S \propto \int d^2\boldsymbol{r}' \langle \boldsymbol{r}'|\hat{T}_{b,a}|\psi,a\rangle. \tag{6.132}$$

In the current example, $\hat{T}_{b,a} = \exp\left[ik_0\int_a^b dz' n_2 I(\hat{\mathbf{x}}_I,z')\right]$, and it is possible to obtain that

$$\langle \boldsymbol{r}'|\hat{T}_{z,a}|\psi,a\rangle \propto \sum_{m=0}^{\infty} \frac{\left[i\Delta\Phi_{NL}\left(\frac{w_0}{w(z)}\right)^2\right]^m}{m!} e^{-\left[\frac{2m}{w^2(z)}-\frac{ik}{2q(z)}\right]\boldsymbol{r}'^2}. \tag{6.133}$$

The integral in $d^2\boldsymbol{r}'$ in (6.132) now becomes simple. The power transmitted through the small aperture can be normalized by the transmittance when the sample is not present, or $T_{\text{z-scan}}(z) = \left|\langle \mathbf{0}|\psi,d\rangle_S\right|^2 / \left|\langle \mathbf{0}|\psi,d\rangle_S\right|^2_{n_2=0}$, where

$$T_{\text{z-scan}} = 1 + \frac{4\Delta\Phi_{NL}\frac{z}{z_0}}{\left(1+\frac{z^2}{z_0^2}\right)\left(9+\frac{z^2}{z_0^2}\right)}. \tag{6.134}$$

An important aspect of using the IP to obtain Eq. (6.134) is that the propagation problem did not require the definition of special propagation parameters, as used in [158]. The on-axis field can be calculated directly using the initial field profile, Eq. (6.131), and the sample NL response.

D4σ curves with a Gaussian beams in third-order Kerr media

Another application is to determine the theoretical curves associated the NL response of a sample using the D4σ technique [171]. Similarly to the Z-scan, in the D4σ method one also has a sample scanning along the optical axis near the light beam focus. However, while the Z-scan determines the NL refractive response by looking at the light transmitted by a small aperture, the D4σ determines the beam width using the TIM. It should be remarked that the general result (6.129) was previously unknown, and to understand the beam width variations in the D4σ experiment the authors needed a calibration of the signal with computer calculations. The D4σ technique does have several important benefits regarding Z-scan, as being immune to the beam pointing instability and being easier to correctly consider the effects due to non-symmetric Gaussian beams. The theoretical results reported below are part of our work presented in ref. [6].

It will be considered an elliptical beam described by

$$\langle \boldsymbol{r}|\psi,z\rangle = \frac{1}{N}\left(\frac{w_{0,1}}{w_1(z)}\frac{w_{0,2}}{w_2(z)}\right)^{1/2} \exp\left[-i\frac{k_0}{2M_1^2}\frac{x_1^2}{q_1} - i\frac{k_0}{2M_2^2}\frac{x_2^2}{q_2} - \frac{t^2}{\tau_p^2} + i\phi(z,t)\right], \tag{6.135}$$

where τ_p represents the pulse duration, $1/q_i = 1/R_i(z) - i2M_i^2/k_0 w_i^2(z)$ is the inverse of the beam complex curvature for a multimode beam [164], and $\phi(z,t)$ includes all phase terms without transverse dependence. For such beams, the case $M_i^2 = 1$ correspond to a pure Gaussian mode. When $M_i^2 > 1$, there is a superposition of different Hermite-Gauss modes, which leads to a beam divergence M^2 times higher than for a single mode Gaussian beam. The effective beam width and curvature are described by $w_i(z) = w_{0,i}\sqrt{1+\overline{z}_i^2}$ and $R_i(z) = z_{R,i}\overline{z}_i\left(1+1/\overline{z}_i^2\right)$ respectively, where $\overline{z}_i = \left(z - z_{c,i}\right)/z_{R,i}$. Notice that the current description may include effects of astigmatism through $z_{c,i}$, that are very important for various high power sources as titanium sapphire lasers. In order to have a consistent description of the beam evolution with the field represented by Eq. (6.135) it is necessary to resize the angles, what can be achieved by scaling the transverse derivatives and momentum operators in (6.126) and following equations as $\frac{\partial}{\partial x_i} \rightarrow M_i^2 \frac{\partial}{\partial x_i}$. The usual expressions for a single mode Gaussian field are recovered in the limit $M_i^2 = 1$.

Using (6.129) with (6.135),

$$\frac{m_{1,1}^{(NL)}(d)}{m_{1,1}^{(lin)}(d)} = 1 - \frac{\Phi_0^{(NL)}/\sqrt{2}}{\left(1+\bar{z}_2^2\right)^{1/2}} \frac{\bar{z}_1}{\left(1+\bar{z}_1^2\right)^{3/2}} + \frac{4}{9}\frac{\left(\Phi_0^{(NL)}\right)^2/\sqrt{3}}{\left(1+\bar{z}_2^2\right)} \frac{1}{\left(1+\bar{z}_1^2\right)^2}, \tag{6.136}$$

where $\Phi_0^{(NL)} = k_0 n_2 I_0 l$ is the on-axis phase-shift for a thin sample of length l, where $l \ll z_{R,i}$, and the factors of $\sqrt{2}$ and $\sqrt{3}$ are associated with the temporal averages of the NL response for slow detectors. The curve for $m_{2,2}^{(NL)}(d)/m_{2,2}^{(lin)}(d)$ is obtained by interchanging the subindices 1 and 2 in Eq. (6.136). If the beam has a circular profile, it is possible to extract the NL phase variation by analyzing the peak-to-peak value for $\Phi_0^{(NL)} \ll 1$. It is easy to verify that the peak and valley are located at $\bar{z} = \pm 1/\sqrt{3}$, and the peak-to-peak value is

$$\Delta m = 0.459\Phi_0^{(NL)}, \tag{6.137}$$

a correspondence equivalent to the one found numerically in [171]. Even for elliptical beams Eq. (6.137) is useful, as is shown in sec. (6.5).

Characterization of optical nonlinearities through the SLIM technique

The Scattered Light Imaging Method (SLIM) [172] is a technique to evaluate the light beam width near the focus by using samples that scatter the incident radiation in the direction of an imaging system [see Fig. 29(b)]. The SLIM is very practical in the determination of the beam propagation parameter, M^2, and has as an important characteristic the ability to fully characterize the beam propagation inside the sample using a single laser shot [172]. The single-shot capability is specially important for unstable laser sources which can exhibit large power fluctuations (as is common in Q-switch lasers) or beam pointing instability, and is also an useful characteristic for NL optics [5]. Since the interest in this section is in NL optics applications, it is possible to demonstrate how to use the IP formalism to describe the

NL behavior of light propagating along a thick scattering material. The theoretical results depicted below are our contribution to Ref. [5].

Experimentally it is somewhat difficult to precisely determine the beam width along the sample, because the scattered light intensity can vary strongly between the focal region and the diffraction region, what may lead to intensity saturation of the beam profile near the focus due to lack of sufficient dynamic range of the camera sensor. The saturated profile cannot be trusted for a correct determination of the beam width, since the field profile is unknown at that region. Therefore, the approach used was to consider the beam width near the diffraction region, where the NL effects initiate to become less relevant. At this region, the beam width varies almost linearly [see Fig. 29(d)] along the propagation axis z.

For this problem only the beam irradiance profile will be needed, and the Gaussian beam profile in Eq. (6.130) is used. At the experimental setup it is considered that a light beam has its waist positioned at the border of the NL sample. Since the beam widths are proportional to the square root of the respective TIM, it is possible to consider that the ratio of the beam width near the focus to the corresponding linear value is

$$\sqrt{\frac{m_{1,1}^{(NL)}(z)}{m_{1,1}^{(lin)}(z)}} \approx 1 - \frac{z}{f_{eff}}, \tag{6.138}$$

$$\frac{1}{f_{eff}} = \frac{\left\langle \psi_a \left| \frac{2\hat{x}_1}{k} \frac{\partial \hat{\Phi}^{(NL)}}{\partial \hat{x}_1} \right| \psi_a \right\rangle}{\left\langle \psi_a \left| (\hat{x}_1)^2 \right| \psi_a \right\rangle} = \frac{4\pi n_2 I_0}{g\lambda M^2} J, \tag{6.139}$$

$$J = \int_0^{z/z_R} \left(1+u^2\right)^{-2} du \approx \frac{\pi}{4}. \tag{6.140}$$

The parameter g is "introduced by hand" at the end of the calculation, and is associated with a geometrical correction factor. The IP calculates in the current approximations $g_{\mathrm{IP}} = 8$, while a numerical calculation [173] indicates that $g_{\mathrm{Numerical}} = 6.4$ agrees better with the observed experimental values [5, 173]. The $J \approx \frac{\pi}{4}$ approximation is correct within 2% for $z \geq 3z_R$. As a final remark, it should be noticed that Eq. (6.138) corresponds to Eq. (3) in Ref. [5], but using the notation of this chapter.

6.5 Experimental results

While most of this chapter discussed theoretical aspects of light propagation and the IP, it is reported below some experimental results associated with the previous discussion. The results regarding the D4σ method refer to Ref. [6], while the SLIM technique was reported in [5].

D4σ curves with Gaussian beams in third-order Kerr media

The TIM of the incident laser (amplified titanium sapphire, central wavelength $\lambda = 800$ nm, pulse duration 85 ± 5 fs) were characterized by scanning the beam profile near the focal re-

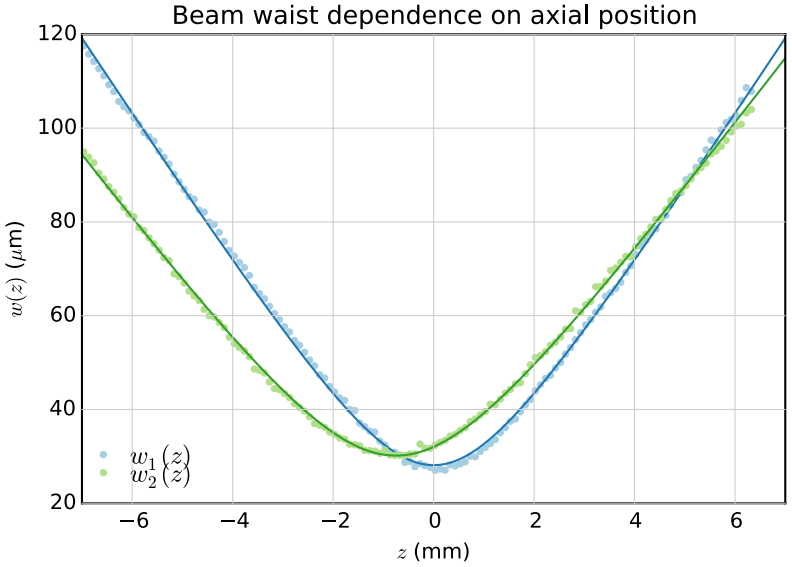

Figure 24 – Propagation of the beam width along the principal axes. The determined experimental parameters are $w_{0,1} = (28.1 \pm 0.1)$ μm, $z_{R,1} = (1.699 \pm 0.001)$ mm, $w_{0,2} = (30.1 \pm 0.1)$ μm, $z_{R,2} = (2.108 \pm 0.001)$ mm. The distance between the minima is $z_{C,1} - z_{C,2} = (0.752 \pm 0.001)$ mm. The beam propagation factors are $M_1^2 = 1.82 \pm 0.01$ and $M_2^2 = 1.69 \pm 0.01$.

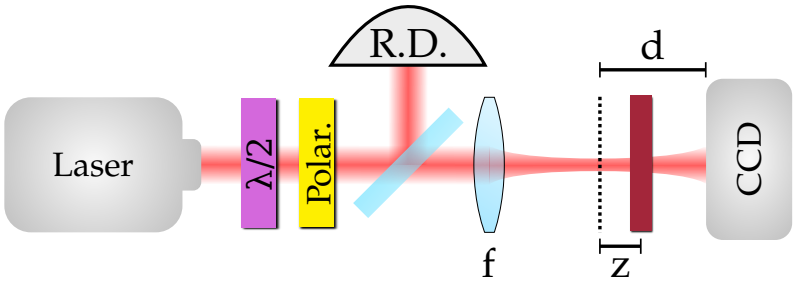

Figure 25 – Experimental setup. The camera is at a fixed distance $d \gg z_{R,i}$, for $i = 1,2$, while the sample is scanned in the focal region of a lens with focal distance $f = 15$ cm. z and d are referred to the beam waist along direction 1. A set of a $\lambda/2$ waveplate and a polarizer is used to adjust the incident power, while a reference detector (R.D.) connected to an oscilloscope monitors power fluctuations.

gion with an imaging system. For all experimental results reported in this work a standard 8 bits CMOS camera was used, and the second order TIM was calculated from the acquired images. In Fig. 24 it is shown the beam widths variation along the two transverse principal directions. Notice that the astigmatism due to the beam ellipticity implies in a non-negligible separation of the focus along x_1 and x_2 directions, and also that the M_i^2 factors differ significantly from 1.

After the beam characterization, the NL modification of the beam width due to samples of carbon dissulfide (CS_2, $l = 2.0$ mm) and fused quartz (SiO_2, $l = 3.3$ mm) was determined using the experimental setup described in Fig. 25. Typical TIM curves versus the sample position are shown in Figs. 26 and 27. It is important to notice in Figs. 26 (a) and 27 (a) that the

NL response influences differently the width along the principal directions. Since the experimental beam is elliptical, a symmetrized TIM, $m_{symm}^{(NL)}(d)/m^{(lin)}(d) = \left(m_{1,1}+m_{2,2}\right)/2$, was used. To determine the NL phase shift using the peak-to-peak width variation, Eq. (6.136) was used with our beam parameters to obtain $\Delta m_{symm} = 0.424\Phi_0^{(NL)}$. The solid lines represent the fits to the experimental data using (6.136). It can be observed that the measured TIM are well adjusted by the model, while the symmetrized versions of the data can be well represented by the curve associated with a circular beam profile. A remarkable feature is that with our experimental implementation it is possible to observe small width variations (<1%) with a relatively small noise, as can be seen in Fig. 26. Notice that the signal-to-noise ratio may improve even more by using a cooled camera sensor with higher bit depth. Also, even though the sample widths used are larger than the Rayleigh lengths, the TIM curves were not significantly distorted with respect to the thin sample approximation.

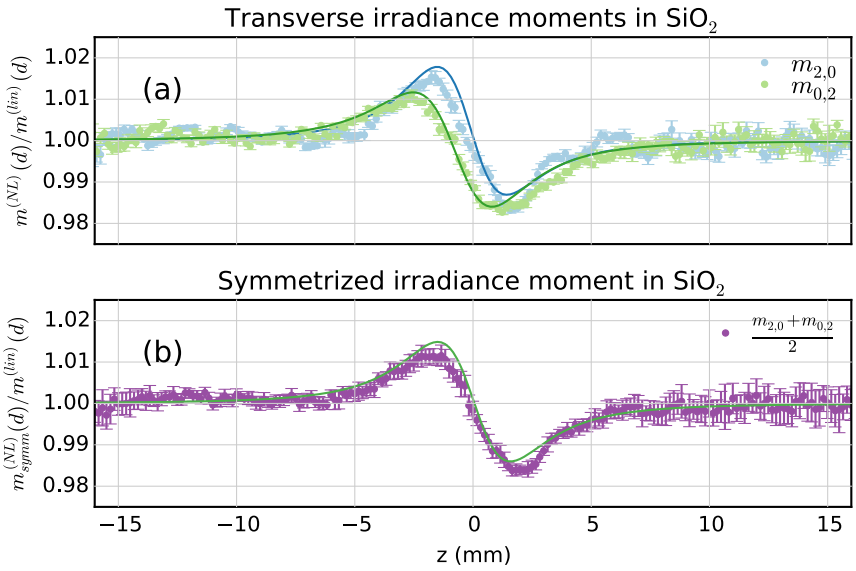

Figure 26 – Transverse irradiance moments obtained for SiO_2 at $I_0 = 11.6\,\mathrm{GW}\cdot\mathrm{cm}^{-2}$. Solid lines represent the fit by Eq. (6.136).

Figure 28 presents the dependence, as a function of intensity, of the NL phase shift determined, simultaneously, by the fits to the experimental data for the beam width along the principal axes using Eq. (6.136) and by the symmetrized peak-to-peak waist variation. According to Fig. 28, $\Delta m_{symm}/0.424$ and Φ_0^{NL} obtained from the fitted curves have a good agreement. The solid lines represent a linear fit to $\Phi_0^{NL} = k_0 n_2 I_0 l$, where n_2 is the only free parameter for each dataset. The linear behavior indicates that higher-order NL effects (such as due to fifth- and seventh-order) are not present in our results. In addition, notice that, similarly to the regular Z-scan technique, a simple peak-to-peak width analysis using Δm_{symm} determines the the sample NL phase. For slightly elliptical beams, Eq. (6.137) provides a reasonable approximation to the peak-to-peak behavior, while the exact value can be obtained after the characterization of the beam width under propagation.

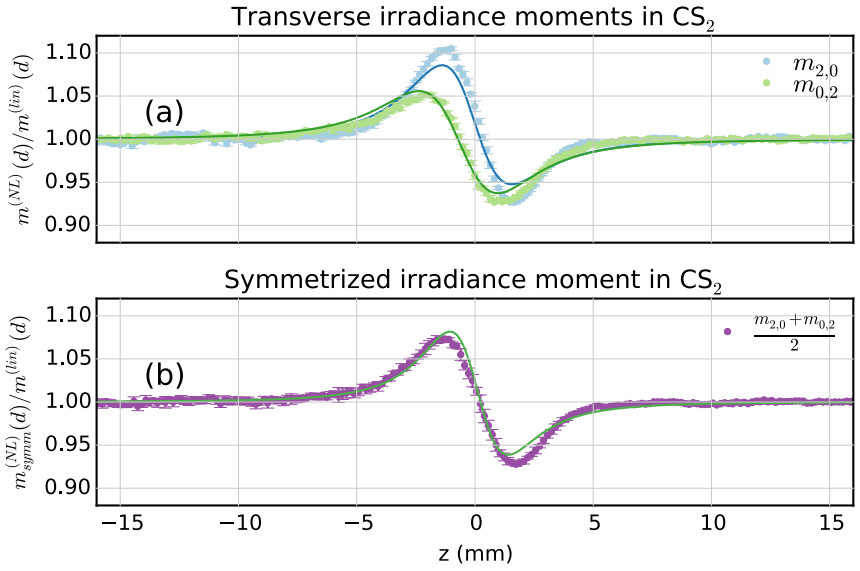

Figure 27 – Transverse irradiance moments obtained for CS_2 at $I_0 = 9.0$ GW·cm^{-2}. Solid lines represent the fit by Eq. (6.136).

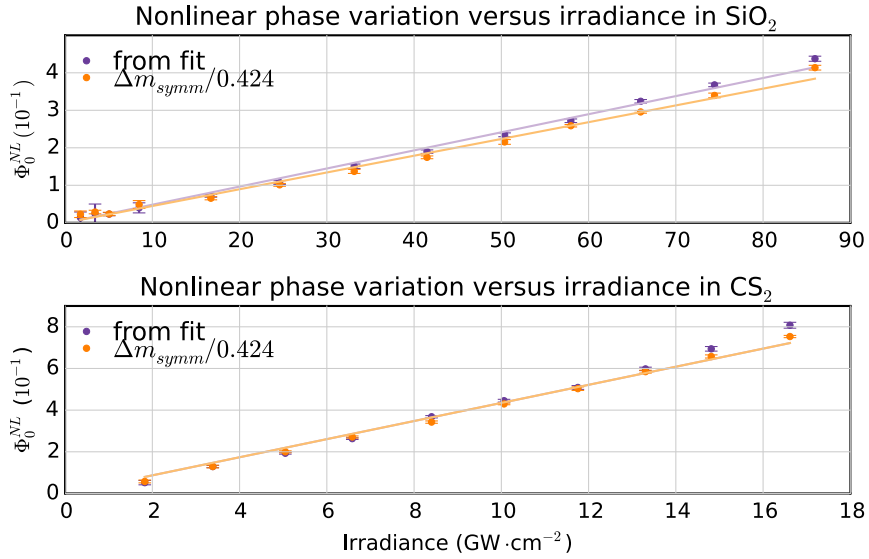

Figure 28 – NL phase variation in CS_2 and SiO_2 determined from the irradiance moments. The values determined for the NL refractive index are $n_2\,(CS_2) = (2.8 \pm 0.3) \cdot 10^{-15}\,cm^2/W$, $n_2\,(SiO_2) = (1.9 \pm 0.4) \cdot 10^{-16}\,cm^2/W$.

In summary, this work reports how to describe the effect of refractive and absorptive optical nonlinearities in the beam width, as determined by the second order irradiance moments. The theoretical results are supported by experiments performed in reference materials (CS_2 and SiO_2), where the NL refractive index was measured. The phase distortion resolution is $\lambda/700$ in our implementation, indicating that this is a sensitive technique [171,174]. Our n_2 measurements are in good agreement with the absolute measurements reported in [175,176], where $n_2\,(CS_2) = (3.0 \pm 1.0) \cdot 10^{-15}\,cm^2/W$, and $n_2\,(SiO_2) = (2.1 \pm 0.5) \cdot 10^{-16}\,cm^2/W$.

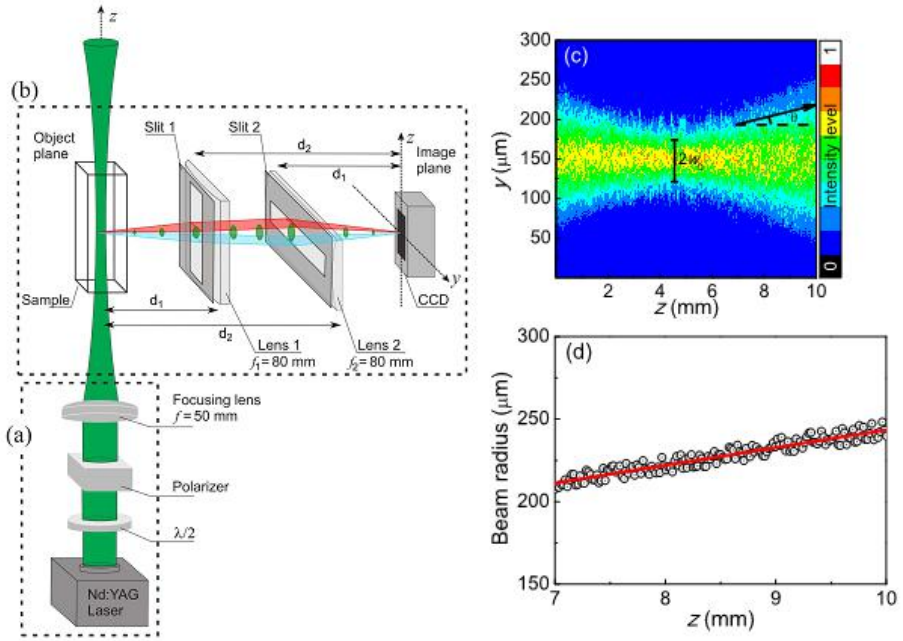

Figure 29 – SLIM operating principles. (a) a laser system with power adjustable through a set of $\lambda/2$ and a polarizer is focused at a scattering sample. (b) The scattered light is imaged in a CCD through a set of cylindrical lenses, such that the magnifications are 1/3 and 3 along and perpendicular to the beam propagation axis, respectively. (c) A typical profile of the scattered light, and (d) the beam radius determined through the TIM.

Even though a good signal-to-noise ratio was achieved in this implementation, the use of a cooled camera sensor with higher bit depth may increase even further the sensitivity of the technique, allowing NL spectroscopy of samples with weak NL response.

Characterization of optical nonlinearities through the SLIM technique

The SLIM experiments described below were performed by Kelly C. Jorge, Hans A. Garcia and Albert S. Reyna in Ref. [5]. As was previously mentioned, in SLIM the beam transverse width is determined along the beam propagation direction through a linear scattering of light inside the sample. A schematic of the experimental setup is depicted in Fig. 29(a-b). A Q-Switched mode-locked Nd:YAG laser (10 Hz, 80 ps, 532 nm) was used to verify the NL refractive index n_2 of a solution containing mainly ethanol and acetone. Silica nanoparticles were added at a small concentration (filling factor $f < 4.05 \cdot 10^{-4}$) just to provide a sufficient level of light scattering. A typical transverse profile of the scattered light can be seen in Fig. 29(c), where the waist was positioned at the center of the camera for visualization purposes. Notice that in Fig. 29(d) the beam radius increases almost linearly after a certain distance from the beam waist. Through determination of the slope associated with light propagation inside a NL sample, it is possible to know n_2 through f_{eff} in Eq. (6.138).

Since the NL refractive index is much smaller in ethanol than in acetone, $n_2^{\text{Ethanol}} \ll n_2^{\text{Acetone}}$, it is possible to adjust the effective index of the sample, n_2^{eff}, by controlling the

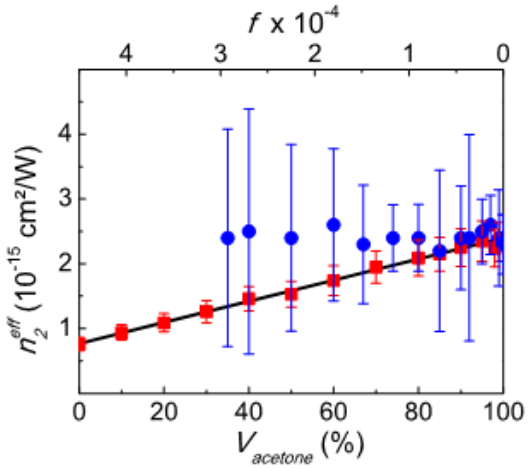

Figure 30 – A comparison between SLIM (squares) and Z-scan (circles) techniques with the predicted values of n_2^{eff} (solid) as a function of the volumetric fraction of acetone. Notice that the error bars associated with the SLIM measurements are significantly smaller than in Z-scan, indicating a higher signal to noise ratio. For $V_{acetone} < 35\%$ it was not possible to determine the sample NL response using Z-scan.

volumetric fraction of each constituent. Its worth mentioning that the NL contribution due to the scatterers is negligible because of the smallness of n_2^{Silica} and also the small filling factor f. The experimental results are shown in Fig. 30. The predicted value for n_2^{eff} (solid line in Fig. 30) was calculated through the average

$$n_2^{eff} = \frac{n_2^{\text{Ethanol}} V_{\text{Ethanol}} + n_2^{\text{Acetone}} V_{\text{Acetone}} + n_2^{\text{Silica}} V_{\text{Silica}}}{V_{\text{Ethanol}} + V_{\text{Acetone}} + V_{\text{Silica}}}, \tag{6.141}$$

where the values for $n_2^{\text{Ethanol}}, n_2^{\text{Acetone}}, n_2^{\text{Silica}}$ were obtained in the literature [37].

From the results in Fig. 30 it can be seen that the SLIM technique is very sensitive and accurate, being able to determine very small NL refractive effects. Besides that, it is remarkable that the SLIM can operate at the single-shot level. Another important characteristic of SLIM is its adequacy for scattering samples, which is often a limiting factor in other techniques [5].

6.6 Summary

In this chapter it was discussed how to use the Interaction Picture (IP), an ordinary analytical tool used in Quantum Mechanics (QM), to solve propagation problems in linear and nonlinear (NL) optics. While the calculations here were mainly based in very simple systems, it was possible to verify important connections provided by the IP. For example, it was showed that for simple optical elements the propagation of the IP transverse position and momentum (or angle) operators can be described through the familiar formalism of ABCD matrices from geometrical optics. This is important because the propagation in the geometrical optics regime is much simpler than in a wave optics approach, and the IP corresponds to a full

paraxial wave solution for the propagation problem. As a remarkable result in the context of linear optics, the general Siegman's formulas to characterize the beam width were simply obtained from the square of the IP position operator.

In QM, the IP is specially adequate for interacting systems, and it was showed here that in optics the IP can be a valuable analytical tool for NL problems. For instance, it was possible to describe the light behavior in Z-scan [158], D4σ [6, 171] and SLIM [5] experiments. This indicates the importance of this approach for NL optical problems in general, specially with respect to NL refractive media. Some experimental efforts were already performed to verify the IP predictions, as in [5, 6], but there are several indicatives that the insights provided by the IP can be exploited in other NL spectroscopy applications.

It should be stressed that the formalism discussed in this chapter describes light in the classical approximation. The tools of QM were used here to solve the paraxial wave optics propagation problem. Important improvements for the future are the full solution of the Maxwell equations using this formalism, a careful discussion of the action of operators near boundaries between two materials, the description of extended absorptive media and the effect of apertures, the inclusion of operators in the temporal domain [156], and the description of optical coherence effects.

Finally, we remark that the operator formalism can be used directly to find analogies with QM. It was previously stated that the TIM, Eq. (6.114), are directly related with the Duan-Simon criteria for continuous variable entanglement [166, 167]. Therefore, another set of important perspectives for this work consists in developing analogies between classical optics and QM. For example, it should be fruitful to perform studies on geometrical and holonomic phases, the adiabatic theorem, weak measurements and quantum metrology.

7 Summary and perspectives

This thesis contains two main sets of results. First, as described in chapters 4 and 5, it is possible to adjust the dark intensity profile of a light beam containing optical vortices (OV) by distributing Topological Charges (TCs) over the beam transverse profile. Several geometries were obtained, as a dark line, corner and a triangle, as reported in [1]. However, to adequately characterize the TC distributions a more general approach was developed in [2] through the experimental measurement of the field amplitude and phase profiles. It was determined for the TC distributions along a line, a corner and a triangle that for all distributions the TC is equal to the value designed in the phase mask, while the beam OAM is slightly reduced due to the reduced azimuthal phase variation between spatially separated TCs with the same TC signal. Further work indicated that such TC distributions can be described by a relationship analogous to the two-dimensional (2D) electrostatic potential, which was called the Topological Potential (TP) [3]. Several mathematical properties of the TP were studied, and it was also verified the existence of TC multipoles and a 2D radial TC distribution. It was shown that through the TP it is possible to express a large variety of fields containing complex compositions of OV. The use of the TP allows the design of OAM beams for various purposes, and in principle can be of interest for many applications where singular wavefronts are applied. For example, the TP can be important in the design of optical tweezers [27], laser traps [88] or atom guides [140]. The TC multipoles form a complete basis (Fourier), and may be applied for data transfer using classical light [142] or also in the quantum regime [26]. However, an important step that still needs to be addressed is the propagation of the TP solutions, since the discussion within sec. 4.3 is restricted to the plane $z = 0$. For example, it may be possible to find a set of constraints that the TC distribution must satisfy to ensure that the field profile remains simply related between different z planes. It is also highly desirable to have expressions that indicate how to optimize the TP solutions for each application, as the transverse forces in an optical tweezer.

Second, the set of results presented in chapter 6 are related to properties of light propagation in the paraxial regime using a formalism based on quantum mechanics-like operators. The introduction of the Interaction Picture for wavefront propagation [4] indicates that this approach can be applied for a large variety of optical systems. It was obtained that for simple paraxial optical systems the position and momentum operators propagate according to ABCD matrices in sec. 6.4. Also, the IP was used to describe the beam width inside a sample with a nonlinear refractive index in [5] and also to understand the propagation of the beam width after a nonlinear sample in [6]. Since light propagation in nonlinear materials introduces intrinsic aberrations, the IP should also be adequate for example to describe light propagation through optical elements containing spherical aberrations or astigmatism. From a fundamental aspect, it should be remarked that since the IP is a full wave optics solu-

tion but intrinsically related to geometrical optics methods, the IP can be useful in problems where geometrical optics solutions are simple but the wave solution is difficult, as in the problem of caustics [177]. There are several improvements to be added to the results presented in chapter 6. For instance, it would be very useful to include operators in the temporal domain [156] and spatial and temporal dispersion, to calculate the propagation of optical pulses in nonlinear materials. Other important improvements would be the inclusion of polarization effects, and the solution to the full wave equation without the paraxial approximation. The inclusion of polarization seems to be possible by introduction of a spinorial notation, while a full wave solution seems harder because of the second order derivative along z among other issues. The spatial coherence was not considered, but it should be possible to include its effects through a density matrix representation for the field and the operators.

References

1 AMARAL, A. M.; FALCÃO-FILHO, E. L.; ARAÚJO, C. B. de. Shaping optical beams with topological charge. **Opt. Lett.**, v. 38, p. 1579–1581, 2013.

2 AMARAL, A. M.; FALCÃO-FILHO, E. L.; ARAÚJO, C. B. de. Characterization of topological charge and orbital angular momentum of shaped optical vortices. **Opt. Express**, v. 22, p. 30315–30324, 2014.

3 AMARAL, A. M.; FALCÃO-FILHO, E. L.; ARAÚJO, C. B. de. Optical vortices: the concept of topological potential and analogies with two-dimensional electrostatics. submitted.

4 AMARAL, A. M.; FALCÃO-FILHO, E. L.; ARAÚJO, C. B. de. Using the interaction picture in paraxial wave and geometrical optics problems. in preparation.

5 JORGE, K. C. et al. Measurements of the nonlinear refractive index in scattering media using the scattered light imaging method - SLIM. **Opt. Express**, v. 23, p. 19512–19521, 2015.

6 AMARAL, A. M. et al. D4σ curves described analytically through propagation analysis of transverse irradiance moments. **Opt. Lett.**, v. 41, n. 9, p. 2081–2084, 2016.

7 HELL, S. W. Far-field optical nanoscopy. **Science**, v. 316, n. 5828, p. 1153–1158, 2007.

8 The LIGO Scientific Collaboration et al. Advanced ligo. **Class. Quantum Grav.**, v. 32, n. 7, p. 074001, 2015.

9 HELL, S. W. Nanoscopy with focused light (Nobel lecture). **Angew. Chem. Int. Ed.**, v. 54, n. 28, p. 8054–8066, 2015.

10 SCHRÖDINGER, E. Are there quantum jumps?: Part II. **Br. J. Philos. Sci.**, III, n. 11, p. 233–242, 1952.

11 MOERNER, W. E. Single-molecule spectroscopy, imaging, and photocontrol: Foundations for super-resolution microscopy (Nobel lecture). **Angew. Chem. Int. Ed.**, v. 54, n. 28, p. 8067–8093, 2015.

12 MOERNER, W. E.; KADOR, L. Optical detection and spectroscopy of single molecules in a solid. **Phys. Rev. Lett.**, v. 62, p. 2535–2538, 1989.

13 BETZIG, E. Proposed method for molecular optical imaging. **Opt. Lett.**, v. 20, n. 3, p. 237–239, 1995.

14 BETZIG, E. Single molecules, cells, and super-resolution optics (Nobel lecture). **Angew. Chem. Int. Ed.**, v. 54, n. 28, p. 8034–8053, 2015.

15 ABBOTT, B. P. et al. Observation of gravitational waves from a binary black hole merger. **Phys. Rev. Lett.**, v. 116, p. 061102, 2016.

16 NYE, J.; BERRY, M. Dislocations in wave trains. **Proc. R. Soc. London A**, v. 336, p. 165–190, 1974.

17 DENNIS, M. R.; O'HOLLERAN, K.; PADGETT, M. J. Chapter 5 singular optics: Optical vortices and polarization singularities. In: WOLF, E. (Ed.). [S.l.]: Elsevier, 2009, (Progress in Optics, v. 53). p. 293 – 363.

18 BERKHOUT, G. C. G.; BEIJERSBERGEN, M. W. Measuring optical vortices in a speckle pattern using a multi-pinhole interferometer. **Opt. Express**, v. 18, n. 13, p. 13836–13841, 2010.

19 ZHAN, Q. Cylindrical vector beams: from mathematical concepts to applications. **Adv. Opt. Photon.**, OSA, v. 1, p. 1–57, 2009.

20 KOGELNIK, H.; LI, T. Laser beams and resonators. **Appl. Opt.**, OSA, v. 5, p. 1550–1567, 1966.

21 ALLEN, L. et al. Orbital angular momentum of light and the transformation of Laguerre-Gaussian laser modes. **Phys. Rev. A**, v. 45, n. 11, p. 8185–8189, 1992.

22 BETH, R. A. Mechanical detection and measurement of the angular momentum of light. **Phys. Rev.**, v. 50, p. 115–125, 1936.

23 YAO, A. M.; PADGETT, M. J. Orbital angular momentum: origins, behavior and applications. **Adv. Opt. Photon.**, v. 3, n. 2, p. 161–204, 2011.

24 BOZINOVIC, N. et al. Terabit-scale orbital angular momentum mode division multiplexing in fibers. **Science**, v. 340, n. 6140, p. 1545–1548, 2013.

25 MIRHOSSEINI, M. et al. Efficient separation of the orbital angular momentum eigenstates of light. **Nature comm.**, v. 4, p. 2781, 2013.

26 VINCENZO, D. et al. Complete experimental toolbox for alignment-free quantum communication. **Nature Comm.**, v. 3, p. 961, 2012.

27 DHOLAKIA, K.; ČIŽMÁR, T. Shaping the future of manipulation. **Nature Photon.**, v. 5, p. 335, 2011.

28 CHEN, M. et al. Dynamics of microparticles trapped in a perfect vortex beam. **Opt. Lett.**, v. 38, p. 4919–4922, 2013.

29 AMARAL, A. M. **Nanoestruturas Plasmônicas para Aplicações em Ótica Não Linear**. Dissertação (Mestrado) — Universidade Federal de Pernambuco, 2012.

30 BARREIRO, S. et al. Spectroscopic observation of the rotational Doppler effect. **Phys. Rev. Lett.**, v. 97, p. 113601, 2006.

31 KLIMOV, V. V. et al. Mapping of focused Laguerre-Gauss beams: The interplay between spin and orbital angular momentum and its dependence on detector characteristics. **Phys. Rev. A**, v. 85, p. 053834, 2012.

32 KASPERCZYK, M. et al. Excitation of magnetic dipole transitions at optical frequencies. **Phys. Rev. Lett.**, v. 114, p. 163903, 2015.

33 DEGIORGI, S. V. B. **Estudo de Efeitos Coerentes e Geração de Luz com Momento Angular Orbital via Mistura de Quatro Ondas em Átomos Frios de Césio**. Tese (Doutorado) — Universidade Federal de Pernambuco, 2005.

34 MORETTI, D. **Armazenamento e Manipulação de Luz em Coerências Zeeman de Átomos Frios**. Tese (Doutorado) — Universidade Federal de Pernambuco, 2009.

35 OLIVEIRA, R. A. de. **Armazenamento e Manipulação de Luz em Coerências Zeeman de Átomos de Césio Frios e Superradiância no Regime de Fóton Único**. Tese (Doutorado) — Universidade Federal de Pernambuco, 2014.

36 GIOVANNINI, D. et al. Spatially structured photons that travel in free space slower than the speed of light. **Science**, v. 347, n. 6224, p. 857–860, 2015.

37 BOYD, R. W. **Nonlinear Optics**. [S.l.]: Academic Press, 2008.

38 HICKMANN, J. M. et al. Unveiling a truncated optical lattice associated with a triangular aperture using light's orbital angular momentum. **Phys. Rev. Lett.**, v. 105, p. 053904, 2010.

39 GLOGE, D.; MARCUSE, D. Formal quantum theory of light rays. **J. Opt. Soc. Am.**, v. 59, p. 1629–1631, 1969.

40 SAKURAI, J. J. **Modern Quantum Mechanics**. [S.l.]: Addison-Wesley Publishing Company, 1994.

41 SCHWARTZ, M. D. **Quantum Field Theory and the Standard Model**. [S.l.]: Cambridge Univ. Press, 2013.

42 SIEGMAN, A. E. New developments in laser resonators. **Proc. SPIE**, v. 1224, p. 2–14, 1990.

43 SIEGMAN, A. E. Defining the effective radius of curvature for a nonideal optical beam. **IEEE J. Quant. Electron.**, v. 27, n. 5, p. 1146–1148, 1991.

44 SHEN, Y. R. **The Principles of Nonlinear Optics**. [S.l.]: Wiley-Interscience, 2002.

45 KASSAB, L. R. P.; SILVA, D. S. da; ARAÚJO, C. B. de. Influence of metallic nanoparticles on electric-dipole and magnetic-dipole transitions of Eu^{3+} doped germanate glasses. **J. Appl. Phys.**, v. 107, n. 11, p. 113506, 2010.

46 ROXWORTHY, B. J.; TOUSSAINT, K. C. Simultaneously tuning the electric and magnetic plasmonic response using capped bi-metallic nanoantennas. **Nanoscale**, v. 6, p. 2270–2274, 2014.

47 LANDAU, L. D.; LIFSHITS, E. M.; PITAEVSKII, L. P. **Electrodynamics of Continuous Media**. [S.l.]: Pergamon Press, 1984.

48 BIALYNICKI-BIRULA, I.; BIALYNICKA-BIRULA, Z. The role of the Riemann-Silberstein vector in classical and quantum theories of electromagnetism. **J. Phys. A: Math. Theor.**, v. 46, n. 5, p. 053001, 2013.

49 JACKSON, J. D. **Classical Electrodynamics**. [S.l.]: John-Wiley and Sons, 1999.

50 LAX, M.; LOUISELL, W. H.; MCKNIGHT, W. B. From Maxwell to paraxial wave optics. **Phys. Rev. A**, v. 11, p. 1365–1370, 1975.

51 YARIV, A.; YEH, P. **Photonics: optical electronics in modern communications**. [S.l.]: Oxford Univ. Press, 2007.

52 AIELLO, A. et al. Transverse angular momentum and geometric spin Hall effect of light. **Phys. Rev. Lett.**, v. 103, p. 100401, 2009.

53 KONG, L.-J. et al. Effects of orbital angular momentum on the geometric spin Hall effect of light. **Phys. Rev. A**, v. 85, p. 035804, 2012.

54 SOTO-CRESPO, J. M.; AKHMEDIEV, N. Description of the self-focusing and collapse effects by a modified nonlinear Schrödinger equation. **Opt. Commun.**, v. 101, p. 223–230, 1993.

55 ABRAMOCHKIN, E.; VOLOSTNIKOV, V. Spiral-type beams. **Opt. Commun.**, v. 102, p. 336–350, 1993.

56 ABRAMOCHKIN, E. G.; VOLOSTNIKOV, V. G. Spiral light beams. **Phys.-Usp.**, v. 47, p. 1177–1203, 2004.

57 FENG, S.; WINFUL, H. G. Physical origin of the Gouy phase shift. **Opt. Lett.**, v. 26, n. 8, p. 485–487, 2001.

58 FALCÃO-FILHO, E. L. **Propriedades Não Lineares de Nanocompósitos e Vidros Especiais**. Tese (Doutorado) — Universidade Federal de Pernambuco, 2005.

59 SIEGMAN, A. E. **Lasers**. [S.l.]: University Science Books, 1986.

60 SALEH, B. E. A.; TEICH, M. C. **Fundamentals of Photonics**. [S.l.]: Wiley-Interscience, 2007.

61 MAGNI, V.; CERULLO, G.; SILVESTRI, S. D. ABCD matrix analysis of propagation of Gaussian beams through Kerr media. **Opt. Commun.**, v. 96, p. 348 – 355, 1993.

62 GOLDSTEIN, H.; POOLE, C.; SAFKO, J. **Classical Mechanics**. [S.l.]: Addison-Wesley Publishing Company, 2000.

63 BOIVIN, A.; DOW, J.; WOLF, E. Energy flow in the neighborhood of the focus of a coherent beam. **J. Opt. Soc. Am.**, v. 57, p. 1171–1175, 1967.

64 BANZER, P. et al. The photonic wheel - demonstration of a state of light with purely transverse angular momentum. **J. Eur. Opt. Soc., Rap. Publ.**, v. 8, p. 13032, 2013.

65 MONTEIRO, P. B.; NETO, P. A. M.; NUSSENZVEIG, H. M. Angular momentum of focused beams: Beyond the paraxial approximation. **Phys. Rev. A**, v. 79, p. 033830, 2009.

66 GOODMAN, J. W. **Introduction to Fourier Optics**. [S.l.]: McGraw-Hill Companies, Inc., 1996.

67 BECKERS, J. M. Adaptive optics for astronomy: Principles, performance, and applications. **Annu. Rev. Astron. Astrophys.**, v. 31, n. 1, p. 13–62, 1993.

68 BOOTH, M. J. Adaptive optics in microscopy. **Phil. Trans. R. Soc. A**, v. 365, n. 1861, p. 2829–2843, 2007.

69 BACKER, A. S.; MOERNER, W. E. Extending single-molecule microscopy using optical Fourier processing. **J. Phys. Chem. B**, v. 118, n. 28, p. 8313–8329, 2014.

70 GABOR, D. A new microscopic principle. **Nature**, v. 161, p. 777–778, 1948.

71 GABOR, D. Microscopy by reconstructed wave-fronts. **Proc. R. Soc. London A**, v. 197, p. 454–487, 1949.

72 GABOR, D. Nobel lecture: Holography, 1948-1971. **Nobelprize.org**, 1971.

73 MIRHOSSEINI, M. et al. Rapid generation of light beams carrying orbital angular momentum. **Opt. Express**, v. 21, n. 25, p. 30196–30203, 2013.

74 WHYTE, G.; COURTIAL, J. Experimental demonstration of holographic three-dimensional light shaping using a Gerchberg-Saxton algorithm. **New J. Phys.**, v. 7, n. 1, p. 117, 2005.

75 BRIF, C.; CHAKRABARTI, R.; RABITZ, H. Control of quantum phenomena: past, present and future. **New J. Phys.**, v. 12, n. 7, p. 075008, 2010.

76 KIRK, J. P.; JONES, A. L. Phase-only complex-valued spatial filter. **J. Opt. Soc. Am.**, v. 61, n. 8, p. 1023–1028, 1971.

77 ARRIZÓN, V. et al. Pixelated phase computer holograms for the accurate encoding of scalar complex fields. **J. Opt. Soc. Am. A**, v. 24, n. 11, p. 3500–3507, 2007.

78 BOLDUC, E. et al. Exact solution to simultaneous intensity and phase encryption with a single phase-only hologram. **Opt. Lett.**, v. 38, n. 18, p. 3546–3549, 2013.

79 BERRY, M. V. Optical vortices evolving from helicoidal integer and fractional phase steps. **J. Opt. A: Pure Appl. Opt.**, v. 6, p. 259–268, 2004.

80 GÖTTE, J. et al. Quantum formulation of fractional orbital angular momentum. **J. Mod. Opt.**, v. 54, p. 1723–1738, 2007.

81 WALT, S. van der; COLBERT, S.; VAROQUAUX, G. The NumPy array: A structure for efficient numerical computation. **Comput. Sci. Eng.**, v. 13, n. 2, p. 22–30, 2011.

82 PÉREZ, F.; GRANGER, B. IPython: A system for interactive scientific computing. **Comput. Sci. Eng.**, v. 9, n. 3, p. 21–29, 2007.

83 FREUND, I. Optical vortices in Gaussian random wave fields: statistical probability densities. **J. Opt. Soc. Am. A**, v. 11, n. 5, p. 1644–1652, 1994.

84 BERRY, M. V.; DENNIS, M. R. Phase singularities in isotropic random waves. **Proc. R. Soc. London A**, v. 456, n. 2001, p. 2059–2079, 2000.

85 WANG, W. et al. Experimental investigation of local properties and statistics of optical vortices in random wave fields. **Phys. Rev. Lett.**, v. 94, p. 103902, 2005.

86 WANG, W. et al. Optical vortex metrology for nanometric speckle displacement measurement. **Opt. Express**, v. 14, n. 1, p. 120–127, 2006.

87 GRIER, D. G. A revolution in optical manipulation. **Nature**, v. 424, n. 6950, p. 810–816, 2003.

88 JAOUADI, A. et al. Bose-Einstein condensation in dark power-law laser traps. **Phys. Rev. A**, v. 82, p. 023613, 2010.

89 KIM, H. et al. Synthesis and dynamic switching of surface plasmon vortices with plasmonic vortex lens. **Nano Lett.**, v. 10, n. 2, p. 529–536, 2010.

90 TOYODA, K. et al. Using optical vortex to control the chirality of twisted metal nanostructures. **Nano Lett.**, v. 12, n. 7, p. 3645–3649, 2012.

91 GUO, C. et al. Generation of optical vortices with arbitrary shape and array via helical phase spatial filtering. **Opt. Commun.**, v. 259, p. 449–454, 2006.

92 CURTIS, J. E.; GRIER, D. G. Modulated optical vortices. **Opt. Lett.**, v. 28, n. 11, p. 872–874, 2003.

93 NAKAHARA, M. **Geometry, Topology and Physics**. [S.l.]: Taylor & Francis, 2003.

94 CHÁVEZ-CERDA, S. et al. Holographic generation and orbital angular momentum of high-order Mathieu beams. **J. Opt. B: Quantum and Semiclass. Opt.**, v. 4, p. S52–S57, 2002.

95 ROUX, F. S. Distribution of angular momentum and vortex morphology in optical beams. **Opt. Commun.**, v. 242, p. 45–55, 2004.

96 BEKSHAEV, A. Y.; VASNETSOV, M. V.; SOSKIN, M. S. Description of the morphology of optical vortices using the orbital angular momentum and its components. **Opt. Spectrosc.**, v. 100, p. 910–915, 2006.

97 BIALYNICKI-BIRULA, I.; BIALYNICKA-BIRULA, Z. Why photons cannot be sharply localized. **Phys. Rev. A**, American Physical Society, v. 79, p. 032112, 2009.

98 BERRY, M. V. Optical currents. **J. Opt. A: Pure Appl. Opt.**, v. 11, p. 094001, 2009.

99 PUGATCH, R. et al. Topological stability of stored optical vortices. **Phys. Rev. Lett.**, v. 98, n. 20, p. 203601, 2007.

100 ROUX, F. S. Coupling of noncanonical optical vortices. **J. Opt. Soc. Am. B**, v. 21, p. 664–670, 2004.

101 SMYTHE, W. R. **Static and Dynamic Electricity**. [S.l.]: McGraw-Hill Book Company, Inc., 1950.

102 PANOFSKY, W. K. H.; PHILLIPS, M. **Classical Electricity and Magnetism**. [S.l.]: Addison-Wesley Publishing Company, Inc., 1962.

103 ABRAMOCHKIN, E.; VOLOSTNIKOV, V. Spiral-type beams: optical and quantum aspects. **Opt. Commun.**, v. 125, n. 4, p. 302–323, 1996.

104 SCHAKEL, A. M. J. **Boulevard of Broken Symmetries**. [S.l.]: World Scientific, 2008.

105 RUDIN, W. **Real and Complex Analysis**. [S.l.]: McGraw-Hill Book Company, Inc., 1970.

106 GROSSMAN, M.; KATZ, R. **Non-Newtonian Calculus**. [S.l.]: Lee Press, 1972.

107 DOLLARD, J. D.; FRIEDMAN, C. N. Product integrals and the Schrödinger equation. **J. Math. Phys.**, v. 18, n. 8, p. 1598–1607, 1977.

108 MORA, M.; CÓRDOVA-LEPE, F.; DEL-VALLE, R. A non-Newtonian gradient for contour detection in images with multiplicative noise. **Pattern Recogn. Lett.**, v. 33, n. 10, p. 1245 – 1256, 2012.

109 FLORACK, L.; ASSEN, H. van. Multiplicative calculus in biomedical image analysis. **J. Math. Imaging Vis.**, v. 42, n. 1, p. 64–75, 2012.

110 LEVIN, B. J. **Distribution of zeros of entire functions**. [S.l.]: American Mathematical Society, 1964.

111 GRADSHTEYN, I. S.; RYZHIK, I. M. **Table of integrals, series and products**. [S.l.]: Academic Press, 2007.

112 GUNNING, R. C.; ROSSI, H. **Analytic function of several complex variables**. [S.l.]: Prentice-Hall, Inc., 1965.

113 TAKEDA, M.; INA, H.; KOBAYASHI, S. Fourier-transform method of fringe-pattern analysis for computer-based topography and interferometry. **J. Opt. Soc. Am.**, v. 72, p. 156–160, 1982.

114 FIENUP, J. R. Phase retrieval algorithms: a comparison. **Appl. Opt.**, v. 21, n. 15, p. 2758–2769, 1982.

115 ANDO, T. et al. Structure of optical singularities in coaxial superpositions of Laguerre-Gaussian modes. **J. Opt. Soc. Am. A**, v. 27, n. 12, p. 2602–2612, 2010.

116 FIENUP, J. R. Phase retrieval algorithms: a personal tour [invited]. **Appl. Opt.**, v. 52, n. 1, p. 45–56, 2013.

117 BERKHOUT, G.; BEIJERSBERGEN, M. Method for probing the orbital angular momentum of optical vortices in electromagnetic waves from astronomical objects. **Phys. Rev. Lett.**, v. 101, n. 10, p. 100801, 2008.

118 SOSKIN, M. et al. Topological charge and angular momentum of light beams carrying optical vortices. **Phys. Rev. A**, v. 56, p. 4064–4075, 1997.

119 LEACH, J.; YAO, E.; PADGETT, M. J. Observation of the vortex structure of a non-integer vortex beam. **New J. Phys.**, v. 6, p. 71, 2004.

120 SCHULZE, C. et al. Measurement of the orbital angular momentum density of light by modal decomposition. **New J. Phys.**, v. 15, p. 073025, 2013.

121 FERREIRA, Q. S. et al. Fraunhofer diffraction of light with orbital angular momentum by a slit. **Opt. Lett.**, v. 36, n. 16, p. 3106–3108, 2011.

122 AMBUJ, A.; VYAS, R.; SINGH, S. Diffraction of Laguerre-Gauss vortex beams by regular polygons. In: **Frontiers in Optics 2014**. [S.l.]: Optical Society of America, 2014. p. JTu3A.10.

123 AMBUJ, A.; VYAS, R.; SINGH, S. Diffraction of orbital angular momentum carrying optical beams by a circular aperture. **Opt. Lett.**, v. 39, n. 19, p. 5475–5478, 2014.

124 SILVA, J. G. et al. Unveiling square and triangular optical lattices: a comparative study. **Opt. Lett.**, v. 39, n. 4, p. 949–952, 2014.

125 ARAUJO, L. E. E. de; ANDERSON, M. E. Measuring vortex charge with a triangular aperture. **Opt. Lett.**, v. 36, p. 787–789, 2011.

126 INDEBETOUW, G. Optical vortices and their propagation. **J. Mod. Opt.**, v. 40, n. 1, p. 73–87, 1993.

127 ROZAS, D.; LAW, C. T.; SWARTZLANDER, J. G. A. Propagation dynamics of optical vortices. **J. Opt. Soc. Am. B**, v. 14, n. 11, p. 3054–3065, 1997.

128 BAUMANN, S. M. et al. Propagation dynamics of optical vortices due to Gouy phase. **Opt. Express**, v. 17, n. 12, p. 9818–9827, 2009.

129 KUMAR, A.; VAITY, P.; SINGH, R. P. Crafting the core asymmetry to lift the degeneracy of optical vortices. **Opt. Express**, v. 19, n. 7, p. 6182–6190, 2011.

130 JESACHER, A. et al. Optical tweezers of programmable shape with transverse scattering forces. **Opt. Commun.**, v. 281, n. 8, p. 2207–2212, 2008.

131 AHNERT, K.; ABEL, M. Numerical differentiation of experimental data: local versus global methods. **Comput. Phys. Commun.**, v. 177, p. 764–774, 2007.

132 DENNIS, M. Rows of optical vortices from elliptically perturbing a high-order beam. **Opt. Lett.**, v. 31, p. 1325–1327, 2006.

133 ROUX, F. Dynamical behavior of optical vortices. **J. Opt. Soc. Am. B**, v. 12, p. 1215–1221, 1995.

134 MALEEV, I.; SWARTZLANDER, G. Composite optical vortices. **J. Opt. Soc. Am. B**, v. 20, p. 1169 – 1176, 2003.

135 ALONZO, C. A.; RODRIGO, P. J.; GLÜCKSTAD, J. Helico-conical optical beams: a product of helical and conical phase fronts. **Opt. Express**, v. 13, n. 5, p. 1749–1760, 2005.

136 DARIA, V. R.; PALIMA, D. Z.; GLÜCKSTAD, J. Optical twists in phase and amplitude. **Opt. Express**, v. 19, n. 2, p. 476–481, 2011.

137 DESYATNIKOV, A. S.; SUKHORUKOV, A. A.; KIVSHAR, Y. S. Azimuthons: spatially modulated vortex solitons. **Phys. Rev. Lett.**, v. 95, n. 20, p. 203904, 2005.

138 CHENG-WEI, Q. et al. Engineering light-matter interaction for emerging optical manipulation applications. **Nanophotonics**, v. 3, p. 181–, 2014.

139 BRASSELET, E. et al. Topological shaping of light by Closed-Path nanoslits. **Phys. Rev. Lett.**, v. 111, p. 193901, 2013.

140 RHODES, D. P. et al. Atom guiding along high order Laguerre-Gaussian light beams formed by spatial light modulation. **J. Mod. Opt.**, v. 53, p. 547, 2006.

141 ROUX, F. Spatial evolution of the morphology of an optical vortex dipole. **Opt. Commun.**, v. 236, p. 433, 2004.

142 WANG, J. et al. Terabit free-space data transmission employing orbital angular momentum multiplexing. **Nature Photon.**, v. 6, p. 488, 2012.

143 WANG, L.; ZHENG, W. The effect of atmospheric turbulence on the propagation properties of optical vortices formed by using coherent laser beam arrays. **J. Opt. A: Pure Appl. Opt.**, v. 11, p. 065703, 2009.

144 BORN, M.; WOLF, E. **Principles of Optics**. [S.l.]: Cambridge Univ. Press, 1999.

145 BREHM, J. J.; MULLIN, W. J. **Introduction to the Structure of Matter: A Course in Modern Physics**. [S.l.]: John Wiley & Sons, 1989.

146 BROGLIE, L.-V. de. **On the Theory of Quanta**. Tese (Doutorado) — University of Paris, 1924.

147 MONTGOMERY, W. D. Algebraic formulation of diffraction applied to self imaging. **J. Opt. Soc. Am.**, v. 58, n. 8, p. 1112–1124, 1968.

148 NAZARATHY, M.; SHAMIR, J. Fourier optics described by operator algebra. **J. Opt. Soc. Am.**, v. 70, n. 2, p. 150–159, 1980.

149 STOLER, D. Operator methods in physical optics. **J. Opt. Soc. Am.**, v. 71, n. 3, p. 334–341, 1981.

150 NAZARATHY, M.; SHAMIR, J. Holography described by operator algebra. **J. Opt. Soc. Am.**, v. 71, n. 5, p. 529–541, May 1981.

151 NAZARATHY, M.; SHAMIR, J. First-order optics: operator representation for systems with loss or gain. **J. Opt. Soc. Am.**, v. 72, n. 10, p. 1398–1408, 1982.

152 NIENHUIS, G.; ALLEN, L. Paraxial wave optics and harmonic oscillators. **Phys. Rev. A**, v. 48, p. 656–665, 1993.

153 VISSER, J.; NIENHUIS, G. Spectrum of an optical resonator with spherical aberration. **J. Opt. Soc. Am. A**, v. 22, n. 11, p. 2490–2497, 2005.

154 HABRAKEN, S. J. M.; NIENHUIS, G. Modes of a twisted optical cavity. **Phys. Rev. A**, v. 75, p. 033819, 2007.

155 MILLER, D. A. B. All linear optical devices are mode converters. **Opt. Express**, v. 20, p. 23985–23993, 2012.

156 AGRAWAL, G. P. **Nonlinear Fiber Optics**. [S.l.]: Academic Press, 2001.

157 ZHANG, Z.; CHEN, L.; BAO, X. A fourth-order Runge-Kutta in the interaction picture method for numerically solving the coupled nonlinear Schr̈odinger equation. **Opt. Express**, v. 18, n. 8, p. 8261–8276, 2010.

158 SHEIK-BAHAE, M. et al. Sensitive measurement of optical nonlinearities using a single beam. **IEEE J. Quantum Electron.**, v. 26, n. 4, p. 760–769, 1990.

159 KOGELNIK, H. Coupled wave theory for thick hologram gratings. **Bell Syst. Tech. J.**, v. 48, p. 2909–2947, 1969.

160 SIEGMAN, A. E. How to (maybe) measure laser beam quality. In: **DPSS (Diode Pumped Solid State) Lasers: Applications and Issues**. [S.l.]: Optical Society of America, 1998. p. MQ1.

161 VISSER, J.; ZELDERS, N. J.; NIENHUIS, G. Wave description of geometric modes of a resonator. **J. Opt. Soc. Am. A**, v. 22, n. 8, p. 1559–1566, 2005.

162 KOGELNIK, H. On the propagation of gaussian beams of light through lenslike media including those with a loss or gain variation. **Appl. Opt.**, v. 4, n. 12, p. 1562–1569, 1965.

163 NAZARATHY, M.; HARDY, A.; SHAMIR, J. Generalized mode propagation in first-order optical systems with loss or gain. **J. Opt. Soc. Am.**, v. 72, n. 10, p. 1409–1420, 1982.

164 ALDA, J. Laser and gaussian beam propagation and transformation. In: ____. Encyclopedia of optical engineering. [S.l.]: Marcel Dekker, Inc., 2003. p. 999–1013.

165 TEAGUE, M. R. Irradiance moments: their propagation and use for unique retrieval of phase. **J. Opt. Soc. Am.**, v. 72, n. 9, p. 1199–1209, 1982.

166 DUAN, L.-M. et al. Inseparability criterion for continuous variable systems. **Phys. Rev. Lett.**, v. 84, p. 2722–2725, 2000.

167 SIMON, R. Peres-Horodecki separability criterion for continuous variable systems. **Phys. Rev. Lett.**, v. 84, p. 2726–2729, 2000.

168 CAPPELLARO, P. et al. Entanglement assisted metrology. **Phys. Rev. Lett.**, v. 94, p. 020502, 2005.

169 GIOVANNETTI, V.; LLOYD, S.; MACCONE, L. Advances in quantum metrology. **Nat. Photon.**, v. 5, n. 4, p. 222–229, 2011.

170 ESCHER, B. M.; FILHO, R. L. de M.; DAVIDOVICH, L. General framework for estimating the ultimate precision limit in noisy quantum-enhanced metrology. **Nat. Phys.**, v. 7, n. 5, p. 406–411, 2011.

171 BOUDEBS, G. et al. Nonlinear characterization of materials using the D4σ method inside a Z-scan 4f-system. **Opt. Lett.**, v. 38, n. 13, p. 2206–2208, Jul 2013.

172 JORGE, K. C. et al. Scattered light imaging method (SLIM) for characterization of arbitrary laser beam intensity profiles. **Appl. Opt.**, v. 53, n. 20, p. 4555–4564, 2014.

173 SHEIK-BAHAE, M. et al. Nonlinear refraction and optical limiting in "thick" media. **Opt. Eng.**, v. 30, n. 8, p. 1228–1235, 1991.

174 FERDINANDUS, M. R. et al. Dual-arm z-scan technique to extract dilute solute nonlinearities from solution measurements. **Opt. Mater. Express**, v. 2, n. 12, p. 1776–1790, 2012.

175 REICHERT, M. et al. Temporal, spectral, and polarization dependence of the nonlinear optical response of carbon disulfide. **Optica**, v. 1, n. 6, p. 436–445, 2014.

176 FLOM, S. R. et al. Ultrafast z-scan measurements of nonlinear optical constants of window materials at 772, 1030, and 1550 nm. **Appl. Opt.**, v. 54, n. 31, p. F123–F128, 2015.

177 BERRY, M. V.; UPSTILL, C. Catastrophe optics: Morphologies of caustics and their diffraction patterns. **Progress in Optics**, v. 18, p. 257–323, 1980.

APPENDIX A – *List of journal publications*

Published

1. AMARAL, A. M.; MEJÍA, H. A.; FALCÃO-FILHO, E. L.; DE ARAÚJO, C. B., D4σ curves described analytically through propagation analysis of transverse irradiance moments, Opt. Lett., v. 41, p. 2081-2084, 2016.

2. JORGE, K. C.; GARCIA, H. A.; AMARAL, A. M.; REYNA, A. S.; DE S. MENEZES, L.; DE ARAÚJO, C. B., Measurements of the nonlinear refractive index in scattering media using the Scattered Light Imaging Method - SLIM, Opt. Express, v. 23, p. 19512-19521, 2015.

3. AMARAL, A. M.; FALCÃO-FILHO, E. L.; DE ARAÚJO, C. B., Characterization of topological charge and orbital angular momentum of shaped optical vortices, Opt. Express, v. 22, p. 30315-30324, 2014.

4. AMARAL, A. M.; FALCÃO-FILHO, E. L.; DE ARAÚJO, C. B., Shaping optical beams with topological charge, Opt. Lett., v. 38, p. 1579-1581, 2013.

Submitted

1. AMARAL, A. M.; FALCÃO-FILHO, E. L.; DE ARAÚJO, C. B., Optical vortices: the concept of topological potential and analogies with two-dimensional electrostatics.

In preparation

1. AMARAL, A. M.; FALCÃO-FILHO, E. L.; DE ARAÚJO, C. B., Using the interaction picture in paraxial wave and geometrical optics problems.

2. AMARAL, A. M.; FALCÃO-FILHO, E. L.; DE ARAÚJO, C. B., Probability distributions for orbital angular momentum and local circulation in vortex beams.

APPENDIX B – *List of conference papers*

1. AMARAL, A. M.; FALCÃO-FILHO*, E. L.; DE ARAÚJO, C. B., Orbital angular momentum and topological charge in shaped optical vortex beams, European Conference on Lasers and Electro-Optics - European Quantum Electronics Conference, Optical Society of America, CH_2_2, 2015.

2. AMARAL*, A. M.; FALCÃO-FILHO, E. L.; DE ARAÚJO, C. B., A Coulomb-like Potential for Optical Vortices[1], Frontiers in Optics 2015, Optical Society of America, FTh1C.3, 2015.

3. AMARAL*, A. M.; FALCÃO-FILHO, E. L.; DE ARAÚJO, C. B., Probability Distributions for Orbital Angular Momentum and Local Circulation in Vortex Beams[1], Frontiers in Optics 2015, Optical Society of America, FTh1C.2, 2015.

4. AMARAL*, A. M.; FALCÃO-FILHO, E. L.; DE ARAÚJO, C. B., Non-cylindrical optical vortices, CLEO: 2014, Optical Society of America, JW2A.102, 2014.

5. AMARAL*, A. M.; FALCÃO-FILHO, E. L.; DE ARAÚJO, C. B., Measurement of orbital angular momentum and topological charge in optical vortices with shaped vortex cores, Frontiers in Optics, Optical Society of America, FTu1C.6, 2014.

6. AMARAL*, A. M.; FALCÃO-FILHO, E. L.; DE ARAÚJO, C. B., Shaping Optical Vortex Beams with Topological Charge, Frontiers in Optics, Frontiers in Optics 2013, Optical Society of America, FM3F.6, 2013.

7. AMARAL, A. M.; FALCÃO-FILHO*, E. L.; DE ARAÚJO, C. B., Effective high-order susceptibilities in composites containing ellipsoidal nanoparticles and nanoshells, Latin America Optics and Photonics Conference, Optical Society of America, LT2A.9, 2012.

[1] (not presented)

APPENDIX C – *Useful mathematical methods*

Throughout this thesis there are various mathematical techniques which are not usually taught in standard physics courses. Due to the importance of such techniques in understanding some of the results discussed, a short review of these topics is given in this appendix. Also, if the reader feels the need for further deepening his understanding of a given topic, there is always some reference which contains more rigorous, detailed and deep discussions.

C.1 *Some properties of Green's functions*

One of the most important tools in solving differential equations are the Green's functions. To introduce the important concepts associated with them, it will be considered as an example the simple case of a classical harmonic oscillator. The position, x, as a function of time, t, when the oscillator has a damping constant γ and natural frequency ω_0^2 and is under an external force $F(t)$ is given by

$$\left(\frac{d^2}{dt^2}+2\gamma\frac{d}{dt}+\omega_0^2\right)x(t)=F(t)\,. \tag{C.1}$$

The solutions to Eq. (C.1) can be split in two parts. Notice that if $F(t)=0$, there must be nontrivial solutions to the problem, which we denote by $x_0(t)$. These are the so called homogeneous solutions, and are such that

$$\left(\frac{d^2}{dt^2}+2\gamma\frac{d}{dt}+\omega_0^2\right)x_0(t)=0. \tag{C.2}$$

To keep the solution general, there must be some part which depends intrinsically of $F(t)$, the inhomogeneous solution, denoted by $x_F(t)$, such that

$$\left(\frac{d^2}{dt^2}+2\gamma\frac{d}{dt}+\omega_0^2\right)x_F(t)=F(t)\,, \tag{C.3}$$

$$x_F(t)=0, \text{ if } F=0. \tag{C.4}$$

An arbitrary solution to Eq. (C.1) shall include both contributions, since their origins are distinct. Notice that these solutions can be added without interfering with each other. Therefore, in general, one has that

$$x(t)=x_0(t)+x_F(t)\,. \tag{C.5}$$

The most important characteristic of Green's functions is that they allow to obtain a solution which is applicable to any $F(t)$. Even if the solution becomes just a formal expression,

without exact solution, it can make the problem amenable to perturbative approximations. This is specially important for nonlinear problems, because $F(t)$ may contain powers of x, and usually there is no analytic solution in such cases. In this appendix, it will be shown how to obtain solutions for the classical harmonic oscillator using Green's functions. Later, it will be discussed how the concept of Green's functions can be generalized for arbitrary partial differential equations. The discussion contained in this appendix is inspired in the Chapter 7 of "Mathematics of Classical and Quantum Physics, Byron and Fuller".

C.1.1 Solution to the classical harmonic oscillator using Green's functions

It is simpler to solve Eq. (C.1) using Fourier transforms. Assuming that $F(t)$ is turned on after $t \to -\infty$ and off before $t \to \infty$, it will have a well behaved Fourier transform. Then, we may represent

$$\tilde{F}(\omega) = \frac{1}{\sqrt{2\pi}} \int_{-\infty}^{\infty} dt F(t)\, e^{i\omega t}, \tag{C.6}$$

and Fourier transforming Eq. (C.1), we have that

$$\frac{1}{\sqrt{2\pi}} \int_{-\infty}^{\infty} dt \left(\frac{d^2}{dt^2} + 2\gamma \frac{d}{dt} + \omega_0^2 \right) x(t)\, e^{i\omega t} = \tilde{F}(\omega). \tag{C.7}$$

Observe that integrating by parts, $\int_{-\infty}^{\infty} dt \ddot{x} e^{i\omega t} = \dot{x} e^{i\omega t}|_{t=-\infty}^{\infty} - \int_{-\infty}^{\infty} dt\,(i\omega)\, \dot{x} e^{i\omega t} = \dot{x} e^{i\omega t}|_{t=-\infty}^{\infty} + (i\omega)\, \dot{x} e^{i\omega t}|_{t=-\infty}^{\infty} + \int_{-\infty}^{\infty} dt\,(i\omega)^2 x e^{i\omega t}$, while $\int_{-\infty}^{\infty} dt \dot{x} e^{i\omega t} = \dot{x} e^{i\omega t}|_{t=-\infty}^{\infty} - \int_{-\infty}^{\infty} dt\,(i\omega)\, x e^{i\omega t}$. Assuming that at $t \to \pm\infty$ both x and $\dot{x}$ tend to zero due to the damping term,γ, the "surface" terms can be neglected and the Fourier transforms pair of x can be written as

$$x(t) = \frac{1}{\sqrt{2\pi}} \int_{-\infty}^{\infty} d\omega \tilde{x}(\omega)\, e^{-i\omega t}, \tag{C.8}$$

$$\tilde{x}(\omega) = \frac{1}{\sqrt{2\pi}} \int_{-\infty}^{\infty} dt\, x(t)\, e^{i\omega t}, \tag{C.9}$$

while the derivatives can be calculated by substituting $\frac{d}{dt} \to -i\omega$. Using this prescription, Eq. (C.7) becomes

$$\left[-\omega^2 - 2i\omega\gamma + \omega_0^2 \right] \tilde{x}(\omega) = \tilde{F}(\omega). \tag{C.10}$$

The term inside the square brackets is never zero for real values of the frequency ω, and since it is not singular, it can be affirmed that

$$\tilde{x}(\omega) = \frac{\tilde{F}(\omega)}{\left[-\omega^2 - 2i\omega\gamma + \omega_0^2 \right]}. \tag{C.11}$$

Equation (C.11) evidently consists of the term x_F as discussed at the beginning of this appendix. There is also the homogeneous solution, x_0, which does not present any interest

for the current discussion. Therefore, the general solution to the harmonic oscillator can be stated as

$$x(t) = x_0(t) + \frac{1}{\sqrt{2\pi}} \int_{-\infty}^{\infty} d\omega \frac{\tilde{F}(\omega)}{\left[-\omega^2 - 2i\omega\gamma + \omega_0^2\right]} e^{-i\omega t}. \tag{C.12}$$

The above expression is a formal solution to the problem, but it is written in terms of the frequency spectrum of the external force. Since both the force and particle position are determined in time, it would be more clarifying if it was possible to express the particle position as a function of $F(t)$. In such representation, it becomes possible to relate a features in $x(t)$ with those from $F(t)$. Using Eq. (C.6) in Eq. (C.12), and integrating in ω, $x(t)$ is rewritten as

$$x(t) = x_0(t) + \int_{-\infty}^{\infty} dt' G\left(t, t'\right) F\left(t'\right), \tag{C.13}$$

$$G\left(t, t'\right) = \int_{-\infty}^{\infty} \frac{d\omega}{2\pi} \frac{e^{-i\omega(t-t')}}{\left[-\omega^2 - 2i\omega\gamma + \omega_0^2\right]}. \tag{C.14}$$

$G\left(t, t'\right)$ is the Green's function for the classical harmonic oscillator, and it contains all of the system response to the input force $F(t)$. The expression for $G\left(t, t'\right)$ can be obtained via a contour integration [Byron and Fuller], and since the calculation details are not relevant for the present discussion, only the result is shown below

$$G\left(t, t'\right) = \theta\left(t - t'\right) e^{-\gamma\left(t-t'\right)} \frac{\sin\left[\sqrt{\omega_0^2 - \gamma^2}\left(t - t'\right)\right]}{\sqrt{\omega_0^2 - \gamma^2}}.$$

For this work, the most important property of this $G\left(t, t'\right)$ is that it satisfies the harmonic oscillator equations of motion in the following form,

$$\left(\frac{d^2}{dt^2} + 2\gamma\frac{d}{dt} + \omega_0^2\right) G\left(t, t'\right) = \delta\left(t - t'\right), \tag{C.15}$$

which can be easily verified by using Eq. (C.14) and remembering the Fourier representation of Dirac delta, $\delta\left(t - t'\right) = \int_{-\infty}^{\infty} d\omega \exp\left[-i\omega\left(t - t'\right)\right]/2\pi$. The relation between the Green's function and the Dirac δ is an extremely useful property, that allow these differential equations to be solved in general under very general conditions. In the following subsection, this argument will be discussed in greater detail.

C.1.2 Green's functions for partial differential equations in n-dimensions

Suppose that L is an operator which contains derivatives, up to the second order, over many variables $x_1, x_2, \ldots, x_N$, where x_n can represent spatial coordinates or time. Then,

$$L = a_0 + a_{1,1}\frac{\partial}{\partial x_1} + a_{1,2}\frac{\partial^2}{\partial x_1^2} + a_{2,1}\frac{\partial}{\partial x_2} + \ldots, \tag{C.16}$$

where the coefficients $a_{n,m}$ are labeled by the indexes m and n which correspond m-th derivative of the variable x_n. Considering that a system being acted upon an external source

$F(x)$ is described by $\psi(x)$, where x is a short-hand notation for all x_n variables, it is wanted to find the solution to the problem

$$L\psi(x) = F(x). \tag{C.17}$$

Neglecting the boundary conditions, the homogeneous solution to Eq. (C.17) is simple to obtain in terms of harmonic functions. The inhomogeneous terms require some extra effort, which is dramatically simplified in terms of the Dirac δ function. The original problem in Eq. (C.17) is very complicated, because it depends on the specifics of $F(x)$ to find the solution to the differential equation. However, notice the following identity

$$F(x) = \int_{-\infty}^{\infty} dx' \delta\left(x - x'\right) F\left(x'\right), \tag{C.18}$$

where it is considered that the integral and the δ is extended over all variables in the system. The dependence on the system variables is entirely contained inside $\delta\left(x - x'\right)$. Physically, if someone knows how to describe the system response to a localized source, the solution to the problem for an specific $F(x)$ can be given by representing $F(x)$ as a sum of such localized sources. Since the system response to a $\delta\left(x - x'\right)$ source should be independent of $F(x)$, one could expect from Eqs. (C.17) and (C.18) that

$$\psi(x) = \int_{-\infty}^{\infty} dx' G\left(x, x'\right) F\left(x'\right), \tag{C.19}$$

what implies that the system response to the impulse is fully contained in the term $G\left(x, x'\right)$. Through a direct substitution, it can be verified that Eq. (C.19) is the solution to Eq. (C.17), given that the Green's function $G\left(x, x'\right)$ satisfies

$$LG\left(x, x'\right) = \delta\left(x - x'\right). \tag{C.20}$$

Since Eq. (C.20) is a differential equation, $G\left(x, x'\right)$ must also satisfy the system's boundary conditions. This is an involved subject, since any homogeneous solution of L, such that $L\psi_0(x) = 0$ can be added to $G\left(x, x'\right)$, and the problem is usually overdetermined. For a more detailed discussion, see [Jackson] Chapter 1. Only simple boundary conditions will be used here, and such refinements will not be considered. To solve Eq. (C.20), it is noticed that the δ function can be represented as the following Fourier transform

$$\delta\left(x - x'\right) = \int_{-\infty}^{\infty} \frac{d^N k}{(2\pi)^N} e^{-ik(x-x')}, \tag{C.21}$$

where it was denoted that $kx = \sum_{n=1}^{N} k_n x_n$ and $d^N k = dk_1 dk_2 \ldots dk_N$.

Taking the Fourier transform of Eq. (C.20) and performing manipulations similar to those done in Eq. (C.7), it is possible to neglect the surface terms and obtain

$$\tilde{L}\tilde{G}(k) / (2\pi)^{N/2} = 1, \tag{C.22}$$

$$\tilde{L} = a_0 + a_{1,1}(-ik_1) + a_{1,2}(-ik_1)^2 + a_{2,1}(-ik_2) + \ldots. \tag{C.23}$$

Assuming that $\tilde{L}$ is not singular for real values of k_n, it is possible to represent

$$\tilde{G}(k) = \frac{1}{(2\pi)^{N/2}} \frac{1}{a_0 + a_{1,1}(-ik_1) + a_{1,2}(-ik_1)^2 + a_{2,1}(-ik_2) + \ldots}, \tag{C.24}$$

and therefore,

$$G(x,x') = \int_{-\infty}^{\infty} \frac{d^N k}{(2\pi)^N} \frac{e^{-ik(x-x')}}{a_0 + a_{1,1}(-ik_1) + a_{1,2}(-ik_1)^2 + a_{2,1}(-ik_2) + \ldots}. \tag{C.25}$$

Up to satisfying the problem's boundary conditions, Eq. (C.25) can be used to solve a large variety of differential equations using the Green's functions approach. In what follows, some cases of interest will be discussed.

C.1.3 Green's function for the SVEA equation

As is discussed in Sec. 2.2, light beams in the regime of wave optics whose transverse extension is much larger than the wavelength can be described by

$$\left(\nabla_\perp^2 + 2ik_0 \frac{\partial}{\partial z}\right) A = 0. \tag{C.26}$$

In this case, $L = \nabla_\perp^2 + 2ik_0 \frac{\partial}{\partial z}$. Using Eq. (C.25), and representing $\mathbf{r} = (x,y,z)$ and $\mathbf{k} = (k_x, k_y, k_z)$, the Green function for this problem is

$$G_{\text{SVEA}}(\mathbf{r},\mathbf{r}') = \int_{-\infty}^{\infty} \frac{d^3\mathbf{k}}{(2\pi)^3} \frac{e^{-i\mathbf{k}(\mathbf{r}-\mathbf{r}')}}{2k_0 k_z - k_x^2 - k_y^2 + i\epsilon}. \tag{C.27}$$

where it was added an infinitesimal displacement $i\epsilon$ in the complex plane. The idea behind this term the displacement is that it operates in a similar way to the dissipative term in the harmonic oscillator, and will avoid the pole at $k_z = \left(k_x^2 + k_y^2\right)/2k_0$. The dk_z integral can be easily performed using the residue theorem. When $z > z'$, the integration contour must be closed in the lower complex plane, and

$$\int_{-\infty}^{\infty} dk_z \frac{e^{-ik_z(z-z')}}{2k_0 k_z - k_x^2 - k_y^2 + i\epsilon} = 2\pi i \exp\left[\frac{-i(z-z')}{2k_0}\left(k_x^2 + k_y^2\right) - \frac{i\epsilon}{2k_0}(z-z')\right], \tag{C.28}$$

while for $z < z'$, the contour must be closed in the upper complex plane, which does not contain any pole and

$$\int_{-\infty}^{\infty} dk_z \frac{e^{-ik_z(z-z')}}{2k_0 k_z - k_x^2 - k_y^2 + i\epsilon} = 0. \tag{C.29}$$

Therefore, in the limit $\epsilon \to 0$,

$$G_{\text{SVEA}}(\mathbf{r},\mathbf{r}') = i\theta(z-z') \int_{-\infty}^{\infty} \frac{dk_x dk_y}{(2\pi)^2} \exp\left[\frac{-i(z-z')}{2k_0}\left(k_x^2 + k_y^2\right) - ik_x(x-x') - ik_y(y-y')\right]. \tag{C.30}$$

In the context of the current work, $G_{\text{SVEA}}(x,x')$ is written in two equivalent representations. One representation consists in performing the integrals along k_x and k_y, such that

$G_{\mathrm{SVEA}}\left(\mathbf{r},\mathbf{r}'\right)$ is an explicit function of the coordinates. Observing that the integrands are Gaussians, and using the identity

$$\int dk e^{-ak^2+bk} = \sqrt{\frac{\pi}{a}} e^{-b^2/4a}, \tag{C.31}$$

it is easily verified that

$$G_{\mathrm{SVEA}}\left(\mathbf{r},\mathbf{r}'\right) = \theta\left(z-z'\right)\frac{k_0}{2\pi\left(z-z'\right)}\exp\left[-i\frac{k_0}{2\left(z-z'\right)}\left(\mathbf{r}_\perp-\mathbf{r}'_\perp\right)^2\right], \tag{C.32}$$

where $\mathbf{r}_\perp = \left(x,y,0\right)$.

The representation of $G_{\mathrm{SVEA}}\left(x,x'\right)$ which shows a greater interest for the current work consists in identifying the previously expressed property of Fourier transforms, that $(-ik_n)$ and $\partial/\partial x_n$ can be used interchangeably, as long as the function under analysis and its derivatives decays sufficiently fast far from the sample. We assume that the physical field of interest are square integrable, and therefore such assumption is valid. Considering in Eq. (C.30) that $\left(k_x^2+k_y^2\right) = -\nabla_\perp^2$, where $\nabla_\perp^2$ acts only over x,y, this operator can be removed from the integral, resulting in

$$G_{\mathrm{SVEA}}\left(\mathbf{r},\mathbf{r}'\right) = i\theta\left(z-z'\right)\exp\left[\frac{i\left(z-z'\right)}{2k_0}\nabla_\perp^2\right]\delta\left(\mathbf{r}_\perp-\mathbf{r}'_\perp\right). \tag{C.33}$$

Equation (C.33) is very interesting because, contrarily to Eq. (C.32), the dependencies in the propagation and in the transverse coordinates were factorized in a product. Therefore, transversal effects and propagation can be independently considered. Although this might seem to be a minor difference, if this fact is adequately used, it can simplify the calculations of many complex systems in optics. It becomes possible to completely specify the behavior of a given optical system for any input light beam, since the propagation and the optical elements can be considered.

The usage envisioned for Eq. (C.33) is to obtain, given an initial field configuration at a plane $z=a$, $A_0\left(\mathbf{r}_\perp,a\right)$, the solution in a plane $z=b$, $A\left(\mathbf{r}_\perp,b\right)$. This in principle requires the correct matching of the propagator to this boundary condition. It will be shown here that this is indeed the case for Eq. (C.33). Notice that

$$\lim_{z\to z'^+} G_{\mathrm{SVEA}}\left(\mathbf{r},\mathbf{r}'\right) = i\delta\left(\mathbf{r}_\perp-\mathbf{r}'_\perp\right), \tag{C.34}$$

and therefore the solution at the plane $z'=a$ can be represented as

$$A_0\left(\mathbf{r}_\perp,a\right) = -i\lim_{z\to a^+}\int dx'dy' G_{\mathrm{SVEA}}\left(\mathbf{r},\mathbf{r}'\right)A_0\left(\mathbf{r}'_\perp,a\right). \tag{C.35}$$

It then becomes reasonable to hypothesize that the solution at $z=b$ is given by

$$A_0\left(\mathbf{r}_\perp,b\right) = -i\int dx'dy' G_{\mathrm{SVEA}}\left(\mathbf{r},\mathbf{r}'\right)A_0\left(\mathbf{r}'_\perp,a\right), \tag{C.36}$$

$$= \theta\left(b-a\right)\exp\left[\frac{i\left(b-a\right)}{2k_0}\nabla_\perp^2\right]A_0\left(\mathbf{r}_\perp,a\right). \tag{C.37}$$

C.2 Some useful operator identities

In this appendix, some operator identities used throughout the manuscript are summarized, for the reader's convenience.

Commutator

Given two operators $\hat{A}$ and $\hat{B}$, their commutator is defined as [40]

$$\left[\hat{A},\hat{B}\right] = \hat{A}\hat{B} - \hat{B}\hat{A}. \tag{C.38}$$

Baker-Hausdorff lemma

Given two operators $\hat{G}$ and $\hat{A}$, and λ number, the Baker-Hausdorff lemma [40] can be stated as

$$e^{i\hat{G}\lambda}\hat{A}e^{-i\hat{G}\lambda} = \hat{A} + i\lambda\left[\hat{G},\hat{A}\right] + \frac{i^2\lambda^2}{2!}\left[\hat{G},\left[\hat{G},\hat{A}\right]\right] + \ldots + \frac{i^n\lambda^n}{n!}\left[\hat{G},\left[\hat{G},\ldots\left[\hat{G},\hat{A}\right]\right]\right] + \ldots. \tag{C.39}$$

Similarity transformation over functions of operators

Suppose that a function can be written as $f = f\left(\hat{\boldsymbol{x}},\hat{\boldsymbol{p}}\right)$. If there is an invertible operator $\hat{S}$, such that $\hat{S}^{-1}\hat{S} = \hat{1}$, one might want to calculate $\hat{S}^{-1}f\left(\hat{\boldsymbol{x}},\hat{\boldsymbol{p}}\right)\hat{S}$. For example, this operator might be needed to change between distinct representations. If $f\left(\hat{\boldsymbol{x}},\hat{\boldsymbol{p}}\right)$ can be expressed as a Taylor series of the operators $\hat{\boldsymbol{x}}$ and $\hat{\boldsymbol{p}}$, by inserting $\hat{S}^{-1}\hat{S}$ between the products of $\hat{\boldsymbol{x}}$ and $\hat{\boldsymbol{p}}$ it can be showed that

$$\hat{S}^{-1}f\left(\hat{\boldsymbol{x}},\hat{\boldsymbol{p}}\right)\hat{S} = f\left(\hat{S}^{-1}\hat{\boldsymbol{x}}\hat{S},\hat{S}^{-1}\hat{\boldsymbol{p}}\hat{S}\right). \tag{C.40}$$

Commutator of an operator $\hat{A}$ with a function of a non-commuting operator $\hat{B}$

Consider two operators $\hat{A}$ and $\hat{B}$ such that $\left[\hat{A},\hat{B}\right] = 1$. If $f = f\left(\hat{B}\right)$ can be expanded in a Taylor series, it can be showed that

$$\left[\hat{A},f\left(\hat{B}\right)\right] = \frac{df\left(\hat{B}\right)}{d\hat{B}}, \tag{C.41}$$

where it should be understood that the derivative is taken with respect to the argument $\hat{B}$. In particular for 1D, for functions $f\left(\hat{p}_x\right)$ and $g\left(\hat{x}\right)$ it can be obtained that [40]

$$\left[\hat{x},f\left(\hat{p}_x\right)\right] = i\frac{df\left(\hat{p}_x\right)}{d\hat{p}_x}, \tag{C.42}$$

$$\left[\hat{p}_x,g\left(\hat{x}\right)\right] = -i\frac{dg\left(\hat{x}\right)}{d\hat{x}}. \tag{C.43}$$

C.3 $\hat{\boldsymbol{p}}$ operator in $\hat{\boldsymbol{x}}$ basis

To obtain the $\hat{\boldsymbol{p}}$ operator in $\hat{\boldsymbol{x}}$ basis, it is considered initially the 1D case. In this appendix, only the SP is used, but the sub-indices are omitted for clarity in the notation. The matrix element of the commutator (6.9) is $\langle x|\left[\hat{x}\hat{p}_x - \hat{p}_x\hat{x}\right]|x'\rangle = i\langle x|x'\rangle$, or

$$\langle x|\,\hat{p}_x\,|x'\rangle = \frac{i}{(x-x')}\langle x|x'\rangle, \tag{C.44}$$

where the last line is verified for all $x \neq x'$, to avoid a division by zero. Assuming $x' = x+\epsilon$, the action of $\hat{p}_x$ over a state ket can be computed using the completeness relation, $1 = \int dx'\,|x'\rangle\langle x'|$, as $\langle x|\hat{p}_x|\psi\rangle = \int_{x'\neq x} dx'\langle x|\hat{p}_x|x'\rangle\langle x'|\psi\rangle = \int_{\epsilon\neq 0} d\epsilon\frac{-i}{\epsilon}\langle x|x+\epsilon\rangle\langle x+\epsilon|\psi\rangle$. Since $\langle x+\epsilon|\psi\rangle = \psi(x+\epsilon)$, one may write

$$\langle x|\hat{p}_x|\psi\rangle \approx \int_{\epsilon\neq 0} d\epsilon\frac{-i}{\epsilon}\langle x|x+\epsilon\rangle\left[\psi(x)+\epsilon\frac{d\psi(x)}{dx}\right]. \tag{C.45}$$

The first term in the integrand is odd with respect to the integration variable, since ϵ is odd, while the Dirac delta is even, and thus integrates to zero. Terms of higher order in ϵ are null because they the integration interval is small due to $\langle x|x+\epsilon\rangle \approx \delta(\epsilon)$. By the other hand, the second term in the square bracket is well behaved. Using that $\langle x|x+\epsilon\rangle = \delta(\epsilon)$, and, since the removal of a single point does not change the area enclosed by the curve, it is true that $\int_{\epsilon\neq 0} d\epsilon\delta(\epsilon) = 1$, implying that

$$\langle x|\hat{p}_x|\psi\rangle = \left(-i\frac{d}{dx}\right)\langle x|\psi\rangle. \tag{C.46}$$

The generalization to 2D is straightforward and follows closely the description above, resulting in

$$\langle \mathbf{r}|\hat{\mathbf{p}}|\psi\rangle = -i\nabla_\perp\langle \mathbf{r}|\psi\rangle. \tag{C.47}$$

Another important relation between $\hat{\boldsymbol{x}}$ and $\hat{\boldsymbol{p}}$ is the calculation of the basis overlap $\langle \mathbf{r}|\mathbf{p}\rangle$. Using in (C.47) $\psi = \mathbf{p}$, where $\hat{\mathbf{p}}\,|\mathbf{p}\rangle = \mathbf{p}\,|\mathbf{p}\rangle$, it becomes possible to verify that

$$\langle \mathbf{r}|\mathbf{p}\rangle = \frac{1}{2\pi}\exp\left(i\mathbf{p}\cdot\mathbf{r}\right), \tag{C.48}$$

where the factor of $(2\pi)^{-1}$ ensures the normalization.

C.4 Field solution in SP

In this appendix it is performed the detailed calculation of $|\psi,z;a\rangle_S$ in SP. Starting from Eq. (6.18)

$$|\psi,z;a\rangle_S = |\psi,a;a\rangle_S + \int_a^z \frac{dz'}{i}\hat{H}_S\left(\hat{\mathbf{x}}_S,\hat{\mathbf{p}}_S,z'\right)|\psi,z';a\rangle_S, \tag{C.49}$$

and considering $\hat{H}_S = \lambda\hat{H}_S$, and the following series expansion of the state,

$$|\psi,z;a\rangle_S = |\psi,z;a\rangle_S^{(0)} + \lambda\,|\psi,z;a\rangle_S^{(1)} + \lambda^2\,|\psi,z;a\rangle_S^{(2)} + \ldots. \tag{C.50}$$

By equating to zero the coefficients of the distinct powers of λ,

$$\left|\psi,z;a\right\rangle_S^{(0)} = \left|\psi,a;a\right\rangle_S + \int_a^z \frac{dz'}{i}\hat{H}_S\left|\psi,z';a\right\rangle_S^{(0)}, \tag{C.51}$$

$$\left|\psi,z;a\right\rangle_S^{(n)} = \int_a^z \frac{dz'}{i}\hat{H}_S\left(\hat{\mathbf{x}}_S,\hat{\mathbf{p}}_S,z'\right)\left|\psi,z';a\right\rangle_S^{(n-1)}. \tag{C.52}$$

Equations (C.51) and (C.52) are Volterra equations of the first kind, and thus have unique, well defined solutions. The lowest order terms are

$$\left|\psi,z;a\right\rangle_S^{(0)} = \left|\psi,a;a\right\rangle_S, \tag{C.53}$$

$$\left|\psi,z;a\right\rangle_S^{(1)} = \int_a^z \frac{dz'}{i}\hat{H}_S\left(\hat{\mathbf{x}}_S,\hat{\mathbf{p}}_S,z'\right)\left|\psi,a;a\right\rangle_S, \tag{C.54}$$

$$\left|\psi,z;a\right\rangle_S^{(2)} = \int_a^z \frac{dz'}{i}\hat{H}_S\left(\hat{\mathbf{x}}_S,\hat{\mathbf{p}}_S,z'\right)\int_a^{z'} \frac{dz"}{i}\hat{H}_S\left(\hat{\mathbf{x}}_S,\hat{\mathbf{p}}_S,z"\right)\left|\psi,a;a\right\rangle_S. \tag{C.55}$$

The above expressions can be simplified in terms of the z ordering operator $\hat{Z}$, which puts the higher values of z inside the integrands to the left. This is equivalent to the time ordering operator from quantum field theory [41], but considered for the z coordinate, instead of time. The above expressions can be simplified as

$$\begin{aligned}
\left|\psi,z;a\right\rangle_S^{(0)} &= \hat{Z}\{1\}\left|\psi,a;a\right\rangle_S,\\
\left|\psi,z;a\right\rangle_S^{(1)} &= \hat{Z}\left\{\frac{1}{1!}\int_a^z \frac{dz'}{i}\hat{H}_S\left(\hat{\mathbf{x}}_S,\hat{\mathbf{p}}_S,z'\right)\right\}\left|\psi,a;a\right\rangle_S,\\
\left|\psi,z;a\right\rangle_S^{(2)} &= \hat{Z}\left\{\frac{1}{2!}\left[\int_a^z \frac{dz'}{i}\hat{H}_S\left(\hat{\mathbf{x}}_S,\hat{\mathbf{p}}_S,z'\right)\right]^2\right\}\left|\psi,a;a\right\rangle_S,\\
&\vdots\\
\left|\psi,z;a\right\rangle_S^{(m)} &= \hat{Z}\left\{\frac{1}{m!}\left[\int_a^z \frac{dz'}{i}\hat{H}_S\left(\hat{\mathbf{x}}_S,\hat{\mathbf{p}}_S,z'\right)\right]^m\right\}\left|\psi,a;a\right\rangle_S.
\end{aligned}$$

The solution then becomes,

$$\left|\psi,z;a\right\rangle_S = \hat{G}_{z,a}\left|\psi,a;a\right\rangle_S, \tag{C.56}$$

$$\hat{G}_{z,a} = \hat{Z}\left\{\exp\left[-i\int_a^z dz'\hat{H}_S\left(\hat{\mathbf{x}}_S,\hat{\mathbf{p}}_S,z'\right)\right]\right\}. \tag{C.57}$$

C.5 Evolution of operators in HP

Starting from Eqs. (6.26) and (6.27), and omitting the z dependence for clarity,

$$\hat{O}_H = \hat{G}_H^\dagger \hat{O}_S \hat{G}_H, \tag{C.58}$$

$$i\frac{d\hat{G}_H}{dz} = \hat{H}_S\hat{G}_H, \tag{C.59}$$

one has that $i\frac{d\hat{O}_H}{dz} = i\frac{d\hat{G}_H^\dagger}{dz}\hat{O}_S\hat{G}_H + \hat{G}_H^\dagger\hat{O}_S i\frac{d\hat{G}_H}{dz} + \hat{G}_H^\dagger i\frac{\partial\hat{O}_S}{\partial z}\hat{G}_H$. Using that $-i\frac{d\hat{G}_H^\dagger}{dz} = \hat{G}_H^\dagger\hat{H}_S^\dagger$, denoting by $\left[\frac{\partial\hat{O}_S}{\partial z}\right]_H = \hat{G}_H^\dagger\frac{\partial\hat{O}_S}{\partial z}\hat{G}_H$ the HP representation of the z derivative of $\hat{O}_S$, and inserting $\hat{G}_H^{\dagger(-1)}\hat{G}_H^\dagger = \hat{1}$ in the first term, and $\hat{G}_H\hat{G}_H^{-1} = \hat{1}$ in the second,

$$i\frac{d\hat{O}_H}{dz} = -\hat{G}_H^\dagger\hat{H}_S^\dagger\hat{G}_H^{\dagger(-1)}\hat{O}_H + \hat{O}_H\hat{G}_H^{-1}\hat{H}_S\hat{G}_H + i\left[\frac{\partial\hat{O}_S}{\partial z}\right]_H. \tag{C.60}$$

Equation (C.60) suggests the definition of

$$\hat{H}_{H'} = \hat{G}_H^{-1}\hat{H}_S\hat{G}_H. \tag{C.61}$$

Notice that defining $\hat{H}_H$ by Eq. (C.58), $\hat{H}_{H'} \neq \hat{H}_H$. For problems that does not include absorption, $\hat{G}_H^{-1} = \hat{G}_H^\dagger$ and $\hat{H}_{H'} = \hat{H}_H = \hat{H}_H^\dagger$. In terms of $\hat{H}_{H'}$, Eq. (C.60) becomes

$$i\frac{d\hat{O}_H}{dz} = \hat{O}_H\hat{H}_{H'} - \hat{H}_{H'}^\dagger\hat{O}_H + i\left[\frac{\partial\hat{O}_S}{\partial z}\right]_H, \tag{C.62}$$

while if the system does not include absorption, the more well known limit [40] is obtained

$$i\frac{d\hat{O}_H}{dz} = \left[\hat{O}_H, \hat{H}_H\right] + i\left[\frac{\partial\hat{O}_S}{\partial z}\right]_H. \tag{C.63}$$

As a final comment, it is worth mentioning that if $\hat{O}_H$ is Hermitean, $\hat{O}_H = \hat{O}_H^\dagger$, one has that Eq. (C.62) implies that $\hat{O}_H$ remains Hermitian under propagation.

C.6 Evolution of operators in IP

For the evolution of operators in IP, we notice that the mean value of an operator $\hat{O}_I$ is written in terms of the initial condition as

$$\left\langle\hat{O}_I\right\rangle = \frac{\left\langle\psi_a\middle|\hat{T}_{z,a}^\dagger\hat{O}_I\hat{T}_{z,a}\middle|\psi_a\right\rangle}{\left\langle\psi_a\middle|\hat{T}_{z,a}^\dagger\hat{T}_{z,a}\middle|\psi_a\right\rangle}, \tag{C.64}$$

$$\hat{O}_I = \hat{G}_{z,a}^{(0)-1}\hat{O}_S\hat{G}_{z,a}^{(0)}, \tag{C.65}$$

where the arguments of the operators were suppressed for clarity.

Using Eq. (6.48) in (6.44) one obtains that

$$i\frac{\partial}{\partial z}\hat{T}_{z,a} = \hat{V}_I(\hat{\mathbf{x}}_I, z)\,\hat{T}_{z,a}. \tag{C.66}$$

Now it becomes possible to evaluate $i\frac{d}{dz}\left\langle\hat{O}_I\right\rangle$. Including the derivative of the denominator of Eq. (C.64) in the evolution equation for $\hat{O}_I$, one obtains that $i\frac{d}{dz}\left\langle\hat{O}_I\right\rangle = \left\langle i\frac{d}{dz}\hat{O}_I\right\rangle$ or

$$i\frac{d}{dz}\hat{O}_I = \hat{T}_{z,a}^{\dagger-1}i\frac{d}{dz}\left(\hat{T}_{z,a}^\dagger\hat{O}_I\hat{T}_{z,a}\right)\hat{T}_{z,a}^{-1} - i\gamma(z)\,\hat{O}_I, \tag{C.67}$$

$$\gamma(z) = \frac{\left\langle\psi_a\middle|\frac{d}{dz}\left(\hat{T}_{z,a}^\dagger\hat{T}_{z,a}\right)\middle|\psi_a\right\rangle}{\left\langle\psi_a\middle|\hat{T}_{z,a}^\dagger\hat{T}_{z,a}\middle|\psi_a\right\rangle}. \tag{C.68}$$

Equation (C.67) contains two terms: $\hat{T}_{z,a}^{\dagger -1} i \frac{d}{dz}\left(\hat{T}_{z,a}^{\dagger} \hat{O}_I \hat{T}_{z,a}\right) \hat{T}_{z,a}^{-1}$ is equivalent to the terms to the right of Eq. (C.60), while the factor $\gamma(z)$ represents the change of the field normalization over $\hat{O}_I$ due to the absorption. Evaluating separately, it is obtained that

$$\hat{T}_{z,a}^{\dagger -1} i \frac{d}{dz}\left(\hat{T}_{z,a}^{\dagger} \hat{O}_I \hat{T}_{z,a}\right) \hat{T}_{z,a}^{-1} = \hat{O}_I \hat{H}_I - \hat{H}_I^{\dagger} \hat{O}_I + i\alpha_0 \hat{O}_I + \left[i \frac{\partial}{\partial z}\left(\hat{O}_S\right)\right]_I, \tag{C.69}$$

$$\gamma(z) = \frac{\left\langle \psi_a \middle| \hat{T}_{z,a}^{\dagger}\left(-\hat{\alpha}_I'\right) \hat{T}_{z,a} \middle| \psi_a \right\rangle}{\left\langle \psi_a \middle| \hat{T}_{z,a}^{\dagger} \hat{T}_{z,a} \middle| \psi_a \right\rangle}, \tag{C.70}$$

where $\hat{\alpha}_I'$ is the spatially dependent absorption profile, which is contained in $\hat{V}_I$.

Notice that, according to the definition (6.46), $\gamma(z) = -\left\langle \hat{\alpha}_I' \right\rangle$. Thus, using Eqs. (C.69) and (C.70) in Eq. (C.67),

$$i \frac{d}{dz} \hat{O}_I = \hat{O}_I \hat{H}_I - \hat{H}_I^{\dagger} \hat{O}_I + i \left\langle \hat{\alpha}_I \right\rangle \hat{O}_I + \left[i \frac{\partial}{\partial z}\left(\hat{O}_S\right)\right]_I, \tag{C.71}$$

where now $\langle \hat{\alpha}_I \rangle$ is the average of the total absorption operator, $\hat{\alpha}_I = \alpha_0 + \hat{\alpha}_I'$. Notice that, contrarily to what happened for the HP, $\hat{H}_I$ is the Hamiltonian in the IP for any $\hat{V}_I$, including absorption or not. In HP, it was defined in Eq. (C.61) an operator $\hat{H}_{H'}$ which was the HP Hamiltonian only when the system did not include absorption. Since $\hat{H}_I^{\dagger} = \hat{H}_I + i\hat{\alpha}_I$, Eq. (C.71) can be rewritten as Eq. 6.50.

C.7 Some useful relations for Gaussian beams

Gaussian-shaped beams are ubiquitous in optics, and also it is very simple to evaluate many of their characteristics. Assuming that we have a beam as

$$\left\langle \boldsymbol{r} | \phi \right\rangle = N e^{-a\boldsymbol{r}^2}, \tag{C.72}$$

where a is complex, it is possible to verify that in the $\left|\boldsymbol{p}\right\rangle$ basis,

$$\left\langle \boldsymbol{p} | \phi \right\rangle = \frac{N}{2a} e^{-\frac{\boldsymbol{p}^2}{4a}}. \tag{C.73}$$

If we want to evaluate the beam width in position or in transverse momentum, we may use for example that

$$\frac{\int d^2\boldsymbol{r}\, \boldsymbol{r}^2 \left|\left\langle \boldsymbol{r} | \psi \right\rangle\right|^2}{\int d^2\boldsymbol{r} \left|\left\langle \boldsymbol{r} | \psi \right\rangle\right|^2} = -\frac{d}{dc} \log\left[\int d^2\boldsymbol{r} e^{-c\boldsymbol{r}^2} \right]\Bigg|_{c=a}, \tag{C.74}$$

$$\frac{\int d^2\boldsymbol{p}\, \boldsymbol{p}^2 \left|\left\langle \boldsymbol{p} | \psi \right\rangle\right|^2}{\int d^2\boldsymbol{p} \left|\left\langle \boldsymbol{p} | \psi \right\rangle\right|^2} = -\frac{d}{dc} \log\left[\int d^2\boldsymbol{p} e^{-c\boldsymbol{p}^2} \right]\Bigg|_{c=\frac{1}{4a}}, \tag{C.75}$$

Index